UNIVERSITY OF OKLAHOMA

GRADUATE COLLEGE

MESOSCALE, POROUS MEDIA HEAT RECIRCULATING COMBUSTOR

A Dissertation

SUBMITTED TO THE GRADUATE FACULTY

In partial fulfillment of the requirements for

The degree of

Doctor of Philosophy

By

TIMOTHY L. MARBACH
Norman, Oklahoma
2005

Downloaded from SHAREOK. Persistent Handle URL: https://hdl.handle.net/11244/902

UMI Number: 3176315



UMI Microform 3176315

Copyright 2005 by ProQuest Information and Learning Company.
All rights reserved. This microform edition is protected against unauthorized copying under Title 17, United States Code.

ProQuest Information and Learning Company
300 North Zeeb Road
P.O. Box 1346
Ann Arbor, MI 48106-1346

MESOSCALE, POROUS MEDIA HEAT RECIRCULATING COMBUSTOR

A Dissertation APPROVED FOR THE
SCHOOL OF AEROSPACE AND MECHANICAL ENGINEERING

By

_____
Ajay K. Agrawal

_____
Ramkumar Parthasarathy

_____
Cengiz M. Altan

_____
Feng-Chyuan Lai

_____
Dimitrios V. Papavassiliou

© Copyright by TIMOTHY L. MARBACH 2005
All Rights Reserved.

Acknowledgements

This dissertation is dedicated to my father, Steve Marbach, Sr (1954-1998).

I would like to thank many people for their help throughout my doctoral work and throughout my life.

I would especially like to thank my mentor, Ajay Agrawal, for his guidance during my graduate studies. He took the time to learn about me as a researcher and as a person and he used that knowledge to guide, push and challenge me to achieve great things. His eagerness to venture into new areas, such as PIM and mesoscale combustion, was inspirational. In addition to the technical, problem solving and critical thinking skills that he fostered, he served as an example that a positive attitude and hard work will help you achieve your goals.

I am very grateful for the guidance of my committee members, Cengiz Altan, Feng-Chyuan Lai, Kumar Parthasarathy, and Dimitrios Papavassiliou. Billy Mays, Greg Williams and the AME shop staff were extremely helpful throughout the course of my graduate studies and helped me tremendously by transforming conceptual drawings into first-class experimental apparatuses.

I would like to thank many colleagues that have helped me in so many ways, including Sandeep Alavandi, Vijay Sadasivuni, Ryan Heatly, Ryan Newburn, Don Wicksall, Rajani Satti, Ozgur Pulat and Chendhil Periasamy.

I would also like to thank the Graduate Assistance in Areas of National Need (GAANN) Fellowship program and the U.S. Army Research Laboratory for supporting this work.

Finally and most importantly, I would like to thank the two women in my life, my mother and my fiancé. Without their love, support and encouragement, this would not have been possible.

Table of Contents

1. Introduction……....1
    1.1 Mesoscale Combustion ……2
    1.2 Porous Inert Media (PIM) Combustion …….....5
    1.3 Heat Recirculating, PIM Combustor Concept ……....9

2. Objectives ……..12

3. Experimental Study of Macroscale PIM Combustion ……..14
    3.1 Experimental Setup and Procedure ……..14
    3.2 Results and Discussion ……..19
        3.2.1 Flow Characteristics ……..19
        3.2.2 Combustion Characteristics ……..25
            3.2.2.1 Effect of Reactant Flowrate ……..26
            3.2.2.2 Surface vs. Interior Combustion ……..27
            3.2.2.3 Effect of Combustion Zone Pore Size ……..28
            3.2.2.4 Effect of Preheat Zone Pore Size ……..29
    3.3 Conclusions ……..39

4. Mesoscale Combustor Experiments……41
    4.1 Experimental Setup and Procedure ……..42
    4.2 Results and Discussion ……..47
        4.2.1 Pressure Loss ……..49
        4.2.2 Reactant Preheat Temperature ……..52
        4.2.3 Exterior Surface Temperature ……..54
        4.2.4 Product Gas Temperature ……..59
            4.2.4.1 General Characteristics ……..60
            4.2.4.2 Effect of PIM in Preheating Annulus ……..60
            4.2.4.3 Effect of Exterior Surface Insulation ……..61
            4.2.4.4 Effect of Reactant Flowrate ……..62
            4.2.4.5 Effect of Equivalence Ratio ……..62
        4.2.5 Pollutant Emissions ……..72
            4.2.5.1 General Characteristics ……..72
            4.2.5.2 Effect of PIM in Preheating Annulus ……..73
            4.2.5.3 Effect of Exterior Surface Insulation ……..74
            4.2.5.4 Effect of Heat Release Rate ……..74
            4.2.5.5 Effect of Equivalence Ratio ……..75
        4.2.6 Energy Balance Calculations ……..81
            4.2.6.1 Heat Recirculation ……..81
            4.2.6.2 Heat Loss: Method 1 ……..83
            4.2.6.3 Heat Loss: Method 2 ……..85
    4.3 Conclusions ……..89

5. Computational Fluid Dynamics Analyses ……..91
5.1 Description of the Model ……..91
5.1.1 Computational Domain ……..92
5.1.2 Governing Equations ……..94
5.1.3 Modifications to the Governing Equations ……..95
5.1.3.1 Reactant Inlet ……..96
5.1.5.2 Reaction Zone ……..97
5.1.5.3 PIM Zone ……..98
5.1.5.4 Radiation ……..99
5.1.4 Physical Properties ……103
5.1.5 Boundary Conditions ……105
5.1.6 Computational Procedure ……106
5.2 Validation of the Model ……108
5.2.1 Numerical Validity ……108
5.2.1.1 Grid Size ……108
5.2.1.2 Discrete Ordinates Model ……114
5.2.2 Physical Validity ……117
5.3 Fluid Flow and Temperature Fields ……125
5.3.1 Fluid Flow ……125
5.3.2 Temperature Contours ……132
5.4 Thermal Analysis ……138
5.4.1 Gas Enthalpy Analysis ……139
5.3.2 Heat Conduction at Combustor Wall ……142
5.3.3 Surface Heat Transfer ……146
5.5 Conclusions ……156

6. Parametric Studies ……158
6.1 Axial Conduction ……159
6.1.1 Combustor Wall Thickness (t) ……160
6.1.2 Combustor Wall Thermal Conductivity (k) ……166
6.1.3 Lid Thermal Conductivity (k_{Lid}) ……171
6.1.4 Conclusions ……180
6.2 Radiation Across the Preheating Annulus ……181
6.2.1 Surface Emissivities ……181
6.2.2 PIM in Preheating Annulus ……189
6.2.3 Radiation Shield……197
6.2.4 Conclusions ……205
6.3 Proposed Phase II Combustor Design ……206
6.3.1 Design Description ……207
6.3.2 Predicted Performance of Phase II Combustor Design ……211
6.3.2.1 Effect of Equivalence Ratio ……214
6.3.2.2 Effect of Reactant Flowrate ……219
6.2.3.3 Effect of Combustor Size ……224
6.4 Conclusions ……229

7. Phase II Mesoscale Combustion Experiments ……230
7.1 Experimental Setup and Procedure ……230
7.2 Results and Discussion ……237
7.3 Conclusions ……244

8. Conclusions and Recommendations ……245

Bibliography ……247

Appendix A: Uncertainty Analysis Sample Calculations ……251

Appendix B: User Defined Function for Heat Source Calculation ……252

Appendix C: Comparison of Specific Heat Capacity of Air, Reactants, and Products ……253

Appendix D: Physical Properties for Computational Model ……254

Appendix E: Equivalence Ratio Calculation for Phase II Mesoscale Combustor….257

Appendix F: Radiation Correction for Product Gas Temperature Measurement…..258

List of Tables

Table 4.1. Heat recirculation calculations ……..82

Table 4.2. Heat loss calculations by the exterior surface temperature method ..84

Table 4.3. Heat Loss Calculations: Product Gas Temperature Method ……..86

Table 4.4. Summary of Heat Transfer Calculations ……..88

Table 5.1. Physical Property Correlations ……104

Table 5.2. Under-Relaxation Factors ……107

Table 5.3. Summary of Surface Heat Flux ……155

Table 6.1. Effect of equivalence ratio operating conditions ……214

Table 6.2. Effect of reactant flowrate operating conditions ……....219

Table 6.3. Effect of combustor size operating conditions ……224

Table 7.1. Effect of flowrate on average exterior surface temperature and percent heat loss to the surroundings ($\Phi = 0.70$) ……238

Table 7.2. Effect of reactant flowrate on heat loss to the surroundings ($\Phi = 0.70$)...239

List of Figures

Figure 1.1. Schematic representation of (a) surface combustion and (b) interior combustion ……8

Figure 1.2. Heat recirculating combustor concept using porous inert media. ..11

Figure 3.1. Schematic Diagram of the Experimental Setup for Macro-scale PIM Combustion ……..18

Figure 3.2. Effect of Pore Size on Cold Flow Pressure Drop ……..21

Figure 3.3. Effect of Combustion on Pressure Drop for Baseline Configuration (32-8-8-8), $\Phi = 0.6$ ……..22

Figure 3.4. Contour plot of axial velocity at the PIM exit using cold air for L = 60 cm ……..23

Figure 3.5. Profile of turbulence intensity at the PIM exit Profile for L = 60 cm ..24

Figure 3.6. Visual images at baseline conditions (a) surface combustion and (b) interior combustion ……..30

Figure 3.7. Effect of vertical measurement location on emissions (a) NOx and (b) CO ……..31

Figure 3.8. Effect of horizontal measurement location on emissions (a) NOx and (b) CO ……..32

Figure 3.9. Effects of mean inlet velocity on emissions from surface combustion, (a) NOx and (b) CO ……..33

Figure 3.10. Effects of mean inlet velocity on emissions from interior combustion, (a) NOx and (b) CO ……..34

Figure 3.11. Emissions measurements for the two combustion modes, (a) NOx and (b) CO ……..35

Figure 3.12. Effect of combustion zone pore size on emission from surface Combustion at V_{in} = 1.0 m/s, (a) NOx and (b) CO ……..36

Figure 3.13. Effect of combustion zone pore size on emission from interior combustion at V_{in} = 1.0 m/s, (a) NOx and (b) CO ……..37

Figure 3.14. Effect of preheat zone pore size on emissions from interior combustion at V_{in} = 1.0 m/s, (a) NOx and (b) CO ……..38

Figure 4.1. Schematic of the heat recirculating combustor used for experiments ..45

Figure 4.2. Picture of the heat recirculating combustor used for experiments ..46

Figure 4.3. Transient nature of preheat and product gas temperature during warm-up ……..48

Figure 4.4. Effect of PIM in preheating annulus on cold flow pressure drop ..51

Figure 4.5. Effect of equivalence ratio on reactant preheat temperature ……..53

Figure 4.6. Effect of PIM in preheating annulus on exterior surface temperature ..56

Figure 4.7. Effect of insulation on exterior surface temperature ……..57

Figure 4.8. Effect reactant flowrate on exterior surface temperature ……..58

Figure 4.9. Effect of (a) streamwise and (b) radial location on product gas temperature ……..64

Figure 4.10. Effect of PIM in preheating annulus on radial profiles of product gas temperature at (a) z = 20 mm and (b) z = 63 mm ……..65

Figure 4.11. Effect of PIM in preheating annulus on streamwise temperature profiles of product gas temperature at (a) r = 0.0 mm and (b) r = 7.6 mm ..66

Figure 4.12. Effect of exterior surface insulation on radial profiles of product gas temperature at (a) z = 20 mm and (b) z = 63 mm ……..67

Figure 4.13. Effect of exterior surface insulation on streamwise profiles of product gas temperature at (a) r = 0.0 mm and (b) r = 7.6 mm ……..68

Figure 4.14. Effect of reactant flowrate on radial profiles of product gas temperature at (a) z = 20 mm and (b) z = 63 mm ……..69

Figure 4.15. Effect of reactant flowrate on streamwise profiles of product gas temperature at (a) r = 0.0 mm and (b) r = 7.6 mm ……..70

Figure 4.16. Effect of Equivalence ratio on product gas temperature at r = 0.0 mm and z = 63 mm ……..71

Figure 4.17. Effect of streamwise location on radial profiles of (a) CO and (b) NOx concentration ……..76

Figure 4.18. Effect of PIM in the preheating annulus on radial profiles of (a) CO and (b) NOx concentration ……..77

Figure 4.19. Effect of exterior surface insulation on radial profiles of (a) CO and (b) NOx concentration ……..78

Figure 4.20. Effect of reactant flowrate on radial profiles of (a) CO and (b) NOx concentration ……..79

Figure 4.21. Effect of equivalence ratio on radial profiles of (a) CO and (b) NOx concentration ……..80

Figure 5.1. Computational domain for phase I combustor ……..93

Figure 5.2. Discrete ordinates radiation model ……102

Figure 5.3. Effect of grid cell size on temperature at combustor exhaust plane (z = 63 mm) ……110

Figure 5.4. Effect of grid cell size on temperature at z = 20 mm ……111

Figure 5.5. Effect of grid cell size on temperature at combustor centerline (r = 0 mm) ……112

Figure 5.6. Effect of grid cell size on axial velocity magnitude at z = 20 mm 113

Figure 5.7. Effect of discrete ordinates radiation model on temperature at z = 63 mm ……115

Figure 5.8. Effect of discrete ordinates radiation model on temperature at z = 20 mm ……116

Figure 5.9. Product gas temperature profiles at z = 63 mm ……119

Figure 5.10. Product gas temperature profiles at z = 40 mm……120

Figure 5.11. Product gas temperature profiles at z = 20 mm ……121

Figure 5.12. Exterior surface temperature profiles without PIM in preheating annulus ……122

Figure 5.13. Product gas temperature profiles with PIM in preheating annulus at z = 63 mm ……123

Figure 5.14. Exterior surface temperature profiles with PIM in preheating annulus (r = 20 mm) ……124

Figure 5.15. Static pressure contours ……127

Figure 5.16. Axial velocity magnitude contours ……128

Figure 5.17 Velocity vector plot ……129

Figure 5.18. Axial velocity magnitude in annulus ……130

Figure 5.19. Axial velocity magnitude in combustor ……131

Figure 5.20. Static temperature contours ……134

Figure 5.21. Static temperature contours ……135

Figure 5.22. Static temperature profiles in annulus ……136

Figure 5.23. Static temperature profiles in combustor ……137

Figure 5.24. Gas enthalpy in preheating annulus, flame stabilizing PIM and combustor chamber ……141

Figure 5.25. Combustor wall (r = 11.75 mm) temperature profile ……144

Figure 5.26. Axial conduction in combustor wall ……145

Figure 5.27. Surface heat flux across combustor wall in preheating annulus (r = 10.0 mm) ……151

Figure 5.28. Surface heat flux across combustor wall in preheating annulus (r = 13.5 mm) ……152

Figure 5.29. Surface heat flux across outer wall in preheating annulus (r = 17.0 mm) ……153

Figure 5.30. Surface heat flux across exterior surface (r = 20.0 mm) ……154

Figure 5.31. Summary of Surface Heat Flux ……155

Figure 6.1. Effect of combustor wall thickness on heat loss to the surroundings 163

Figure 6.2. Effect of wall thickness on temperature at the midplane of the combustor wall ……164

Figure 6.3. Effect of combustor wall thickness on radiation heat flux on the outer wall of the annulus ……165

Figure 6.4. Effect of wall thermal conductivity (k) on heat loss to the surroundings ……168

Figure 6.5. Effect of wall thermal conductivity on temperature at midplane of the combustor wall (r = 11.75 mm) ……169

Figure 6.6. Effect of combustor wall thermal conductivity on radiation heat flux on the outer wall of the annulus (r = 17.0 mm) ……170

Figure 6.7. Illustration of combustor lid region ……174

Figure 6.8. Effect of lid thermal conductivity on heat loss to the surroundings 175

Figure 6.9. Temperature contours in the combustor wall, preheating annulus and outer wall for (a) k_{lid} = 21.5 W/m.K and (b) k_{lid} = 0.5 W/m.K ……176

Figure 6.10. Effect of lid thermal conductivity on temperature at midplane of combustor wall (r = 11.75 mm) ……177

Figure 6.11. Effect of lid thermal conductivity on radiation heat flux on the outer wall of the annulus (r = 17.0 mm) ……178

Figure 6.12. Effect of lid thermal conductivity on exterior surface temperature (r = 20.0 mm) ……179

Figure 6.13. Effect of surface emissivities on percent heat loss to the Surroundings ……185

Figure 6.14. Effect of combustor wall emissivity on temperature at midplane of the combustor wall (r = 11.75 mm) ……186

Figure 6.15. Effect of combustor wall emissivity on heat flux on outer wall of preheating annulus (r = 17.0 mm) ……187

Figure 6.16. Effect of combustor wall emissivity on exterior surface temperature (r = 20.0 mm) ……188

Figure 6.17. Effect of PIM thermal conductivity on heat loss to the surroundings 192

Figure 6.18. Effect of PIM thermal conductivity on temperature at midplane of the combustor wall (r = 11.75 mm) ……193

Figure 6.19. Effect of PIM thermal conductivity on radiation heat flux on outer wall of preheating annulus (r = 17.0 mm) ……194

Figure 6.20. Effect of PIM thermal conductivity on total heat flux on outer wall of preheating annulus (r = 17.0 mm) ……195

Figure 6.21. Effect of PIM thermal conductivity on exterior surface temperature (r = 20 mm) ……196

Figure 6.22. Temperature contours with radiation shield (ε_{Shield} = 1.00) ……200

Figure 6.23. Effect of radiation shield emissivity on heat loss to the surroundings 201

Figure 6.24. Effect of radiation shield emissivity on temperature at midplane of combustor wall (r = 11.75 mm) ……202

Figure 6.25 Effect of radiation shield emissivity on radiation heat flux on outer wall of preheating annulus (r = 17.0 mm) ……203

Figure 6.26 Effect of radiation shield emissivity on exterior surface temperature (r = 20.0 mm) ……204

Figure 6.27. Proposed design for M100 mesoscale, heat recirculating combustor 209

Figure 6.28. Proposed design for M1000 mesoscale, heat recirculating combustor 210

Figure 6.30. Predicted heat loss for M100 combustor ……212

Figure 6.31. Predicted heat loss for M1000 combustor ……215

Figure 6.32. Effect of equivalence ratio on temperature at midplane of combustor wall (r = 3.0 mm) ……216

Figure 6.33. Effect of equivalence ratio on radiation heat flux on outer wall of preheating annulus (r = 4.5 mm) ……217

Figure 6.34. Effect of equivalence ratio on exterior surface temperature (r = 5.5 mm) ……218

Figure 6.35. Effect of reactant flowrate on temperature at midplane of combustor wall (r = 3.0 mm) ……221

Figure 6.36. Effect of reactant flowrate on radiation heat flux on outer wall of preheating annulus (r = 4.5 mm) ……222

Figure 6.37. Effect of reactant flowrate on exterior surface temperature (r = 5.5 mm) ……223

Figure 6.38. Effect of combustor size on temperature at midplane of the combustor wall ……226

Figure 6.39. Effect of combustor size on radiation heat flux on outer wall of preheating annulus ……227

Figure 6.40. Effect of combustor size on exterior surface temperature ……228

Figure 7.1. Schematic of phase II combustor components ……233

Figure 7.2. Schematic of assembled phase II combustor ……234

Figure 7.3. Photographs of phase II combustor (a) before and (b) after assembly 235

Figure 7.4. Photograph of phase II combustor experimental setup ……236

Figure 7.5. Effect of reactant flowrate on product gas temperature (z = 11.5 mm) for the Phase II combustor ……....241

Figure 7.6. Effect of flowrate on phase II mesoscale combustor CO emissions 242

Figure 7.7. Effect of flowrate on phase II mesoscale combustor NOx emissions 243

Nomenclature

a	Grid size parameter
A	Area
c_P	Specific heat capacity
h	Convective heat transfer coefficient
h(T)	Enthalpy
I	Radiation intensity
k	Thermal conductivity
$\dot{m}$	Reactant mass flowrate
$\dot{m}_f$	Fuel mass flowrate
M	Molecular weight
P	Pressure
$\dot{Q}_{Loss}$	Rate of heat loss
$\dot{Q}_{Recirculation}$	Rate of heat recirculation
r	Radial distance from centerline
$R_{Axial_Conduction}$	Thermal resistance to axial conduction
Re	Reynolds Number
R_u	Universal gas constant
$\vec{s}$	Direction vector
S_m	Mass source
S_E	Energy source

t	Combustor wall thickness
T	Temperature
T_{∞}	Temperature of the surroundings
T_{Ad}	Adiabatic flame temperature
T_{Exh}	Product gas temperature at exit plane
T_{Pre}	Reactant preheat temperature
T_{Surf}	Exterior surface temperature
v_r	Radial velocity
v_Z	Axial Velocity
$\forall$	Volume
V_{in}	Mean inlet velocity
X	Transverse direction perpendicular to flow direction
Y	Transverse direction perpendicular to flow direction
z	Streamwise distance from of PIM in flow direction
z^*	Non-dimensional streamwise distance in flow direction
ε	Surface emissivity
ϕ	Porosity
ρ	Density
μ	Dynamic viscosity
σ	Stefan-Boltzmann coefficient
Φ	Combustion equivalence ratio
Ω'	Solid angle

Abstract

Small-scale power generation systems offer an alternative to traditional batteries because of the high energy density of hydrocarbon fuels. Combustion at small scales presents several challenges, including high heat loss and short flow residence times. Heat recirculation is an effective method to limit heat loss and improve combustion performance. However, new methods of achieving heat recirculation in a small volume must be developed for practical devices. To meet this requirement, a heat recirculating, lean premixed combustion system utilizing porous inert media (PIM) has been developed. Combustion with the use of silicon carbide PIM was investigated experimentally with the flame stabilized above the surface and within the interior of the PIM. The two flame stabilization locations were directly compared at identical conditions. The interior combustion mode extended the lean blowoff limit, allowing for reduction in NOx pollutant emissions. The combustion and heat transfer characteristics of the mesoscale, heat recirculating combustor design were determined experimentally with a system of 125 cm^3 using methane fuel. The combustor featured an annulus around the combustion chamber to preheat reactants and reduce heat loss to the surroundings. The presence of PIM in the preheating annulus and exterior surface insulation improved combustion performance by increasing reactant preheating and reducing heat loss to the surroundings. Computational fluid dynamics (CFD) analyses were used to characterize heat transfer and to identify sources of heat loss. Axial conduction through the combustor wall

and radiation across the preheating annulus were the two primary sources of heat loss. Design modifications aimed at reducing heat loss and improving system performance were analyzed. The most effective design improvements were a low thermal conductivity lid and a radiation shield in the preheating annulus. A phase II mesoscale, heat recirculating combustor design, based on the CFD analyses, was developed. Increasing reactant flowrate and increasing the size of the combustor reduced heat loss to the surroundings. Thermal performance of the phase II combustor design was demonstrated experimentally with an overall system volume of 1.5 cm^3. Heat release rates exceeded 90 W, heat loss was less than 13 % of the heat release rate, and combustion efficiency was greater than 99 %. The findings of this work will be useful in guiding small scale combustor designs and advance mesoscale combustion toward practical implementation.

1. Introduction

The interest in advanced small scale combustion systems has arisen in the last decade to develop an alternative to traditional batteries for energy storage [Epstein, 2003]. With the miniaturization of MicroElectroMechanical (MEMS) devices and personal electronics, the power sources have become a larger fraction of the size and weight of the overall system. Micro and mesoscale power generation systems provide a potential solution to this problem because the energy storage density of hydrocarbon fuels is roughly 100 times that of modern batteries. Microthrusters and microrockets are other applications requiring advanced small-scale combustion systems. High heat loss to the surroundings is the primary challenge that impedes the development of practical small-scale power systems. Heat recirculation with the use of Porous Inert Media (PIM) may be a viable method of reducing heat loss and achieving efficient combustion in mesoscale systems. In this chapter, the concepts and issues concerning small-scale and PIM combustion are discussed and a mesoscale, heat recirculating combustor design is introduced.

1.1 Mesoscale Combustion

With regard to small-scale combustion systems, no universal definitions of mesoscale and microscale exist. In this study, the term "mesoscale" signifies combustor diameter from a few millimeters to a few centimeters. The term "microscale" indicates that the combustor diameter is smaller than the quenching diameter of the given fuel. The Massachusetts Institute of Technology (MIT) set out to develop a new generation of micro heat engines in the mid- to late-1990s [Waitz et al., 1998]. It was envisioned that these engines could produce 10 to 100 Watts of electricity in a volume less than 1 cm^3. Feasibility of these systems was shown with hydrogen combustion. Catalytic combustion of hydrogen was also investigated by Vican et al. [2002]. Both groups found that convection and radiation heat loss from their microreactor affected its performance. Much of the early and current research on small-scale power generation has focused on the microscale, such that of Yuasa, et al. [2005], Norton and Vlachos [2005], and Boyarko, et al. [2005].

Mesoscale combustion has received increasing attention in recent years because of many potential applications [Ju and Xu, 2005; Lee and Kwon, 2003; Sirignano et al., 2003]. For example, a mesoscale power generation system could power personal electronics or serve as small a thruster or rocket [Yetter, et al., 2003]. Mesoscale combustion is also useful for gaining insight into combustion phenomena at moderate scales as a step towards developing high power density, microscale systems [Kyritsis et al., 2004].

In a combustion system, heat is generated volumetrically and it is lost to the surroundings through the surface. Thus, miniaturizing a combustor increases the fraction of heat loss to the surroundings compared to that generated within the combustor because of the increase in surface area to volume ratio. Increased fractional heat loss has negative effects on combustion performance, including poor combustion efficiency and flame quenching. Another challenge facing combustor miniaturization is the shorter residence time, limiting fuel/air premixing upstream of the reaction zone. Inadequate flow residence time in the combustion zone may lead to incomplete combustion, low combustion efficiency and high pollutant emissions [Fernandez-Pello, 2002].

Heat recirculation is one method that can be utilized to improve performance of Lean Pre-Mixed (LPM) combustion [Hardesty and Weinberg, 1976]. With heat recirculation, the reactants are preheated using thermal energy from the reaction zone. Thus, the flame temperature is higher than the adiabatic flame temperature of the reactants at inlet conditions. Recently, Ronney and collaborators have applied this concept to achieve combustion in a microscale Swiss roll configuration [Ronney, 2003] and [Ahn et al., 2005]. The reactants and products were brought into proximity in separate spiraling passages upstream and downstream of the reaction zone. Combustion was achieved over a wide range of flow velocities and equivalence ratios using gas phase and catalytic combustion. These studies demonstrated that heat recirculation is a viable method of achieving and sustaining combustion in small volumes.

The Swiss-roll combustor utilizes a relatively small combustion volume compared to the total volume of the system. However, practical devices require a combustion system that effectively preheats reactants and minimizes heat loss in a smaller volume. PIM may be used to recirculate flame energy in a smaller volume than the Swiss-roll configuration, making it more viable for practical use. PIM may also provide more uniform combustion with lower pollutant emissions and higher power density than other small scale combustor designs. The PIM combustion concept is presented in the next section and the mesoscale, heat recirculating combustor design is introduced and discussed in section 1.3.

1.2 Porous Inert Media (PIM) Combustion

A flame can be stabilized on the surface or in the interior of a PIM as illustrated by Fig. 1.1. For a flame stabilized on the surface, the energy released by the reaction is transferred to the porous surface, which might emit it to the surroundings as in radiant burners. A portion of the energy is radiated and conducted upstream to preheat the reactants in the preheat zone.

Although heat transfer mechanisms similar to surface combustion serve as the basis of interior combustion, the amount of heat transferred in each mode can be significantly different. In surface combustion, heat is transferred from the reaction zone to the PIM at and slightly below the burner surface. However, interior combustion allows heat transfer to the PIM both at the reaction zone and downstream by interfacial convection between the products and the porous structure. The result of this additional convective heat transfer is the potential for increased preheating of reactants and consequently a greater control of flame stability and temperature. No direct comparison of surface and interior combustion is available in the literature because nearly all of the research has been focused on either surface or interior combustion.

The concept of recirculating energy from products to reactants or the 'excess enthalpy flame' was introduced by Hardesty and Weinberg [1976]. PIM combustion research has been reviewed by Howell et al. [1996], Viskanta [1995], and Trimis and Durst [1996]. Kotani and Takeno [1982] found that a porous burner increased the laminar flame speed by more than an order of magnitude. Subsequently, various

aspects of combustion with PIM have been investigated experimentally and numerically. Hsu et al. [1993] used two porous ceramic cylinders of different pore sizes stacked together. The flame was stabilized at the interface of two blocks over a range of mixture flow rates for a given equivalence ratio. A similar concept of bi-layered reticulated ceramic burner with an upper layer with larger pores and a lower layer with smaller pores to improve the stable operating regime was used by Rumminger et al. [1996]. Pickenacker et al. [1999] and Sullivan et al. [2000] have developed several commercial concepts involving combustion with PIM.

A critical component of PIM combustion is the porous material. Important characteristics of the porous structure are the maximum operating temperature and thermophysical properties such as adsorptivity, emissivity, and thermal conductivity. Materials used in experimental porous burners are wide ranging, with ceramics being the most common. Although porous ceramics have good thermal resistance, they suffer from structural damage caused by repeated start-up and shutdown and therefore, are not suited for small-scale combustion applications. In recent years, new materials have become available with advancements in manufacturing techniques. Examples include carbon composites and carbon foams. The drawback of these materials is their inability to resist oxidation at temperatures above 775 K. An oxidation-resistant coating of high temperature materials such as silicon carbide (SiC), rhenium, hafnium, or iridium may be deposited on the structure by the chemical vapor deposition (CVD) technique. These porous materials offer structural

rigidity as well as thermal/oxidation resistance required to sustain combustion [Sherman, et al., 1999].

PIM has the potential to benefit combustion at large scales, but several challenges must be overcome before it can be applied to practical, mesoscale applications. PIM capable of withstanding harsh combustion conditions over an extended period of time must be found. Experimental investigations of combustion with PIM have focused on either surface or interior combustion. Therefore, an improved understanding of surface and interior combustion modes is needed and a comparison of the two modes will highlight their relative merits. The effects of flowrate, equivalence ratio and PIM pore size must also be investigated. Investigation of these issues is presented in Chapter 3.

PIM may also be beneficial for small-scale combustion systems. As described in the previous section, heat loss to the surroundings is the primary challenge facing small-scale combustion. PIM may be used to recirculate heat that would otherwise be lost to the surroundings. The next section describes such a system; the mesoscale, heat recirculating combustor design which uses PIM for flame stabilization and reactant preheating.

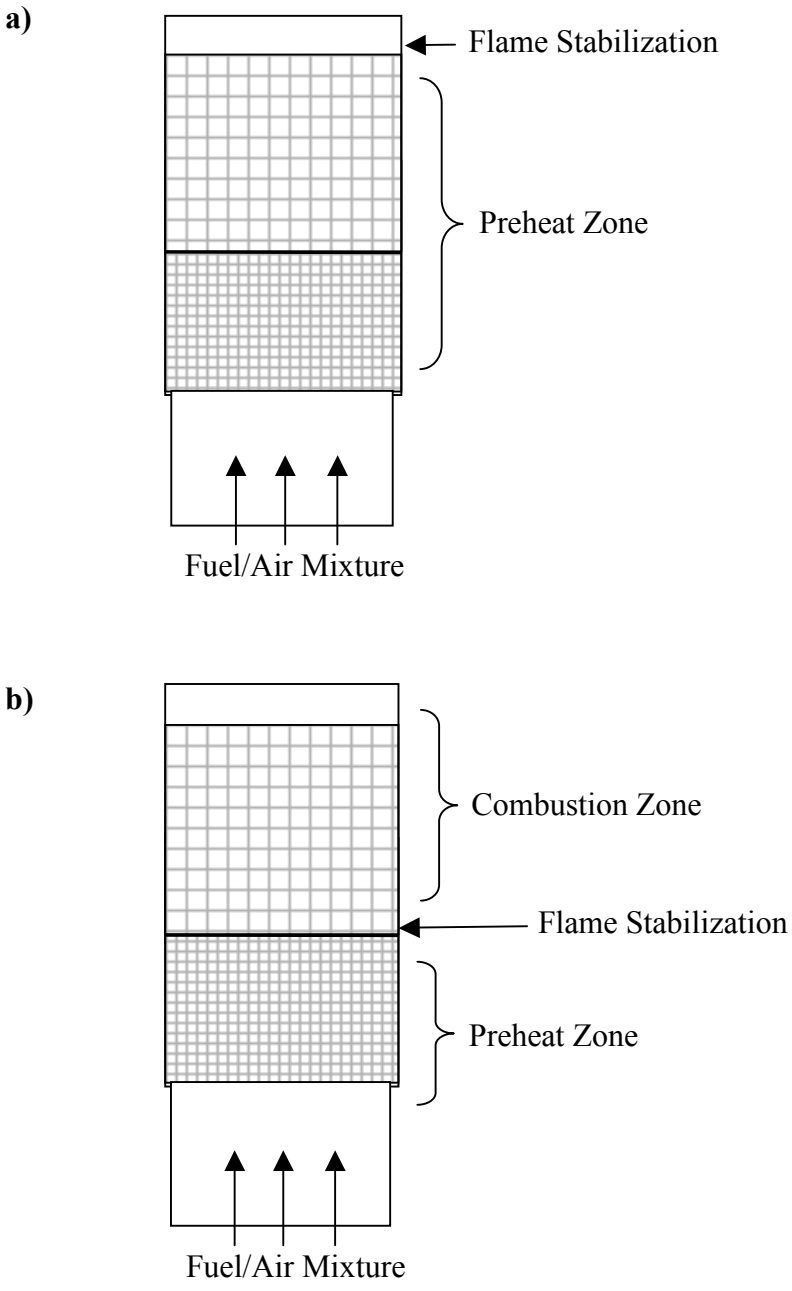

Figure 1.1. Schematic representation of (a) surface combustion and (b) interior combustion.

1.3 Heat Recirculating, PIM Combustor Concept

A combustor concept using PIM to recover energy transferred through the combustor wall to preheat reactants has been developed [Marbach and Agrawal, 2005]. A schematic of the combustor design is presented in Fig. 1.2. Fuel and air are injected into an annulus surrounding the combustion chamber, which may be filled with PIM. The reactants are premixed and preheated in the annulus before reaching the flame stabilizing PIM, which provides additional preheating and premixing of reactants prior to combustion. The flame is stabilized on the downstream surface of PIM, within the combustion chamber. Hot products passing through the combustor chamber transfer heat to the cooler reactants flowing through the annulus. The high surface area of PIM is expected to increase interfacial convection in a smaller volume.

The proposed heat recirculating PIM combustor design has similarities and important differences from similar other designs. Yuasa et al. [2005] introduced the concept of a flat flame burner using stainless steel porous plate for micro-flame applications. In our design, combustion is stabilized on the surface of Silicon Carbide (SiC) coated carbon foam used as PIM. Unlike Yuasa et al., an annular preheat zone is used to reduce heat loss and improve flame stability by preheating the reactants. The Swiss-Roll combustor design used by Ronney et al. [2003] improved flame stability by heat recirculation. However, the combustion volume was small compared to the total volume of the system. Our design uses a single pass annulus which may be filled with PIM to promote heat transfer, instead of multiple passages that increase

the overall system size. Characteristics of the mesoscale, heat recirculating combustor are investigated experimentally in Chapter 4. Computational fluid dynamic (CFD) analysis to study heat transfer characteristics is discussed in Chapter 5 and to improve the combustor design is presented in Chapter 6. In Chapter 7, the feasibility of the design for a mesoscale combustion system of approximately 1 cm^3 is demonstrated experimentally.

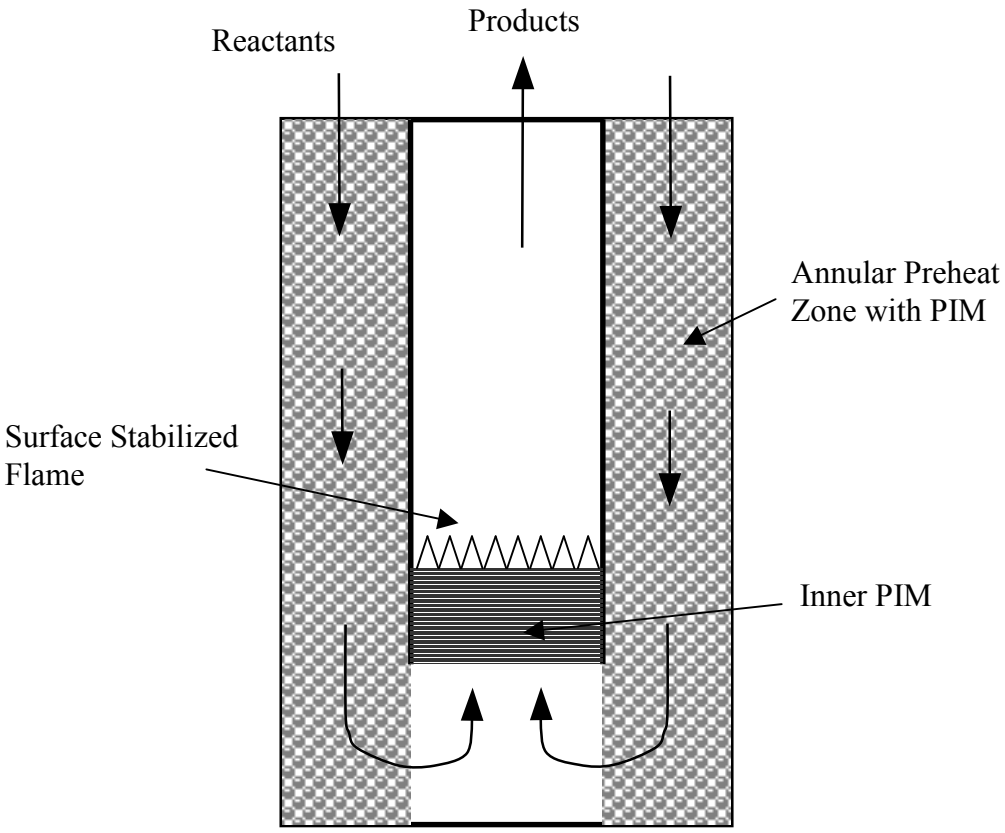

Figure 1.2. Heat recirculating combustor concept using porous inert media.

2. Objectives

The objective of this study is to develop an efficient, mesoscale combustion system with low heat loss to the surroundings. This objective was achieved through a combination of experiments and analysis. The tasks involving five steps, each with specific objectives, are presented below.

Step 1: Experimental Study of Macroscale PIM Combustion (Chapter 3)

- Determine fluid flow and combustion characteristics of SiC coated PIM.
- Compare combustion performance of surface and interior combustion modes and determine merits of each.
- Understand the effects of reactant flowrate, equivalence ratio, and PIM pore size on combustion performance.

Step 2: Experimental Study of Mesoscale Combustion (Chapter 4)

- Demonstrate feasibility of heat recirculating combustor design at a moderate size (100 cm^3).
- Determine the important parameters affecting combustion performance and understand the impact of each parameter.

Step 3: Computational Fluid Dynamics Analysis of Mesoscale Combustion System (Chapter 5)

- Understand heat transfer by conduction, convection and radiation in a mesoscale, heat recirculating combustor.
- Identify important sources of heat loss.
- Determine relative importance of each mechanism of heat loss and identify concepts to reduce heat loss.

Step 4: Parametric Studies (Chapter 6)

- Identify and evaluate design improvements that reduce heat loss to the surroundings.
- Develop optimized combustor designs which utilize appropriate design improvements.
- Predict thermal performance of the optimized design over a range of operating conditions.

Step 5: Phase II Mesoscale Combustion Experiments (Chapter 7)

- Demonstrate feasibility of heat recirculating combustor design with a smaller, 1 cm^3 combustor.
- Determine operating range and characterize heat loss and pollutant emissions from phase II combustor.

3. Experimental Study of Macroscale PIM Combustion

Experiments were conducted to determine the fluid flow and combustion characteristics of porous inert media combustion with the use of SiC coated PIM. The following list describes the characteristics that were investigated.

- Velocity Profile Exiting PIM
- Pressure Loss Through PIM
- Effect of Reactant Flowrate on Pollutant Emissions
- Effect of Reactant Equivalence Ratio on Pollutant Emissions
- Effect of PIM Pore Size on Pollutant Emissions
- Effect of Flame Stabilization Location (Interior or Surface) on Pollutant Emissions

3.1 Experimental Setup and Procedure

The burner for gaseous combustion, depicted in Fig. 3.1, was comprised of four sections: the fuel/air inlet section, the fuel/air mixing section, the PIM section, and the emissions shield. Each section was constructed of stainless steel square tubing of 4.0 cm by 4.0 cm inside cross section and a wall thickness of 0.48 cm. The 15.2 cm long fuel/air mixing section was comprised of a 2.54 cm thick, 32 pores per cm (ppcm) porous-piece at the upstream end to enhance fuel/air mixing, with free space making up the remaining mixing length. The PIM section was 10.2 cm long,

with four 2.54 cm thick porous pieces arranged in various configurations of 4, 8, 12, and 32 ppcm material.

The porous pieces were sanded to fit precisely into the PIM section. A tight fit was critical because space between porous material and combustor wall could cause the flame to propagate around the PIM. A shield was used downstream of the PIM section for emissions measurements without entraining the ambient air. Three pressure taps were located near the exit of the fuel/air mixing section to monitor the pressure drop across the PIM. The pressure downstream of the PIM was assumed to be atmospheric.

An air compressor was used to supply the combustion air, which was dried and measured by a laminar flow element calibrated for 0-300 standard liters per minute (slm) with an uncertainty of ± 2 slm. The combustor inlet air was maintained at 300 K. The natural gas flowrate was measured by a mass flowmeter calibrated in the 0 to 60 slm range with an uncertainty of ± 1 slm.

Axial velocity and turbulence measurements at the PIM exit were taken by a single hot-wire anemometer (TSI IFA 300). A three-way traversing system with a least count of 0.6 mm was used to accurately move the probe to collect data at various locations. The pressure drop in the PIM combustor was found by averaging the wall pressure readings measured with a pressure transducer calibrated for +/- 6.3 cm water. Emission concentrations were measured by a gas analyzer with electrochemical sensors. A quartz probe with outer diameter of 3.0 mm, inner diameter of 2.0 mm and a tapered tip of 4:1 contraction ratio was used to collect the gas sample. The

condensed water from the gas sample was removed upstream of the gas sensors using water traps. Emissions data are reported on an uncorrected dry basis. The uncertainty in NOx and CO measurements is +/- 2 ppm. The chemical composition of natural gas was assumed to be CH_4.

At each set of operating parameters, surface and interior combustion data were obtained. The transition from surface to interior combustion was made by reducing the mean fuel/air mixture inlet velocity (V_{in}) to about 0.4 m/s and increasing the equivalence ratio (Φ) to about 0.8, which caused the flame to propagate upstream into the PIM. After interior combustion was established, the mean inlet velocity was increased and the equivalence ratio was decreased to the desired values for testing. The system was allowed 20 minutes to reach steady state conditions. The Strawberry Tree data acquisition system was used to obtain and log signals from the instrumentation. The sampling rate was 40 Hz and the average of 20 samples was recorded. Experiments were conducted at a range of equivalence ratios. The lowest equivalence ratio used for the experiments was the LBO limit and the highest equivalence ratio was limited to $\Phi = 0.75$ to ensure the structural integrity of the combustor. The higher flame temperatures associated with higher equivalence ratios may have caused significant damage to the combustor walls and/or PIM in the flame stabilizing PIM.

The baseline configuration for the experiment was defined as 32-8-8-8. This refers to the PIM section filled with one 32 ppcm piece in the upstream end (preheat zone), followed by three 8 ppcm pieces (combustion zone). The baseline conditions

were defined as $\Phi = 0.60$ and $V_{in} = 1.0$ m/s. The mean inlet velocity was defined as the volumetric flowrate of reactants divided by the cross sectional area of the fuel/air mixing section.

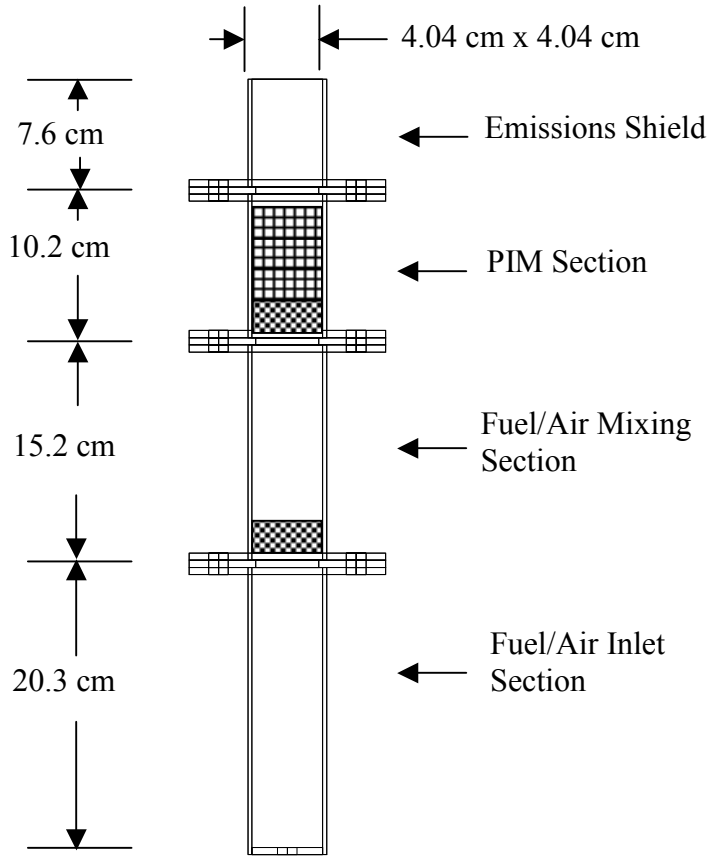

Figure 3.1. Schematic diagram of the experimental setup for macroscale PIM combustion.

3.2 Results and Discussion

The flow characteristics and combustion performance were determined experimentally. Pressure loss and velocity fields were measured and the effects of flowrate and pore size on combustion emissions were determined. The combustion performance of surface and interior combustion modes were compared at identical operating conditions.

3.2.1 Flow Characteristics

Pressure drop resulting from cold flow through the PIM ranged from 0 to 1 percent of the operating pressure. Fig. 3.2 presents the percent pressure drop across various individual porous pieces (each 2.54cm thick) and the baseline configuration (32-8-8-8) at a range of flowrates. As expected, the pressure drop increases with the flowrate. Note that the measured pressure drop across the 32-8-8-8 configuration is within five percent of that calculated by adding the pressure drop across the individual pieces. Fig. 3.3 presents percent pressure drop for surface and interior gaseous fuel combustion over a range of flow rates. With surface combustion, the pressure drop in the PIM is virtually the same as that for cold flow. Interior combustion, however, more than doubles the pressure drop in the PIM section, in part, because of the higher velocity of the product gases moving through the PIM. Results suggest that pore size and thickness of the PIM region are important to minimize the pressure drop for practical applications.

Cold-flow axial velocity was measured at the exit of the PIM section in a 10 by 10 grid to evaluate flow uniformity determined by pore size distribution. The

axial velocity contours in Fig. 3.4 show nearly uniform flow exiting the PIM. The slight increase in velocity near the burner wall is attributed to the blockage by the lip causing the flow to accelerate locally. Highly uniform flow in the middle section suggests that the manufacturing technique used to produce the SiC coated carbon foam did not create plugged pores, as is the case with ceramic PIM [Wharton et al., 2003]. The hot-wire data in Fig. 3.4 are within 10% of the average velocity determined from the flow rate measured by the laminar flow element. Profiles of turbulence intensity in Fig. 3.5 reveal low values of 1 to 2 percent in the middle region of the PIM. Turbulence intensity was taken as the standard deviation of the velocity divided by the average velocity. The increase in turbulence intensity to 4 percent near the wall is attributed to the local flow acceleration caused by the lip.

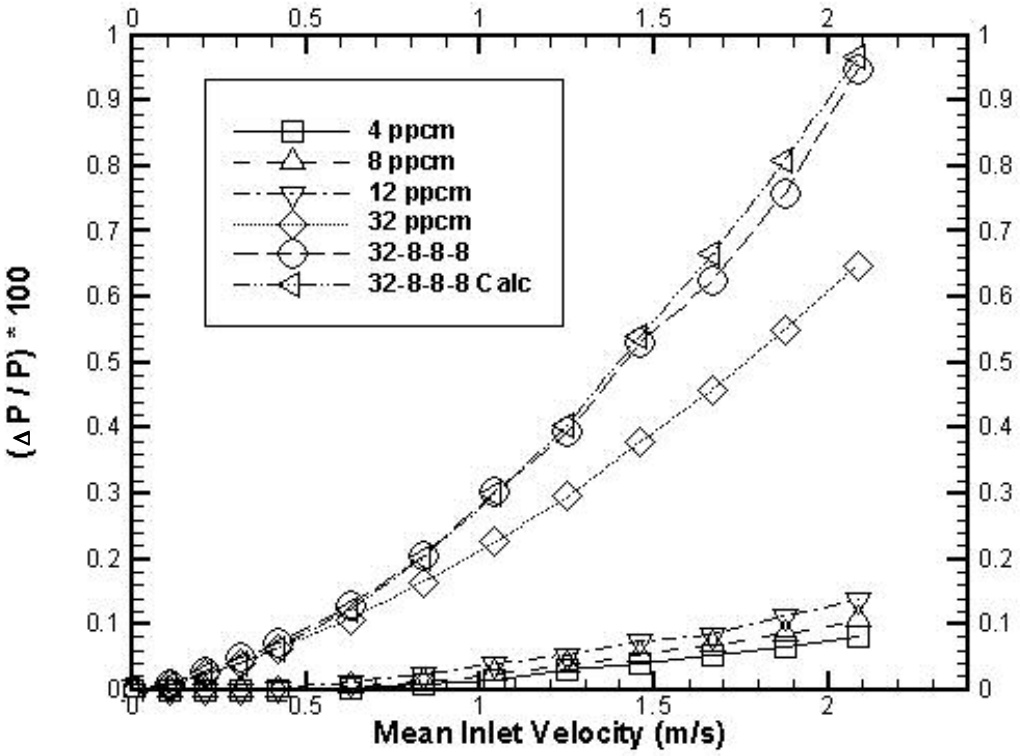

Figure 3.2. Effect of pore size on cold flow pressure drop.

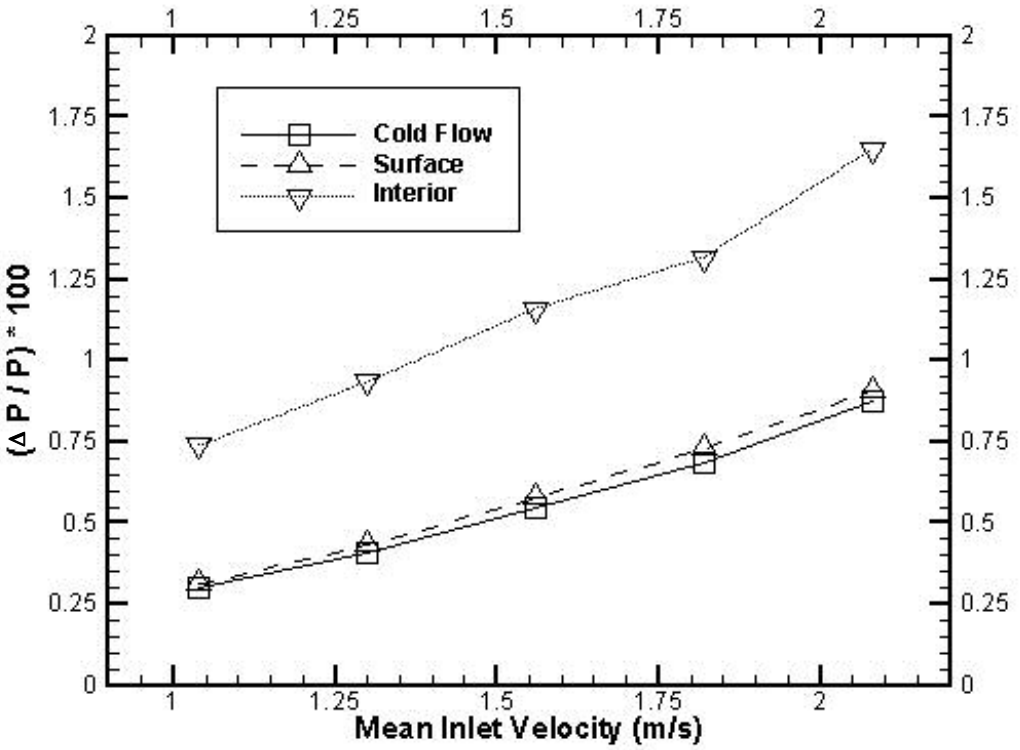

Figure 3.3. Effect of combustion on pressure drop for baseline configuration (32-8-8-8), $\Phi = 0.6$.

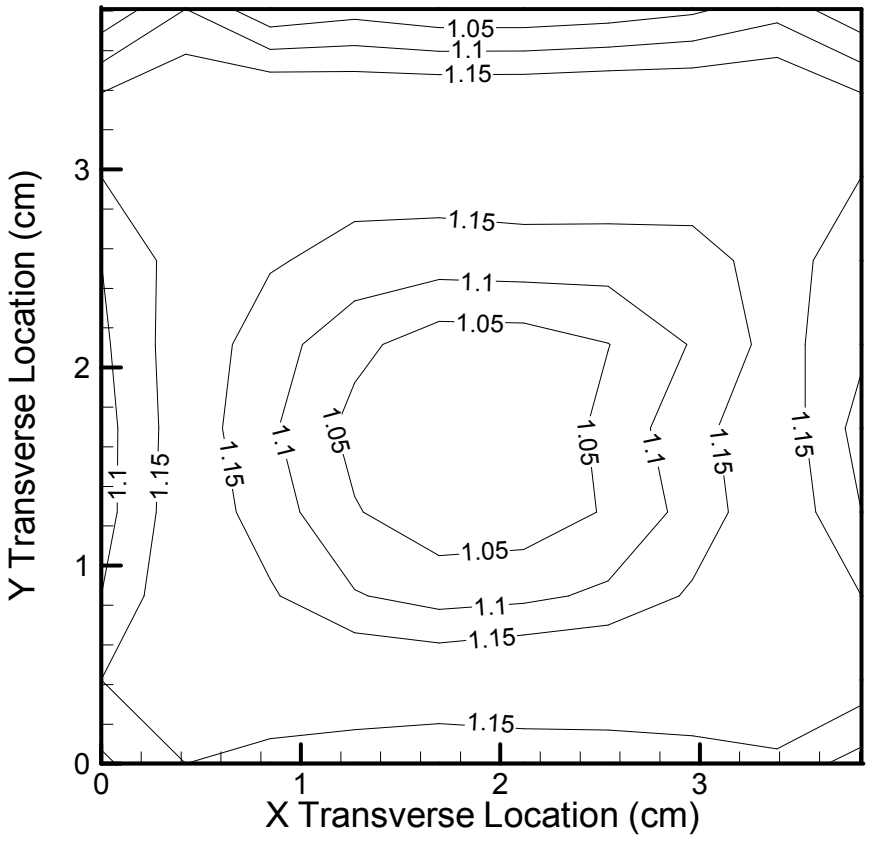

Figure 3.4. Contour plot of axial velocity at the z = 10 mm for cold air.

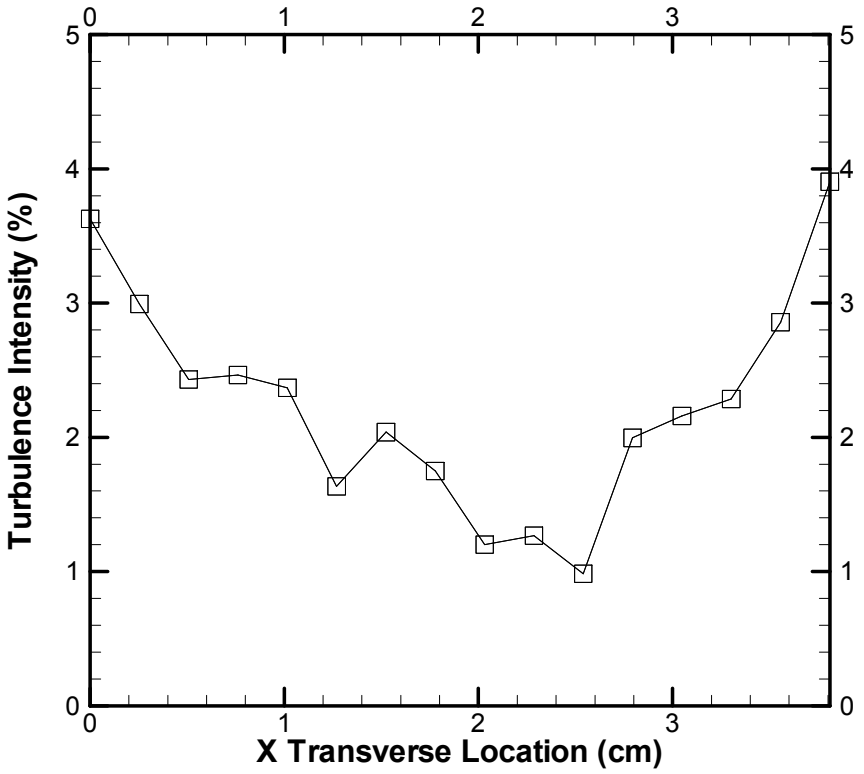

Figure 3.5. Profile of turbulence intensity at z = 10 mm.

3.2.2 Combustion Characteristics

Combustion was stabilized both on the surface and in the interior of the PIM. Fig. 3.6 presents photographs of flames in both stabilization modes. Surface combustion produces a blue, flat-flame while interior combustion produces an orange glow from the radiating PIM. First, experiments were conducted to determine the uniformity and length of the reaction zone. Thus, emissions profiles at baseline conditions were obtained (a) in the flow direction (streamwise) along the combustor midpoint and (b) in the transverse (horizontal) direction at a vertical plane above the PIM surface.

Fig. 3.7 presents data for NOx and CO emissions of surface and interior combustion versus streamwise distance above the PIM surface (z). Both NOx and CO emissions of interior combustion are constant throughout the entire length of the emissions shield. Therefore, all of the NOx and CO emissions are generated within the PIM. However, surface combustion concentrations change radically near the PIM surface. CO concentration increases and NOx concentration decreases sharply as the emissions probe is lowered into the flame front. Results show that the NOx formation was completed within z = 15 mm from the PIM surface. The CO oxidation however continued downstream until about z = 35 mm.

Fig. 3.8 presents NOx and CO concentrations of surface and interior combustion versus transverse distance (Y) from the combustor midpoint at z = 63 mm. Evidently, the CO and NOx emissions are nearly constant over the entire width for the two combustion modes. Emissions profiles obtained with leaner mixtures

showed CO increasing and NOx decreasing near the combustor wall, which suggests a quenching effect of heat loss through the wall. Based on these results, the combustor midpoint at z = 63 mm was selected for all subsequent emissions measurements, representing the post-reaction zone.

3.2.2.1 Effect of Reactant Flowrate

Figs. 3.9a and 3.10a present data for NOx emissions versus equivalence ratio at various mean inlet velocities for surface and interior combustion, respectively. At a given equivalence ratio, the NOx concentration was weakly dependent on the mean inlet velocity, varying over a factor of two. Khanna et al. [1994] produced similar results, citing constant NOx emissions over a range of flame speeds or mixture flowrates. NOx increased nearly exponentially with equivalence ratio, suggesting thermal mechanism as the primary source of NOx generation. Single digit NOx concentrations were obtained in both combustion modes for equivalence ratios of up to 0.65. Figs. 3.9b and 3.10b present CO concentrations for surface and interior combustion, respectively. Fig. 3.9b shows that the CO concentration at a given equivalence ratio was nearly independent of the flowrate for surface combustion. Khanna et al. [1994] observed similar results with little dependence of CO concentration on reactant flowrate. The CO concentration increased with equivalence ratio, similar to the trend for interior combustion using reticulated ceramics observed by Mital et al. [1997]. Data presented at the lowest equivalence ratio in Figs 3.9 and

3.10 correspond to the lean blow-off (LBO) limit. Results show that the equivalence ratio at the LBO limit increased with increasing mean inlet velocity.

The CO concentration for interior combustion increased with equivalence ratio as shown in Fig. 3.10b. In this case, a significant flowrate effect is observed, especially at lower flowrates. Note that the combustor was air-cooled by natural convection to prevent overheating and structural damage to the stainless steel enclosure. At low flowrates, a larger fraction of heat released is believed to be lost to the surroundings. The resulting decrease in the flame temperature would affect the oxidation reactions to produce larger CO concentrations. The fractional heat loss is expected to diminish at higher flow rates, which show minor effect on CO emissions.

3.2.2.2 Surface versus Interior Combustion

NOx and CO concentrations vs. equivalence ratio for surface and interior combustion are compared in Fig. 3.11 for V_{in} = 1.0 m/s. Results show that the combustion mode had little impact on NOx concentration at a given equivalence ratio. Interior combustion extended the LBO limit, offering further NOx reduction. At the baseline conditions, the LBO limit for surface combustion was about 0.58 while that for interior combustion was 0.55. Theoretically, this extension of the lean blow-off limit corresponds to a decrease in flame temperature of about 50 K. CO concentrations of the two combustion modes followed a similar trend with equivalence ratio, although interior combustion results in slightly higher CO

concentrations, attributed to a higher fractional heat loss from conduction and radiation to the combustor walls, as explained above.

3.2.2.3 Effect of Combustion Zone Pore Size

Thermal feedback to reactants in both combustion modes depends upon the geometry of the PIM. To examine this issue, surface combustion experiments were conducted with 4, 8, 12 and 32 ppcm PIM and interior combustion experiments were conducted only with 4 and 8 ppcm PIM because smaller pores would quench the flame. Results in Figs. 3.12a and 3.13a show a relatively weak trend of larger pores yielding higher NOx emissions at a given equivalence ratio. The PIM with larger pores had smaller optical thickness compared to that of a PIM with smaller pores. Therefore, it is plausible that the higher NOx generation of the large pore PIM (32-4-4-4) was an effect of the greater preheating of reactants by radiation from the flame zone. Detailed measurements near the flame front are therefore necessary to fully explain these observations.

Figs. 3.12b and 3.13b present CO concentration vs. equivalence ratio for various combustion zone pore sizes, respectively, for surface and interior combustion. In both cases, CO concentration increases with decreasing pore size. Several phenomena may be responsible for this trend. As discussed above, a porous structure with smaller pores has a larger optical thickness than a similar porous structure with larger pores. Therefore, less heat is radiated upstream and less preheating of reactants occurs. The decrease in preheating is akin to the flame producing to higher CO

emissions. Flow dynamics on the pore size scale level is another factor affecting CO concentration. Small pores cause greater redirection of the gases moving through the structures, resulting in increased local velocities.

3.2.2.4 Preheat Zone Pore Size

The degree of reactant preheating for interior combustion is largely dependent upon pore size of the preheat zone. The size of the pores in this region must be small enough to quench the flame and eliminate flashback. However, the pores should be large enough to allow significant thermal feedback to the reactants. The effect of upstream pore size on emissions for interior combustion is presented in Fig. 3.14. At a given equivalence ratio, NOx concentrations for the two preheat zone pore sizes tested were virtually identical. Fig. 3.14b shows a noticeable reduction in CO concentration with larger preheat zone pore size, suggesting more effective preheating of reactants. Extension of the LBO limit with large pore size further substantiates this observation. No flashback occurred at any of the conditions with the 32 ppcm preheat region. However, flashback occurred with the 12 ppcm preheat region at equivalence ratios above 0.58 and mean inlet velocity of 1.0 m/s. This result indicates that the preheat region pore size should be optimized to increase the heat transfer upstream and to quench the reaction at the most likely flashback conditions.

(a)

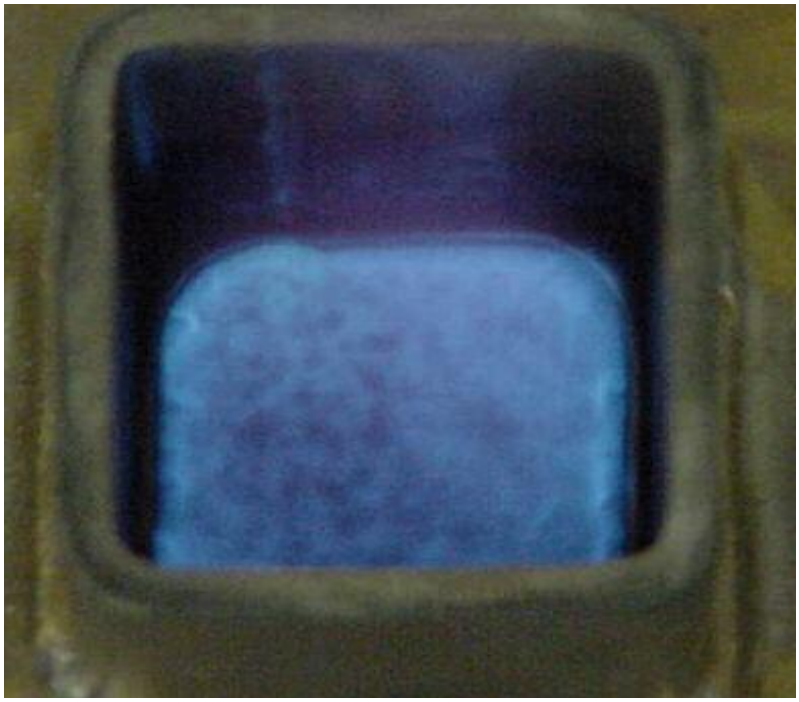

(b)

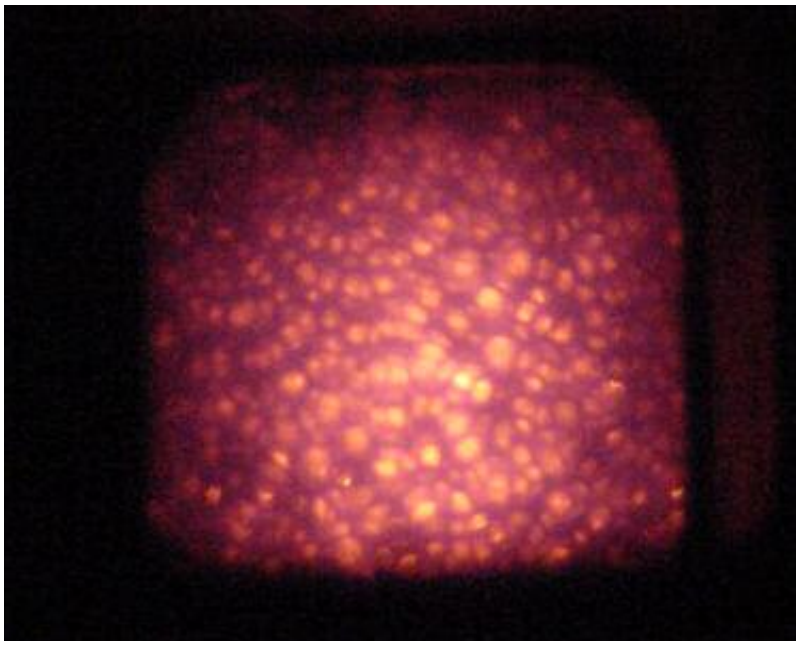

Figure 3.6. Visual images at baseline conditions
(a) surface combustion, (b) interior combustion.

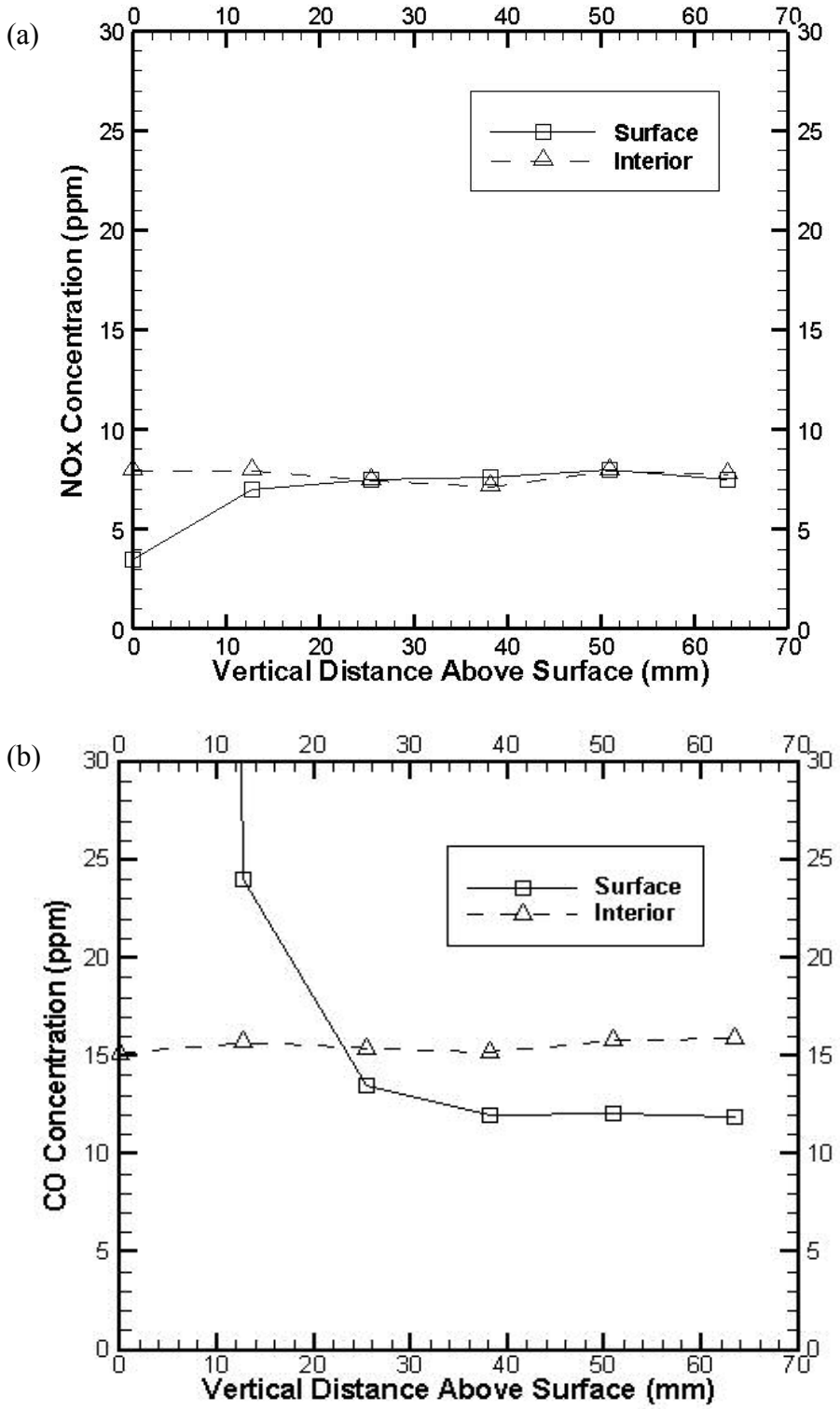

Figure 3.7. Effect of vertical measurement location on emissions (a) NOx and (b) CO.

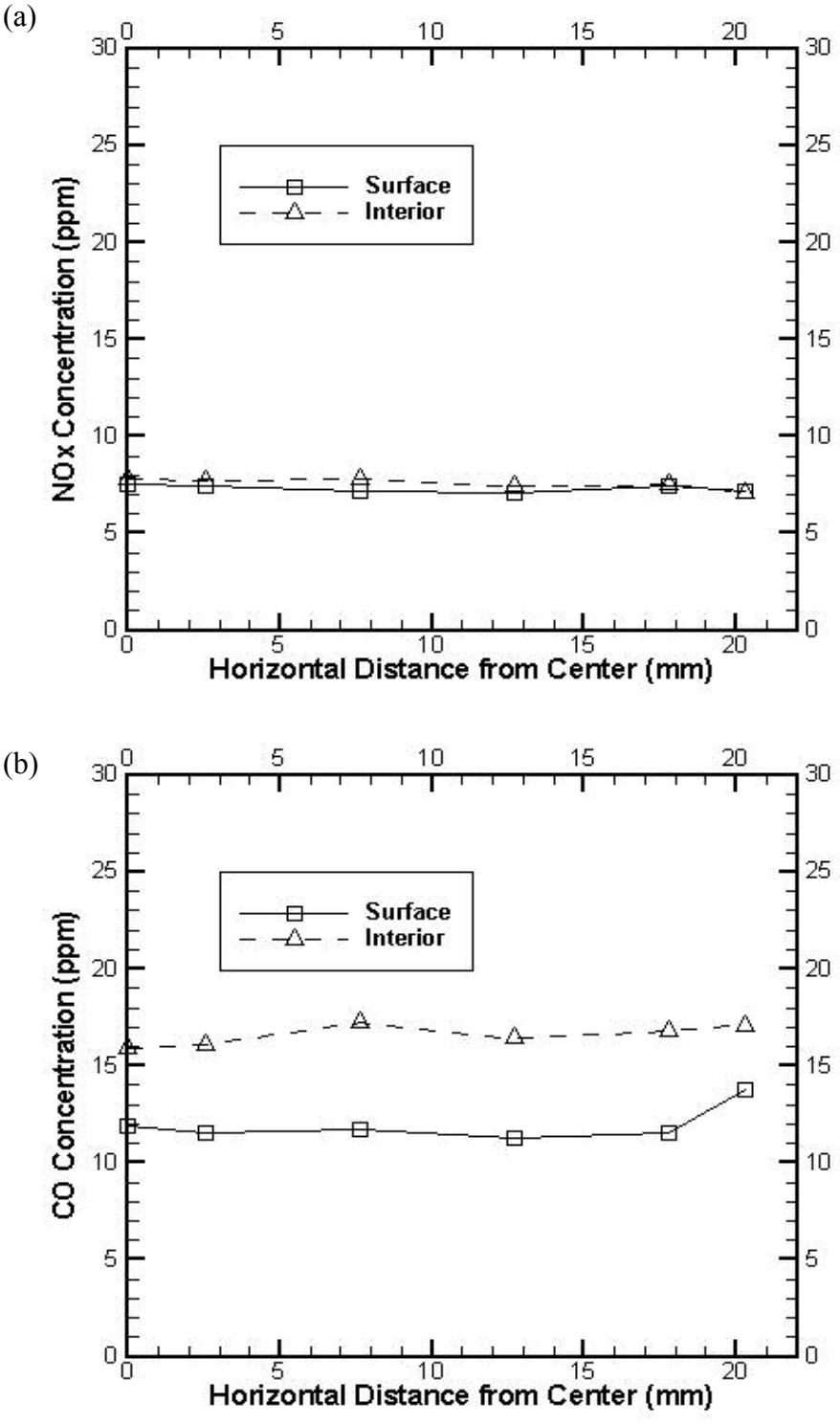

Figure 3.8. Effect of horizontal measurement location on emissions (a) NOx and (b) CO.

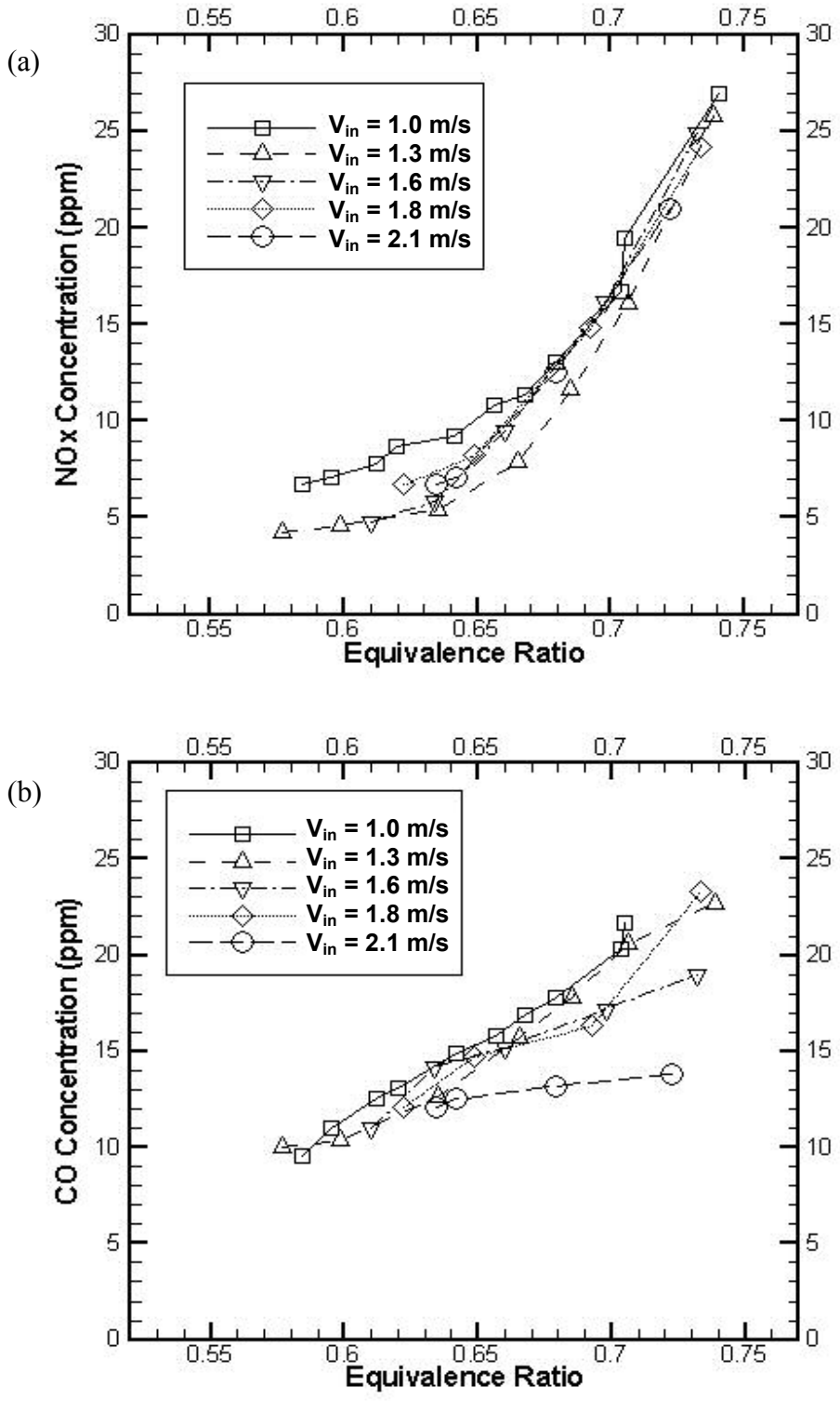

Figure 3.9. Effects of mean inlet velocity on emissions from surface combustion, (a) NOx and (b) CO.

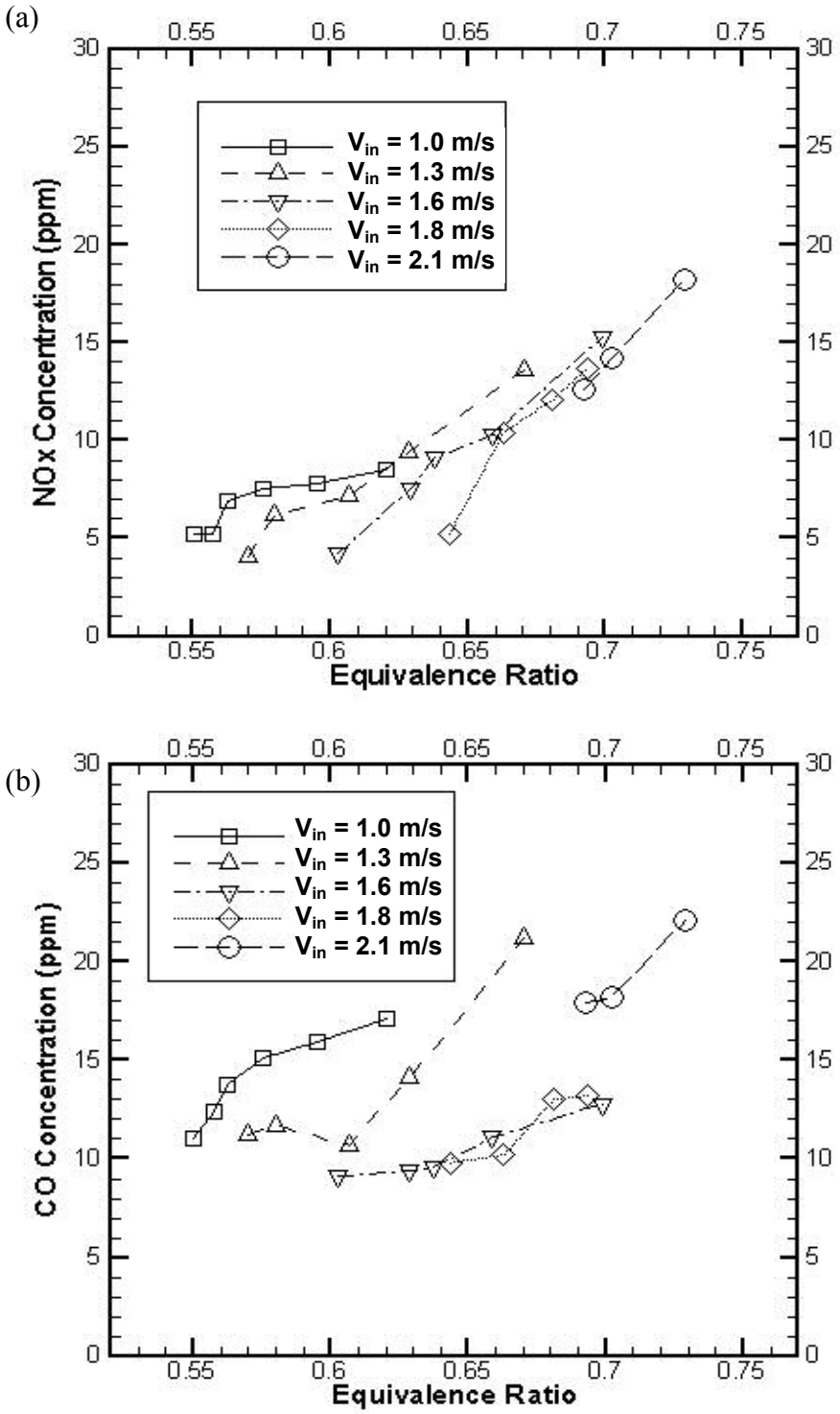

Figure 3.10. Effects of mean inlet velocity on emissions from interior combustion, (a) NOx and (b) CO.

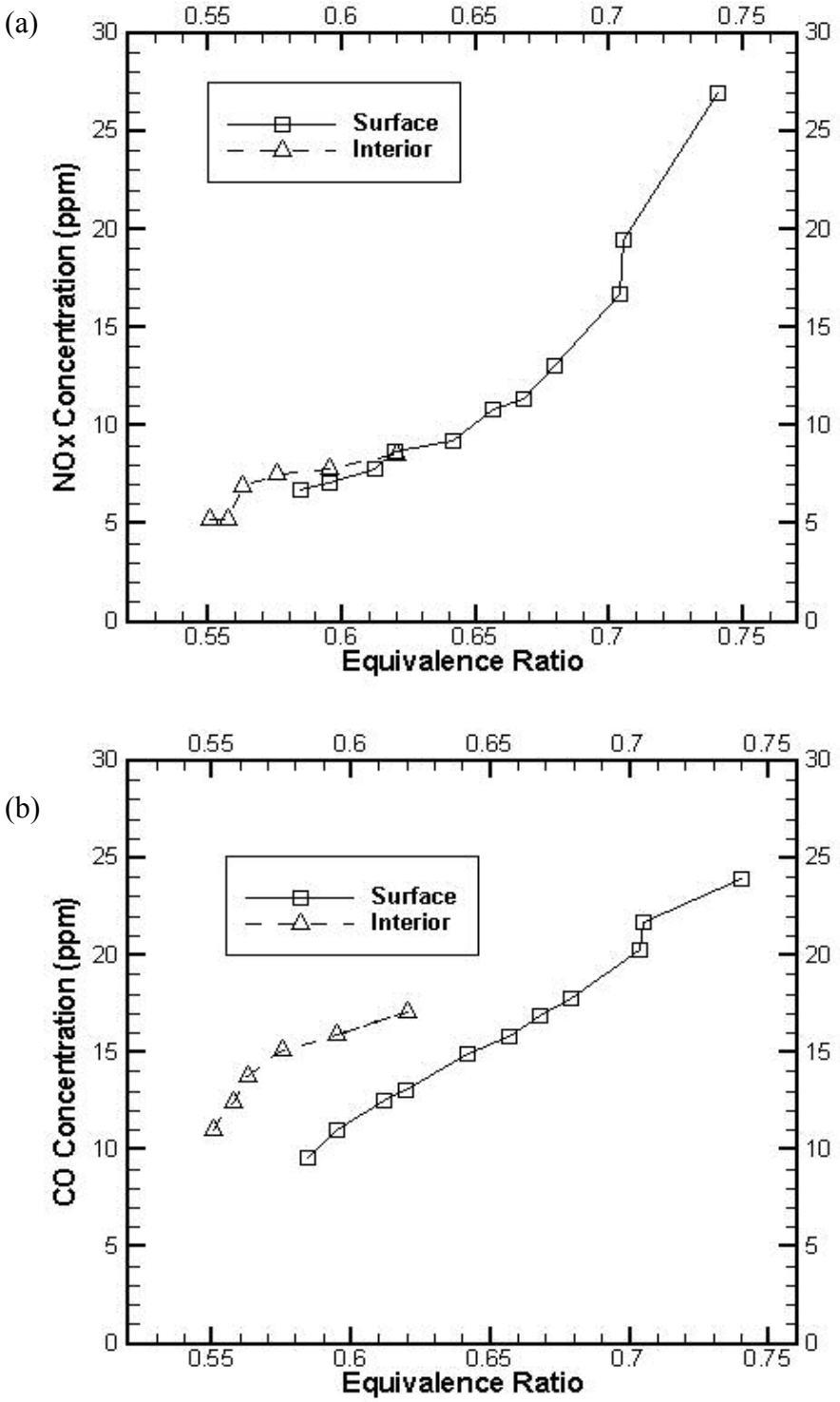

Figure 3.11. Emissions measurements for the two combustion modes, (a) NOx and (b) CO.

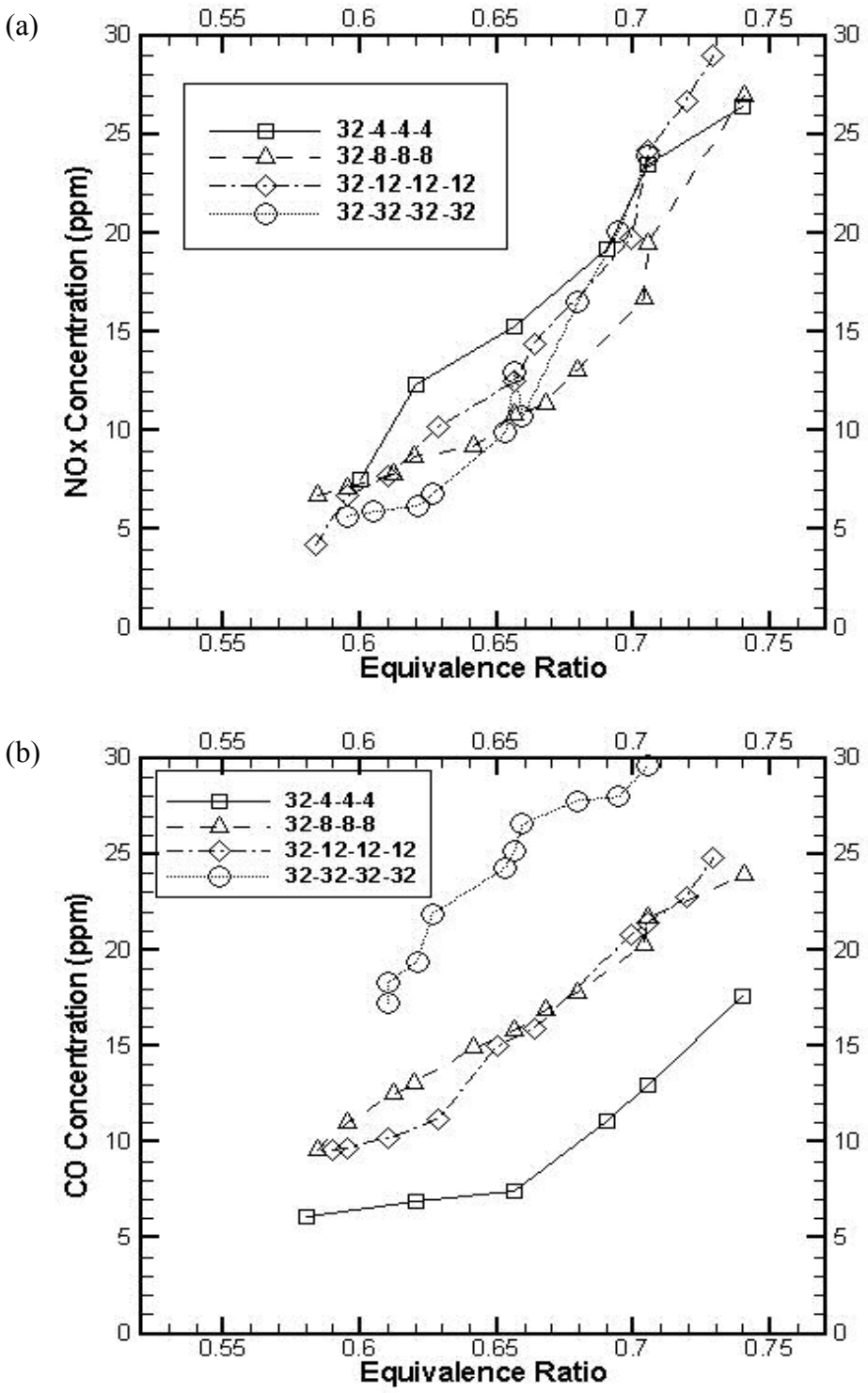

Figure 3.12. Effect of combustion zone pore size on emissions from surface Combustion at V_{in} = 1.0 m/s, (a) NOx and (b) CO.

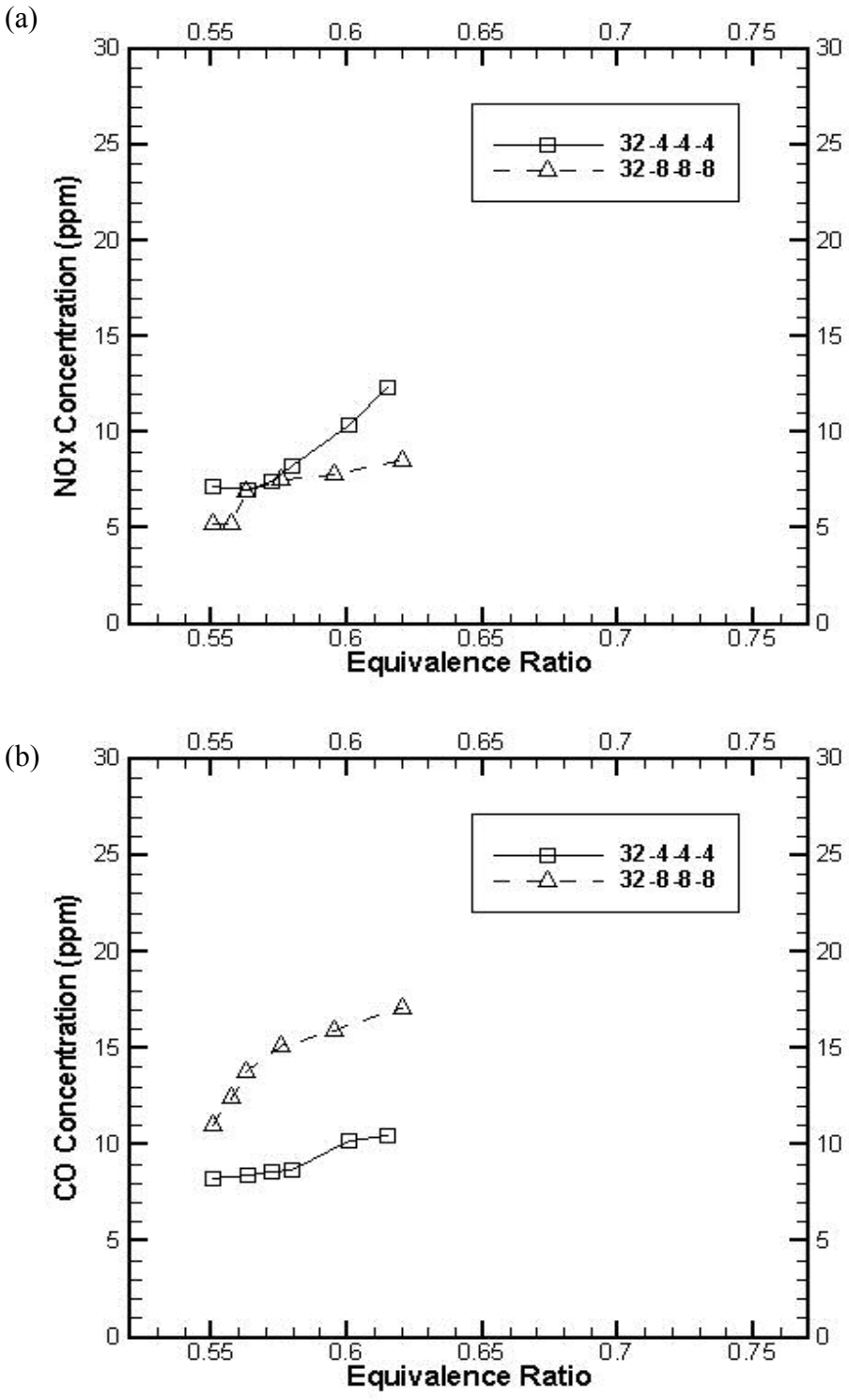

Figure 3.13. Effect of combustion zone pore size on emissions from interior combustion at V_{in} = 1.0 m/s, (a) NOx and (b) CO.

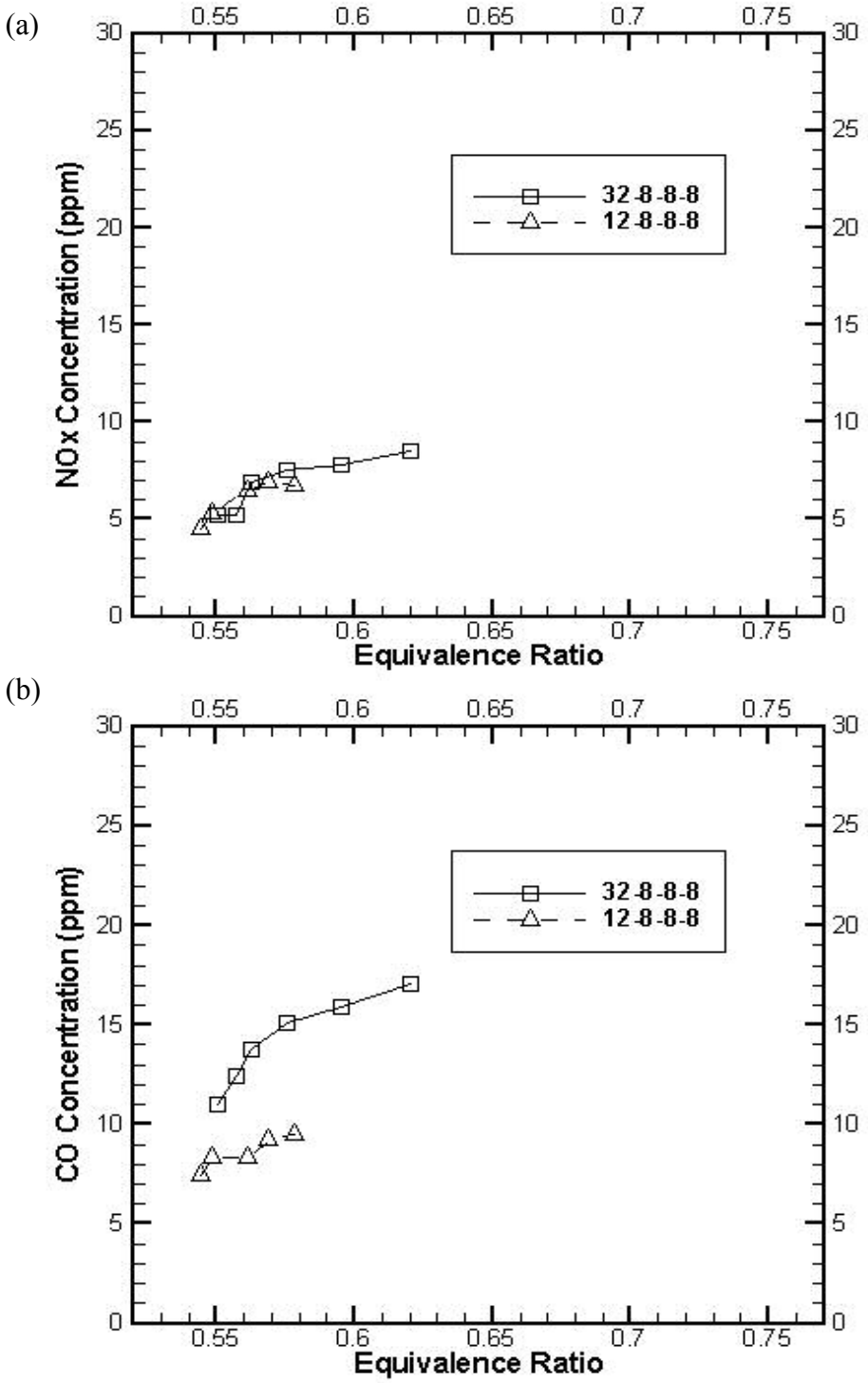

Figure 3.14. Effect of preheat zone pore size on emissions from interior combustion at V_{in} = 1.0 m/s, (a) NOx and (b) CO.

3.3 Conclusions

SiC coated, carbon foam structures, offering superior structural and thermal integrity were investigated as PIM for combustion. Methane/air flames were stabilized on the surface and interior of the PIM at identical operating conditions, allowing for a direct comparison of the two combustion modes. Simultaneous NOx and CO emissions of less than 10 ppm were obtained for a range of equivalence ratios and reactant flowrates. While surface combustion produced noise typical of a flat flame burner, interior combustion was virtually silent. The main results of this study are summarized in the following:

- Surface combustion resulted in only slight increase in pressure drop in the PIM compared to that in cold flow. However, interior combustion increased the pressure drop by more than a factor of two.

- For both combustion modes, the NOx concentration was weakly dependent upon the flow velocity or PIM pore size. NOx concentration increased significantly with equivalence ratio, suggesting thermal mechanism as the primary source of NOx generation.

- For both combustion modes, the CO concentration increased with increasing equivalence ratio. The CO concentration decreased with increasing PIM pore size.

- Interior combustion extended the LBO limit over surface combustion at all conditions tested.

- Increasing preheat zone pore size extended the LBO limit in both combustion modes. The increase in pore size is however constrained by the increased potential of flashback.

The experimental results of this study affirm PIM combustion as an effective method of extending the blow-off limit in lean premixed combustion. Experimental investigation provides evidence that a PIM combustor producing single-digit NOx and CO concentrations is feasible. Practical applications of combustion with PIM would benefit from the extended LBO limit, low NOx and CO emissions, elimination of noise and noise-related combustion instabilities, flashback prevention, and duel-fuel capability feasible with interior combustion in PIM. Small-scale combustors could also benefit from reactant preheating and high space heating rates achieved with PIM combustion, as discussed in the next Chapter.

4. Mesoscale Combustion Experiments

Combustion with the use of PIM provided several benefits for macroscale combustion systems, as documented in Chapter 3. However, combustion at small scales presents several additional challenges, including high heat loss and short flow residence times. Heat recirculation is an effective method of limiting heat loss and improving combustion performance. However, new methods of achieving heat recirculation in a small volume must be developed for practical devices. To meet this requirement, a heat recirculating, lean premixed combustion system utilizing PIM was developed.

Experiments were conducted to gain insight into mesoscale, heat recirculating combustion with the use of PIM. The objectives of the experiments were to:

- Prove the feasibility of the design
- Determine the operating range of the combustor
- Determine the important parameters affecting combustor performance
- Determine the effects of the important parameters

The experimental combustor was 100 mm long and 40 mm in diameter. It utilized PIM in an annular preheat zone around the combustor to recirculate heat transferred through the combustor wall. Combustor performance was evaluated by measurements of pressure loss, exterior surface temperature, preheated reactant temperature, product gas temperature, and pollutant emissions. Experiments were

conducted to determine the effects of reactant flowrate, PIM in the preheating annulus and exterior surface insulation on combustor performance. Temperature measurements were used to calculate system heat loss and heat recirculation.

4.1 Experimental Setup and Procedure

Figure 4.1 shows a schematic of the heat-recirculating combustor constructed to perform the experiments. The system size was selected to determine important characteristics of this new design at a moderate scale. Thus, factors such as the ease of manufacturing and instrumentation for detailed measurements were considered. Radial dimensions were chosen to maintain nearly a constant cross-sectional area in the annulus and combustion chamber. The major components were machined from 304 stainless-steel. Methane fuel and air were injected separately into the annulus at six equally spaced injection ports. The annulus measured 100 mm long with an inner diameter of 27 mm and an outer diameter of 34 mm. The annulus was filled with an 80 mm long bed of packed 304 stainless steel spheres of 3 mm diameter. The preheated fuel/air mixture entered the inner passage through four 12 mm diameter peripheral holes. Combustion was stabilized on the downstream surface of the 25 mm long inner PIM, a monolithic SiC coated, carbon foam of 12 pores per cm (ppcm). The free space of the combustion chamber was 20 mm in diameter and 63 mm long. The combustor was insulated with 25 mm thick Insulfrax insulation, with thermal conductivity of 0.2 W/m.K [Insulfrax, 2005]. Figure 4.2 shows a photograph

of the un-insulated combustor with fuel and air inlets at the top, and a thermocouple probe attached at the bottom surface.

Methane fuel was supplied from a compressed gas cylinder and measured with a mass flowmeter calibrated in the range 0 to 1.0 standard liters per minute (slm) with an uncertainty of ± 0.015 slm. Air was supplied by an air compressor, dried and measured with a mass flowmeter calibrated in the range 0 to 60 slm with an uncertainty of ± 0.9 slm. The preheat temperature was measured by a K-type thermocouple located upstream of the inner PIM, as illustrated in Fig. 4.1. The product gas temperature was measured by an R-type thermocouple with 0.075 mm bead diameter. The product gas temperatures are reported uncorrected for radiation. The maximum radiation correction was estimated to be less than 40 K (Appendix F). The total uncertainty of the temperature measurements was 20 K. Concentrations of NOx and CO were measured with electrochemical gas analyzers calibrated in the range 0 to 200 ppm with an uncertainty of ± 4 ppm. Emissions samples were obtained through a quartz probe of 3 mm outer diameter with a tapered tip of 4:1 expansion ratio to quench the reactions. probe effectively quenched the gas sample. Concentrations are reported on an uncorrected, dry basis. The uncertainties of temperature and emissions measurements were calculated using the bias errors provided by manufacturer and the precision errors calculated by repeating experiments eight times. The temperature and emissions measurements at the combustor centerline and z = 63 mm were used to determine uncertainties.

A 3-way manual traversing system with least count of 0.6 mm was used to obtain temperature and emissions profiles within the combustor in radial (r) and streamwise (z) directions. The downstream surface of the PIM was taken as the reference location (z = 0 mm) for streamwise measurements. Experiments were conducted for two reactant flow velocities, V_{in} = 0.5 m/s and 1.0 m/s. Here, the mean reactant velocity, V_{in}, was calculated from the volume flowrate of the reactants (fuel and air) at ambient conditions divided by the cross sectional area of the combustor chamber. The cold flow Reynolds number based on the diameter of the combustion chamber was 670 and 1330 for the two cases. The heat release rates for the two cases were 230 W (0.7 MW/m^2) and 460 W (1.5 MW/m^2) at equivalence ratio, Φ = 0.50; here PIM surface area has been used to characterize the heat release rate (HRR), which is the typical approach used for surface burners.

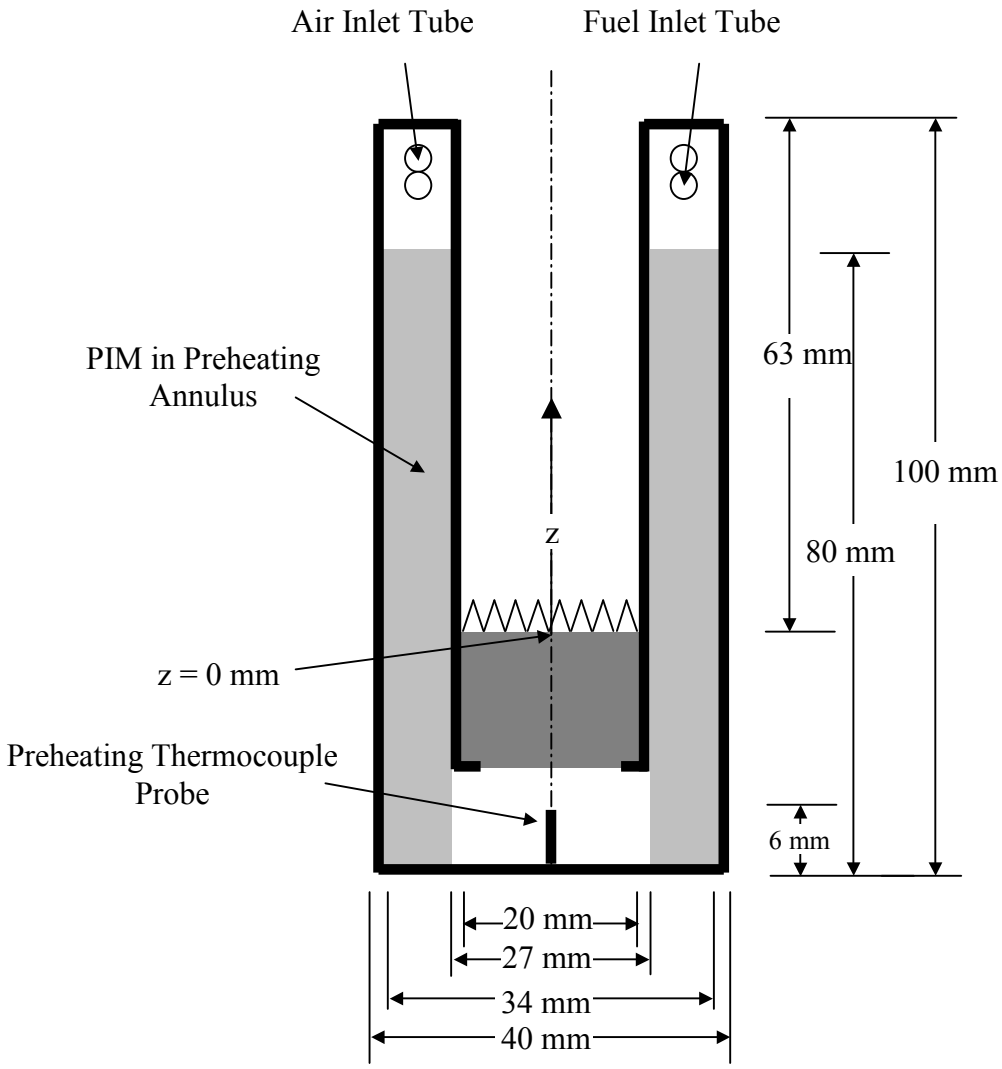

Figure 4.1. Schematic of the mesoscale, heat recirculating combustor.

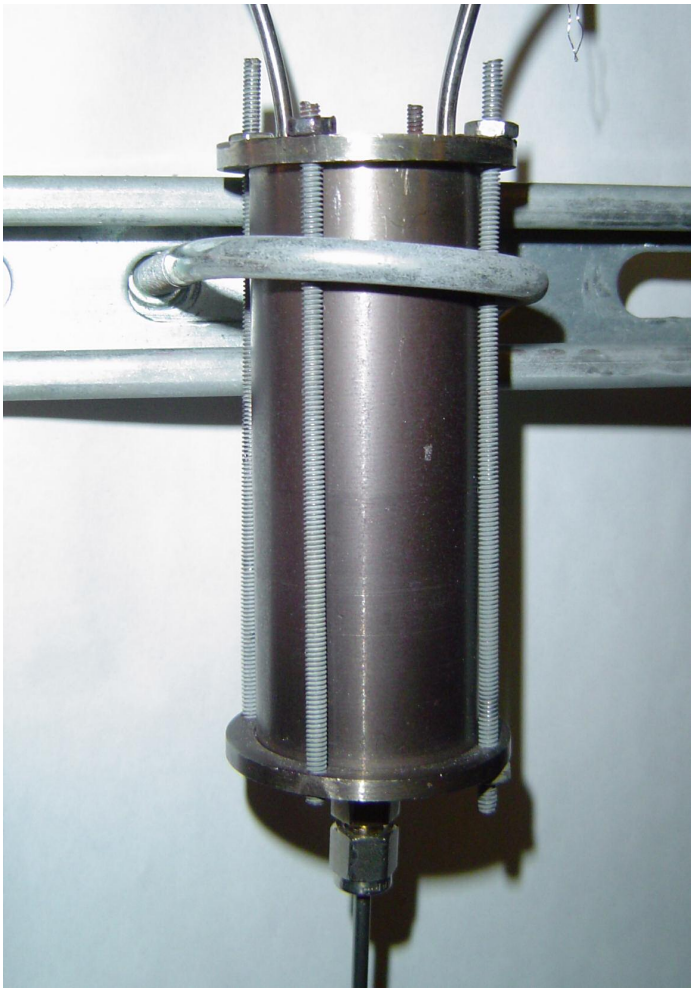

Figure 4.2. Picture of the mesoscale, heat recirculating combustor.

4.2 Results and Discussion

Stable combustion was achieved on the surface of the inner PIM over a range of equivalence ratios and flowrates. Figure 4.3 plots preheat and product gas (at r = 0 mm, z = 63 mm) temperatures during the warm-up period. After ignition, heat was transferred through the combustor wall by conduction and to the reactants by interfacial convection with PIM in the annulus. Increasing heat transfer to the reactants is evident by the increase in the preheat temperature (T_{Pre}) with time. The product gas temperature (T_{Exh}) increased as the preheat temperature increased with time. The warm-up process took about 60 minutes to reach steady-state for an insulated combustor with PIM in the annulus, V_{in} = 1.0 m/s and Φ = 0.50. From practical considerations, future design would require a reduction in the thermal mass of the system to shorten the warm-up period. The effects of reactant flowrate, equivalence ratio, PIM in preheating annulus and exterior surface insulation on system pressure loss, pollutant emissions and reactant preheat, exterior surface and product gas temperatures were determined at steady-state conditions.

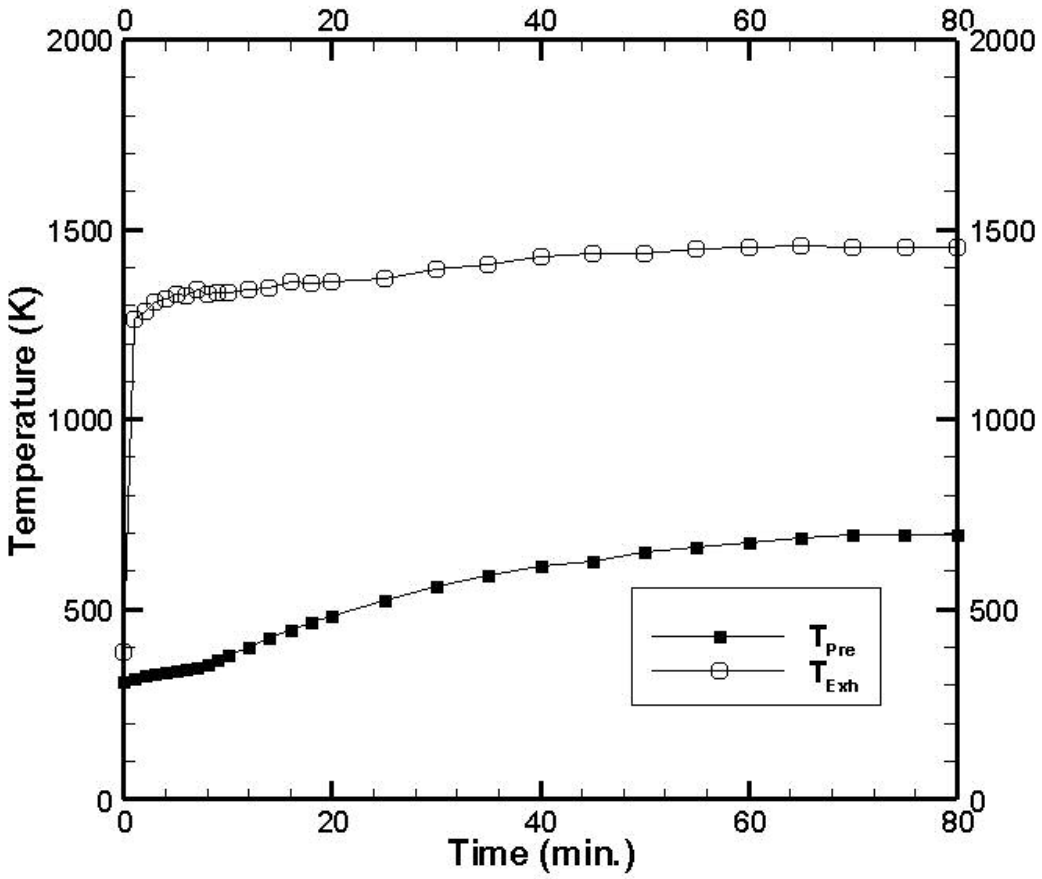

Figure 4.3. Transient nature of preheat and product gas temperature during warm-up (V_{in} = 1.0 m/s, Φ = 0.50, with PIM in preheating annulus and insulated exterior surface).

4.2.1 Pressure Loss

Viscous and inertial forces can cause significant pressure losses in flow through porous media. Hence, it is particularly important to characterize the pressure loss in the heat recirculating combustor design. For large scale combustors that operate at compression ratios ranging from 15:1 to 30:1, pressure loss is typically less than 5 percent of the operating pressure [Saravanamuttoo et al., 2001]. Meso- and microscale combustion systems are expected to operate at much lower compression ratios of 4:1 to 6:1 [Fernandez-Pello, 2002]. Experiments were conducted at atmospheric pressure to characterize system pressure loss.

The Reynolds No. was estimated for locations within the system at baseline conditions of V_{in} = 1.0 m/s and Φ = 0.50. The temperatures within the preheating annulus, flame stabilizing PIM and combustion chamber were taken to be 500 K, 700 K and 1600 K, respectively. The characteristic length was taken to be the bead diameter for the PIM in the preheating annulus and the average pore diameter for the flame stabilizing PIM. The Reynolds number in the annulus was estimated to be 300 without PIM and 130 with PIM. In the flame stabilizing PIM and combustion chamber, the Reynolds numbers were approximately 15 and 400, respectively. These calculations indicate that flow throughout the free spaces of the system was laminar. Within the porous media zones, the Reynolds number was greater than 10, indicating that both viscous and inertial losses were significant [Collins, 1990].

Figure 4.3 presents the cold flow pressure loss between the inlet and the exhaust of the system. At the flowrate corresponding to V_{in} = 1.0 m/s and Φ = 0.50

(0.000365 kg/s), the combustor pressure loss without PIM in the annulus was 260 Pascals (0.26 % of the operating pressure) and it was 310 pascals (0.31 %) with PIM. Thus, the mesoscale, heat recirculating combustor exhibits low pressure loss with and without PIM in the preheating annulus over a large rage of cold-flow conditions.

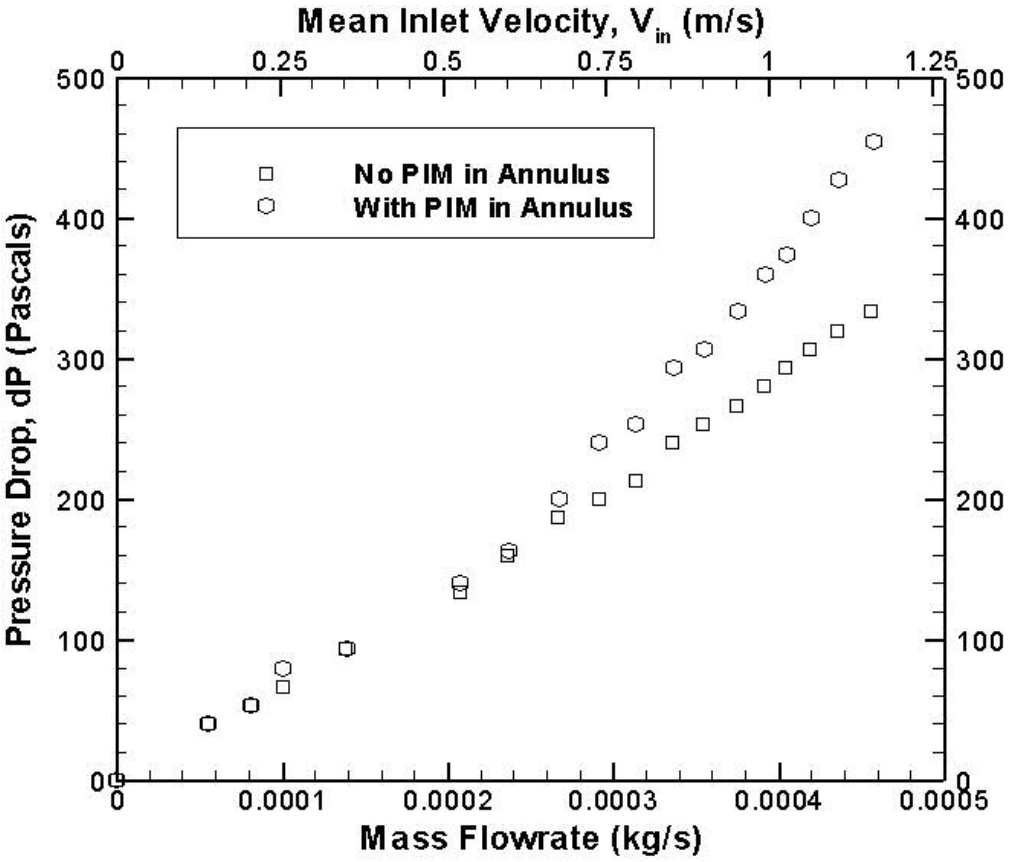

Figure 4.4. Effect of PIM in preheating annulus on cold flow pressure drop.

4.2.2 Reactant Preheat Temperature

The reactant temperature upstream of the flame stabilizing PIM was measured with a K-type thermocouple, as seen in Fig. 4.1. The effects of PIM in the preheating annulus, exterior surface insulation, reactant flowrate, and equivalence ratio on preheating are presented in Fig. 4.5. The reactants were preheated to temperatures exceeding 500 K for all cases and the preheat temperatures increased with increasing equivalence ratio. The higher product gas temperatures associated with higher equivalence ratios increased heat transfer to the combustor wall and contributed to the increased heat recirculation in the annulus.

Surprisingly, the preheat temperature with and without PIM in the preheating annulus were nearly identical. More detailed measurements within the annulus would be required to determine if the reactant temperature increased more quickly with PIM. The addition of exterior surface insulation increased the reactant preheat temperature by about 100 K. Most likely, the temperature of the walls and PIM in the preheating annulus increased with insulation, promoting convective heat transfer from the surfaces to the reactants. Hence, insulation helps recirculate heat that would otherwise be lost to the surroundings, thereby improving the thermal performance of the design. Decreasing the flowrate from V_{in} = 1.0 m/s to 0.5 m/s decreased reactant preheating by about 50 K because of the lower convection heat transfer in the annulus.

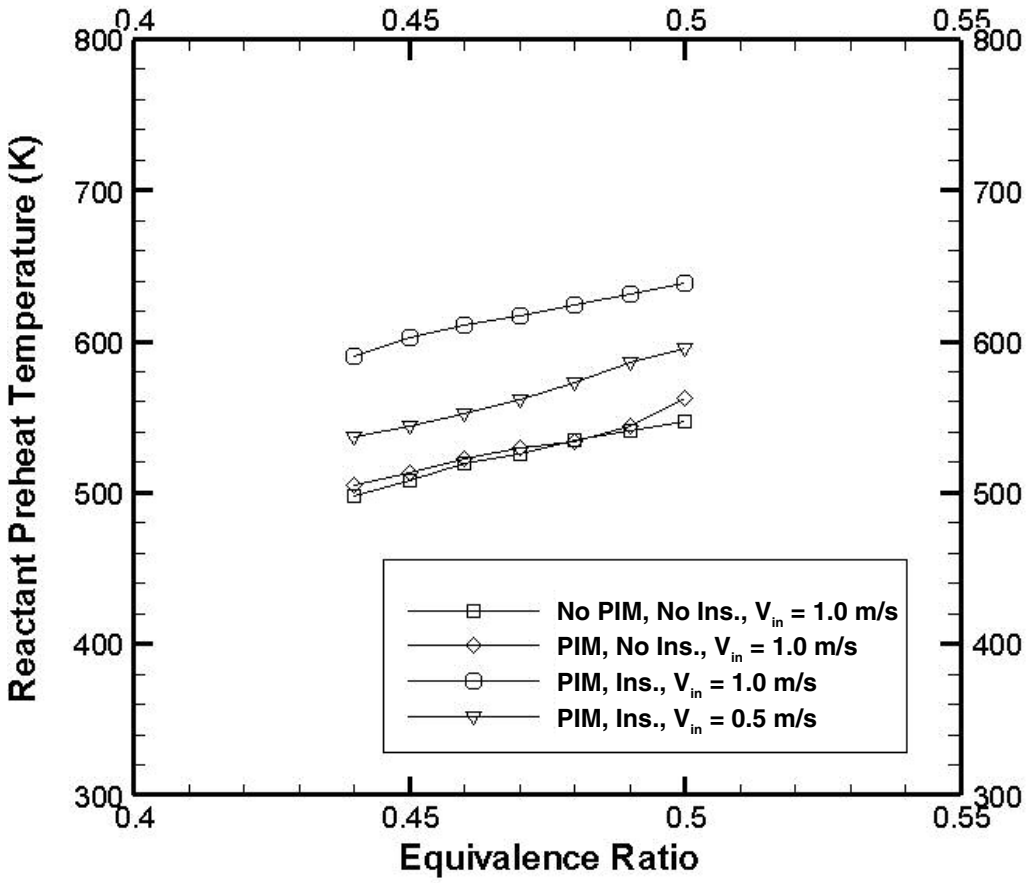

Figure 4.5. Effect of equivalence ratio on reactant preheat temperature.

4.2.3 Exterior Surface Temperature

The exterior surface temperature was measured at various streamwise locations with a K-type thermocouple. The objective was to learn how the surface temperature varied along the length of the combustor and to estimate heat loss to the surroundings.

Figure 4.6 presents the effect of exterior surface temperature with and without PIM in the annulus. The reactant flowrate was 1.0 m/s, equivalence ratio was 0.50 and exterior surface was not insulated. The maximum exterior surface temperature without PIM, 490 K, was measured near the combustor lid (z = 63 mm). The temperature decreased to about 440 K and it was relatively constant in the region -40 < z < 40 mm. It is believed that the maximum temperature was observed near the lid because of significant axial heat conduction through the combustor wall and lid. The addition of PIM to the preheating annulus would affect the exterior surface temperature in one of two ways. Inserting PIM may block radiation across the annulus, reducing the exterior surface temperature and hence, heat loss. However, conduction through the PIM could increase the exterior surface temperature and increase heat loss. Figure 4.6 indicates that the addition of PIM to the preheating annulus increased the exterior surface temperature by 40 to 60 K over the entire length of the combustor. It is possible that a lower thermal conductivity, lower porosity PIM could be used to reduce system heat loss by simultaneously minimizing radiation and conduction across the annulus.

Insulation on the exterior surface decreased the temperature by 80 to 100 K, as seen in Fig. 4.7. However, adding insulation increased the radius of the combustor, increasing its size. Decreasing the reactant flowrate from V_{in} = 1.0 m/s to 0.5 m/s did not significantly affect the exterior surface temperature, as seen in Fig. 4.8. Thus, heat loss for the two flowrates was similar, but the percent heat loss for V_{in} = 1.0 m/s was about half of the percent heat loss for V_{in} = 0.5.

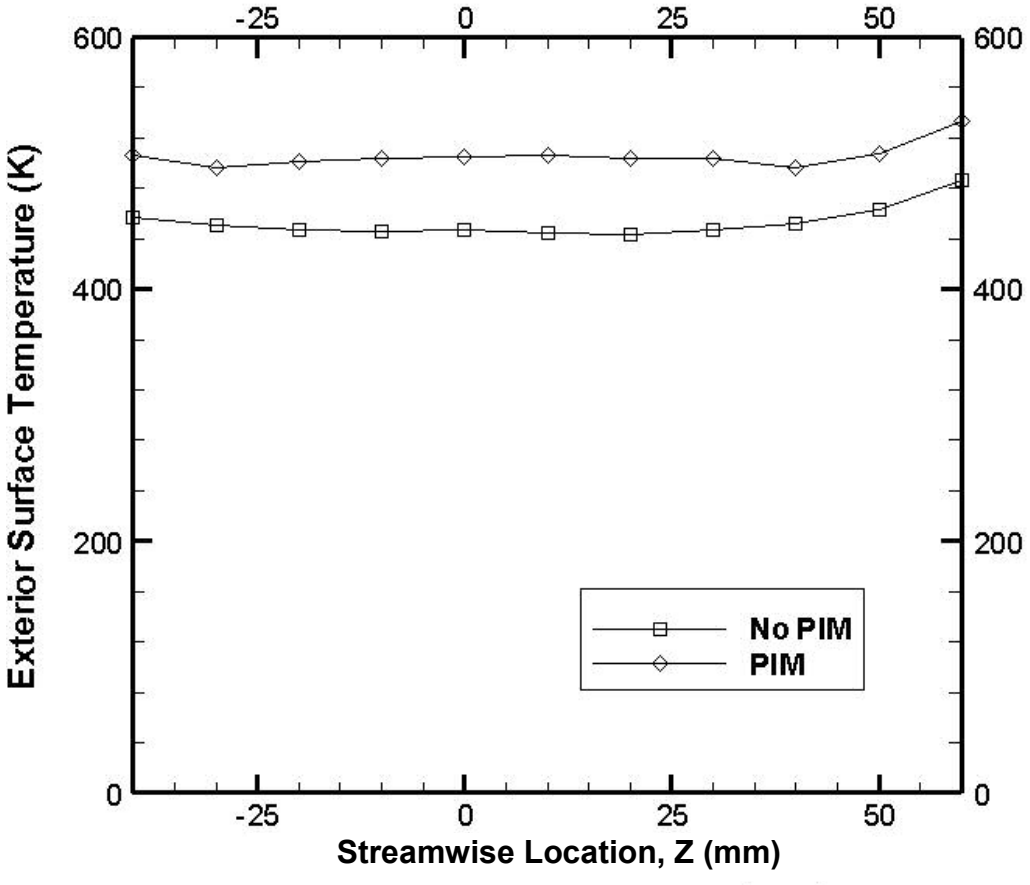

Figure 4.6. Effect of PIM in preheating annulus on exterior surface temperature.

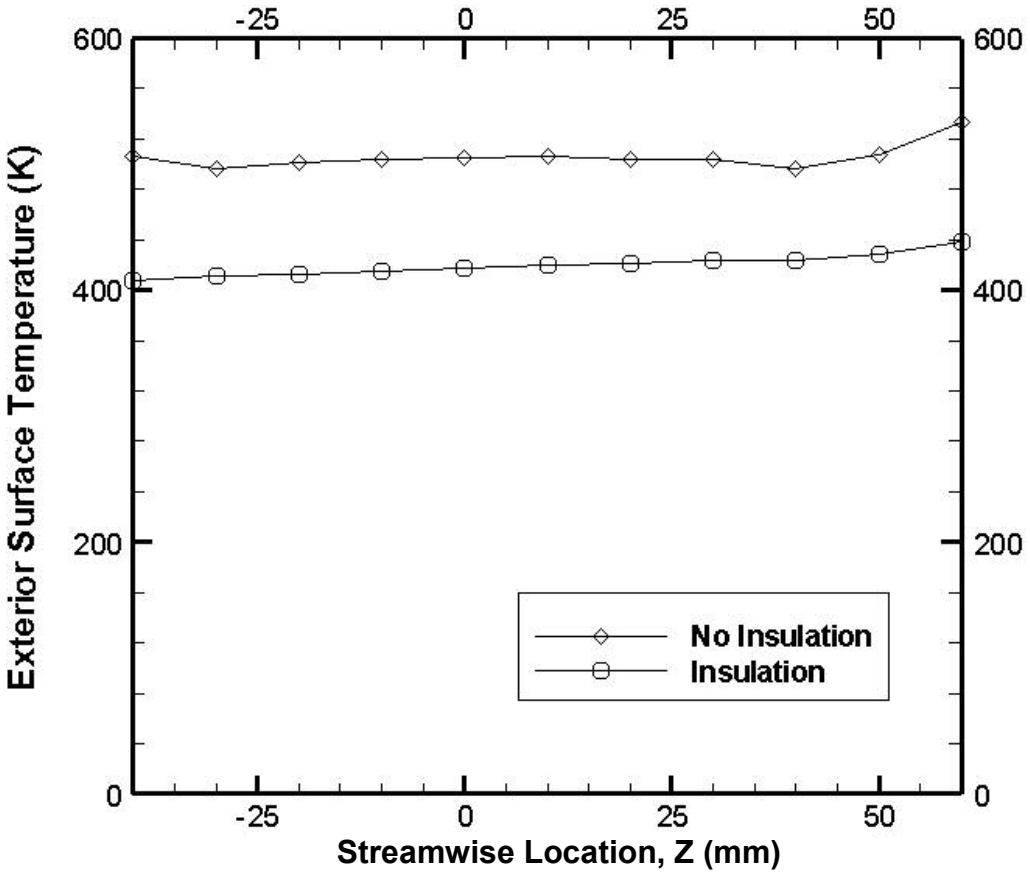

Figure 4.7. Effect of insulation on exterior surface temperature.

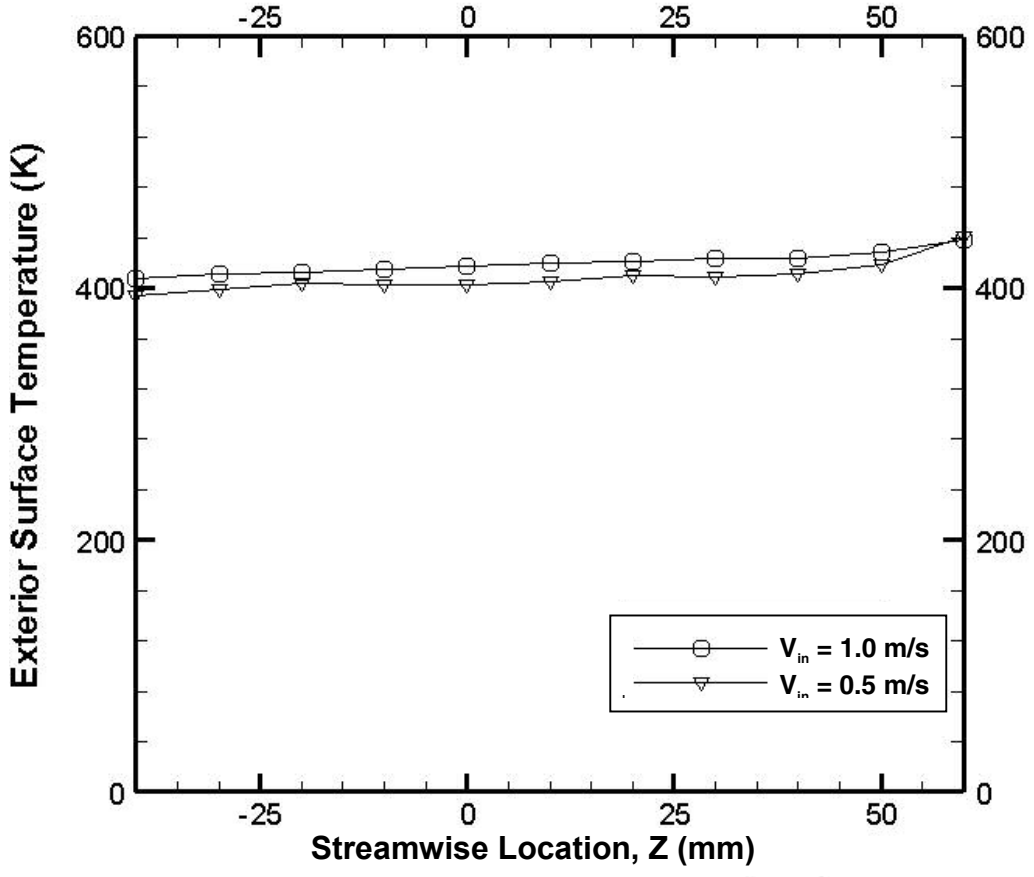

Figure 4.8. Effect of reactant flowrate on exterior surface temperature.

4.2.4 Product Gas Temperature

Product gas temperature profiles were obtained at several radial and streamwise locations. The effects of PIM in the preheating annulus, exterior surface insulation, reactant flowrate and equivalence ratio on the product gas temperatures are presented, discussed, and compared in this section.

4.2.4.1 General Characteristics

Figure 4.9(a) presents product gas temperature for V_{in} = 1.0 m/s, Φ = 0.50, and without PIM in the annulus or exterior surface insulation. The temperature was highest near the centerline and it decreased with increasing radius until a significant temperature gradient was observed near the wall. The temperature profile at z = 20 mm is a relatively uniform from the centerline to r = 7.0 mm. Further downstream, at z = 40 mm, the uniform region became smaller, from the centerline to r = 4.0 mm. At the combustor exit plane, z = 63 mm, the uniform temperature region was no longer present and a more parabolic profile had developed. The decreasing temperature as the products moved downstream indicated that the total enthalpy of the products in the combustor decreased. The decreasing enthalpy and negative temperature gradient near the wall indicated heat transfer from the product gases to the combustor wall.

Figure 4.9(b) illustrates the product gas temperature profile in the streamwise direction. At the combustor centerline, the temperature remained relatively constant at 1700 K from z = 0 mm to z = 40 mm and it decreased to 1620 K at the exit plane (z = 63 mm). At r = 5.1 mm, the temperature near the flame zone (z = 5 mm) was

slightly lower than it was at the centerline, 1670 K near the flame (r = 5 mm) decreasing to 1500 K at the exit plane (z = 63 mm). Near the wall (r = 7.6 mm), the product gas temperature was the lowest, decreasing from 1580 K at z = 5 mm to 1220 K at z = 63 mm. These results show that the temperature of the product gases near the combustor wall was affected more than it was at the centerline. The radial profile of product gas temperature at the exit plane (z = 63 mm) was used to calculate the system heat loss, as described in section 4.2.6.

4.2.4.2 Effect of PIM in Preheating Annulus on Product Gas Temperature

Figure 4.10 presents the effects of PIM in the preheating annulus on radial temperature profiles at z = 20 mm and z = 63 mm. The operating conditions were V_{in} = 1.0 m/s, Φ = 0.50 and the combustor was not insulated. The product gas temperature was slightly higher in the center region of the combustor with PIM, but the difference was small. Figure 4.11 shows streamwise temperature profiles with and without PIM in the preheating annulus at r = 0.0 and r = 7.6 mm. The product gas temperature near the flame zone was slightly higher with PIM. However, the temperature of the product gases decreased more with PIM as the products moved downstream. At the exit plane, the product gas temperature was not significantly affected by the presence of PIM in the preheating annulus. The higher product gas temperature near the flame indicates that slightly more preheating occurred when PIM was used in the annulus. The similar product gas temperature at the exit plane

indicates that the energy retained by product gas and heat loss to the surroundings were similar for the two cases.

These results indicate that PIM in the preheating annulus promoted heat recirculation, but did not reduce heat loss to the surroundings. Detailed quantification of the heat recirculation and heat loss is presented in Section 4.2.6.

4.2.4.3 Effect of Exterior Surface Insulation on Product Gas Temperature

Figure 4.12 presents the effect of exterior surface insulation on radial temperature profiles at z = 20 and z = 63 mm. The reactant flowrate was V_{in} = 1.0 m/s, equivalence ratio was 0.50 and PIM was present in the preheating annulus. The product gas temperature was slightly higher at the combustor exit plane when the exterior surfaces were insulated, indicating less heat loss. Figure 4.13 presents the effect of insulation on streamwise temperature profiles at r = 0.0 and r = 7.6 mm. At the centerline, the temperature near the flame was similar with and without insulation. However, the temperature decreased more rapidly without insulation as the product gases moved through the combustor, indicating that heat transfer from the reactants to the wall was greater without insulation.

These results indicate that exterior surface insulation decreased heat loss to the surroundings. Quantification of the heat recirculation and heat loss are presented in Section 4.2.6.

4.2.4.4 Effect of Reactant Flowrate on Product Gas Temperature

Figure 4.14 presents the effect of reactant flowrate on radial temperature profiles at z = 20 and 63 mm. The equivalence ratio was maintained constant at Φ = 0.50 for both flowrates and the combustor had PIM in the annulus and exterior surfaces were insulated. The product gas temperature was much higher near the flame and at the combustor exit plane for the higher flowrate case. This result indicates significantly higher preheating and lower heat loss at higher reactant velocity. Figure 4.15 shows streamwise temperature profiles for V_{in} = 1.0 m/s and 0.5 m/s at r = 0.0 and r = 7.6 mm, respectively. Throughout the streamwise length of the combustor, the product gas temperature was 150 to 200 K higher for the higher reactant flowrate case.

These results indicate that increasing the reactant flowrate decreases heat loss. The impact of reactant flowrate on product gas temperature was much greater compared to PIM in the annulus or exterior surface insulation. Quantification of the heat recirculation and heat loss is presented in Section 4.2.6.

4.2.4.5 Effect of Equivalence Ratio on Product Gas Temperature

The effect of equivalence ratio on product gas temperature at the center point (r = 0 mm) of the combustor exit plane (z = 63 mm) is presented in Fig. 4.16. Decreasing equivalence ratio would increase the product gas temperature because of the increased excess oxygen and nitrogen. Equivalence ratio was varied by adjusting the air flowrate and fuel flowrates to maintain a constant reactant flowrate. The

product gas temperature at the centerline exceeded the adiabatic flame temperature (T_{Ad}) and it increased with increasing equivalence ratio. For V_{in} = 0.5 m/s, the product gas temperature was approximately 250 K lower than it was for V_{in} = 1.0 m/s, indicating greater fractional heat loss at low flowrates, as discussed in the previous section. The LBO limit, represented by the data point with the smallest Φ, was Φ = 0.39 for V_{in} = 0.5 m/s and Φ = 0.41 for V_{in} = 1.0 m/s. Because of the high level of preheating of the reactants, the LBO limit in the present system is significantly lower than the LBO limit of about Φ = 0.55 in a typical swirl-stabilized combustor operating at similar conditions.

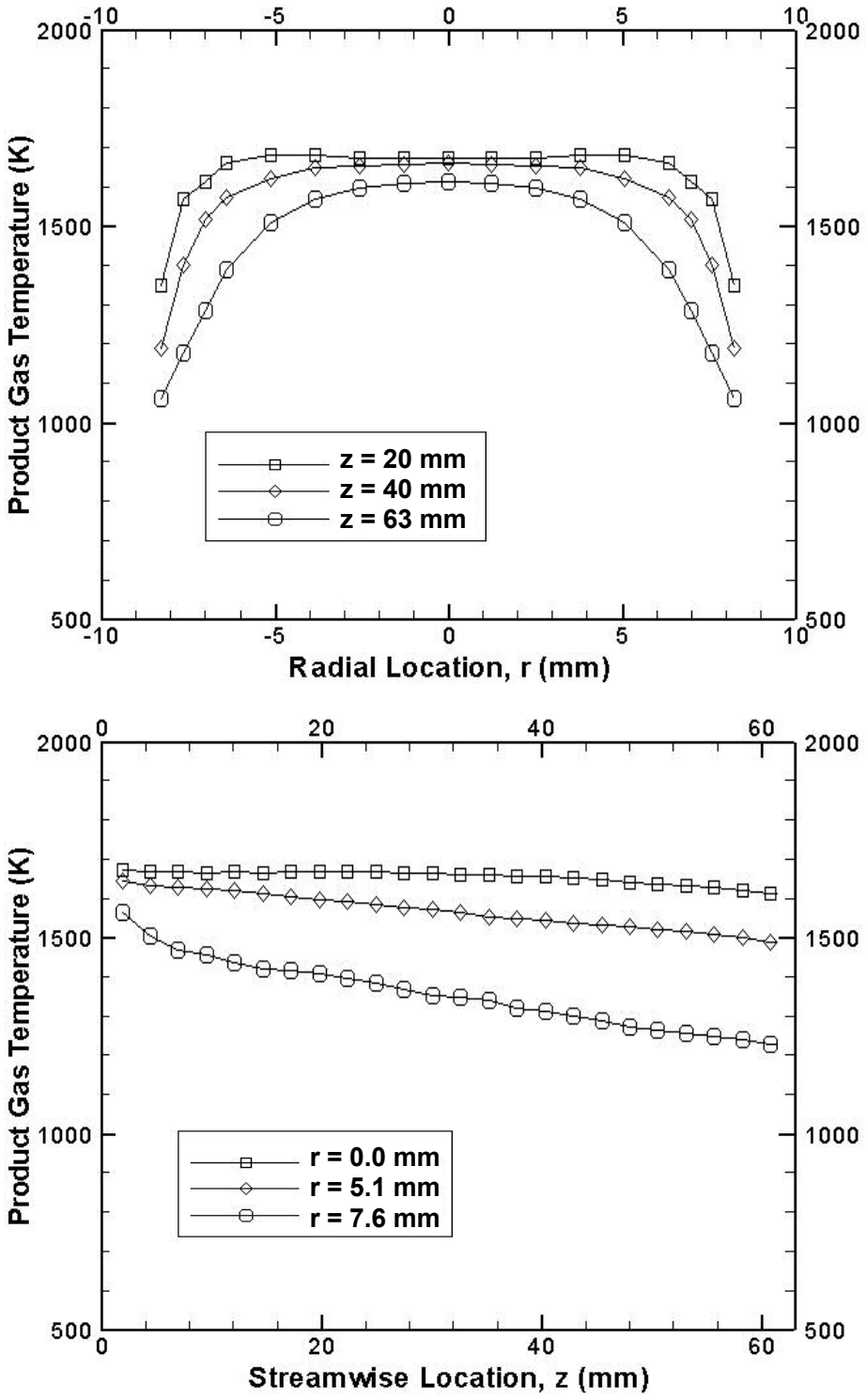

Figure 4.9. Effect of (a) streamwise and (b) radial location on product gas temperature.

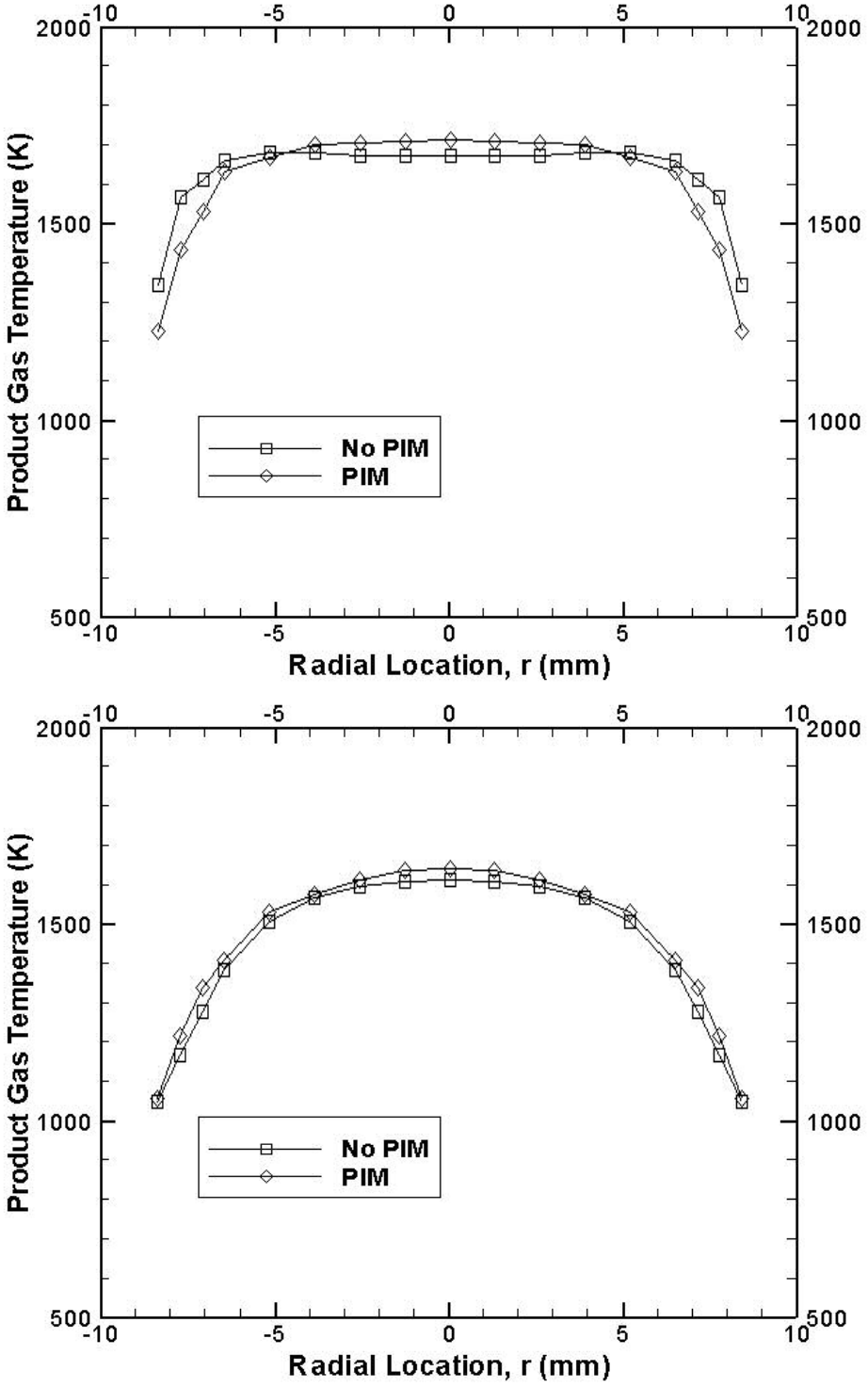

Figure 4.10. Effect of PIM in preheating annulus on radial profiles of product gas temperature at (a) z = 20 mm and (b) z = 63 mm.

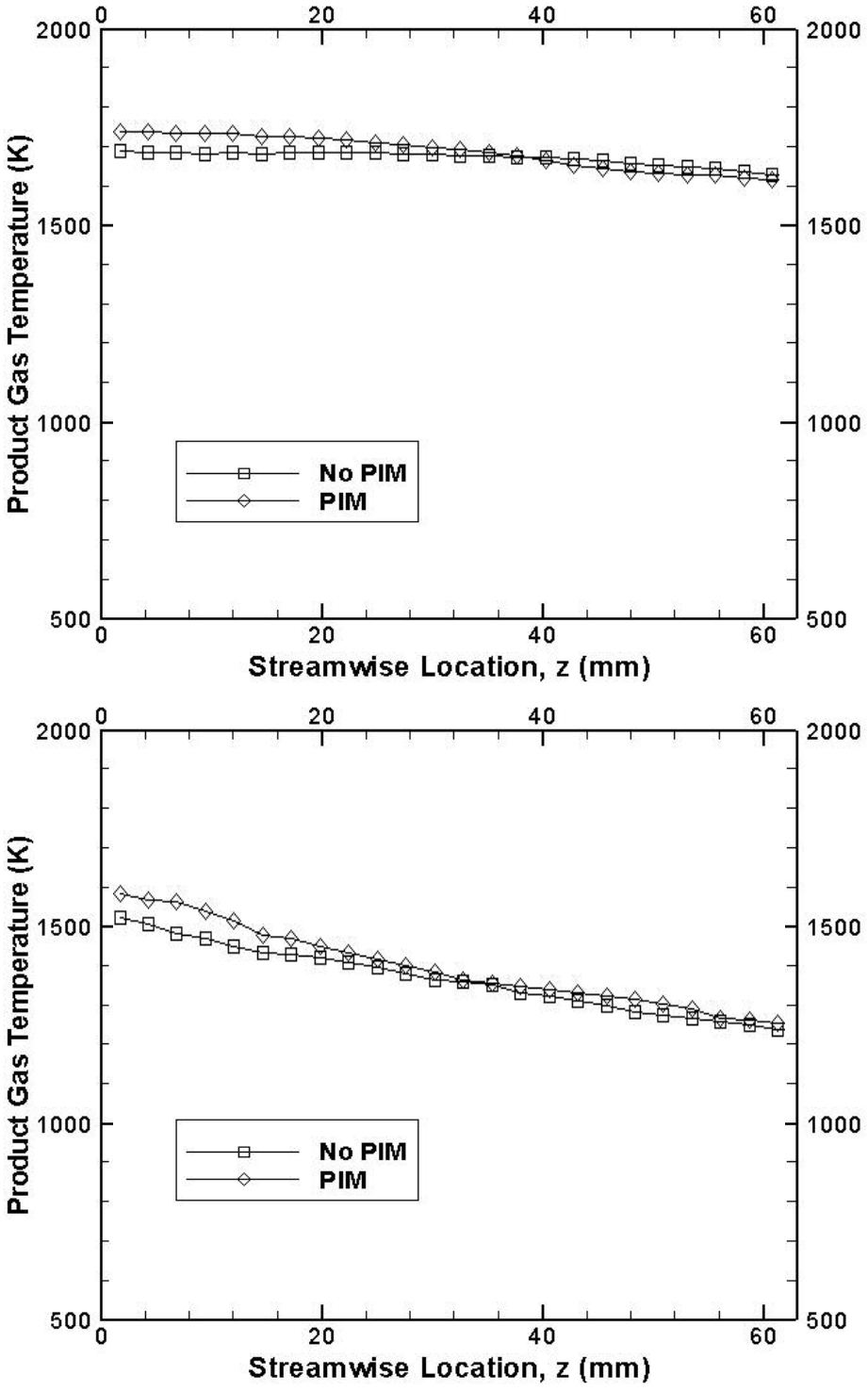

Figure 4.11. Effect of PIM in preheating annulus on streamwise temperature profiles of product gas temperature at (a) r = 0.0 mm and (b) r = 7.6 mm.

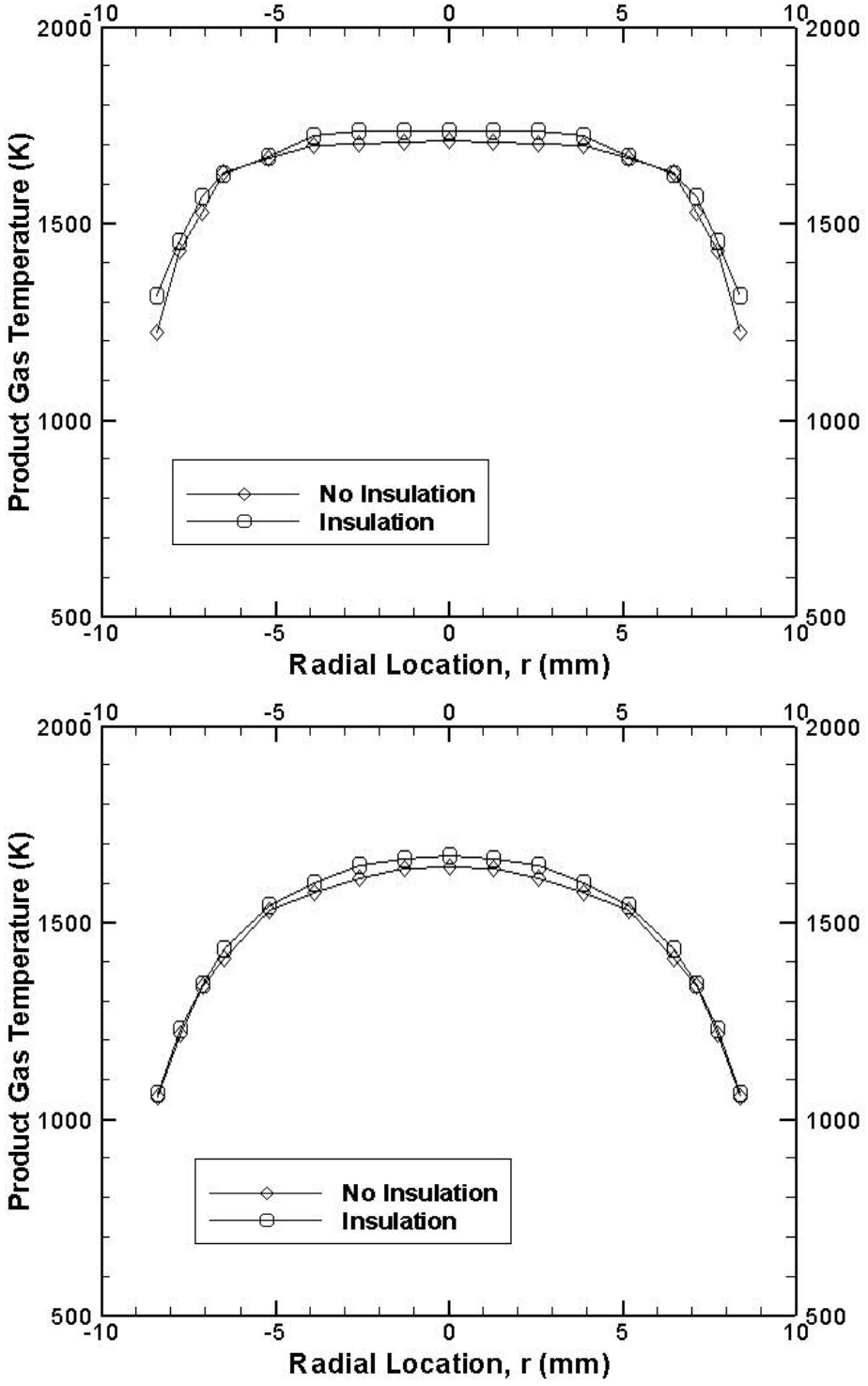

Figure 4.12. Effect of exterior surface insulation on radial profiles of product gas temperature at (a) z = 20 mm and (b) z = 63 mm.

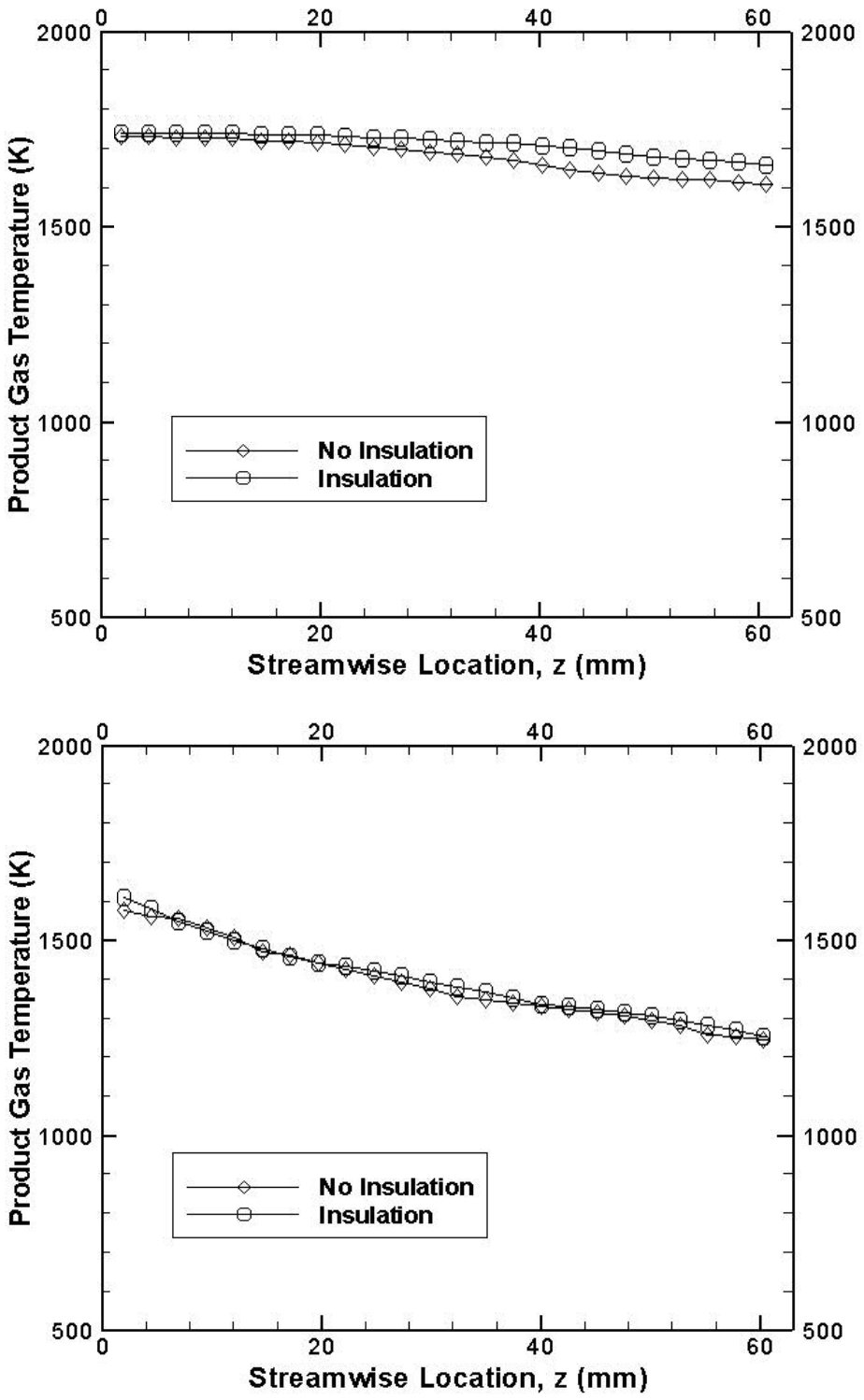

Figure 4.13. Effect of exterior surface insulation on streamwise profiles of product gas temperature at (a) r = 0.0 mm and (b) r = 7.6 mm.

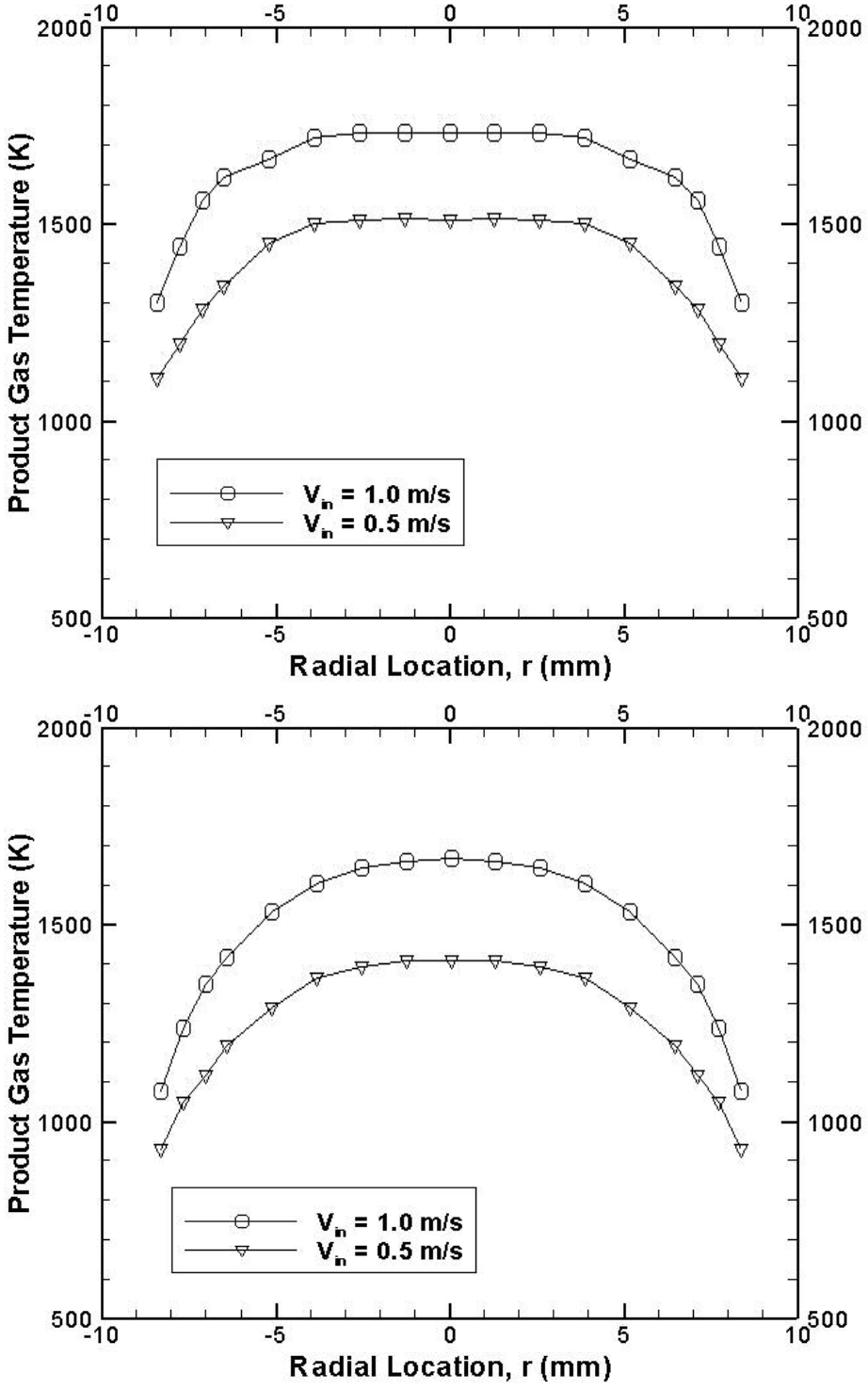

Figure 4.14. Effect of reactant flowrate on radial profiles of product gas temperature at (a) z = 20 mm and (b) z = 63 mm.

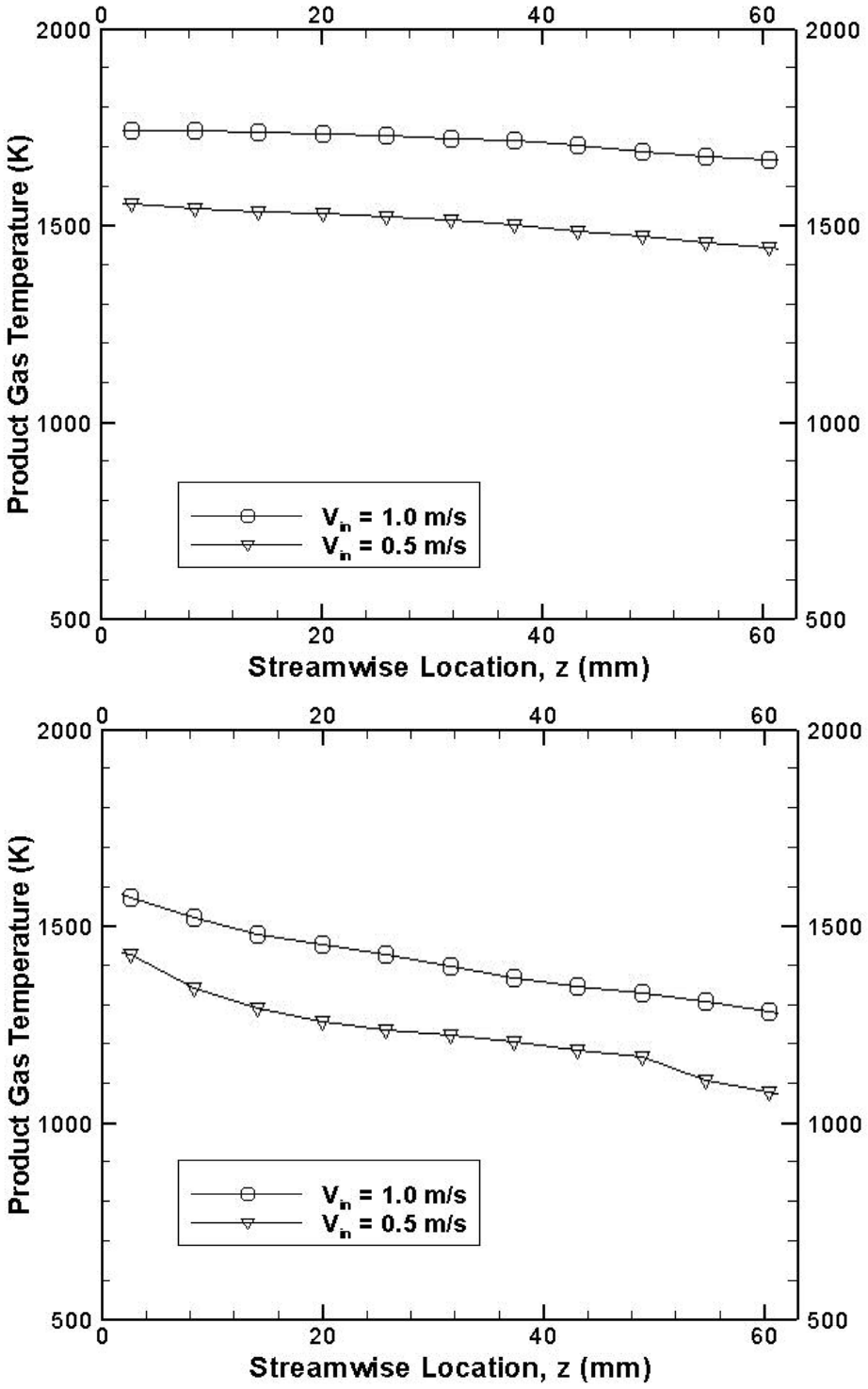

Figure 4.15. Effect of reactant flowrate on streamwise profiles of product gas temperature at (a) r = 0.0 mm and (b) r = 7.6 mm.

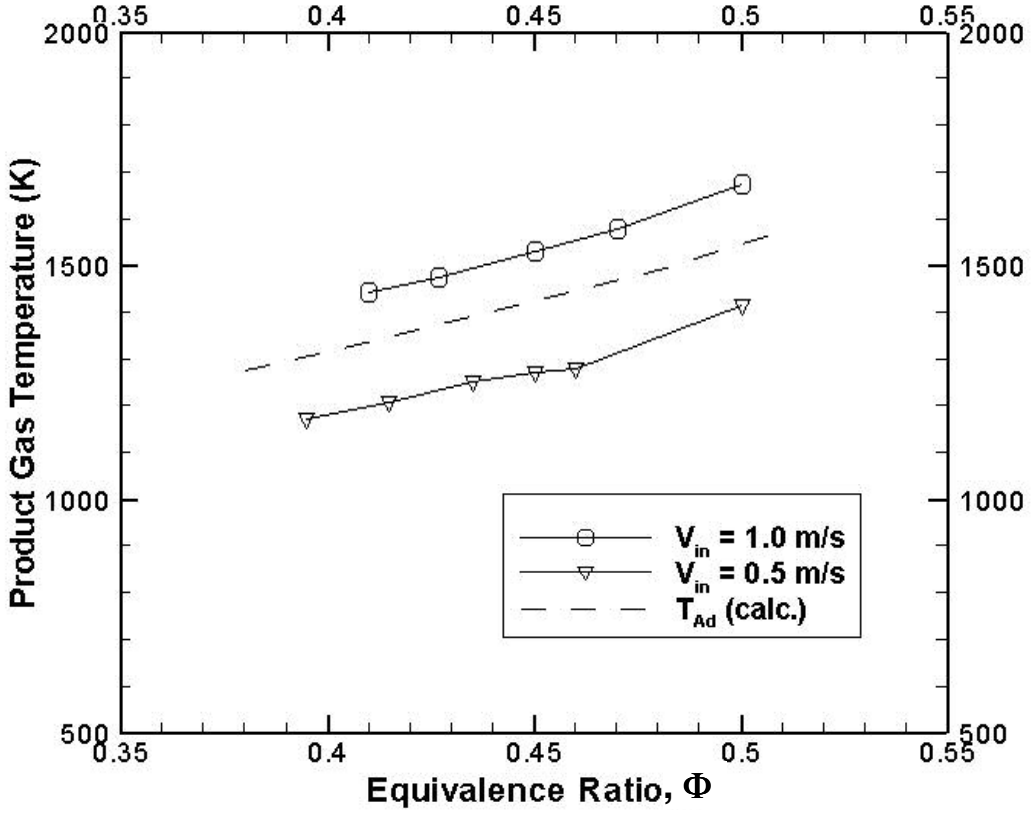

Figure 4.16. Effect of equivalence ratio on product gas temperature at r = 0.0 mm and z = 63 mm.

4.2.5 Pollutant Emissions

The effects of PIM in the preheating annulus, exterior surface insulation, reactant flowrate, and equivalence ratio on CO and NOx pollutant emissions are presented and discussed in this section.

4.2.5.1 General Characteristics

Figure 4.17(a) presents the effect CO concentration in the streamwise direction. Near the flame zone (z = 20 mm) the CO concentration was 22 ppm between r = 0 mm and 3.0 mm and it increased to nearly 100 ppm near the combustor wall. As the product gases moved downstream to z = 63 mm, the CO concentration was 30 ppm from r = 0 mm to 7.0 mm and it increased to nearly 100 ppm near the wall. Higher CO concentrations were observed in the lower temperature regions of the combustor. That is, oxidation of CO proceeded more slowly and the reactions were quenched more quickly near the wall, causing incomplete combustion and high CO concentrations.

Figure 4.17(b) presents NOx concentration in the streamwise direction. Near the flame zone, the highest NOx concentration of 40 ppm was observed at the centerline and the concentration decreased to approximately 20 ppm near the combustor wall. Higher NOx concentrations were observed near the centerline where the product gas temperatures were higher. At the combustor exit plane, the maximum NOx concentration was 33 ppm. The decreasing NOx concentration with increasing streamwise location was an unexpected result. Typically, NOx is formed in the

reaction zone and it remains constant downstream of the flame. Two likely explanations for the decreasing NOx concentration with increasing streamwise location exist; measurement intrusiveness and product mixing. When emissions measurements were taken at z = 63 mm, the quartz probe was located outside of the combustor. As the probe was inserted to the combustor, significant radiation from the emissions probe to the combustor wall took place. This increased the rate of heat transfer to the combustor walls, increasing reactant preheating and hence, flame temperature, yielding higher NOx production by the thermal mechanism. The temperature measured at the preheat thermocouple increased by 25 K as the probe was inserted from z = 63 mm to 20 mm. Additionally, Fig. 4.17(b) shows that NOx was highest near the centerline and lower near the walls. Thus, products with higher NOx concentration near the centerline diffused and mixed with products of lower NOx concentration away from the centerline as the mixture moved downstream. Subsequent measurements were taken at z = 63 mm to minimize measurement intrusiveness and to determine the effects of PIM in the preheating annulus, exterior surface insulation, reactant flowrate and equivalence ratio on CO and NOx emissions.

4.2.5.2 Effect of PIM in Preheating Annulus on Pollutant Emissions

Figure 4.18 shows that the PIM in the preheating annulus slightly reduced CO concentration and NOx concentration was unaffected. The relationship between the product gas temperature and pollutant emissions must be considered when interpreting these results. Since PIM did not significantly affect the gas temperature

(Section 4.2.4.2), the pollutant emissions were not affected. PIM with different properties would affect heat recirculation and heat loss, and hence the temperature distribution within the combustor chamber. PIM properties would also affect pollutant emissions.

4.2.5.3 Effect of Exterior Surface Insulation on Pollutant Emissions

Figure 4.19 presents the effect of exterior surface insulation on CO and NOx concentrations. In Section 4.2.4.3, it was shown that exterior surface insulation slightly increased the product gas temperature near the flame zone. Figure 4.19 indicates that the CO concentration was slightly lower with insulation and NOx emissions were unaffected. Thus, the temperature differences with insulation were not large enough to cause significant difference in NOx emissions. More effective insulation that increased heat recirculation and decreased heat loss would likely increase NOx emissions and decrease CO emissions further.

4.2.5.4 Effect of Reactant Flowrate on Pollutant Emissions

Figure 4.20 shows that CO and NOx emissions decreased as the reactant flowrate was reduced. In Section 4.2.4.4, increasing the flowrate yielded higher product gas temperatures throughout the combustor. Hence, lower CO and higher NOx emissions could be expected at higher flowrates. However, the residence time within the combustor was approximately twice as long for the lower flowrate case. The increase in CO emissions with increasing flowrate, seen in Fig. 4.30, was

attributed to the shorter high temperature residence time, which led to incomplete CO oxidation. The NOx concentration was higher at the higher flowrate because the product gas temperature was higher, thereby increasing NOx production by the thermal mechanism. The effects of PIM in the preheating annulus and exterior surface insulation on pollutant emissions were relatively small because the product gas temperatures were similar with and without PIM or insulation. However, the effect of reactant flowrate was greater because it affected product gas temperature more significantly. The product gas temperature dictates reaction rates and hence, pollutant emissions.

4.2.5.5 Effect of Equivalence Ratio on Pollutant Emissions

The effect of equivalence ratio on CO and NOx emissions at r = 0.0 mm and z = 63 mm is presented in Fig. 4.21. Experiments were conducted with PIM in the preheating annulus and exterior surface insulation. The CO concentration increased with increasing equivalence ratio and it was greater for the higher flowrate case, as discussed in the previous section. NOx concentrations increased with increasing equivalence ratio and were higher for the higher flowrate. The sensitivity of NOx to changes in equivalence ratio was greater because, thermally, NOx production increases exponentially with flame temperature or equivalence ratio [Turns, 2000].

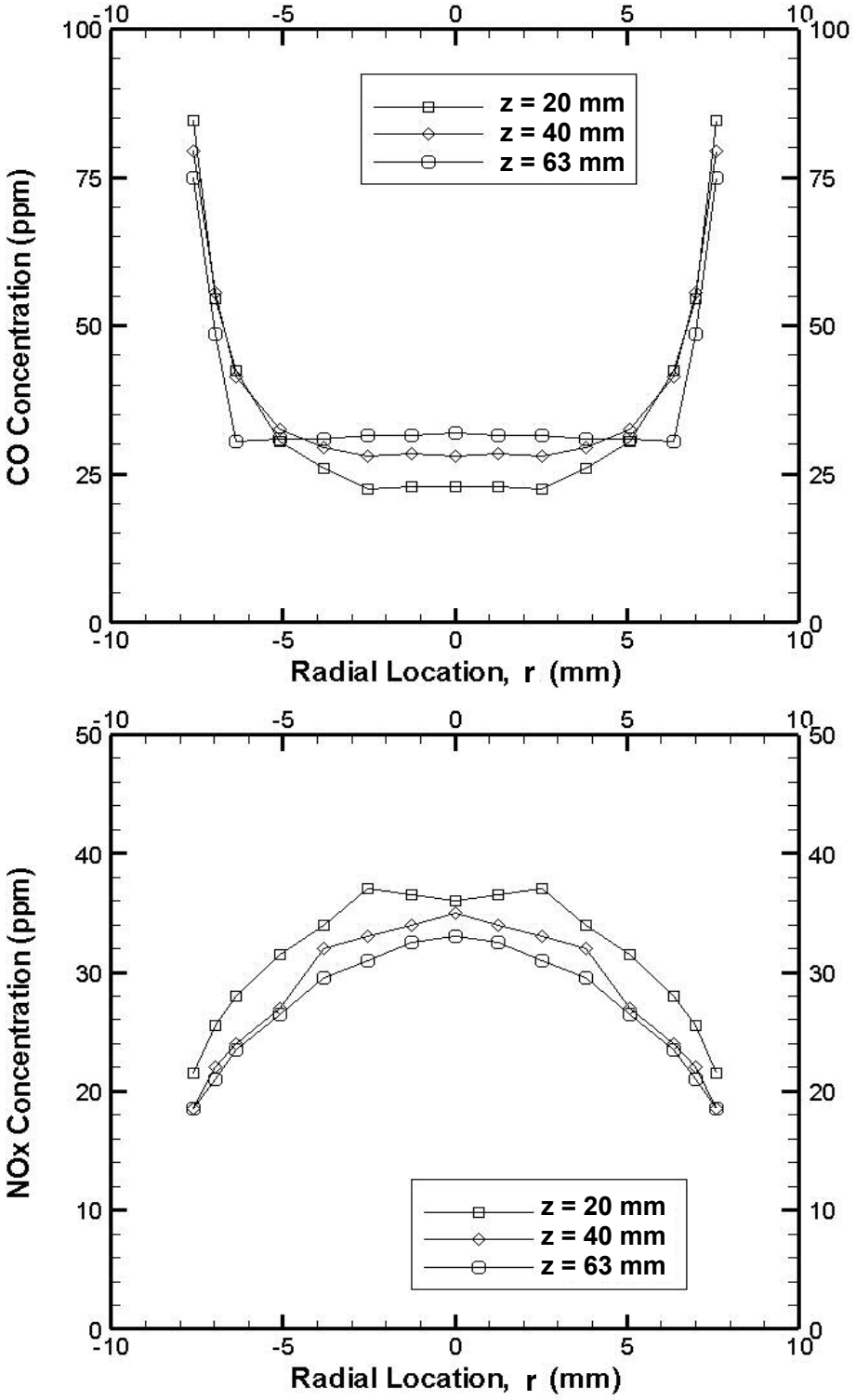

Figure 4.17. Effect of streamwise location on radial profiles of emissions (a) CO and (b) NOx (z = 63 mm).

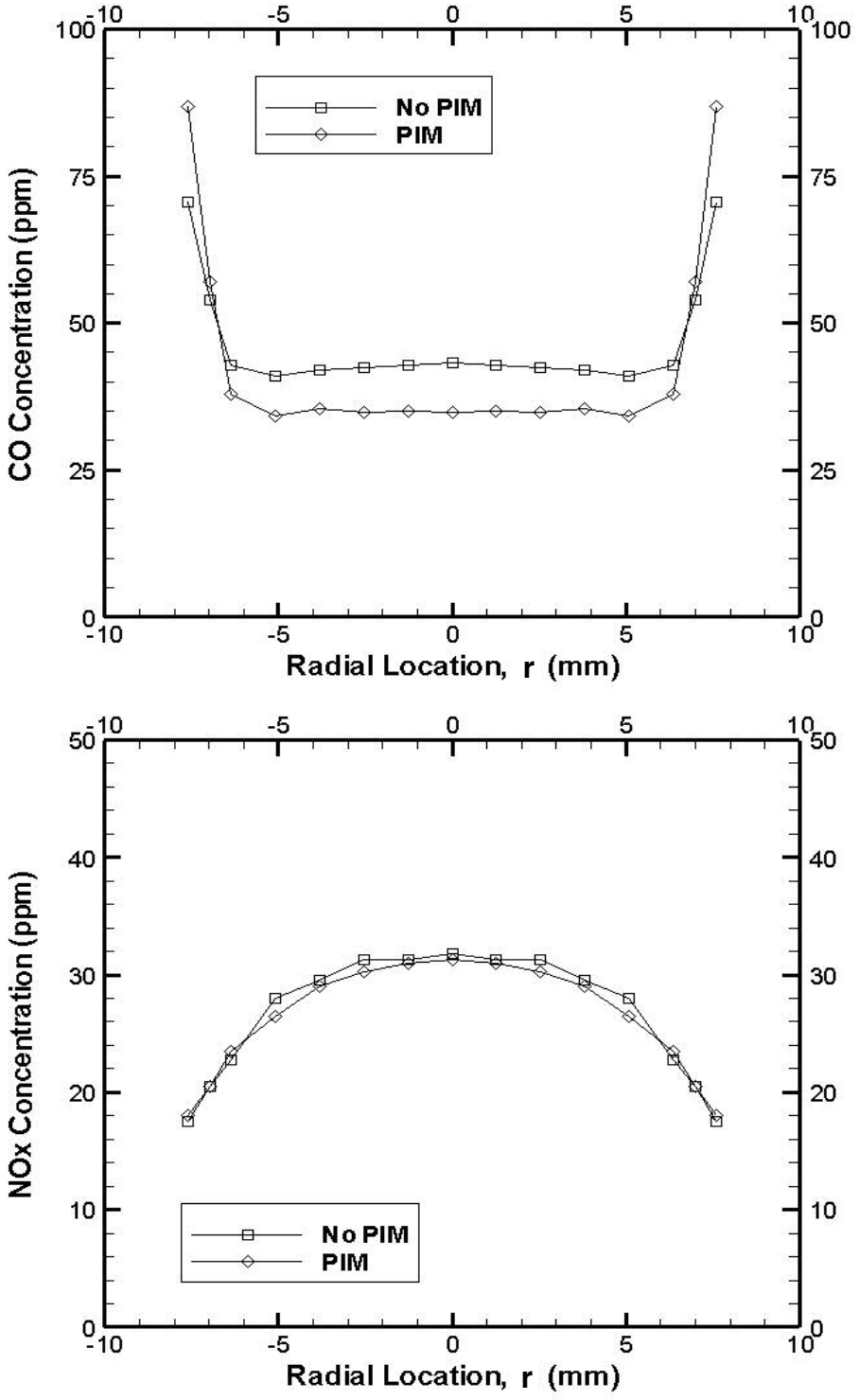

Figure 4.18. Effect of PIM in the preheating annulus on radial profiles of emissions (a) CO and (b) NOx (z = 63 mm).

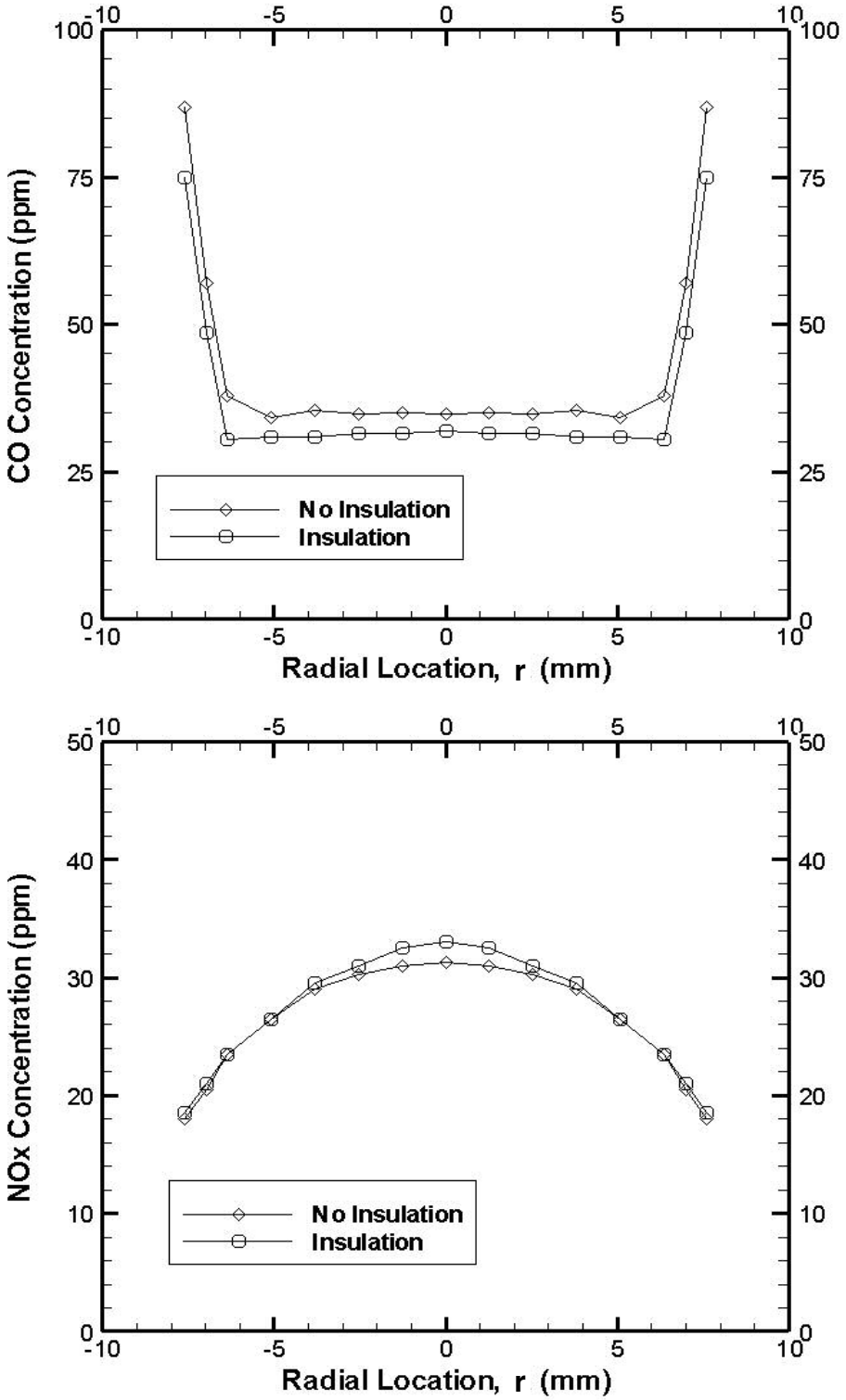

Figure 4.19. Effect of exterior surface insulation on radial profiles of emissions (a) CO and (b) NOx (z = 63 mm).

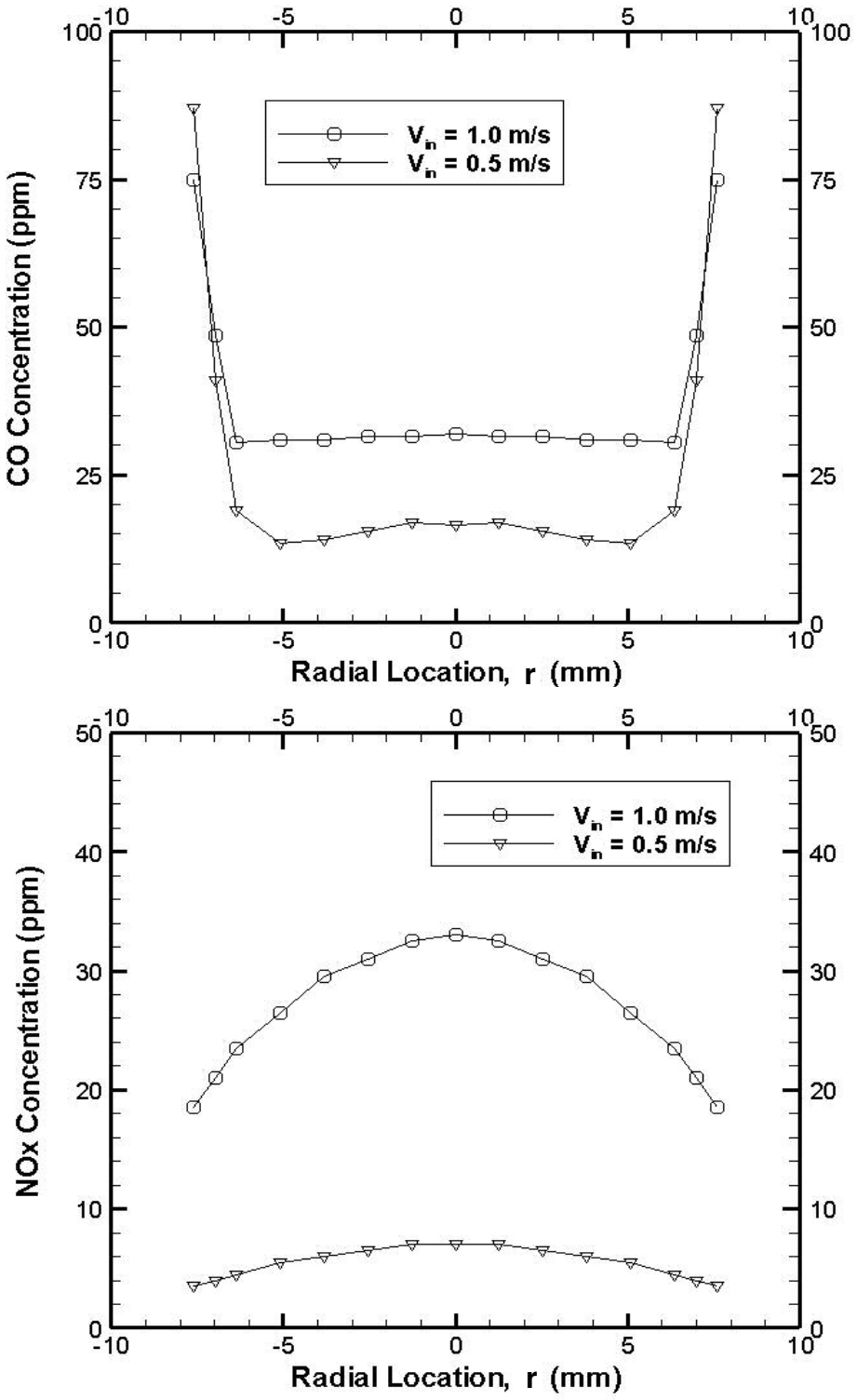

Figure 4.20. Effect of reactant flowrate on radial profiles of emissions (a) CO and (b) NOx (z = 63 mm).

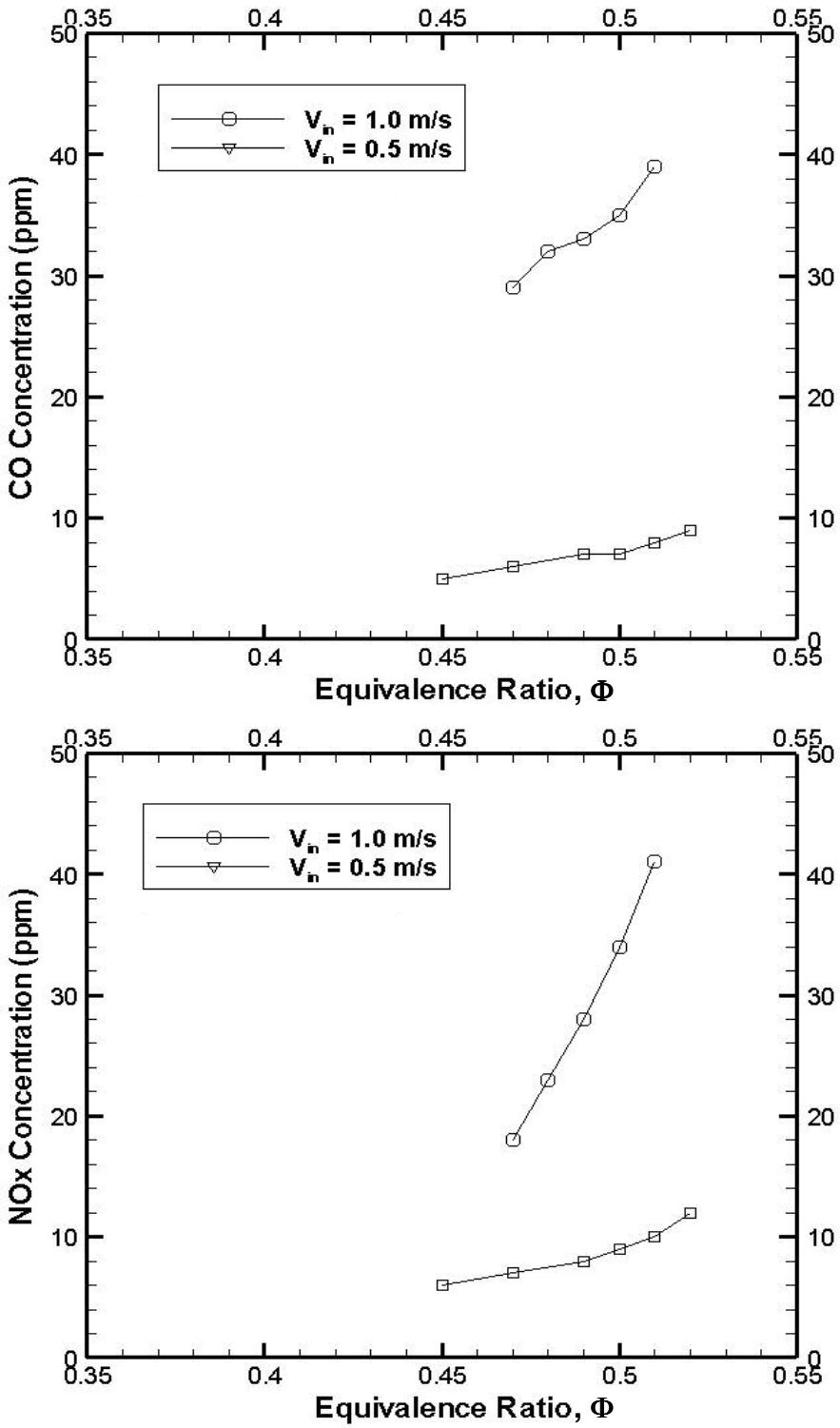

Figure 4.21. Effect of equivalence ratio on radial profiles of emissions (a) CO and (b) NOx (z = 63 mm).

4.2.6 Energy Balance Calculations

An energy balance based on control volume analysis was performed to evaluate thermal characteristics of the combustor design. Heat recirculation was calculated using the reactant preheat temperature data, which were presented in Section 4.2.2. The percent heat loss was calculated in two ways; using the exterior surface temperature data from Section 4.2.3 and the product gas temperature data from Section 4.2.4.

4.2.6.1 Heat Recirculation

The preheating annulus was taken as the control volume to determine the rate of heat recirculation. Heat recirculation to the reactants in the annulus as a percentage of the heat released in combustion was calculated as:

$$\text{Heat Recirculation (\%)} = \frac{\dot{Q}_{\text{Recirculation}}}{\dot{Q}_{\text{Release}}}.100 = \frac{\sum_{\text{Pre}} \dot{m}.h - \sum_{inlet} \dot{m}.h}{\dot{m}_f \cdot LHV}.100 \qquad (4.1)$$

where $\dot{m}$ is the mass flowrate, h is the sensible enthalpy, $\dot{m}_f$ is the fuel mass flow rate, and LHV is the lower heating value of the fuel. Symbols 'inlet' and 'Pre' represent summations taken, respectively, at the annulus inlet and preheat thermocouple location. The temperature at the annulus inlet was 300 K. The temperature measured by the thermocouple located upstream of the flame stabilizing PIM was used to determine the enthalpy of reactants after preheating. Table 4.1

presents the percent heat recirculation for various configurations at an equivalence ratio of 0.50.

Table 4.1. Heat recirculation.

Mean Reactant Velocity	PIM in Preheating Annulus	Exterior Surface Insulation	Heat Recirculation (W)	Percent Heat Recirculation (%)
1.0 m/s	No	No	91.9	20.0
1.0 m/s	Yes	No	96.9	21.0
1.0 m/s	Yes	Yes	127.7	27.8
0.5 m/s	Yes	Yes	55.3	24.1
$\Phi = 0.50$ for all cases				

Table 4.1 shows that over 20 % of the heat released was recirculated to preheat the reactants. The PIM in the preheating annulus did not affect reactant preheating. Exterior surface insulation had a greater effect, increasing heat recirculation from 21 % to 28 %. The percentage heat recirculation was slightly lower for V_{in} = 0.5 m/s compared to V_{in} = 1.0 m/s because of the lower heat transfer by convection.

4.2.6.2 Heat Loss (Method 1)

Heat loss to the surroundings as a percentage of heat release in the combustor was calculated using measured temperature at the exterior surface and equation 4.2:

$$\text{Heat Loss (\%)} = \frac{\dot{Q}_{Loss}}{\dot{m}_{CH4} \cdot LHV_{CH4}} \cdot 100 = \frac{\dot{Q}_{Loss,cylinder} + \dot{Q}_{Loss,toplid} + \dot{Q}_{Loss,bottomlid}}{\dot{m}_{CH4} \cdot LHV_{CH4}} \cdot 100 \qquad (4.2)$$

The temperature profiles presented in Section 4.2.3 were used together with equation 4.3 to determine the heat loss from the exterior surface to the surroundings:

$$\dot{Q}_{Loss,cylinder} = \int_{Z=-40mm}^{Z=63mm} h \cdot (T_{surface} - T_{\infty}) \cdot 2 \cdot \pi \cdot r \, dz \qquad (4.3)$$

where h is the convective heat transfer coefficient, $T_{surface}$ is the exterior surface temperature, T_{∞} is the temperature of the surroundings (taken to be 300 K), r is the radius of the exterior surface, and z is the streamwise distance along the exterior. The heat transfer coefficient, h, was determined using the CFD analyses presented in Chapter 5. The heat transfer coefficient was determined by varying h in the computational model until the product gas temperature predicted by the model agreed with that measured experimentally. A heat transfer coefficient of 12 W/m.K provided the best agreement. Radiation was neglected since the exterior surface temperatures were relatively low, less than 600 K.

Single point temperature measurements were taken on the top and bottom lids. Equations 4.4 and 4.5 were used to calculate the heat loss through the top and bottom faces, respectively.

$$\dot{Q}_{Loss,top} = h \cdot A_{top} \cdot (T_{top} - T_{\infty}) \qquad (4.4)$$

$$\dot{Q}_{Loss,bottom} = h \cdot A_{bottom} \cdot (T_{bottom} - T_{\infty}) \qquad (4.5)$$

Table 4.2 presents the heat loss to the surroundings calculated using method 1.

Table 4.2. Heat loss: method 1

Mean Reactant Velocity	PIM in Preheating Annulus	Exterior Surface Insulation	Heat Loss (W)	Percent Heat Loss (%)
1.0 m/s	No	No	34.4	7.5
1.0 m/s	Yes	No	46.0	10.0
1.0 m/s	Yes	Yes	40.1	8.7
0.5 m/s	Yes	Yes	36.7	16.0
$\Phi = 0.50$ for all cases				

Table 4.2 indicates that the percent heat loss increased with the addition in PIM to the preheating annulus. Most likely, conduction heat transfer through the PIM contributed to the higher heat loss. Note that the PIM in the preheating annulus was composed of stainless steel spheres, creating a high conductivity, low porosity PIM. Optimizing the PIM in the preheating annulus could potentially reduce the overall

heat loss by minimizing both radiation and conduction heat transfer. Insulating the exterior surface reduced the exterior surface temperature, but it also increased the surface area of the combustor. The tradeoff resulted in a slight decrease in system heat loss. Decreasing the reactant flowrate from 1.0 m/s to 0.5 m/s increased the percentage heat loss from 9 to 16 %. These results indicate that PIM in the preheating annulus may increase heat loss, a thin insulating layer may improve performance, and the flowrate should be maximized to reduce the percentage heat loss to the surroundings.

4.2.6.3 Heat Loss Method 2

Heat loss from the system to the surroundings was also calculated using the product gas temperature or method 2 using equation 4.6.

$$\text{Heat Loss (\%)} = \frac{\dot{Q}_{\text{Loss}}}{\dot{Q}_{\text{Release}}}.100 = \frac{\sum_{inlet} \dot{m}.h - \sum_{outlet} \dot{m}.h}{\dot{m}_f \cdot LHV}.100 \qquad (4.6)$$

where the summation at the outlet was obtained using measured product gas temperature profile (Section 4.2.4) and axial velocity (and mass flow rate) profile estimated from the computational fluid dynamic model [Chapter 5].

Table 4.3 indicates that the system heat loss was 7 to 10 % of the HRR when the combustor was operated at V_{in} = 1.0 m/s and Φ = 0.50. Heat loss decreased with

the addition of PIM to the preheating annulus and it was further reduced with exterior surface insulation.

Table 4.3. Heat loss: method 2				
Mean Reactant Velocity	PIM in Preheating Annulus	Exterior Surface Insulation	Heat Loss (W)	Percent Heat Loss (%)
1.0 m/s	No	No	50.9	11.1
1.0 m/s	Yes	No	40.1	8.7
1.0 m/s	Yes	Yes	34.3	7.4
0.5 m/s	Yes	Yes	65.4	28.0
$\Phi = 0.50$ for all cases				

4.2.6.4 Conclusion

Table 4.4 presents a summary of the heat balance calculations. It indicates significant differences between the two heat loss calculations methods. The calculation procedure and source data should be considered when interpreting the results. For the exterior surface temperature method, a constant convective heat transfer coefficient of 12.0 W/m^2K was assumed. In the experiments, the heat transfer coefficient varied around the combustor and forced convection from the exhaust fan may have resulted in a higher convective heat transfer coefficient than the assumed value. Furthermore, the exterior surface temperature would affect natural convection, making the constant heat transfer coefficient assumption invalid. Fewer

assumptions and less uncertainty were associated with the product gas temperature method, which relied upon the velocity profile predicted by CFD simulations. Thus, the wall heat transfer analysis summarized below used heat loss predicted by the product gas temperature method.

Table 4.4 presents combustor wall heat transfer, heat recirculation to the reactants and heat loss to the surroundings calculated as percentage of the HRR. Values calculated as percentages of combustor wall heat transfer are shown in parentheses. Note that the combustor wall heat transfer is the sum of heat recirculation and heat loss predicted by the product gas temperature method. Results in Table 4.4 show that the combustor wall heat transfer decreased from 52 % to 35 % when the reactant velocity increased from V_{in} = 0.5 m/s to 1.0 m/s. For V_{in} = 0.5 m/s, approximately one-half of the combustor wall heat transfer was recirculated to the reactants and the remaining one-half was lost to the surroundings. For V_{in} = 1.0 m/s, the heat loss decreased to about 20% of the wall heat transfer, indicating more effective heat recirculation at higher flowrates. This feature of the present design is important to develop miniature high-intensity combustion systems. PIM in the annulus did not significantly affect combustor wall heat transfer, but it increased the fraction that was recirculated and slightly decreased the fraction of HRR that was lost. With PIM, 71 % of the wall heat transfer was recirculated, compared to 64 % without PIM. Insulating the exterior surfaces increased combustor wall heat transfer; from 30 % to 35 % and it reduced the percentage that was lost to the surroundings from 29 % to 21 % of the wall heat transfer. These results indicate that reactant flowrate has

the greatest impact on the thermal performance of the system and it should be maximized to reduce heat loss and increase heat recirculation.

Table 4.4. Summary of heat transfer calculations.				
Mean Reactant Velocity	1.0 m/s	1.0 m/s	1.0 m/s	0.5 m/s
PIM in Annulus	No	Yes	Yes	Yes
Exterior Surface Insulation	No	No	Yes	Yes
Combustor Wall Heat Transfer	31.1 %	29.7 %	35.2 %	52.1 %
Heat Recirculation	20.0 % (64 %)	21.0 % (71 %)	27.8 % (79 %)	24.1 % (46 %)
Heat Loss (Method 1)	7.5 %	10.0 %	8.7 %	16.0 %
Heat Loss (Method 2)	11.1 % (36 %)	8.7 % (29 %)	7.4 % (21 %)	28.0 % (54 %)
$\Phi = 0.50$ for all cases				

4.3 Conclusions

The feasibility of the heat recirculating combustor using PIM has been proven. Combustion with low pressure loss, significant reactant preheating, low heat loss, and low pollutant emissions was achieved. The important parameters affecting combustion performance were identified and the effects of these parameters were determined.

The general characteristics of the system were measured under lean, premixed combustion conditions. The system pressure loss was less than 500 pascals or 0.5 % of the operating pressure. The reactants were preheated by flame energy to temperatures exceeding 500 K, yielding heat recirculation in excess of 20 % of the HRR. The exterior surface temperature of the combustor was approximately 500 K, yielding heat losses of approximately 10 % of the HRR. CO and NOx emissions of approximately 30 to 40 ppm were observed.

The PIM in the preheating annulus did not significantly affect the combustion performance. Insulation on the exterior surface increased heat recirculation and decreased heat loss to the surroundings. Insulation should be considered carefully because it increases the overall size of the system. Integrating low thermal conductivity materials into the design is a more effective method to improve the system performance. At lower reactant flowrates, the system heat loss increased dramatically, suggesting that small scale systems should operate at the maximum flowrate to optimize performance.

The experiments discussed in this Chapter improved our understanding of mesoscale, heat recirculating combustion. However, a better understanding of the various heat transfer modes in the small-scale combustor is required to optimize the design. CFD analyses aimed at achieving this goal are presented in the next Chapter.

5. Computational Fluid Dynamics Analyses

Computational fluid dynamics (CFD) analyses were performed to gain insights into the heat recirculating, mesoscale combustor design. A model representing the proof of concept experimental combustor was created. The results were investigated for numerical validity and verified using experimental data. General characteristics, such as velocity and temperature contours are presented, followed by in-depth analyses of heat transfer in the system.

5.1 Description of the Model

A CFD model was developed to solve the conservation equations of mass, momentum and energy. In addition, several challenges were faced, such as modeling the chemical reaction or heat release, the porous media zones, and radiation heat transfer. Schemes were developed to modify the conservation equations to simulate these features. Gambit was used to generate the computational grid and the Fluent software package was used for the computational analysis. Model details are presented in this chapter, including descriptions of the computational domain, governing equations, modifications to the governing equations, physical properties, boundary conditions and the computational procedure. The results are presented and compared to experimental data in Chapter 4 for the mesoscale combustor.

5.1.1 Computational Domain

The computational domain was chosen to simulate the experimental mesoscale combustor described in Chapter 4. The domain is illustrated in Fig. 5.1, where the hatched areas represent solid zones. The reactants were injected uniformly in the mass source zone, highlighted in green. This zone across the width of the annulus was 1 mm long. The reactants moved in the negative z-direction through the preheating annulus. When PIM was present in the annulus, the reactants passed through free space before entering the PIM, highlighted in orange. The reactants turned into the center passage, passed through the flame stabilizing PIM, highlighted in blue, and entered the reaction zone, highlighted in red. After the reaction zone, the product gases moved through 63 mm of free space, called the combustion chamber, and exited the system through the exit plane.

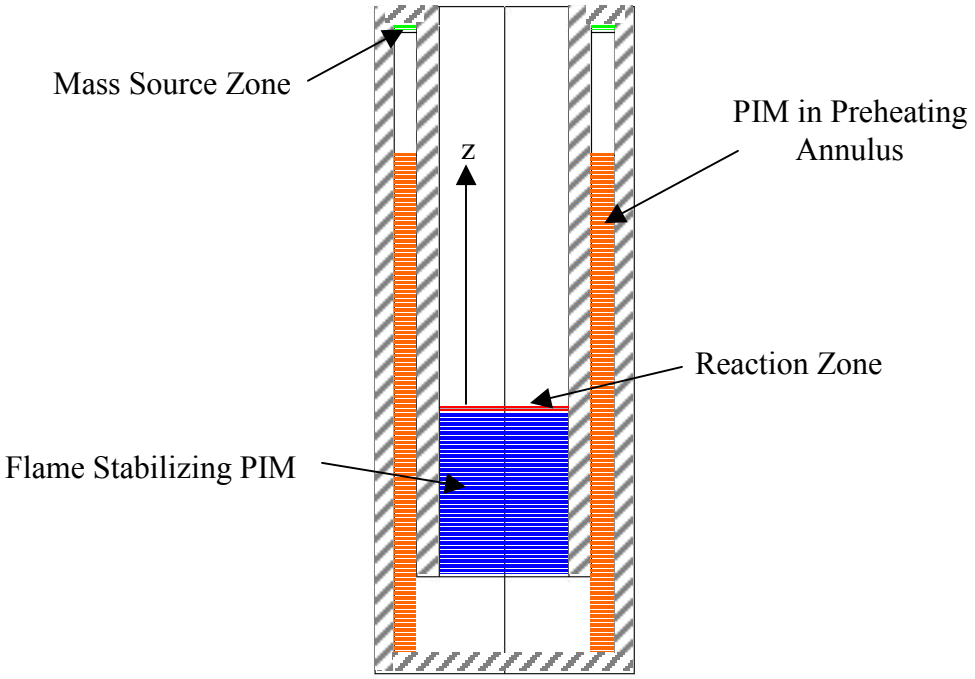

Figure 5.1. Computational domain for phase I combustor.

5.1.2 Governing Equations

A steady, axis-symmetric geometry was selected to model the combustor. The experimental combustor was not perfectly axisymmetric because the fuel-air mixture was injected through six equally spaced holes around the circumference of the annulus. The four combustor wall supports could not be modeled with the axis-symmetric geometry, either. However, the impact of these three-dimensional effects on the overall heat transfer is considered small because the inlets and supports were equally spaced in the circumferential direction. The coordinate system was selected such that r represents the radial direction and z represents the axial direction.

The conservation of mass is presented in equation 5.1, where ρ is the density, v_z is the axial velocity, v_r is the radial velocity, and S_m is a mass source.

$$\frac{\partial}{\partial z}(\rho v_z) + \frac{\partial}{\partial r}(\rho v_r) + \frac{\rho v_r}{r} = S_m \tag{5.1}$$

The conservation of momentum in the axial and radial directions is presented, respectively, in equations 5.2 and 5.3.

$$\frac{1}{r}\frac{\partial}{\partial z}(r\rho v_z v_z) + \frac{1}{r}\frac{\partial}{\partial r}(r\rho v_r v_z) = -\frac{\partial P}{\partial z} + \frac{1}{r}\frac{\partial}{\partial z}\left[r\mu(2\frac{\partial v_z}{\partial z} - \frac{2}{3}\vec{\nabla}\cdot\vec{v})\right] + \frac{1}{r}\frac{\partial}{\partial r}\left[r\mu\left(\frac{\partial v_z}{\partial r} + \frac{\partial v_r}{\partial z}\right)\right] + S_Z \tag{5.2}$$

$$\frac{1}{r}\frac{\partial}{\partial z}(r\rho v_z v_r)+\frac{1}{r}\frac{\partial}{\partial r}(r\rho v_r v_r)=-\frac{\partial P}{\partial r}+\frac{1}{r}\frac{\partial}{\partial z}\left[r\mu(2\frac{\partial v_r}{\partial z}+\frac{\partial v_r}{\partial z}\right]+$$
$$\frac{1}{r}\frac{\partial}{\partial r}\left[r\mu\left(2\frac{\partial v_r}{\partial r}-\frac{2}{3}(\vec{\nabla}\cdot\vec{v})\right)\right]-2\mu\frac{v_r}{r^2}+\frac{2}{3}\frac{\mu}{r}(\vec{\nabla}\cdot\vec{v})+\rho\frac{v_z^2}{r}+S_r \qquad (5.3)$$

Where $\vec{\nabla}\cdot\vec{v}=\frac{\partial v_z}{\partial z}+\frac{\partial v_r}{\partial r}+\frac{v_r}{r}$.

The conservation of energy is presented in equation 5.4.

$$\frac{\partial}{\partial r}\left(\rho c_P v_r \partial T+\frac{\rho {v_r}^2}{2}\right)+\frac{\partial}{\partial z}\left(\rho c_P v_z \partial T+\frac{\rho {v_z}^2}{2}\right)=\left(\frac{1}{r}\frac{\partial}{\partial r}\left(rk\frac{\partial T}{\partial r}\right)\right)+S_E \qquad (5.4)$$

The left hand side of equation 5.4 represents convection and the first term on the right side represents conduction. The term S_E represents an energy source, which includes radiation heat transfer as described in the next section.

5.1.3 Modifications to the Governing Equations

Special zones were used to approximate features such as the mass source zone, reaction zone, porous media zones and radiation heat transfer. This section describes the models to represent these special zones.

5.1.3.1 Reactant Inlet

A mass source zone was selected to approximate the reactant inlet. In the experiments, the reactants were injected through six equally spaced holes of 1.0 mm diameter. The holes were placed at sixty degree intervals around the annulus. In the model, it was assumed that the reactant flow originated uniformly from an annular disk of 13.5 mm inner diameter, 17 mm outer diameter, and 1 mm height. It was also assumed that the reactants entered the system with no dependence upon the radial direction, which was present in the experimental case. Since the mass source zone was placed at the top of the annulus, the flow could only exit the zone in the negative z-direction. The reactants were assumed to enter uniformly over the entire width of the annulus, rather than from a 1.0 mm diameter hole, which would have a velocity profile and momentum associated with it. The model may have overestimated convective heat transfer at the inlet since the velocity predicted near the walls was most likely greater than it was in the experiments. However, the effect of this error on the overall results was small.

The only modification to the governing equations was the addition of a source term to the conservation of mass equation. The magnitude of this term was calculated by dividing the total mass flowrate by the volume of the source zone, as illustrated in equation 5.5. Hence, the reactants were injected uniformly over the mass source zone.

$$S_m = \frac{\dot{m}_{source}}{V_{source_zone}} \qquad (5.5)$$

5.1.3.2 Reaction Zone

A heat source zone was used to simulate the heat released from the flame. This approach was used because heat transfer within the system was the primary focus of the study, rather than the reaction itself. The heat source saved computational time and allowed for greater control over the computations than modeling the chemical reaction. Several important assumptions were inherent in the selection of the heat source zone. It was assumed that the reaction took place in the cylindrical zone occupying the 1 mm length downstream of the inner PIM, as seen in Fig. 5.1. Further, the reaction reached completion and all of the chemical energy was released. In the mesoscale combustion experiments, visual observations indicated that the flame zone was approximately 1 mm long and temperature and emissions measurements showed that combustion was uniform across the entire flame surface. Emissions measurements showed that the combustion efficiency was greater than 99.9 %, indicating that all of the chemical energy was released.

Unlike the mass source zone, a uniform heat source zone would not adequately approximate the heat released from combustion. Instead, the local mass flowrate in the flame zone dictated the rate of heat release. Thus, a scaling factor was added to the energy source zone to account for local differences in mass flowrate. The magnitude of the heat generation in each cell was equal to the local mass flowrate (axial velocity multiplied by density) in the cell, divided by the average mass flowrate through the heat source zone, as seen in Equation 5.6. The user-defined function for calculating the heat source is given in Appendix B.

$$S_E = \frac{\dot{m}}{V_{source_zone}} \cdot \frac{v_{loc} \cdot \rho_{loc}}{v_{avg} \cdot \rho_{avg}} \qquad (5.6)$$

5.1.3.3 PIM Zone

The intricate converging and diverging pathways of the PIM zones created challenges for modeling. However, schemes have been developed to model the effects of porous zones [Collins, 1990]. A simplified porous media model was used in this study. The governing equations were modified in two ways; sink terms were added to the conservation of momentum equations and an effective thermal conductivity was used in the conservation of energy.

Sink terms were added to the momentum equations to approximate flow resistance associated with PIM. As described in Chapter 4, the Reynolds Numbers in the flame stabilizing PIM and the preheating annulus PIM were 15 and 130, respectively. Viscous and inertial losses were significant because Re was greater than 10. The power law correlation, equation 5.7, was used to calculate the magnitude of momentum sinks for the conservation of momentum equations. System pressure loss was measured for three cases, one without PIM, one with the flame stabilizing PIM present and one with both the flame stabilizing and preheating annulus PIM present. The pressure loss through the flame stabilizing PIM was calculated by subtracting the system pressure loss measured with the flame stabilizing PIM present from that measured without the flame stabilizing PIM. Similarly, the pressure loss through the preheating annulus was determined by subtracting the system pressure loss with PIM

in the preheating annulus from that measured with a void annulus. Curve fits of the form presented in Equation 5.7 were applied to the pressure loss through the flame stabilizing and preheating annulus PIM to determine constants C_0 and C_1 for each PIM. For the flame stabilizing PIM, C_0 was 11421 and C_1 was 1.17 and for the PIM in the preheating annulus, C_0 was 1021 and C_1 was 1.83. Note that C_1 was near unity in the flame stabilizing PIM since the Re was low and viscous losses were most significant. C_1 was larger in the preheating annulus, indicating greater impact of the inertial loss term.

$$S_i = -C_0 \cdot |v|^{C_1} \tag{5.7}$$

No changes were made to the conservation of energy equation. However, the thermal conductivity of each PIM zone was calculated based on the conductivities of the solid and fluid and the porosity using equation 5.8 [Bauer, 1993]. Here, k_{eff} is the effective thermal conductivity, ϕ is the porosity, k_f is the thermal conductivity of the fluid and k_s is the thermal conductivity of the solid. This method for calculating effective thermal conductivity, called the parallel method, is valid when the thermal conductivity of the PIM and the fluid are similar. Since the thermal conductivity of the SiC coated PIM and the reactants differed, the effective thermal conductivity was most likely overestimated. The porosity of the flame stabilizing PIM was reported by the manufacturer as 0.80. The porosity of the packed bed in the preheating annulus was estimated to be 0.50 based on the volume of the annulus and the total volume of

the beads used in the packed bed. The thermal conductivity of the flame stabilizing and preheating annulus PIM were taken to be 20.0 W/m.K [Sherman, et al., 1990] and 21.5 W/m.K respectively.

$$k_{eff} = \phi \cdot k_f + (1-\phi) \cdot k_s \qquad (5.8)$$

5.1.3.4 Radiation

The discrete ordinates radiation model was used to modify the conservation of energy equation [Raithby and Chui, 1990]. The discrete ordinates model calculates radiative heat transfer by dividing the viewfactor from each cell into a discrete number of solid angles. The directions θ and ϕ and an example of a discretized solid angle are presented in Fig. 5.2. The number of solid angles was determined by dividing each octant into N_θ x N_ϕ solid angles. Since the geometry was symmetric, four of the octants were solved. Hence, discretization of 2 x 2 would result in 16 solid angles, while discretization of 3 x 3 would yield 36 solid angles. The radiation intensity ($I(\vec{r},\vec{s})$) calculated using equation 5.10 was added to the energy equation as a source term.

$$\nabla \cdot (I(\vec{r},\vec{s}),\vec{s}) + (a+\sigma_s) I(\vec{r},\vec{s}) = an^2 \frac{\sigma T^4}{\pi} + \frac{\sigma_s}{4\pi} \int_0^{4\pi} I(\vec{r},\vec{s}') \Phi(\vec{s} \cdot \vec{s}') d\Omega' \qquad (5.10)$$

where I is the radiation intensity, $\vec{r}$ is the position vector, $\vec{s}$ is the direction vector, a is the adsorption coefficient, σ_s is the scattering coefficient, n is the refractive index, σ is the Stefan-Boltzmann constant, s' is the scattering direction vector, and Ω' is a solid angle.

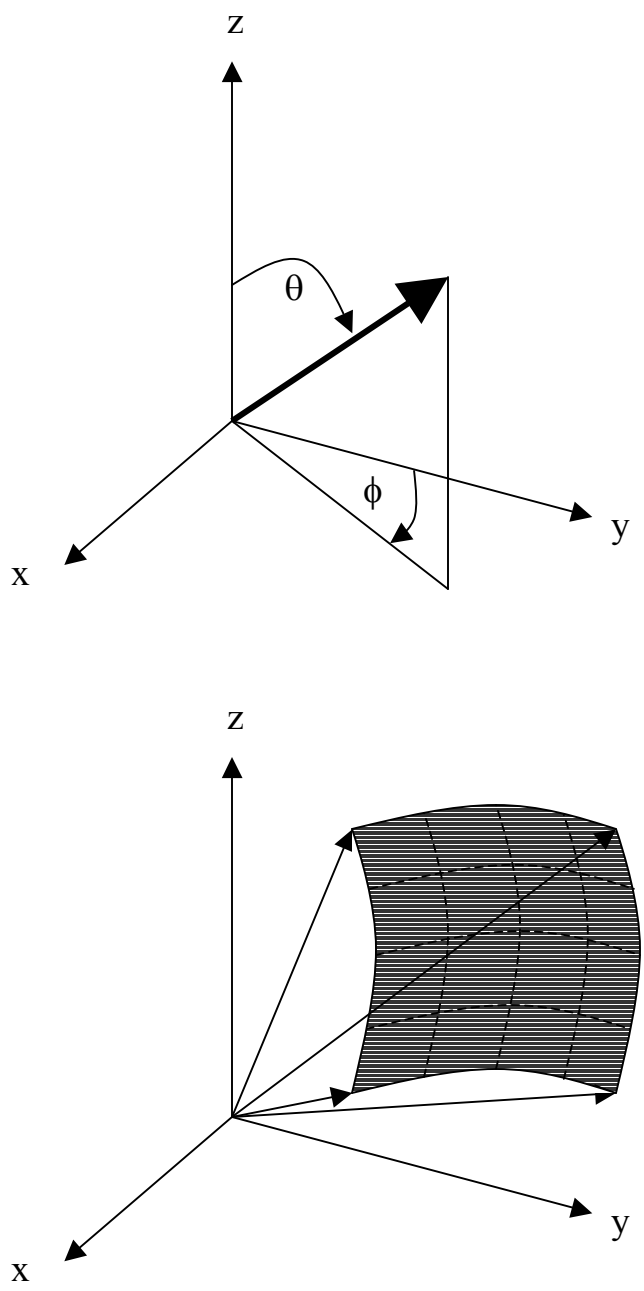

Figure 5.2. Directions θ and ϕ and example solid angle from discrete ordinates radiation model.

5.1.4 Physical Properties

Physical properties of the fluid and solid zones were specified to closely approximate the experimental mesoscale combustor. Air was chosen as the working fluid to simplify the calculations and hence, to save computational time. Air accounted for approximately 95% of the reactant mixture mass for the mesoscale experiments and nitrogen, its main constituent accounted for over 70 % of the product mass. Comparisons of the specific heat capacity of air, reactant, and product mixtures at various temperatures, presented in Appendix C, indicated deviation of less than 10 %.

The fluid density was calculated using the ideal gas law. Equation 5.11 illustrates the calculation procedure:

$$\rho = \frac{P_{Op} - P}{\frac{R_u}{M} \cdot T} \qquad (5.11)$$

where P_{op} is the operating pressure of 101,325 Pa, P is the local gauge pressure, R_u is the universal gas constant, M is the molecular weight of air (28.966 kg/kmol) and T is the local fluid temperature.

Polynomial curve fits were used to calculate the fluid's viscosity, specific heat capacity, and thermal conductivity. Published experimental data for air at standard atmospheric pressure were used to obtain the curve fits [Turns, 2000]. The

correlation coefficient for the curve fits were greater than $R^2 = 0.99$. Details are presented in Appendix C and the curve fit equations are shown in Table 5.1.

Table 5.1. Physical Property Correlations		
Property	Unit	Correlation
Dynamic Viscosity, μ	kg/m.s	$\mu(T) = 1.3095 \cdot 10^{-6} + 6.5402 \cdot 10^{-8} T - 3.2924 \cdot 10^{-11} T^2 + 8.8854 \cdot 10^{-15} T^3$
Thermal Conductivity, k	W/m.K	$k(T) = 9.9902 \cdot 10^{-5} T - 4.6093 \cdot 10^{-8} T^2 + 1.4301 \cdot 10^{-11} T^3$
Specific Heat Capacity, c_P	J/kg.K	$c_P(T) = 1075.8 - 0.60922T + 0.0015797T^2 - 1.2345 \cdot 10^{-6} T^3 + 2.5518 \cdot 10^{-10} T^4 + 1.1751 \cdot 10^{-13} T^5 - 4.4427 \cdot 10^{-17} T^6$

Thermal properties associated with radiation heat transfer were also required. The most significant mode was expected to be solid to solid radiation. However, the discrete ordinates radiation model required participation of the fluid zones. Both adsorption and scattering coefficients of the fluid were specified to be 0.0 m^{-1}. Hence, the radiation intensity was not affected by the fluid.

The combustor and outer walls and the lid were made of stainless seel. The stainless steel properties were taken as follows k = 21.5 W/m.K, c_P = 502 J/kg.K and the ρ = 8030 kg/m^3 [Assael and Gialou, 2003].

5.1.5 Boundary Conditions

Boundary conditions were used to specify flow and thermal variables at the exterior edges of the model. Several boundary types were used as detailed in this section.

Since the combustor exit plane was exposed to the atmosphere, a pressure outlet boundary with an absolute pressure of 101,325 Pa was used. The temperature of the surroundings was taken to be 300 K and the normal diffusive flux at the outlet was assumed to be zero ($\frac{\partial^2 T}{\partial z^2} = 0, \frac{\partial^2 v_z}{\partial z^2} = 0, \frac{\partial^2 v_r}{\partial z^2} = 0$). Symmetric boundary conditions were imposed at the axis of symmetry. Accordingly, the radial velocity and the gradients of all other variables were zero at the axis. Wall boundary conditions were used at the exterior surfaces. Wall imposed no-slip conditions for velocity calculations. The shear stress and surface heat flux was calculated based on the fluid properties in the adjacent cell. The heat transfer between the wall and the surroundings was calculated with equation 5.12.

$$q = h_{\infty}(T_w - T_f) + \varepsilon_{ext}\sigma\left(T_f^{\,4} - T_w^{\,4}\right) \qquad (5.12)$$

The external convective heat transfer coefficient, h_{∞}, was determined by comparing the experimentally measured and computationally predicted temperature profiles in the combustion chamber. The best agreement was obtained at h_{∞} = 12 W/m^2.K. T_w represents the exterior surface temperature, T_f represents the temperature of the

surroundings (assumed to be 300 K), ε_{ext} is the emissivity of the exterior surface (taken to be 0.80), and σ is the Stefan-Boltzmann coefficient. Equation 5.12 shows that heat loss is affected by the temperature of the surroundings. In practice, the temperature of the surroundings varies, but it was assumed to be constant for the analysis since fluctuations would affect all combustor designs the same.

5.1.6 Computational Procedure

The GAMBIT software package was used to create a grid and the Fluent software was used for the CFD analyses. Absolute velocities and temperatures were used for the computations because of the large number of parameters affecting the system. Non-dimensional analysis may provide additional insights into small-scale combustor design by reducing the number of parameters. A finite-volume technique was used to discretize the governing equations into algebraic relationships that could be solved computationally. Face values for convection terms were calculated using the first-order upwind scheme. A segregated solution procedure was used because velocities were significantly lower than the speed of sound and the flow was nearly incompressible. The SIMPLE algorithm was used for pressure-velocity coupling [Patankar, 1980]. Under-relaxation factors are presented in Table 5.2.

Table 5.2. Under-Relaxation Factors	
Equation	Under-Relaxation Factor
Pressure	0.3
Density	1.0
Body Forces	1.0
Momentum	0.7
Energy	1.0
Discrete Ordinates Radiation	1.0

The solution procedure began with evaluation of physical properties, followed by solution of the momentum equation. Next, the continuity equation was solved and the pressure and face mass flowrates were updated. The energy and radiation equations were solved and convergence was checked. Convergence was determined by monitoring the residuals and enthalpy surface integrals at the exhaust and exterior surfaces of the system. Convergence was typically achieved after approximately 80,000 iterations and 3.0 hours on a computer with a 2.4 GHz processor and 512 MB RAM.

5.2 Validation of the Model

The validity of the computational results was tested in two ways. The numerical validity was tested by varying the grid size and the radiation discretization parameters. The physical validity was tested by comparing the computed results to experimental measurements.

5.2.1 Numerical Validity

The effects of several model parameters were investigated to determine the numerical validity of the computational results. The grid size was varied to determine the proper cell spacing for the computations. The discrete ordinates radiation model parameters were also varied to determine the proper angular discretization for radiation heat transfer calculations.

5.2.1.1 Grid Size

Figure 5.3 illustrates the radial temperature profile at z = 63 mm for various grid sizes. The reactant flowrate was 1.0 m/s, equivalence ratio was 0.50, and the HRR was 460 W. The preheating annulus was void of PIM, the exterior surface was un-insulated, and the discrete ordinates radiation model with 2x2 discretization was used. The parameter, a, corresponds to the length of each side of the square quadrilateral computational cells. Hence, reducing the grid spacing from 0.50 mm to 0.25 mm quadrupled the number of computational cells. The temperature profile observed in the region from $0 < r < 10$ mm corresponds to the product gas

temperature at the combustion chamber exit plane. The temperature in the range from 10 mm < r < 20 mm corresponds to exterior surface temperature of the combustor lid. The exterior surface temperature was higher for the 1.0 mm spacing than for the smaller grid sizes. The temperatures for the 0.5 mm and 0.25 mm cases were nearly identical at all radial locations.

Figure 5.4 illustrates the effect of grid size on the radial temperature profile at z = 20 mm. The combustor wall temperature, seen in the range from 10 mm < r < 13.5 mm, was higher for the 1.0 mm grid size, compared to the finer grid cases. The exterior wall temperature, 17 mm < r < 20 mm, was also higher for the 1.0 mm grid spacing. The radial temperature profiles observed for the 0.50 mm and 0.25 mm cases were nearly identical.

Figure 5.5 illustrates the streamwise temperature profile along the centerline of the combustor. Again, the temperature for the 1.0 mm grid spacing was higher than the temperature for the other two cases. Note that the increase in temperature in the range -25 mm < z < 0 mm corresponds to reactant preheating in the flame stabilizing PIM. The sharp increase in temperature near z = 0 mm corresponds to the heat released from combustion. The temperatures predicted by the 0.5 mm and 0.25 mm grid spacing were nearly identical. Figure 5.6 shows the axial velocity profiles at z = 20 mm. The axial velocities predicted by all three grid sizes were nearly identical. Based on these results, grid spacing of 0.50 mm was selected, yielding a grid with 8,240 cells. The cell volume increased linearly in the radial direction from 6.10^{-11} m^3 near the centerline to 5.10^{-9} m^3 near the outer wall of the annulus.

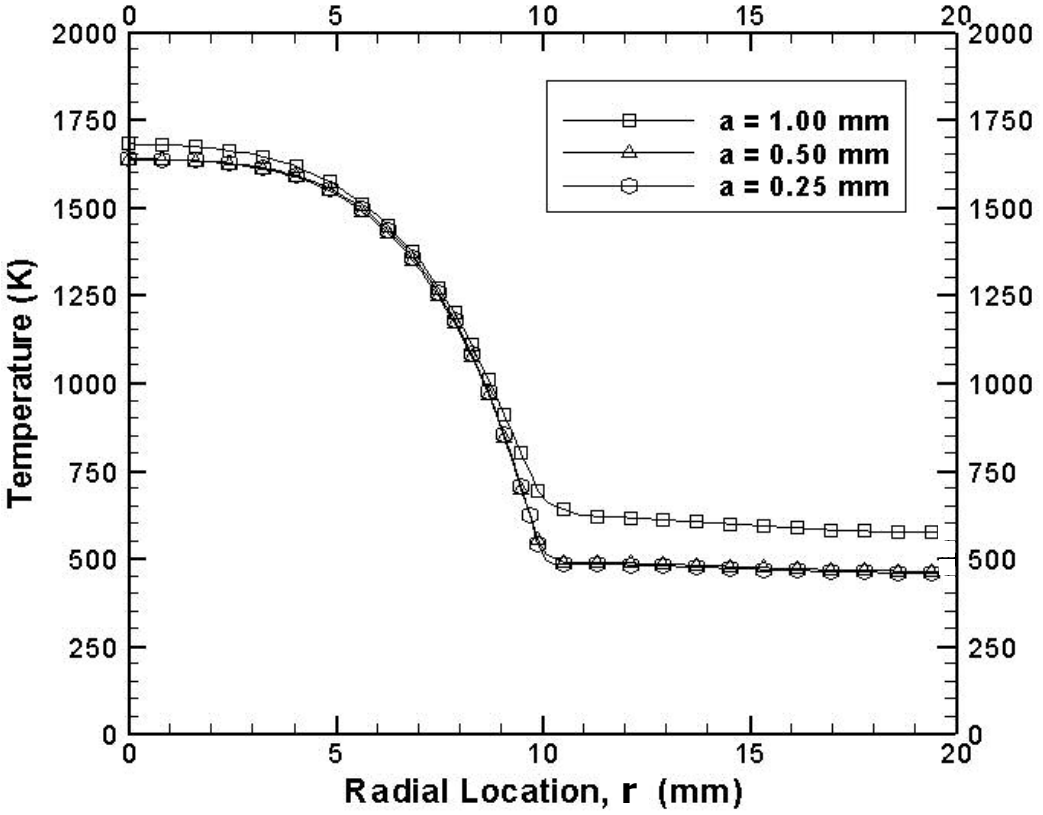

Figure 5.3. Effect of grid cell size on temperature at combustor exhaust plane (z = 63 mm).

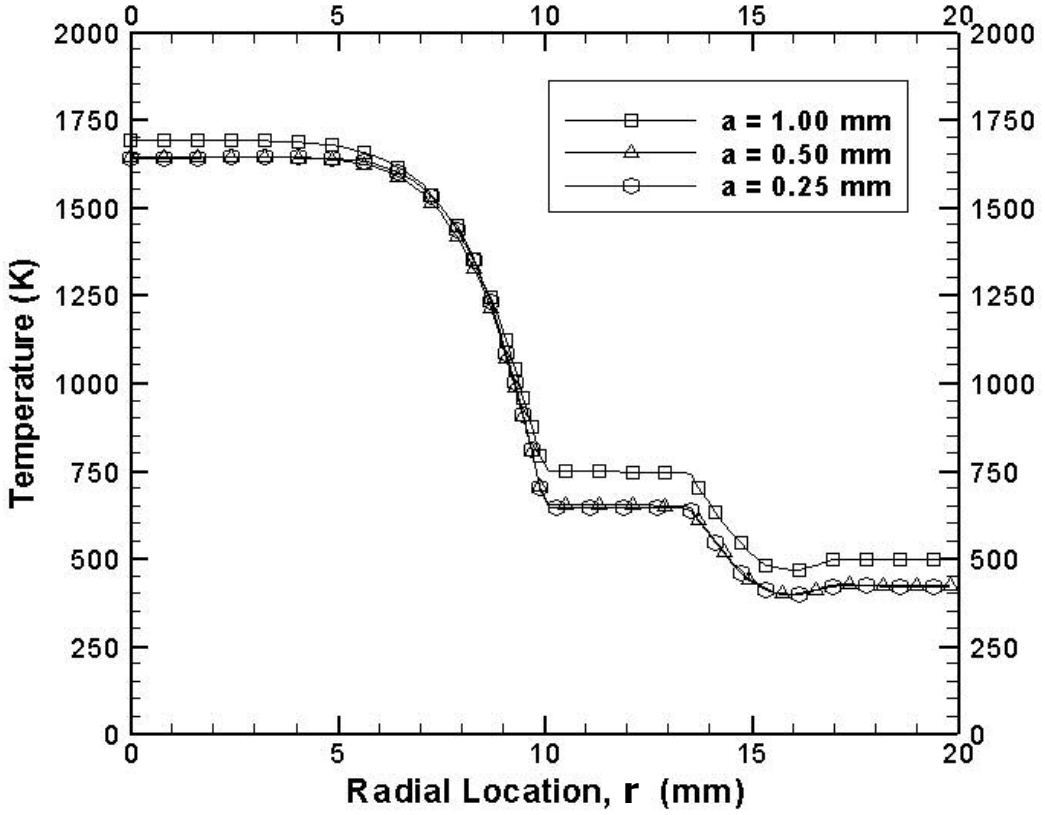

Figure 5.4. Effect of grid cell size on temperature at z = 20 mm.

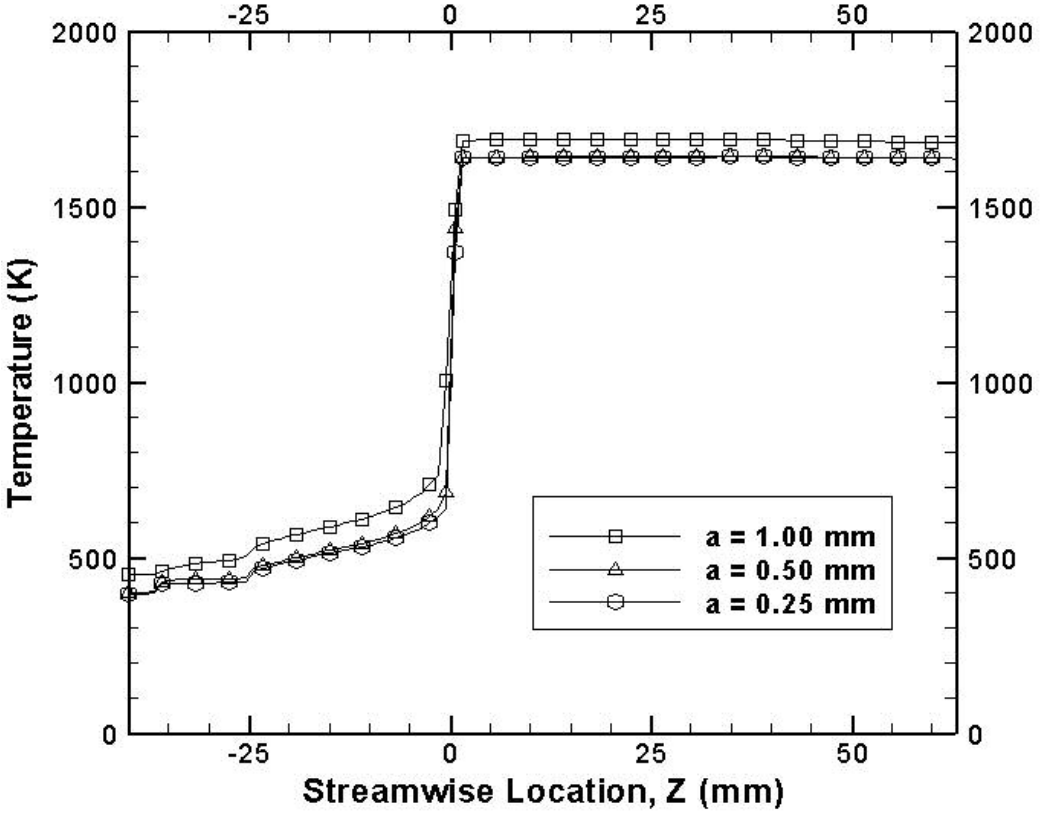

Figure 5.5. Effect of grid cell size on temperature at the combustor centerline (r = 0 mm).

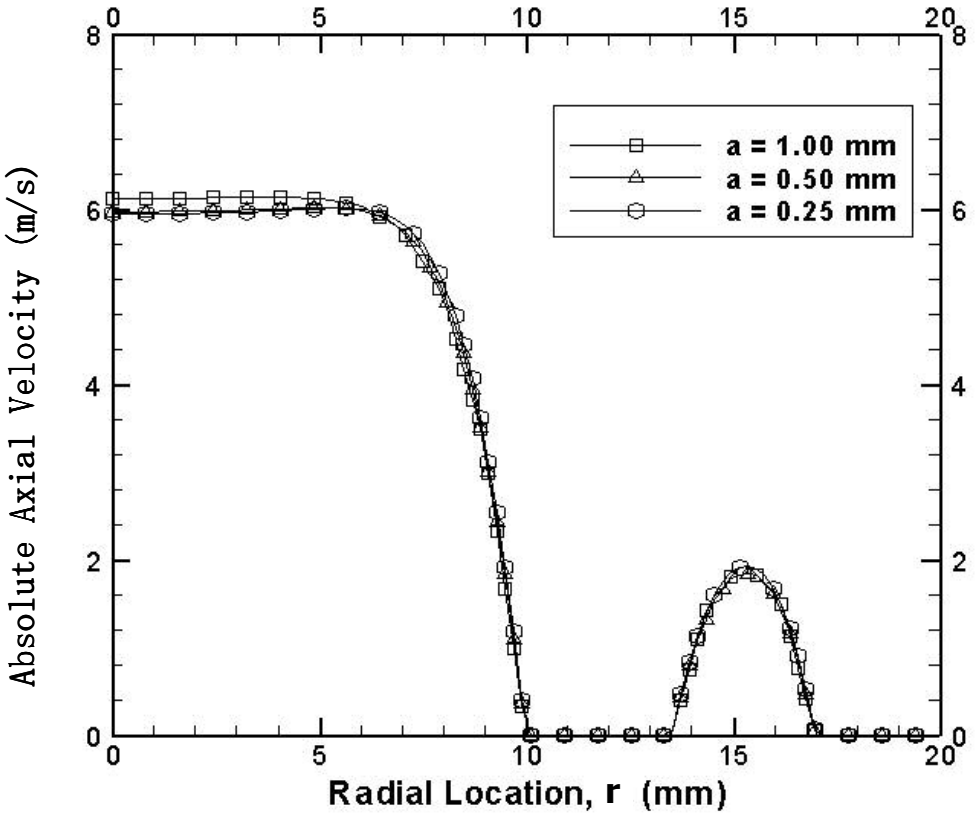

Figure 5.6. Effect of grid cell size on axial velocity magnitude at z = 20 mm.

5.2.1.2 Discrete Ordinates Model

The discrete ordinates method was used for radiation heat transfer. As described in section 5.1.5, the number of solid angles, N_θ and N_ϕ, were controlled by the user. Due to symmetry, the total number of solid angles solved for was 4 x N_θ x N_ϕ. Angular discretization of 1x1 is generally sufficient [Raithby and Chui, 1990]. However, angular discretization up to 3x3 is often required for symmetric, periodic or semi-transparent boundary conditions. Figure 5.7 illustrates the radial profile of temperature at z = 63 mm for various levels of angular discretization. The product gas temperature was slightly higher without radiation, compared to the three cases with radiation. Figure 5.8 illustrates the temperature at z = 20 mm. Again, the product gas temperature in the combustor chamber was slightly higher when radiation was neglected. The combustor wall temperature was lower when radiation was considered, but the outer wall temperature was higher. This result indicates the importance of radiation heat transfer from the combustor wall. Hence, a model to account for radiation is necessary to accurately represent the system. Although the results indicate that 1x1 discretization may be adequate, angular discretization of 2x2 was selected to ensure that radiation was correctly represented throughout the combustor.

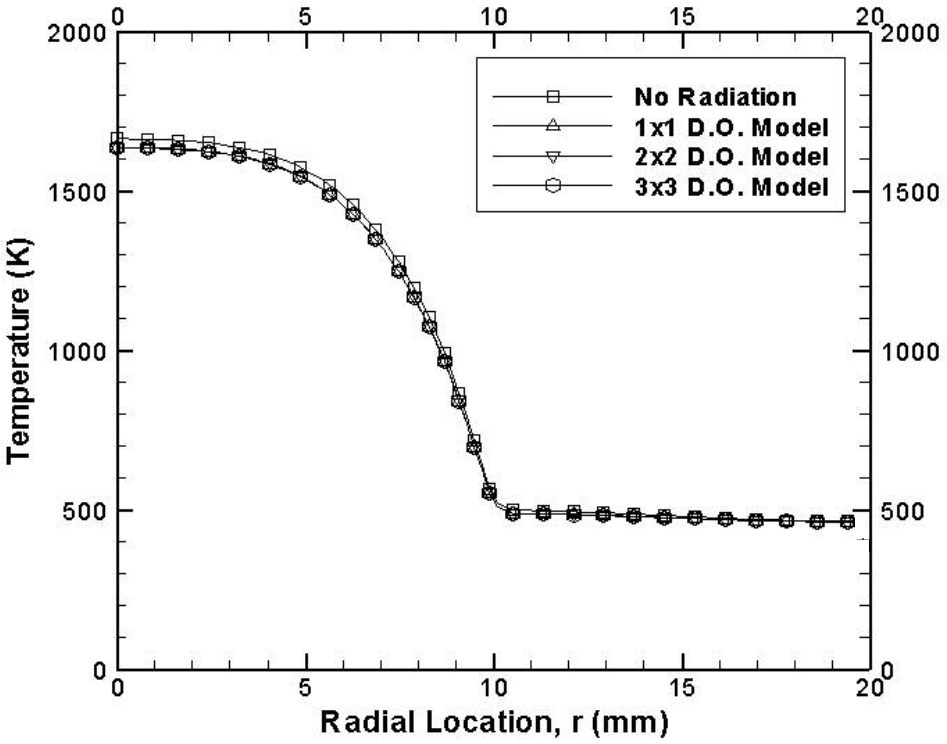

Figure 5.7. Effect of radiation model on radial temperature profile at z = 63 mm.

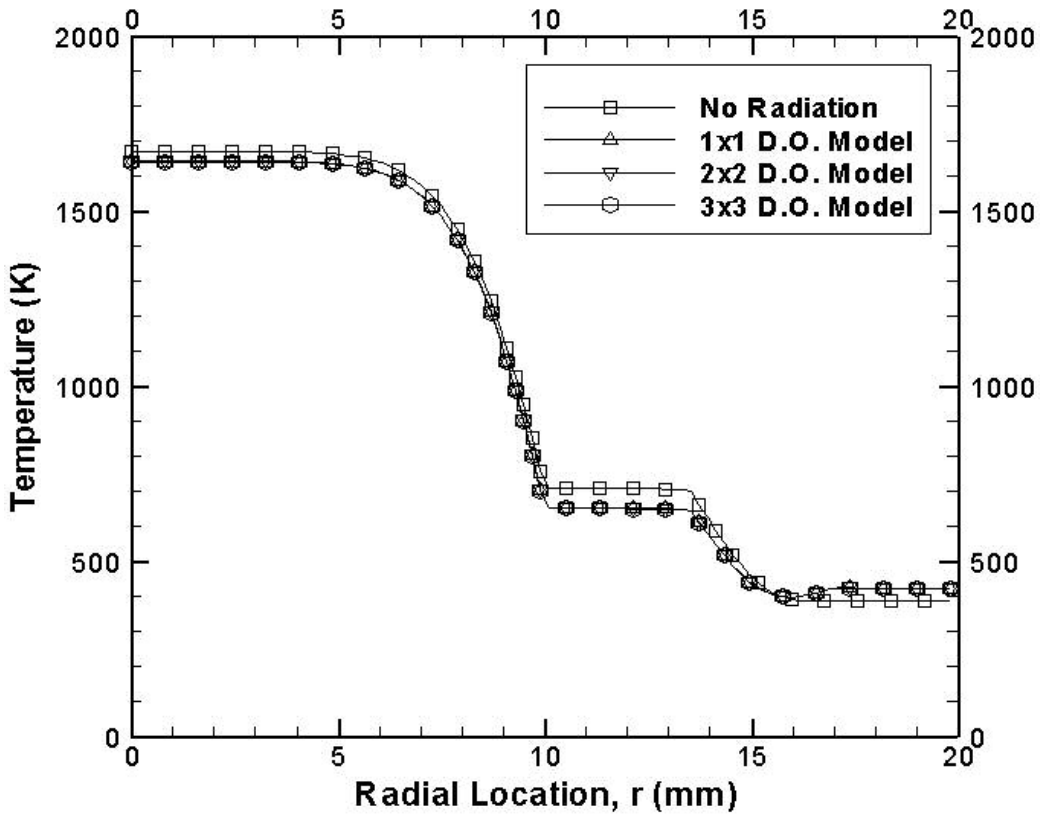

Figure 5.8. Effect radiation model on radial temperature profile at z = 20 mm.

5.2.2 Physical Validity

The physical validity of the CFD analysis was investigated by comparing the computational results to experimental measurements. As described above, CFD baseline model was selected to closely approximate the mesoscale combustion experiments presented in Chapter 3. The operating conditions were characterized by V_{in} = 1.0 m/s, Φ = 0.50, and HRR = 460 W. Baseline experiments and analyses were performed without insulation on the exterior surface. The physical validity of the system was tested with and without PIM in the annulus. The temperature profiles inside the combustor, inside the preheat annulus and on the exterior surface of the system are compared in this section. The percent heat loss and heat recirculation from the experimental and computational cases are also compared.

Figure 5.9 shows that the product gas temperature profile at the exit plane of the system (z = 63 mm) was predicted well. Figure 5.10 presents the product gas temperature profile at z = 40 mm. Again, the trend was predicted well by the model and the temperatures were slightly lower than those measured experimentally. Figure 5.11 shows that the model under predicted the product gas temperature by about 50 K at z = 20 mm. Figure 5.12 shows that the exterior surface temperature predicted by the model was generally within the experimental uncertainty of the measurements.

In the model, the percent heat loss was calculated by dividing the heat flux integrated over all exterior surfaces by the HRR. The computationally predicted heat loss was 10.0 %, which compares well with the experimental heat loss of 9.3 %. The

preheat thermocouple in the experiments measured 503 K and the model predicted a static temperature of 483 K at the thermocouple location.

Figures 5.13 and 5.14 present the predicted and measured exhaust and exterior surface temperatures with PIM in the preheating annulus. The difference between the models and experiments was typically less than 30 K. Note that the exterior surface temperature predicted by the model was differed from that measured experimentally because of the simplified PIM model used for this analysis.

These results show that the computational model predicted the temperature profiles within the combustor and on the exterior surface of the combustor well. The temperature of the preheated reactants (heat recirculation) and system heat loss were also predicted well.

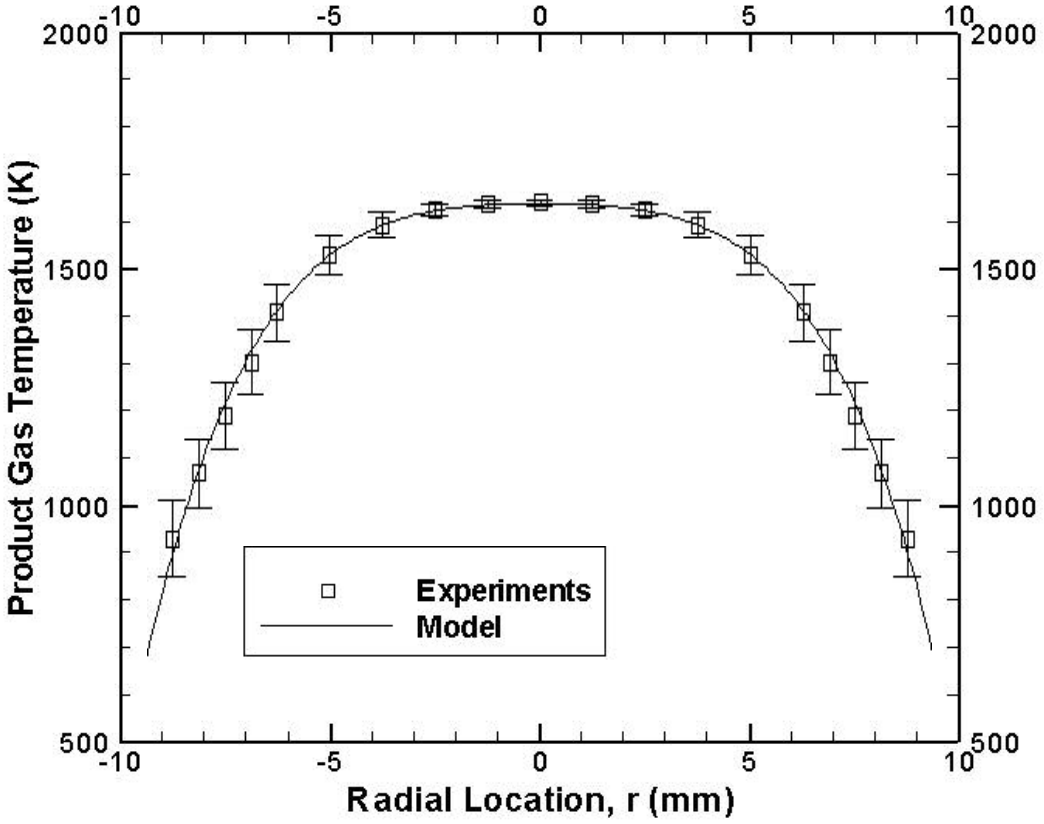

Figure 5.9. Product gas temperature profiles at z = 63 mm; no PIM in preheating annulus.

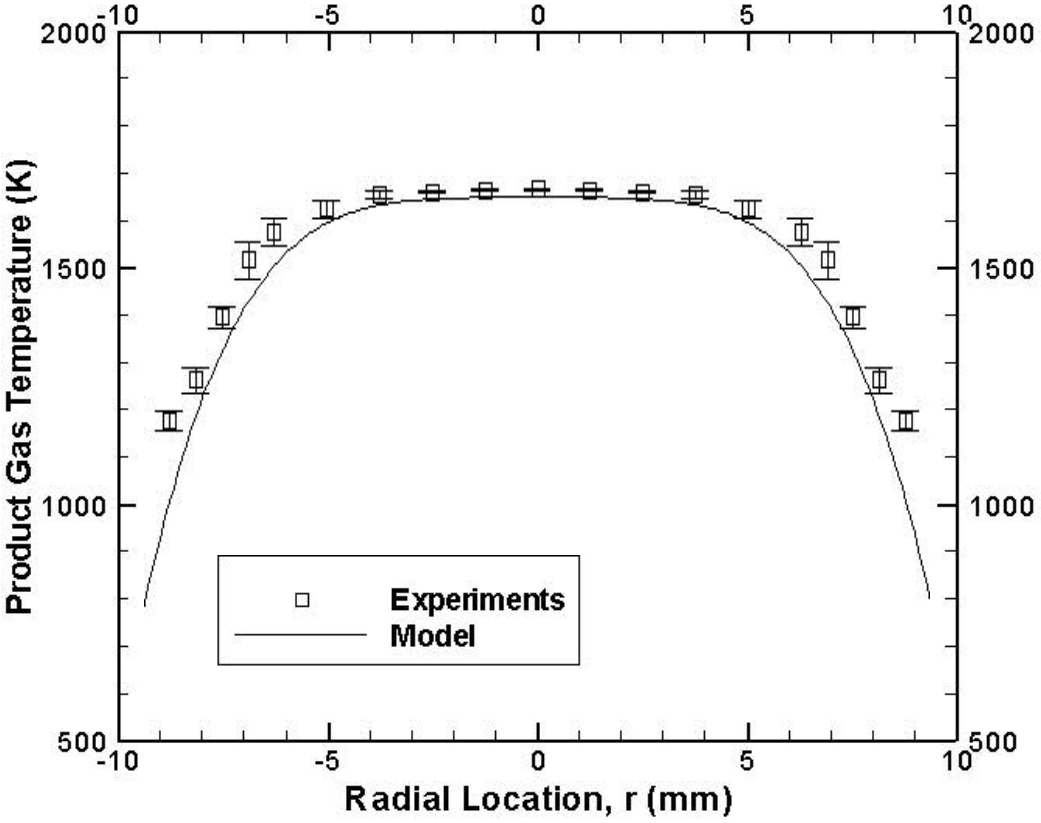

Figure 5.10. Product gas temperature profiles at z = 40 mm; no PIM in preheating annulus.

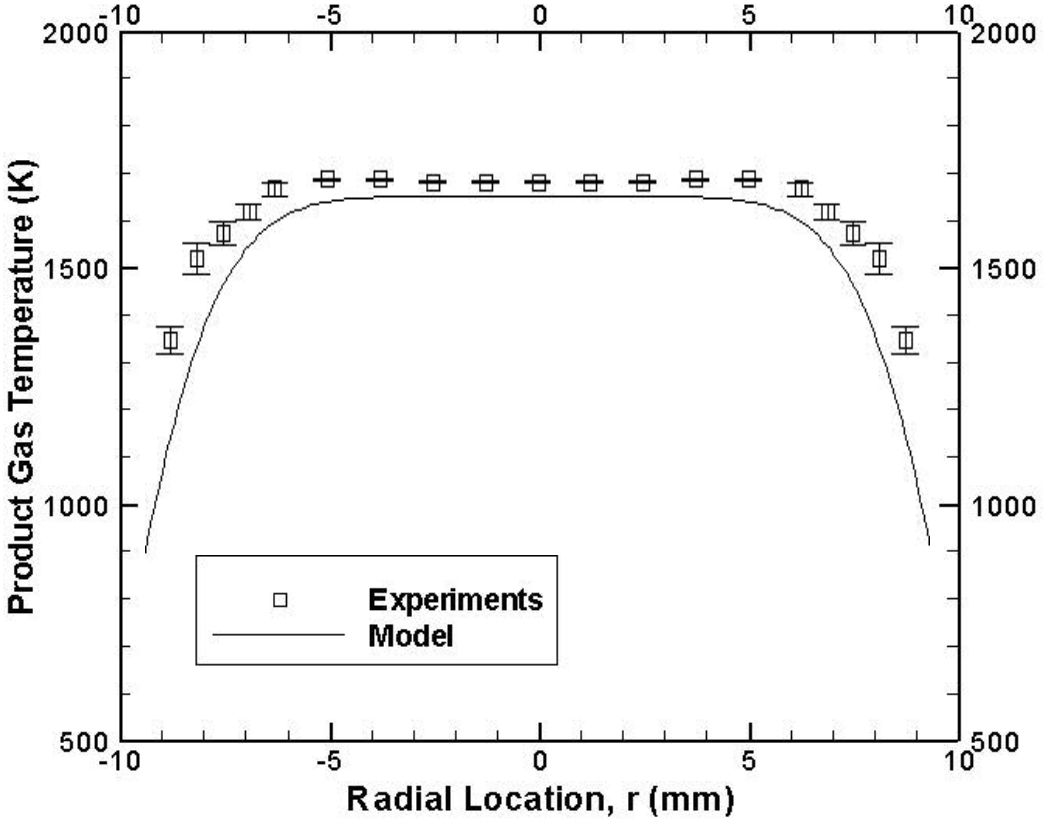

Figure 5.11. Product gas temperature profiles at z = 20 mm; no PIM in preheating annulus.

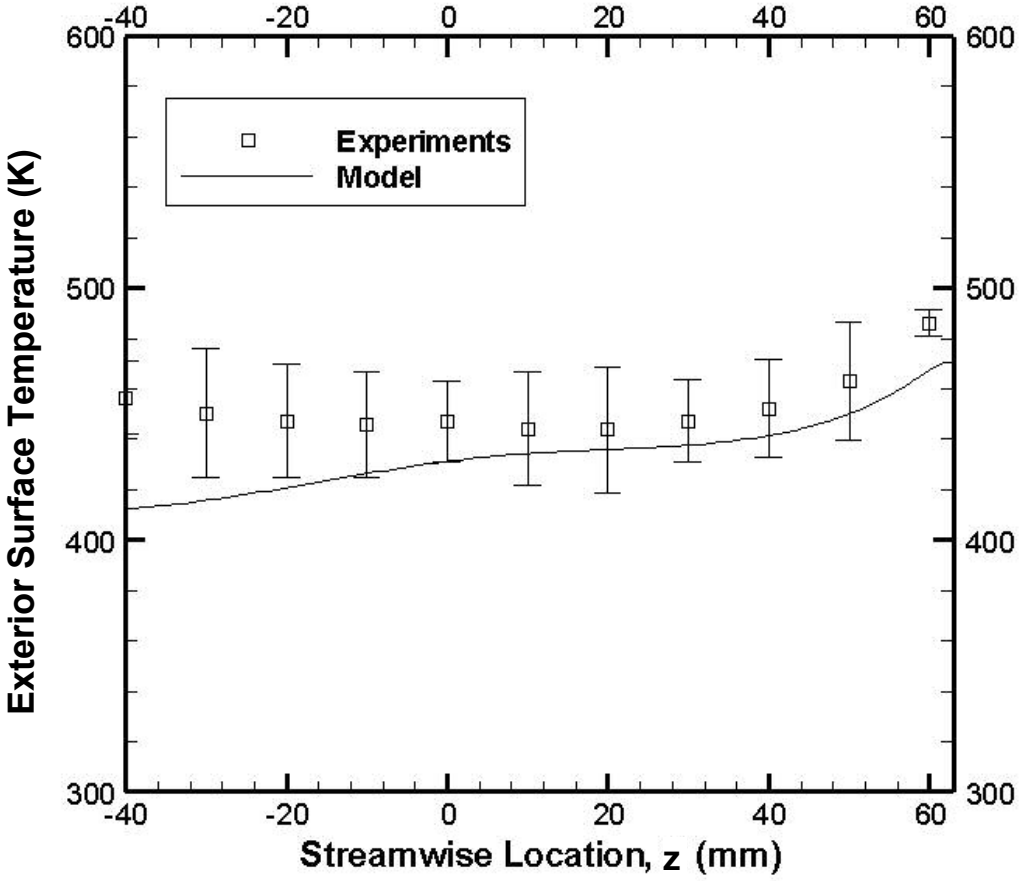

Figure 5.12. Exterior surface temperature profiles without PIM in preheating annulus.

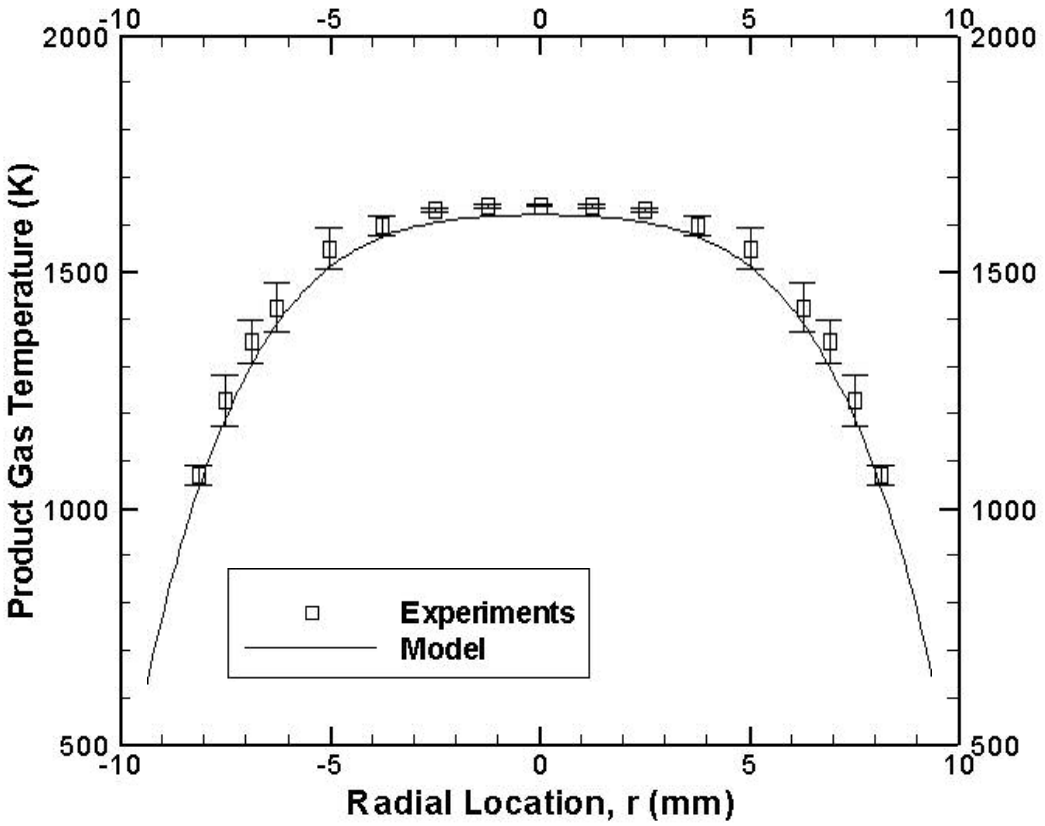

Figure 5.13. Product gas temperature profiles at z = 63 mm; PIM in preheating annulus.

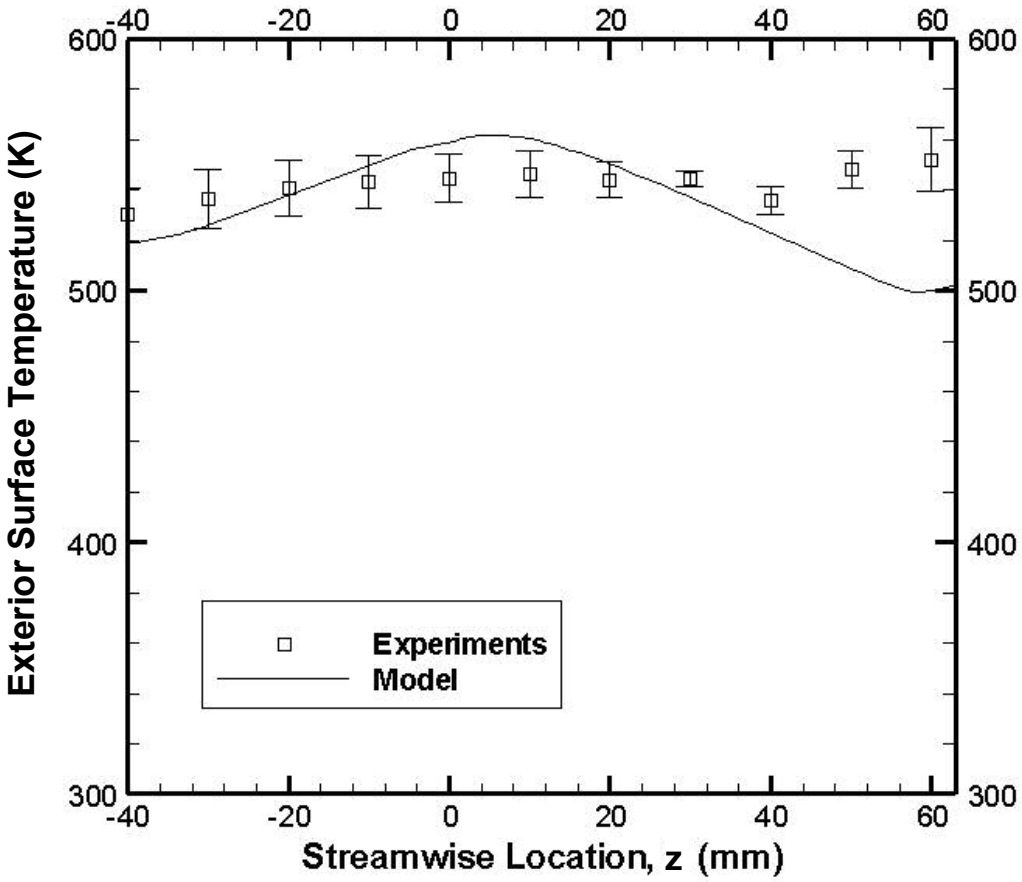

Figure 5.14. Exterior surface temperature profiles with PIM in preheating annulus.

5.3 Fluid Flow and Temperature Fields

This chapter describes the general characteristics of the system by presenting pressure, temperature, and velocity fields using contour plots and profiles at various locations.

5.3.1 Fluid Flow

Static pressure contours are presented in Fig. 5.15. Nearly all of the 500 Pa of pressure loss occurred across the flame stabilizing PIM. Figure 5.16 illustrates the absolute axial velocity contours. In the annulus, the reactant velocity averaged 1.5 m/s. The velocity increased to 1.8 m/s in the flame stabilizing PIM. At the flame zone, the velocity profile was nearly uniform and the velocity rapidly increased to approximately 5.5 m/s. A developing velocity profile and velocity boundary layers are visible within the combustion chamber. A velocity vector plot is presented in Fig. 5.17, where the enlarged region depicts recirculation near the corner of the outer wall and base.

Profiles of the absolute axial velocity in the preheating annulus are presented in Fig. 5.18. Qualitatively, a parabolic profile was observed at z = 40 mm. As the reactants moved through the preheating annulus (negative z direction), the axial velocity magnitude increased. The reactant velocity increased because of reactant preheating, reducing the reactant density.

The axial velocity profiles in the combustion chamber are presented in Fig. 5.19. Prior to the reaction, at z = 0 mm, the axial velocity was nearly constant across

the combustor. The axial velocity increased to nearly 6.0 m/s at z = 10 mm. As the product gases moved downstream, the velocity profile developed and the boundary layer near the wall became thicker. Since the combustor exit plane was only three diameters from the PIM, the products did not reach a fully developed state within the combustor chamber.

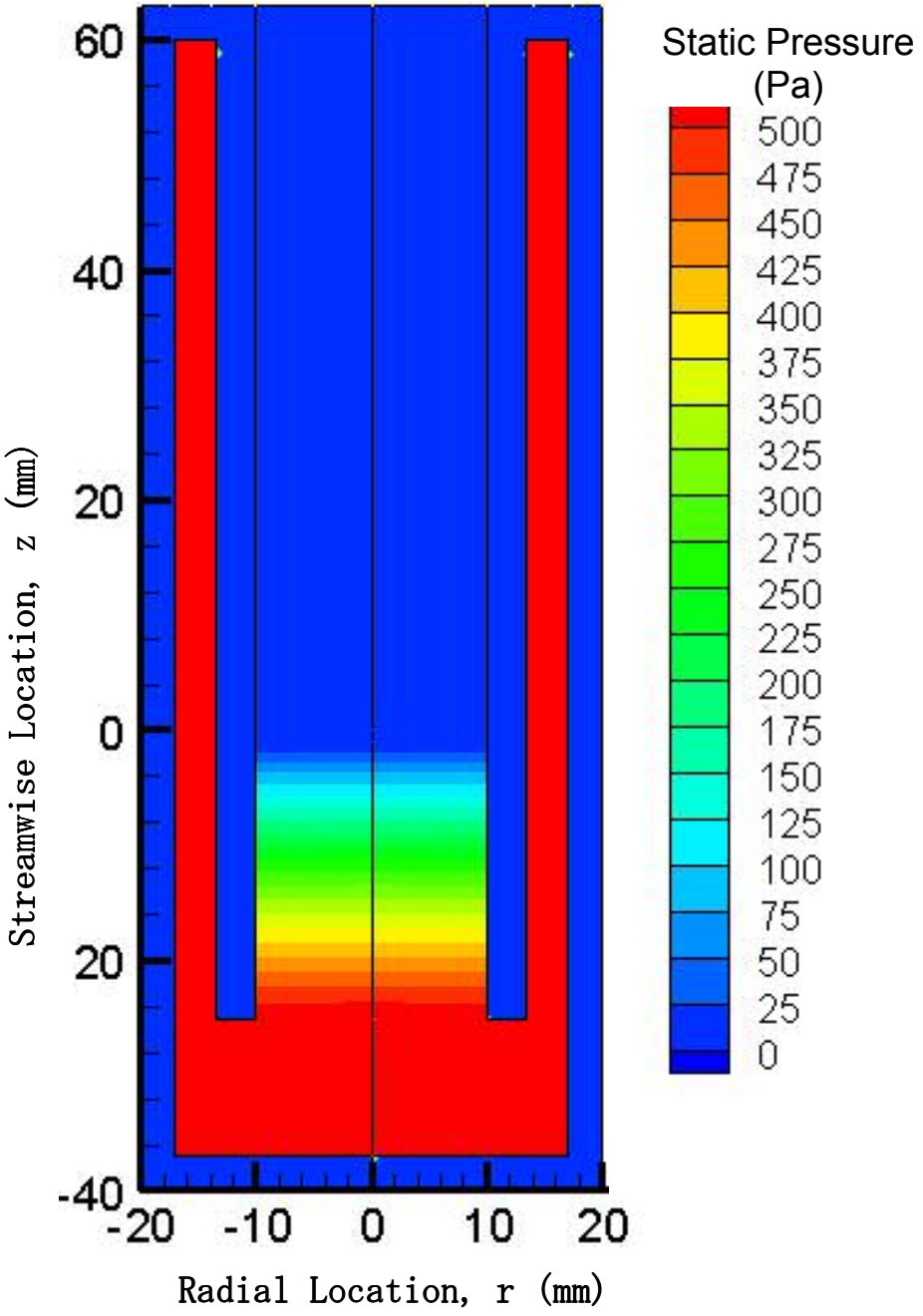

Figure 5.15. Static pressure contours.

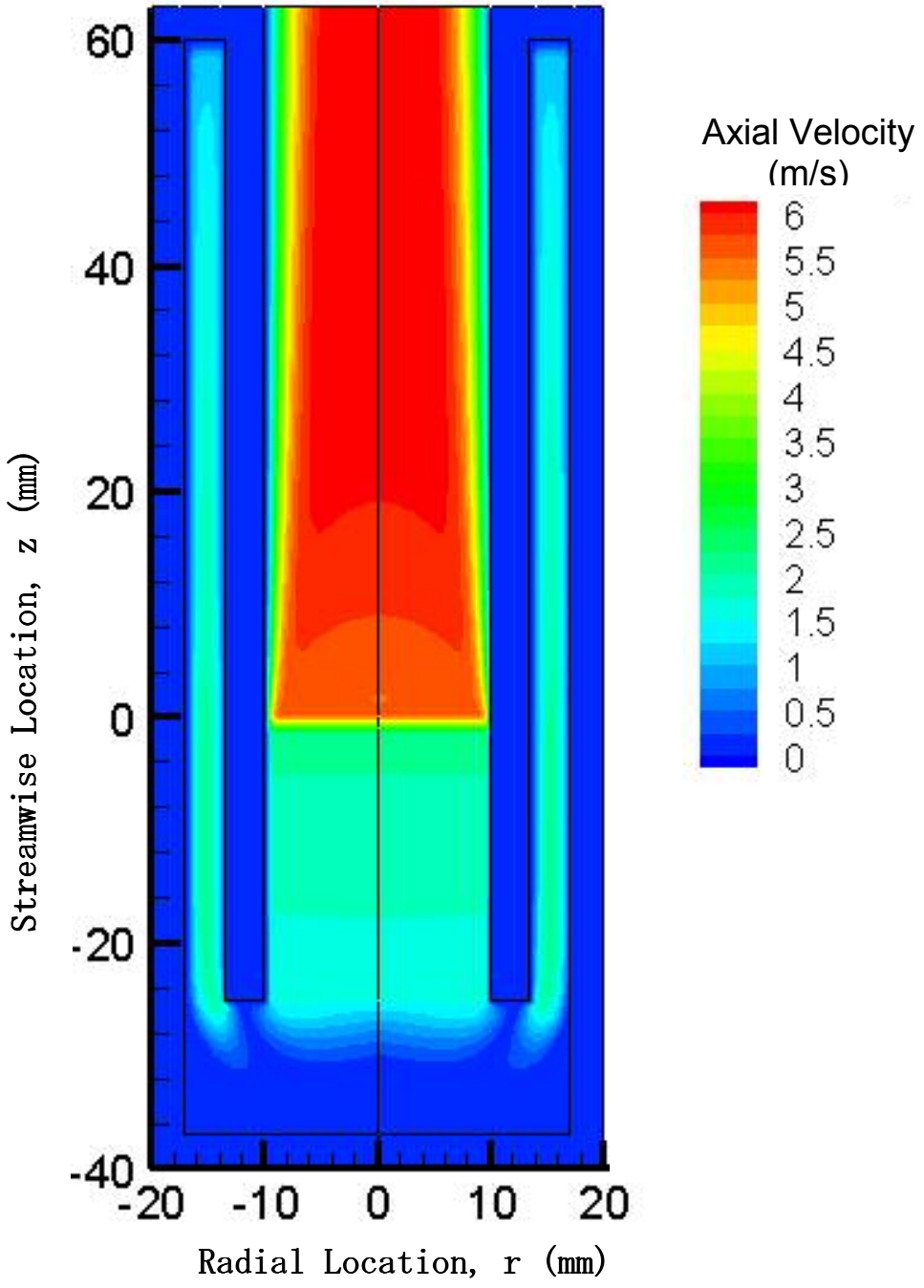

Figure 5.16. Axial velocity magnitude contours.

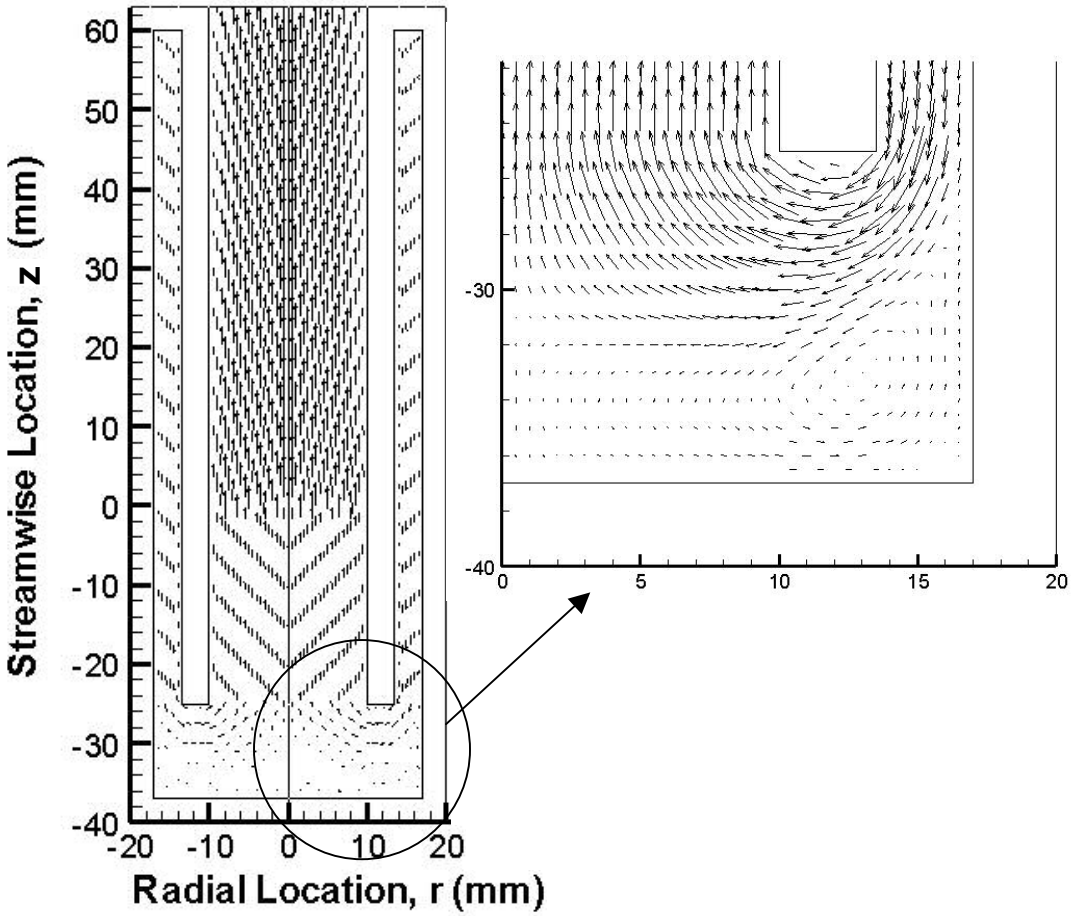

Figure 5.17. Velocity vector plot.

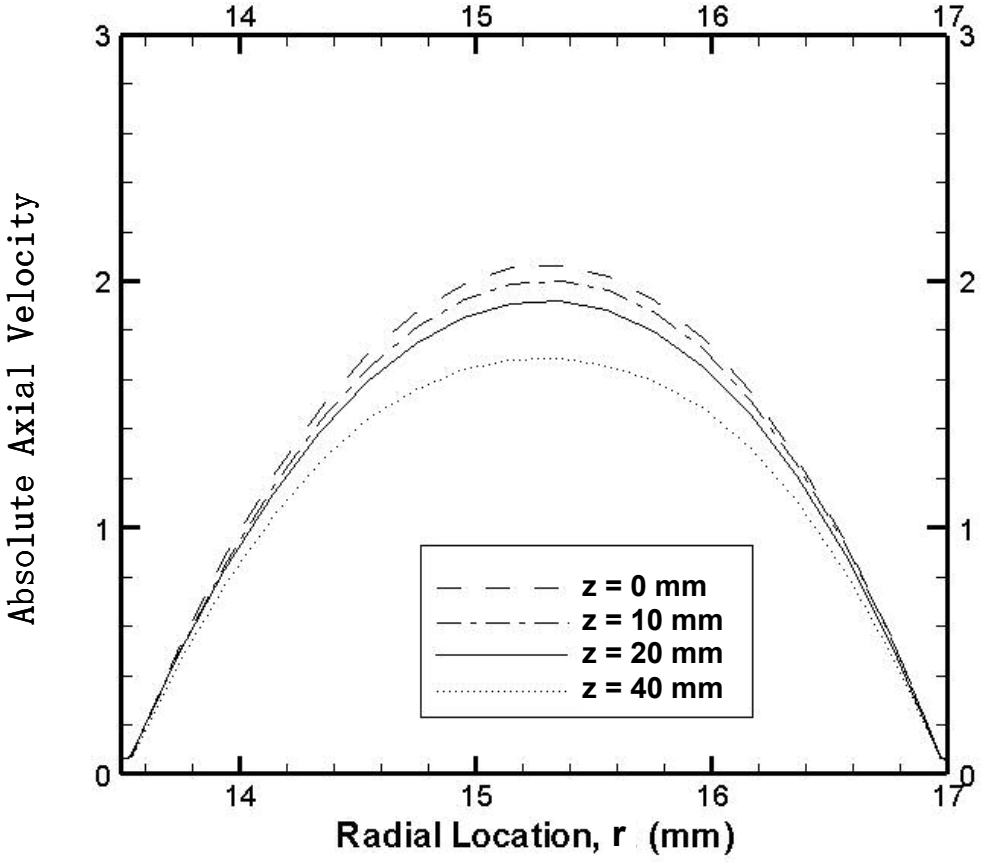

Figure 5.18. Axial velocity magnitude in the annulus.

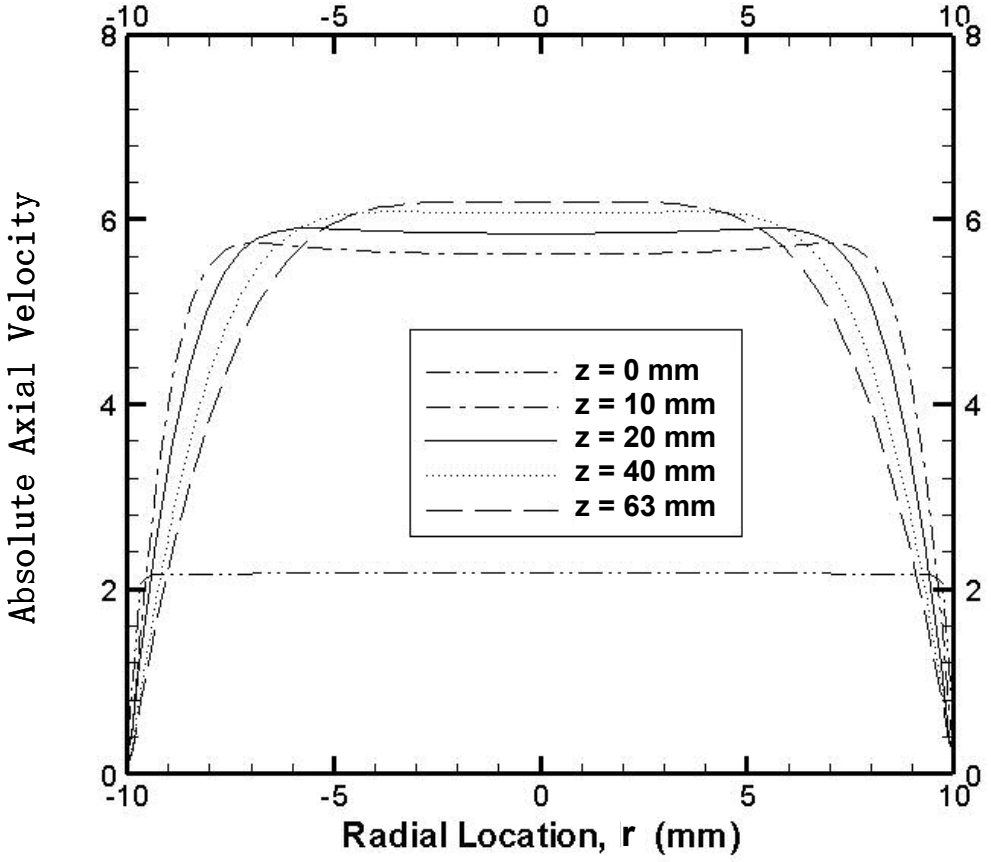

Figure 5.19. Axial velocity magnitude in the combustor chamber.

5.3.2 Temperature Contours

Static temperature contours throughout the computational domain are presented in Fig. 5.20. The reactants entered the system at approximately 300 K. The reactant temperature increased in the preheating annulus and then, in the flame stabilizing PIM to approximately 700 K prior to combustion. The temperature in the flame zone was relatively constant across the combustor chamber. The thermal boundary layer developed on the combustor wall, reaching a thickness of approximately 2 mm at the exit plane.

The temperature contour range was adjusted in Fig. 5.21 to show greater details at lower temperatures. Again, the reactants entered the system at 300 K. Convective heat transfer from the combustor wall to the reactants is depicted by the temperature boundary layer developeding along the length of the outer wall (r = 13.5 mm). The combustor wall temperature was maximum, approximately 680 K, near the flame zone. The annulus outer wall temperature was approximately 430 K.

Radial temperature profiles in the preheating annulus are presented in Fig. 5.22. Near the reactant inlet, at z = 59 mm, the combustor wall and outer wall temperatures were higher than the gas temperature. Heat transfer to the reactants is indicated by the slope of temperature profiles at r = 13.5 mm and r = 17.0 mm. The temperature of the reactants increased in the flow direction from z = 40 mm to 20 mm. At z = 0 mm, the temperature gradient at the outer wall (r = 17.0 mm) was nearly zero, indicating little heat transfer from the wall to the reactants. At z = -20 mm, the temperature of the reactants was higher than that of the outer wall, indicating

heat transfer from the reactants to the outer wall. This mode of heat transfer was undesirable because it leads to heat loss to the surroundings. These results indicate that a shorter annulus could improve the system performance and reduce heat loss to the surroundings.

Figure 5.23 presents static temperature profiles within the combustion chamber. At the interface between the flame stabilizing PIM and the flame (z = 0 mm), the temperature profile was nearly uniform at 700 K. Immediately downstream of the flame (z = 1 mm), the temperature profile was nearly constant at 1600 K. As the product gases moved downstream, heat was transfered to the combustor wall, as evident by the negative temperature gradients at r = ± 10.0 mm.

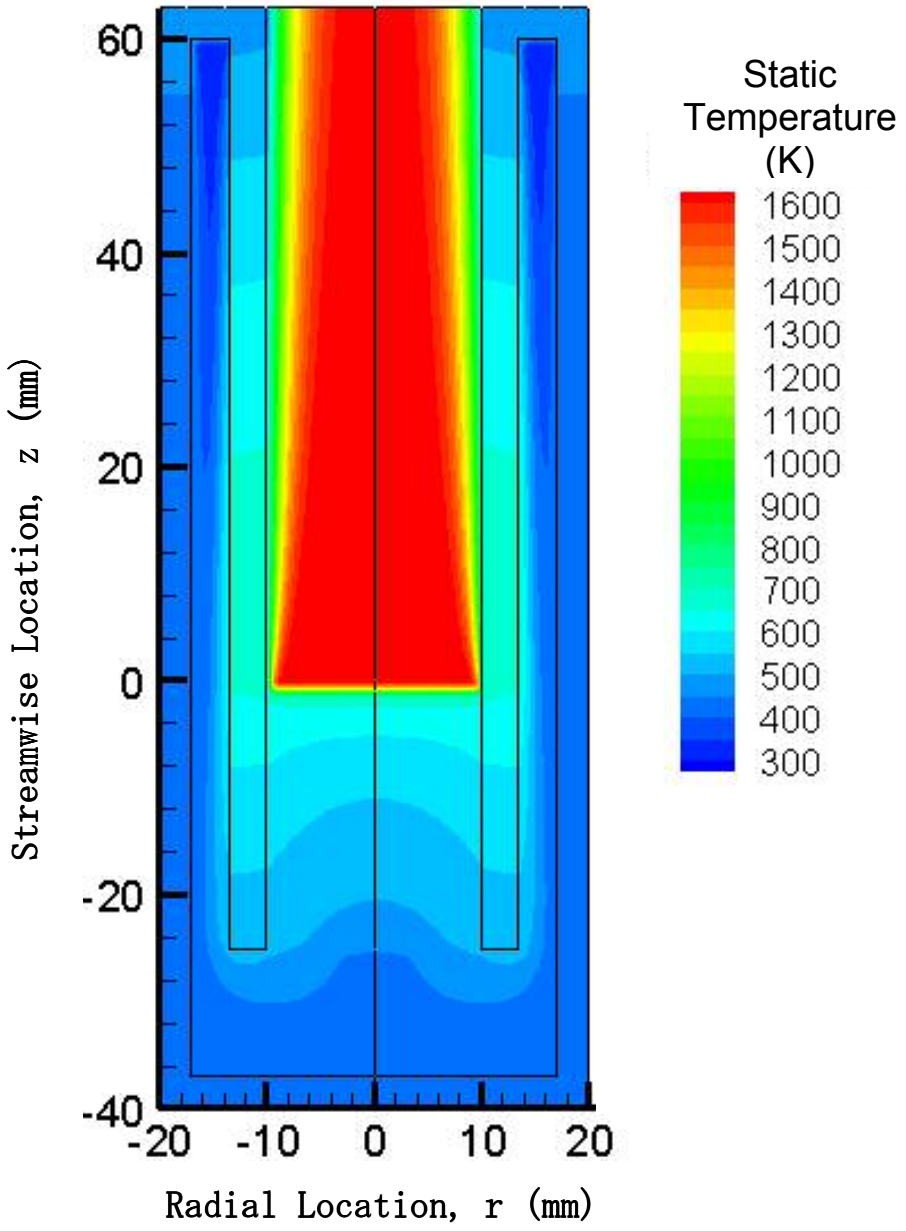

Figure 5.20. Static temperature contours.

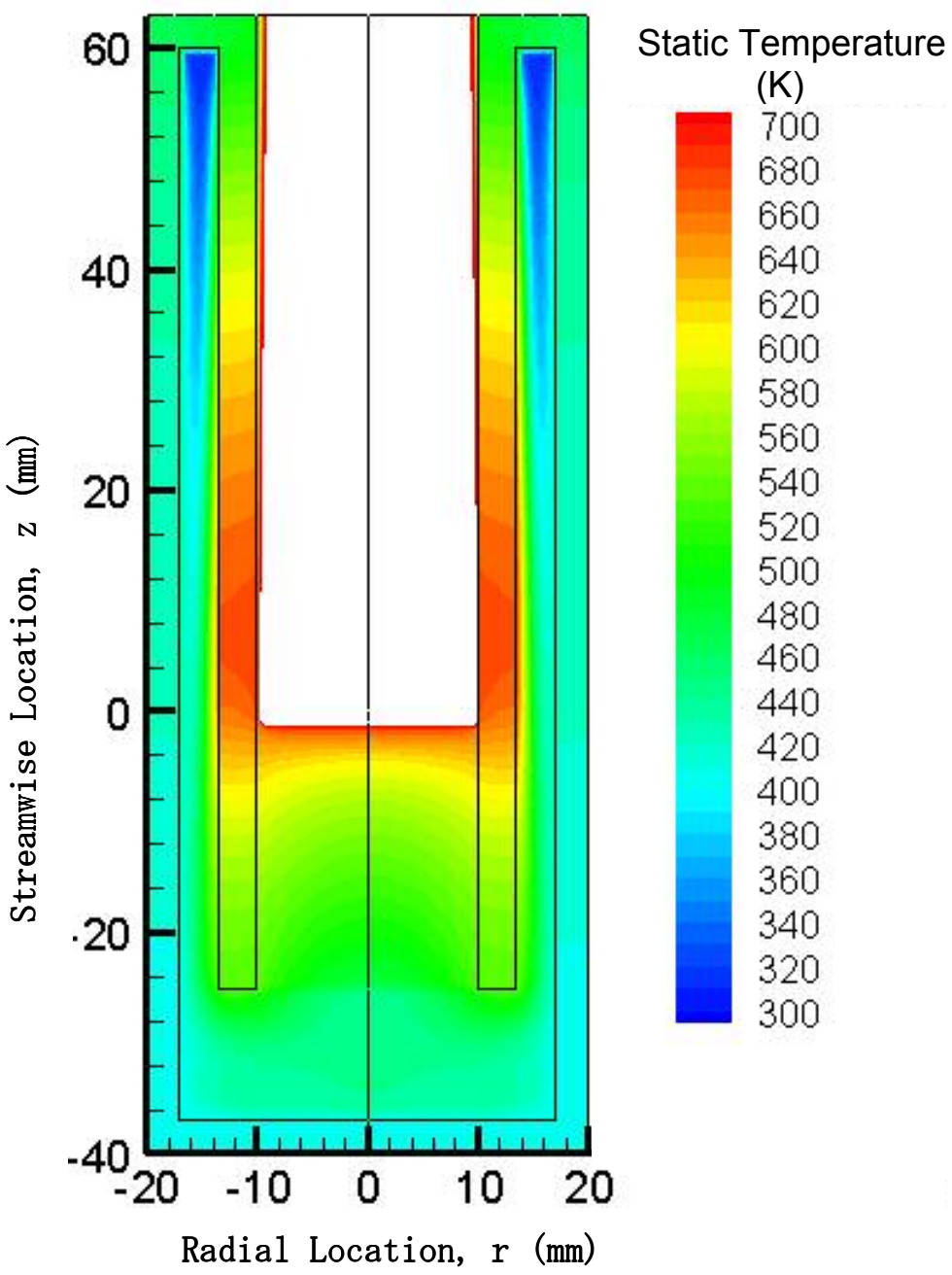

Figure 5.21. Static temperature contours.

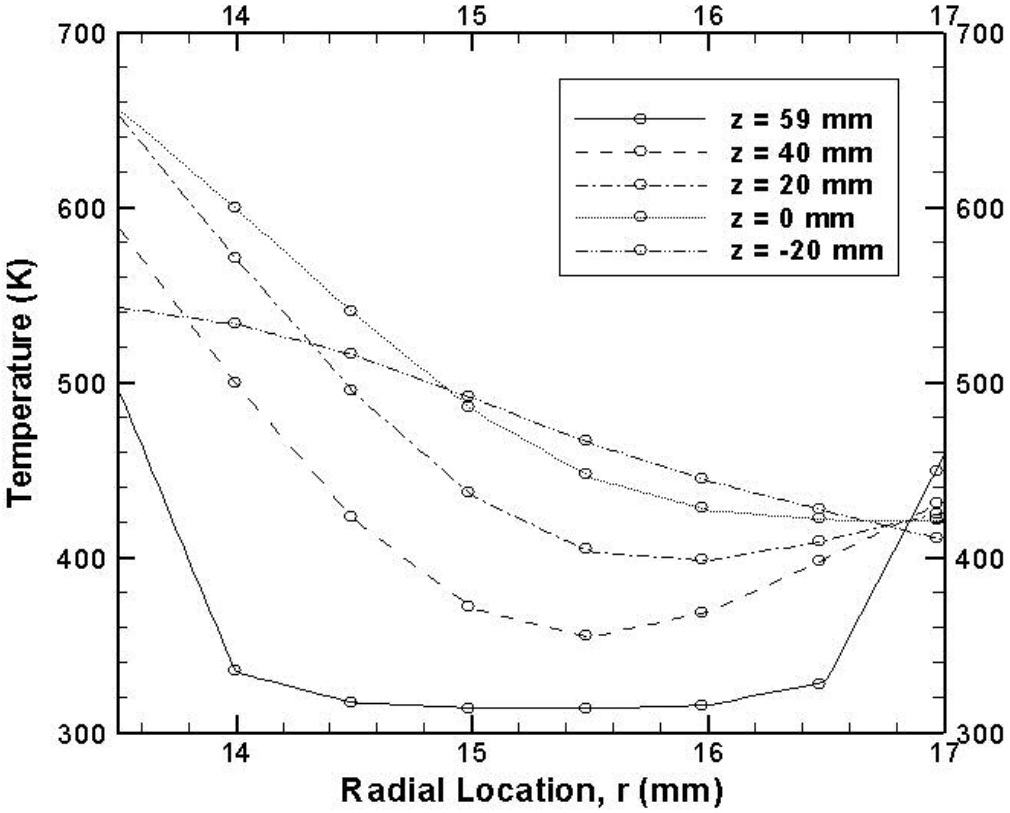

Figure 5.22. Static temperature profiles in the annulus.

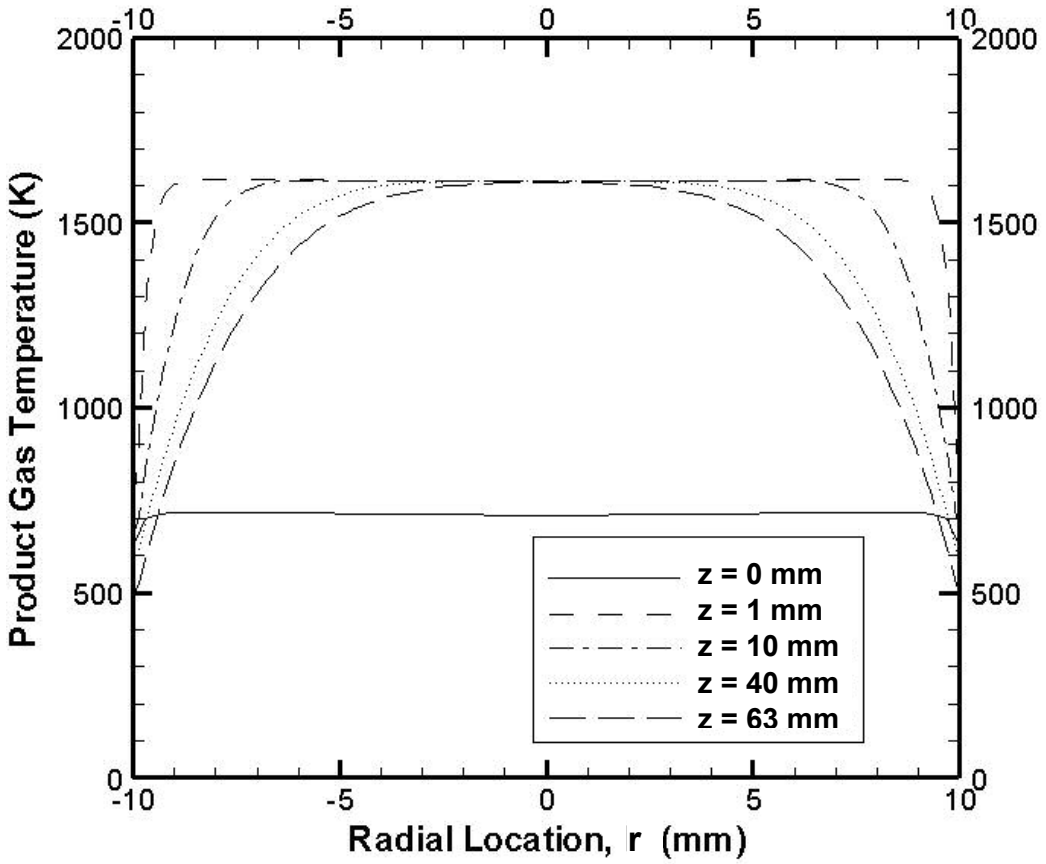

Figure 5.23. Static temperature profiles in the combustor.

5.4 Thermal Analysis

An important objective of the computational analysis was to gain a fundamental understanding of heat transfer in the heat recirculating combustor, so that the design could be improved. In this section, analyses aimed at identifying the relative importance of heat loss sources are discussed.

The fluid flow and temperature fields presented in the previous section indicated three potential sources of heat loss.

- Axial conduction through the combustor wall into the lid.
- Radiation from the combustor wall to the outer wall
- Convection from the preheated reactants to the outer wall.

When PIM was used in the preheating annulus, a fourth mode of heat loss, radial conduction across the annulus was possible as well. Three methods of analysis were used to understand the relative magnitude and importance of the sources of heat loss. First, gas enthalpy profiles within the combustor and annulus were analyzed to identify location of heat transfer to/from the reactants. Second, heat conduction in the solid media was analyzed to characterize axial conduction through the combustor wall. Finally, the heat fluxes across the surfaces of the system were analyzed to identify interactions between solid and gas media. The understanding gained from these analyses helped identify modifications to the combustor design to improve performance.

5.4.1 Gas Enthalpy Analysis

The enthalpy of the reactant and product gases was used to improve understanding of heat transfer mechanisms in the mesoscale, heat recirculating combustor. The calculation process is described below, followed by the results and discussion. The sensible enthalpy flowrate was calculated with Equation 5.13:

$$\text{Enthalpy Flowrate} = 2\pi \int_{r_{inner}}^{r_{outer}} r\,\rho(r)\,v_Z(r)\,\Delta h(T(r))\,dr \qquad (5.13)$$

where ρ is the density, v_Z is the axial velocity and h(T(r)) is the sensible enthalpy. The enthalpy flowrate was calculated across faces perpendicular to the flow direction. In the combustor chamber, r_{inner} was 0.0 mm and r_{outer} was 10.0 mm and in the preheating annulus, r_{inner} was 13.5 mm and r_{outer} was 17.0 mm. The mass flowrate was 0.3654 g/s, corresponding to V_{in} = 1.0 m/s.

Figure 5.24 presents the enthalpy flowrate of the reactant and product gases in the preheating annulus and combustor chamber. The reactants moved in the negative z-direction in the annulus and in the positive z-direction in the combustor. The slope of the profile corresponds to the rate of preheating; a positive slope indicates heat transfer from the walls to the gases and a negative slope indicated heat transfer from the gases to the walls. In the preheating annulus, the reactants were preheated in the region from z = 60 mm to z = 0 mm. Little heat transfer occurred between z = 0 mm and z = -25 mm, where the enthalpy was nearly constant. The maximum rate of

preheating within the annulus occurred at the injection location because of the large temperature difference between the reactants in the annulus and products in the combustor. The enthalpy flowrate at z = -25 mm was 61 W, indicating that preheating in the annulus was 13 % of the heat release in combustion.

Near z = -25 mm, the reactants moved from the annulus into the flame stabilizing PIM. The rate of preheating increased within the flame stabilizing PIM, with 65 W transferred to the reactants in a length of 25 mm. The net heat transfer to the reactants prior to the reaction zone was 126 W, or 27 % of the HRR. Nearly half of the heat was recirculated in the preheating annulus and the remaining half was recirculated in the flame stabilizing PIM.

Heat release in the flame zone was responsible for the large enthalpy increase in the combustor chamber at z = 0 mm. The enthalpy of the product gases decreased throughout the combustor chamber as heat was transferred to the combustor wall. The rate of heat transfer from the product gases to the combustor walls was 135 W. The sensible enthalpy rate exiting the system was 410 W. Since the HRR was 460 W, approximately 50 W or 11 % of the heat released from combustion was lost to the surroundings.

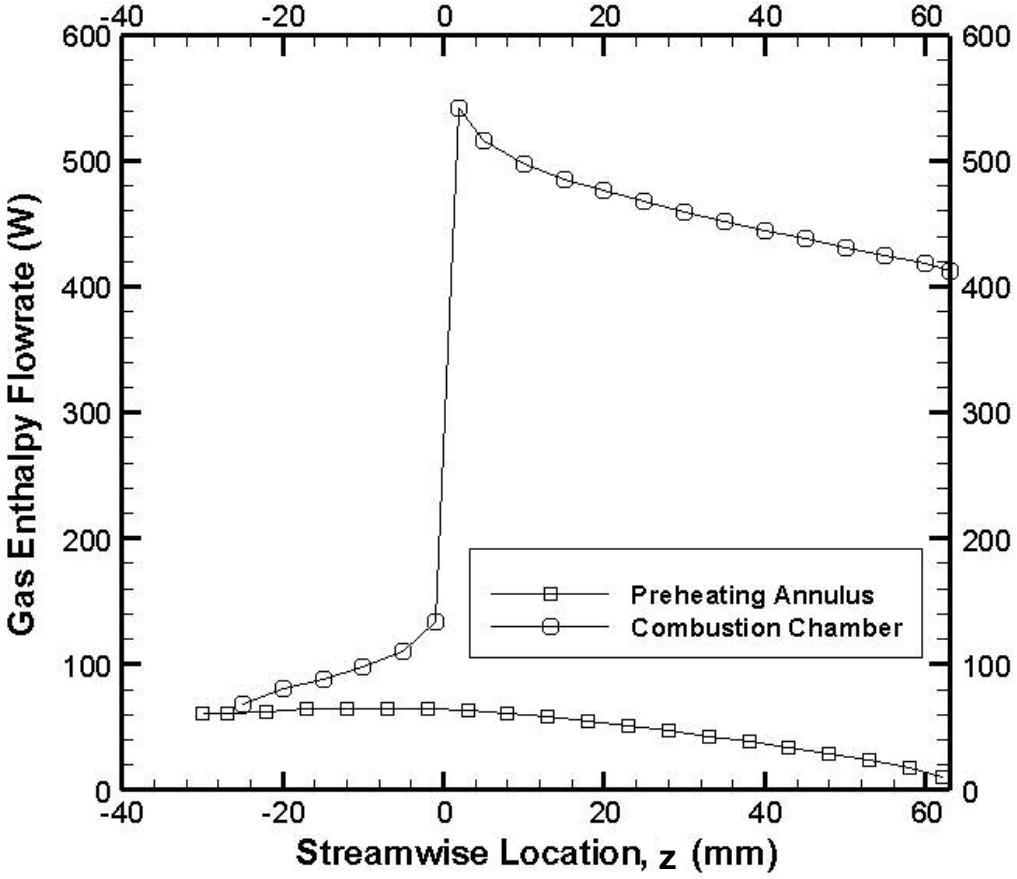

Figure 5.24. Gas enthalpy in preheating annulus, flame stabilizing PIM and combustor chamber.

5.4.2 Heat Conduction at Combustor Wall

The streamwise temperature at the midplane of the combustor wall (r = 11.75 mm) is presented in Fig. 5.25. The large temperature gradient near the lid (z = 60 mm) indicates significant axial conduction, which contributed to heat loss. Analysis was performed to determine the magnitude of axial conduction and to determine its contribution to the overall heat loss.

Equations 5.14 and 5.15 were used to calculate the axial heat flux and total axial heat transfer. The conductivity of the stainless steel wall was taken to be 21.5 W/m.K. Wall temperatures were obtained from the computational results. The distance from r = 10.0 mm to 13.5 mm was discretized into 35 segments for the summation depicted in equation 5.15. The distance δz was 1 mm for all cases.

$$\dot{q}(Z) = -k\frac{dT}{dz} \approx -k\frac{(T_2 - T_1)}{\delta z} \tag{5.14}$$

$$\dot{Q}(Z) = -\int_{r_a}^{r_b} k\frac{(T_2 - T_1)}{\delta z}\,dA \approx -\sum_{r_a}^{r_b} k\frac{(T_2 - T_1)}{\delta z}\Delta A \tag{5.15}$$

Figure 5.26 presents the axial heat flux and heat transfer through the combustor wall at various streamwise locations. Near the combustor lid, approximately 30 W of heat was transferred by axial conduction in the positive z-direction. Most of the axial conduction resulted in heat loss, while a small fraction was transferred to the reactants by interfacial convection from the inner face of the

outer wall, as seen in the next section. These results indicate that axial conduction through the combustor wall in the positive z-direction was a significant contributor to heat loss to the surroundings. In the next section, the interaction between solid and gas media is investigated.

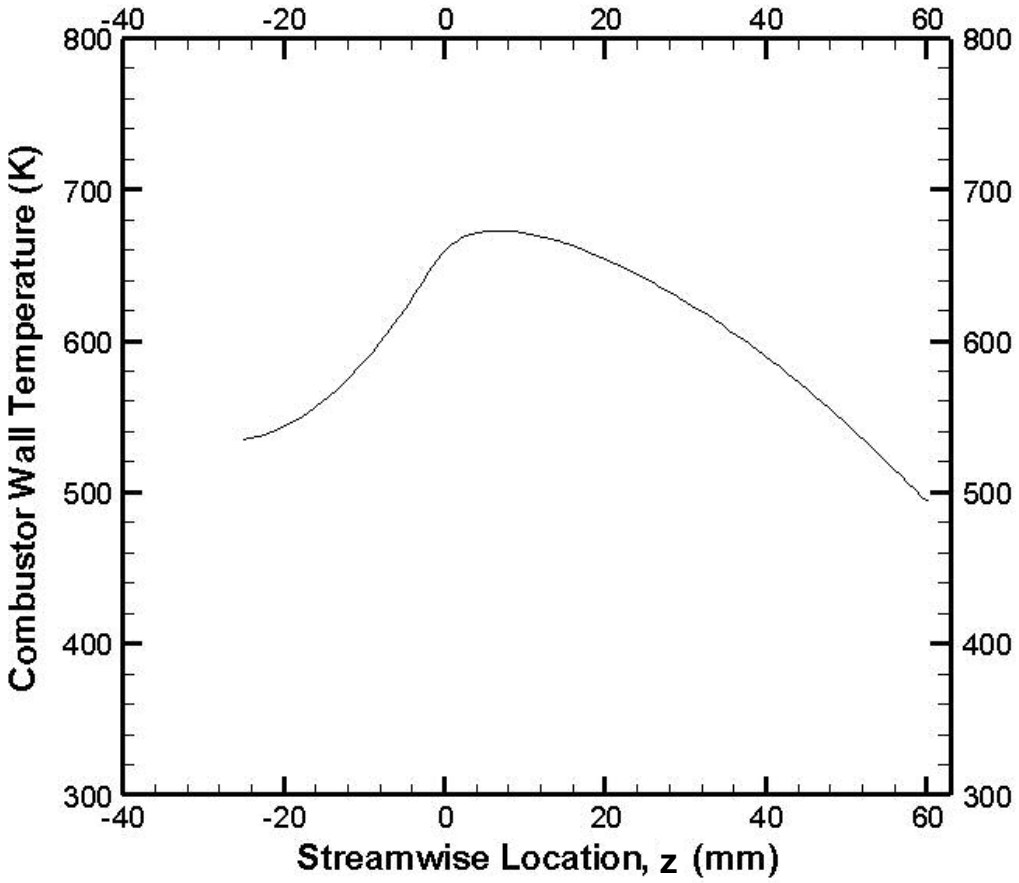

Figure 5.25. Temperature profile at the midplane (r = 11.75 mm) of the combustor wall.

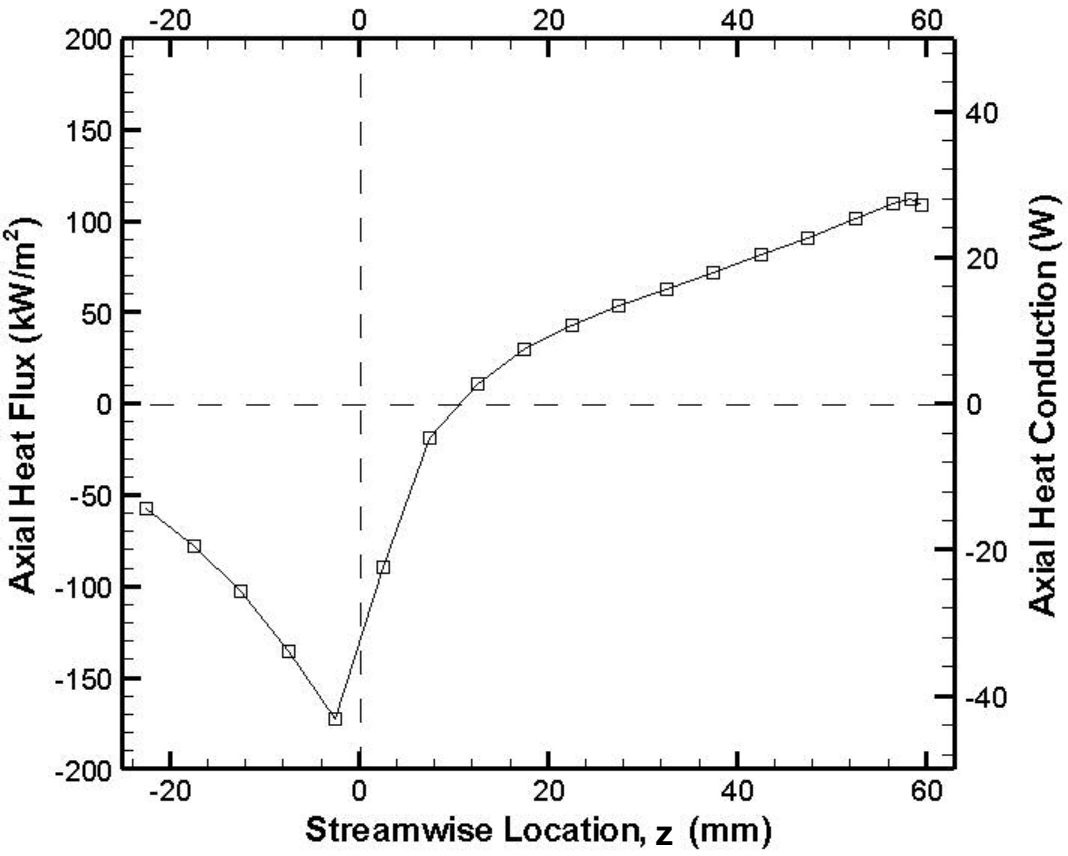

Figure 5.26. Axial heat flux and heat conduction in combustor wall.

5.4.3 Surface Heat Transfer

Investigation of surface heat fluxes provided an understanding of convective and radiative heat transfer at solid/fluid interfaces. This information helped identify dominant modes of heat loss to develop strategies to minimize the loss. The understanding gained from the analysis served as the basis for design improvements presented in Chapter 6.

The sign convention was selected such that a positive heat flux indicated heat transfer into the wall. Recall that r = 10 mm corresponds to the inner surface of the combustor wall and r = 13.5 mm is the outer surface of the combustor wall. The inner surface of the outer wall was at r = 17 mm and the exterior surface was at r = 20 mm. Convective heat flux was determined by the wall and gas temperatures and the fluid flow properties near the wall as given in equation 5.16.

$$\dot{q}_{conv} = h\left(T_w - T_f\right) = k_f \left(\frac{\partial T}{\partial n}\right)_{Wall} \tag{5.16}$$

where h is the convective heat transfer coefficient, T_w is the temperature of the wall, T_f is the temperature of the fluid, k_f is the thermal conductivity of the fluid and n is the local coordinate normal to the wall.

Radiation heat flux ($\dot{q}_{rad}$) was calculated with the discrete ordinates radiation transfer equation (Equation 5.10). The total surface heat flux

($\dot{q}_{total} = \dot{q}_{conv} + \dot{q}_{rad}$) was integrated using Equation 5.17 to determine the surface heat transfer.

$$\dot{Q}_{surf} = \int_{Z_0}^{Z_1} \dot{q}_{total}(Z) \cdot 2\pi \cdot r dz \approx \sum 2\pi \cdot r \cdot \Delta Z \cdot \dot{q}_{total}(z) \qquad (5.17)$$

Figure 5.27 presents the surface heat flux at the inner face of the combustor wall (r = 10 mm). Upstream of the flame (z < 0 mm), heat transfer occurred mainly by convection from the combustor wall to the reactants in the flame stabilizing PIM. Integration of the heat flux profile revealed that 32 W was transferred to the reactants in the region -25 mm < z < 0 mm. Downstream of the flame (z > 0 mm), heat transfer from the product gases to the combustor wall occurred by convection because the gases were at a higher temperature than the wall. The surface heat flux was maximum near the flame zone, where the temperature and velocity adjacent to wall were higher. The rate of heat transfer decreased as the products moved downstream and the thermal and velocity boundary layers developed. The total heat transfer from the product gases to the wall in the combustion chamber was 139 W. Radiation heat transfer on the inner face of the combustor wall was less than 2 W and hence, convection was the dominant mode of heat transfer

Heat flux at the outer surface of the combustor wall (r = 13.5 mm) is presented in Fig. 5.28. The heat flux was maximum near z = 60 mm, where the cool reactants entered the annulus and near z = 10 mm, where the combustor wall temperature was

the highest. The total heat transfer to the reactants of 73 W was composed of convection (44 W) and radiation (29 W). Convection signifies heat recirculated to the reactants. However, radiation from the combustor wall was transferred to the outer wall, where it contributed to heat loss.

Heat flux at the inner surface of the outer wall (r = 17.0 mm) is presented in Fig. 5.29. Heat transfer by convection occurred from the outer wall to the reactants in the annulus from the inlet (z = 60 mm) to the location of the flame (z = 0 mm). As the reactants moved past the flame location (z < 0 mm), the heat flux sign changed, indicating heat transfer from the reactants to the outer wall. Near the inlet, the reactant temperature was lower than the outer wall temperature. However, the reactant temperature increased with passage through the annulus. Past the flame zone location, the reactant temperature was higher than the outer wall temperature (see Fig. 5.21). Integration of the surface heat flux profile over the outer wall revealed that the heat transfer by convection from the wall to the reactants was 10 W. Heat transfer by radiation to the outer wall was 28 W. Hence, the net heat transfer from the annulus to the outer wall was 18 W.

Heat flux at the exterior surface (r = 20 mm) is presented in Fig. 5.29. Since the temperature of the outer wall and the surroundings were relatively low, nearly all of the 38 W of heat loss from the outer wall to the surroundings occurred by convection.

Figure 5.31 and Table 5.3 summarize the surface heat transfer at fluid/solid interfaces for the combustor. A positive heat flux indicates heat transfer into the wall

and a negative heat flux indicates heat transfer away from the wall. Convection heat transfer occurred between the walls and gases. Since the gases did not participate in radiation, radiation heat transfer occurred between surfaces of the system. The heat transfer data in Table 5.3 represent the integrated values over the surfaces shown in Fig. 5.31. The contributions of conduction, radiation and convection to system heat loss were determined using the integrated surface heat transfer data.

As described in section 5.4.1, heat conduction in the positive z-direction at z = 60 mm contributed to heat loss through the lid. The rate of axial conduction to the lid was determined by considering the combustor wall as a control volume. From the conservation of energy, the rate of axial conduction to the lid must be equal to the sum of heat transfer across faces A, B, C and D in Fig. 5.31. Hence, the rate of axial conduction to the lid was 31 W (+139 W – 32 W - 3 W - 73 W = 31 W).

The rate of radiation across face D was 28 W from the combustor wall. Since the reactant gas did not participate in radiation, the radiation was transferred to the outer wall across face F. Since convection from face F to the reactants was 10 W, the net contribution of radiation to system heat loss was 18 W. The temperature of the reactants in the annulus was lower than the temperature of the outer wall throughout most of the annulus. Convection from the reactants to the outer was less than 3 W and was small compared to heat loss by axial conduction and radiation across the annulus. Therefore, the total heat transfer to the exterior surface was 31 W (63%) conduction and 18 W (37 %) radiation.

Heat recirculation in the annulus was equal to the sum of heat transfer by convection over faces D, E and F. The rate of heat transfer to the reactants was 44 W from the combustor wall (face D), 10 W from the outer wall (face F) and 7 W from the lid (face E). Thus, 63 W of thermal energy was recirculated to the reactants in the annulus. A significant fraction of heat, 32 W, was transferred from the combustor wall into the reactants in the flame stabilizing PIM across face B. The total preheating in the flame stabilizing PIM was higher than 32 W, since conduction from the flame zone into flame stabilizing PIM occurred as well.

Overall, the surface heat flux analysis helped identify several important aspects of the heat recirculating combustor design. Radiation across the annulus accounted for 37 % of the heat loss while axial conduction accounted for 63 %. Figs. 5.27-30 showed special difference in heat transfer. Those areas served as the focal point of design improvements, which are described in Chapter 6.

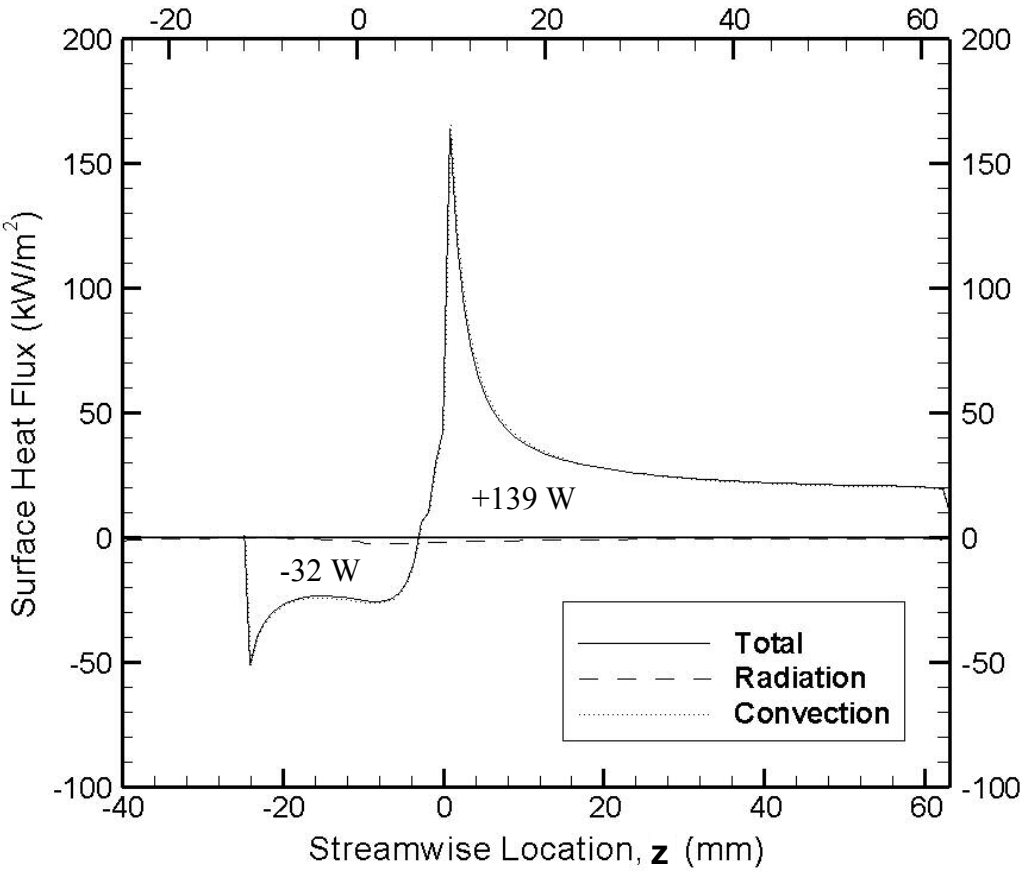

Figure 5.27. Surface heat flux at the combustor wall in combustion chamber (r = 10.0 mm)

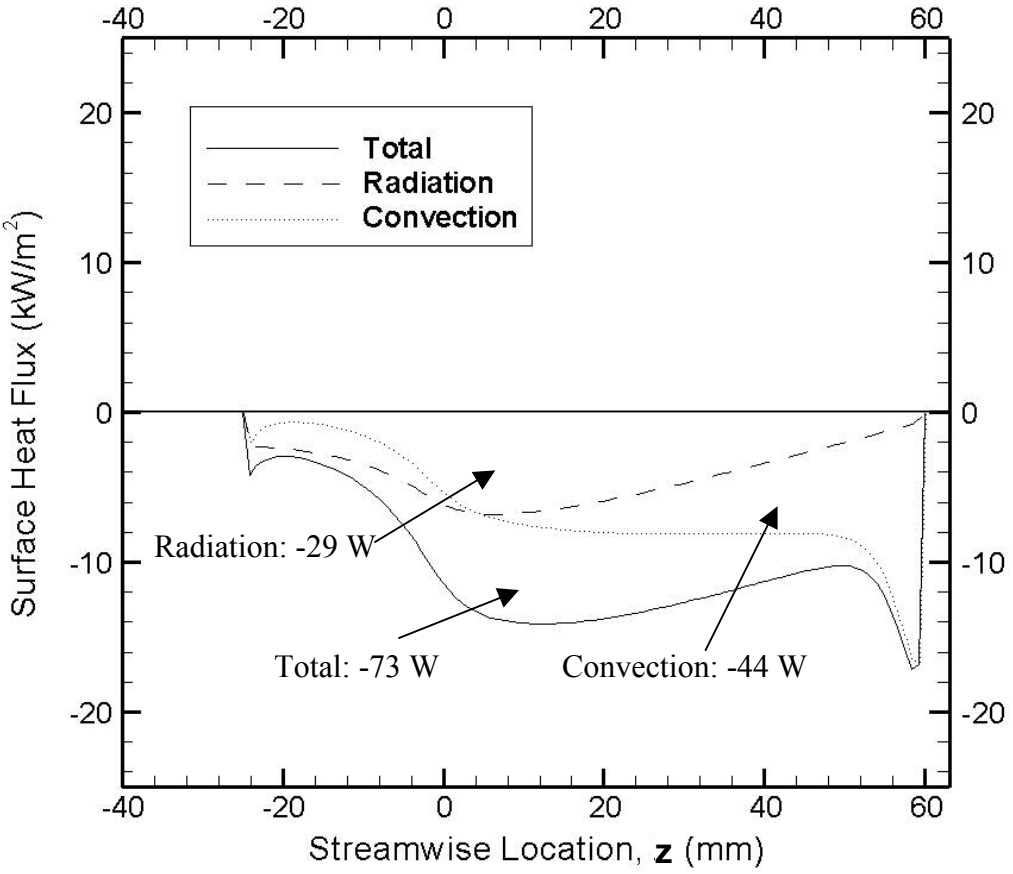

Figure 5.28. Surface heat flux at the combustor wall in preheating annulus (r = 13.5 mm).

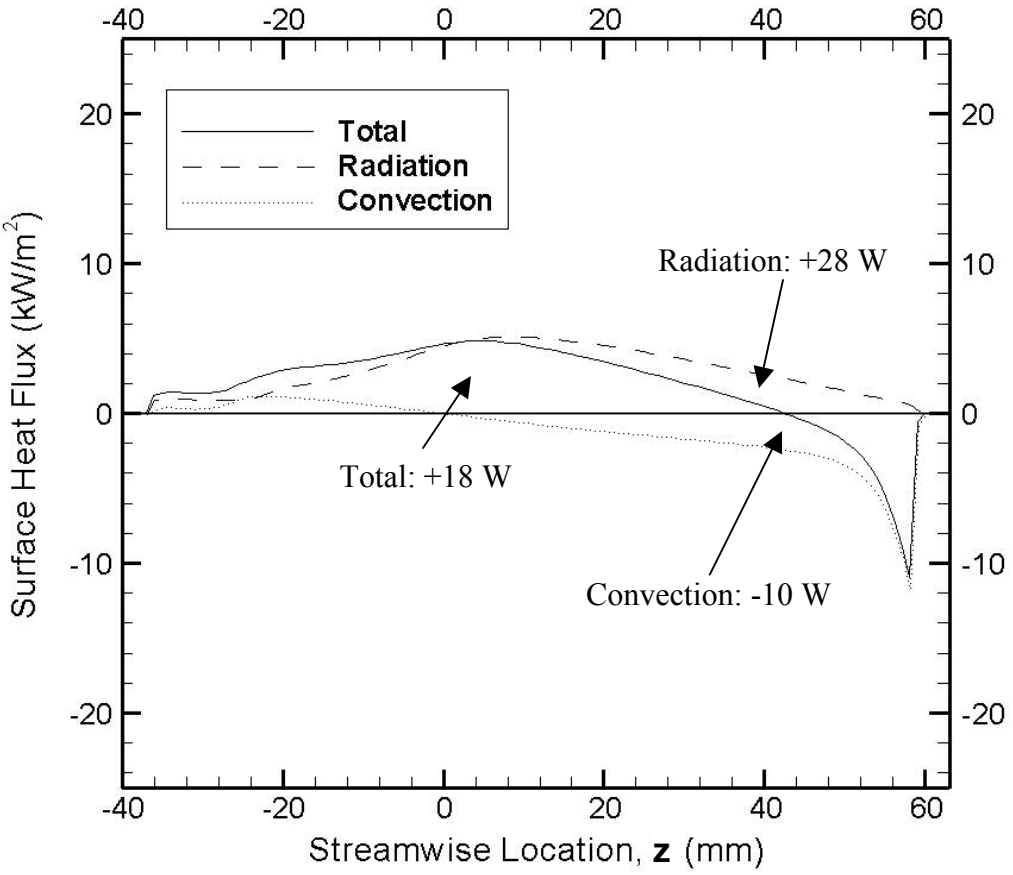

Figure 5.29. Surface heat flux at the outer wall in preheating annulus (r = 17.0 mm).

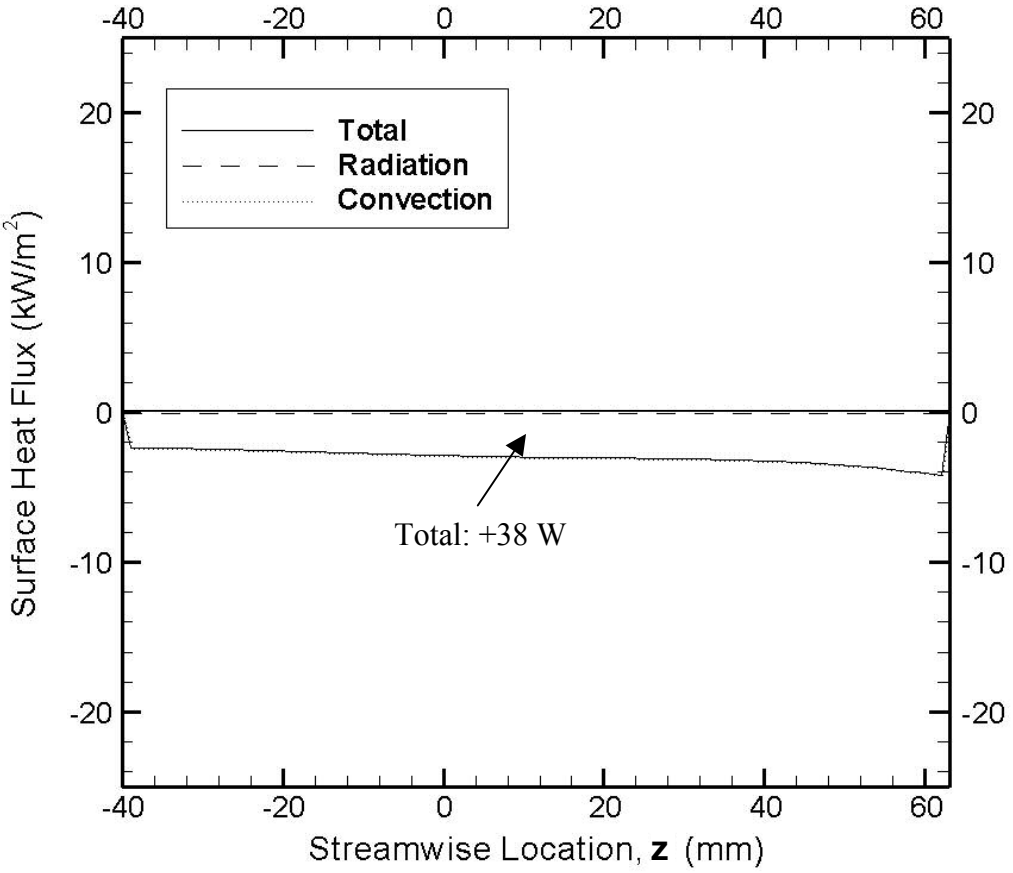

Figure 5.30. Surface heat flux at exterior surface (r = 20.0 mm).

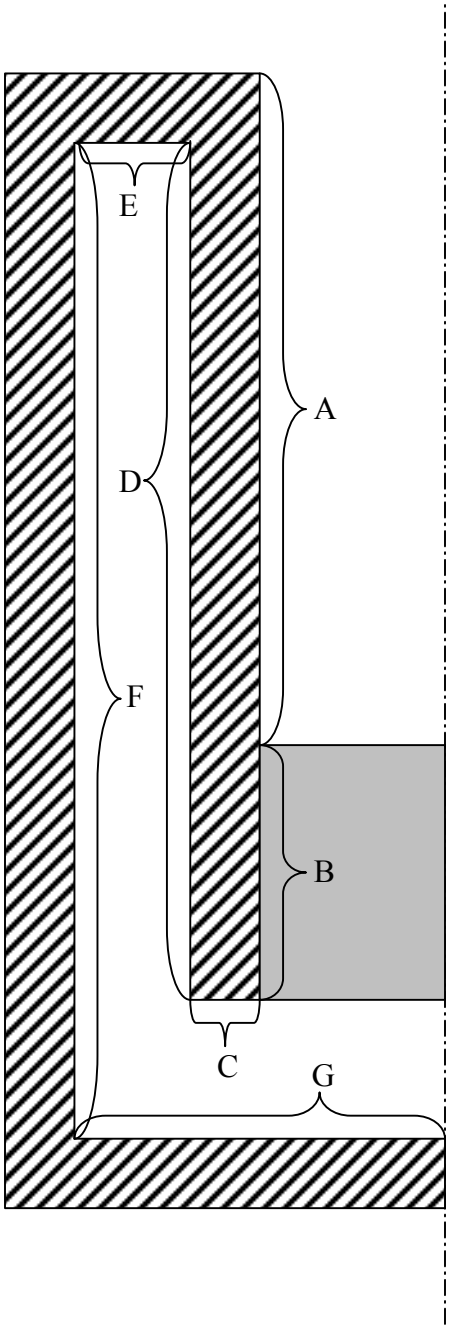

Table 5.3. Summary of Surface Heat Flux			
Face	Convection Heat Transfer	Radiation Heat Transfer	Total Heat Transfer
A	+ 141 W	- 2 W	+139 W
B	- 32 W	0 W	- 32 W
C	- 3 W	0 W	- 3 W
D	- 44 W	-29 W	- 73 W
E	- 7 W	0 W	- 7 W
F	- 10 W	+ 28 W	+ 18 W
G	+ 2 W	0 W	+ 2 W

Figure 5.31. Summary of Surface Heat Flux

5.5 Conclusions

A computational model was developed to simulate the heat recirculating combustor design. The model agreed well with experimental data and it provided insights into the flow and temperature fields that could not be obtained experimentally.

Heat transfer analysis on the gas phase, the solid phase, and the interaction between the two phases was performed. Each of the three analyses revealed important information about the heat recirculating combustor design. The gas enthalpy analysis focused on the heat recirculation process by tracking the enthalpy of the reactant and product gases from the inlet to the exit plane. Heat recirculation was most effective in the flame stabilizing PIM and annulus length could be reduced without significantly affecting heat recirculation. The heat conduction analysis in the solid surfaces indicated that significant heat transfer occurred by axial conduction in the combustor wall. Axial conduction in the negative z-direction enhanced heat recirculation, but conduction in the positive z-direction led to heat loss. The surface heat flux analysis shed insights into modes of heat transfer throughout the system. The relative contributions of radiation (37 %) and conduction (63 %) to heat loss were determined.

Several relationships and comparisons between the three analyses can be made. For example, the gas phase analysis indicated that heat recirculation in the preheating annulus was 61 W, which matched the value of 63 W computed using the surface heat flux. The gas analysis indicated that 135 W was transferred from the

products to the combustor wall, which agreed with a value of 139 W determined from surface heat flux analysis. Similarly, the solid conduction calculations determined that the axial conduction to the lid was 28 W, while the value obtained by surface heat flux analysis was 31 W. The agreement of these quantities supports the validity of the post-processing steps used for the analysis. Note that these analyses are based on computational results and any errors or approximations inherent in the CFD model would remain. Chapter 6 utilizes the findings from this chapter to develop a more effective mesoscale, heat recirculating combustor.

6. Parametric Studies

Heat loss to the surroundings is the most important factor influencing the performance and operating range of a small-scale combustion system. Therefore, the primary objective of a small scale combustor design should be to reduce heat loss to the surroundings. The heat transfer analysis presented in Chapter 5 identified axial conduction through the wall and radiation across the annulus as the two primary modes of heat loss. Hence, improving the design required reduction of heat loss by these two modes. Such design improvements are the concentration of the parametric studies presented in this Chapter. The primary goal is to develop the designs of a miniature system with low heat loss and high volumetric HRR. Effects of geometric parameters and material properties were considered and evaluated for potential improvements. The findings from the parametric study served as the basis for the phase II mesoscale combustor designs. Details of the designs are presented, along with predictions of their thermal performance.

6.1 Axial Conduction

Heat transfer analysis in Chapter 5 determined that approximately 63 % of the heat loss to the surroundings resulted from axial conduction through the combustor wall. Thus, the thermal resistance to axial conduction must be increased to reduce such heat loss. Equation 6.1 presents the thermal resistance for axial conduction through the combustor wall:

$$R_{Axial_Conduction} = \frac{\Delta Z}{k \cdot A} \qquad (6.1)$$

where Δz is the streamwise distance, k is the wall thermal conductivity, and A is the cross-sectional area of the combustor wall. Thermal resistance could be increased in three ways: (a) by reducing the cross-sectional area, (b) by reducing the thermal conductivity, or (c) by increasing the length of the combustor wall. The cross-sectional area of the combustor could be reduced by decreasing the wall thickness, t. Low thermal conductivity materials, such as ceramics, could be used to reduce the thermal conductivity of the wall. Increase in the combustor wall length is less desirable because it would increase the size and hence, decrease the power density of the system. Section 6.1.1 and 6.1.2 present the effects of wall thickness and wall thermal conductivity on combustor performance.

6.1.1 Combustor Wall Thickness (t)

Smaller wall thickness is expected to improve the system performance by reducing the cross-sectional area available for axial conduction, increasing thermal resistance, and reducing heat transfer to the exterior surface. Smaller wall thickness would also decrease the distance between the combustor and annulus and hence, reduce resistance for radial conduction to potentially increase heat recirculation. Combustor wall thickness could also change the combustor wall temperature, affecting radiation heat transfer in the preheating annulus. Understanding of these coupled effects is required to determine the optimal thickness for the combustor wall.

The combustor wall thickness was varied from 0.5 mm to 3.5 mm. The cross-sectional area in the preheating annulus was kept constant for all cases to maintain a constant bulk velocity of the reactants in the annulus. For each case, the reactant velocity was V_{in} = 1.0 m/s and the equivalence ratio was Φ = 0.50.

In Chapter 5, we found that heat loss to the surroundings was 10.0 % of the HRR for the baseline case with t = 3.5 mm. Approximately 60 % of the heat loss was attributed to axial conduction through the combustor wall. Changing the combustor wall thickness from 3.5 mm to 0.5 mm decreases the cross-sectional area by a factor of eight and, hence, increases the resistance to axial conduction by a factor of eight. One might expect that increasing the thermal resistance by a factor of eight would correspondingly decrease the contribution of axial conduction to overall heat loss from 6.0 % to 0.75 % of the HRR and hence, reduce heat loss to the surroundings from 10.0 % to 4.75 %. However, Fig 6.1 shows that decreasing the combustor wall

thickness from 3.5 mm to 0.5 mm reduced the percent heat loss to the surroundings from 10.0 % to 8.6 % of the HRR. Although smaller combustor wall thickness decreased heat loss to the surroundings, the magnitude of the reduction was less than expected. Thus, detailed heat transfer analysis was performed to understand and explain the behavior.

Temperature profiles in the midplane of the combustor wall, presented in Fig. 6.2, show two important effects of varying the wall thickness. First, the temperature gradient near the lid (z = 60 mm) increased as the combustor wall was made thinner. According to Equation 5.9, the axial conduction to the lid decreased from 30 W for t = 3.5 mm to 9 W for t = 0.5 mm, a factor of three reduction, instead of the factor of eight if the temperature gradient were unaffected. Second, Fig. 6.2 shows that the combustor wall temperature increased as wall thickness was reduced. Higher wall temperature increased radiation across the preheating annulus and hence, heat loss through the outer wall.

Figure 6.3 presents the radiation heat flux on the outer wall in the preheating annulus. The rate of heat transfer by radiation increased from 29 W to 49 W as the wall thickness was reduced from 3.5 mm to 0.5 mm. This increase in radiation heat transfer explains the modest decrease in heat loss to the surroundings as the wall thickness was reduced.

These results indicate that decreasing the combustor wall thickness reduced heat loss by axial conduction. However, thinner walls increased the combustor wall temperature and hence, increased heat loss by radiation. The net effect of reducing

the combustor wall thickness was modest, slightly reducing the overall heat loss to the surroundings. However, a thinner wall combined with other modifications to reduce radiation could decrease heat loss to the surroundings and improve thermal performance of the mesoscale, heat recirculating combustor design. The thermal conductivity of the combustor walls could be tailored to reduce heat loss to the surroundings by increasing the resistance to conduction in both the axial and radial directions. The effects of decreasing the combustor wall thermal conductivity are presented in the next section.

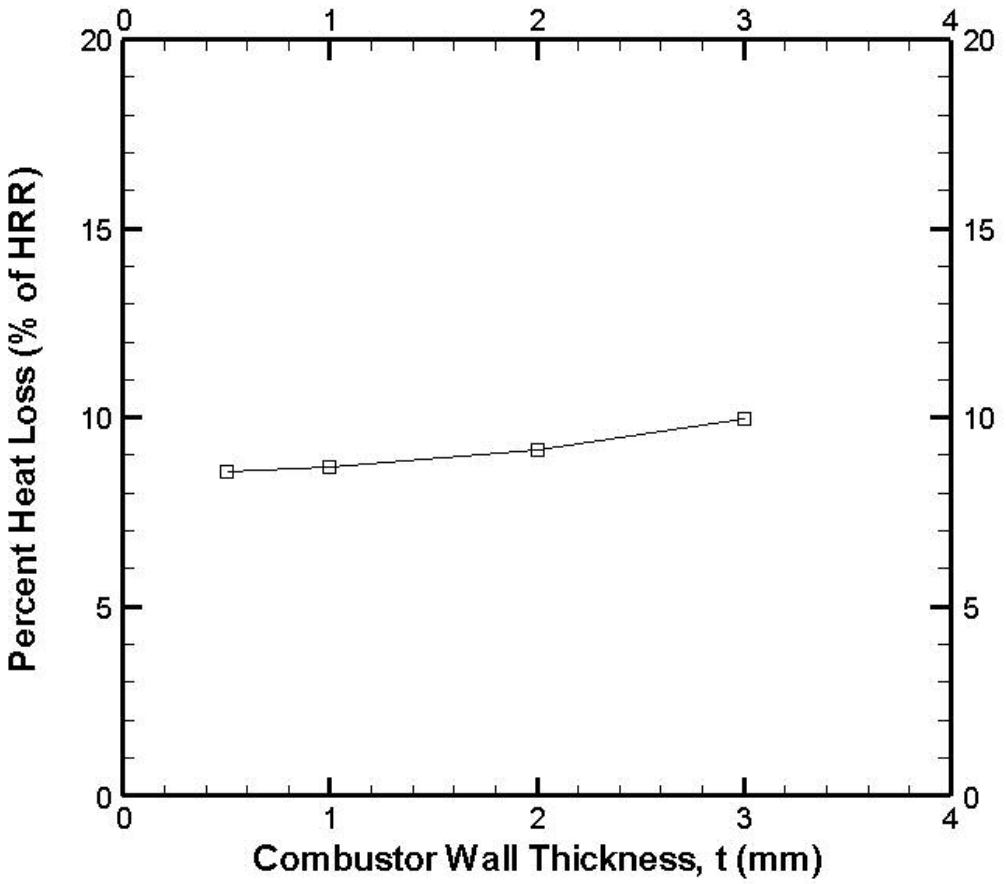

Figure 6.1. Effect of combustor wall thickness on heat loss to the surroundings.

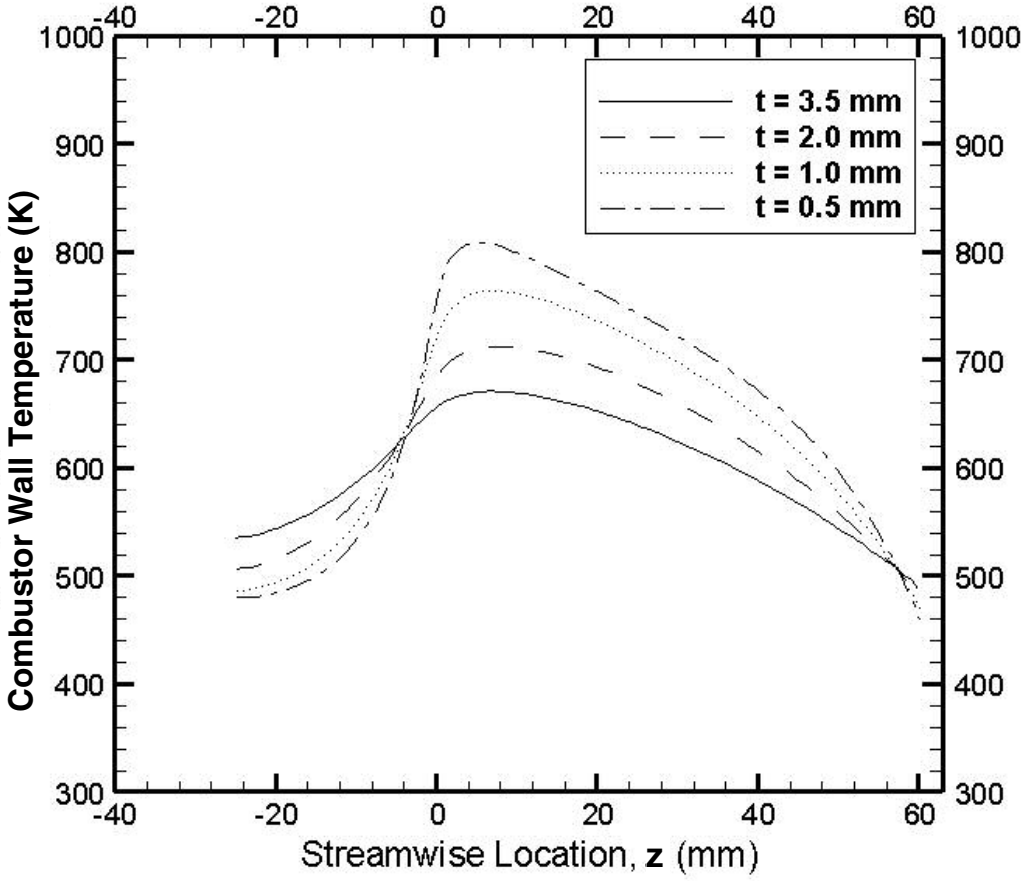

Figure 6.2. Effect of wall thickness on temperature at the midplane of the combustor wall.

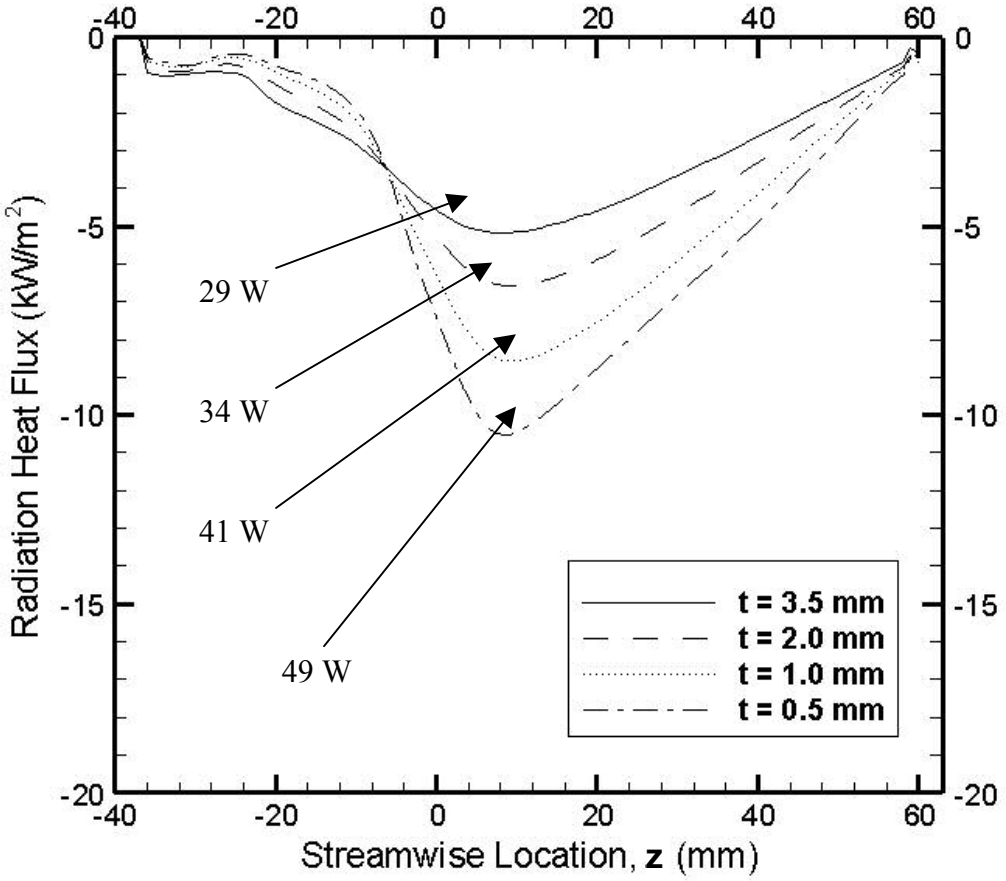

Figure 6.3. Effect of combustor wall thickness on radiation heat flux on the outer wall of the annulus.

6.1.2 Combustor Wall Thermal Conductivity (k)

As described above, axial heat conduction is an important source of heat loss in combustor design. The combustor wall was made of a high thermal conductivity material, stainless steel. Lower conductivity materials, such as ceramics, could increase thermal resistance according to Equation 6.1. The thermal conductivity of the walls was reduced from the baseline value of 21.5 W/m.K to 1.0 W/m.K. The reactant flowrate was V_{in} = 1.0 m/s, the equivalence ratio was Φ = 0.50 and t = 3.5 mm.

Reducing the thermal conductivity of the combustor walls from 21.5 W/m.K to 1.0 W/m.K increases the resistance to axial conduction by a factor of 21.5. Hence, the contribution of axial conduction to heat loss could decrease from 6.0 % to 0.3 % and the total heat loss to the surroundings could potentially be reduced from 10.0 % to 4.3 %. Figure 6.4 shows that heat loss decreased from 10.0 % for k = 21.5 W/m.K to 8.5 % for k = 1.0 W/m.K. Thus, the effect of combustor wall thermal conductivity on heat loss to the surroundings was marginal, similar to that of combustor wall thickness.

Figure 6.5 presents temperature profiles at the midplane of the combustor wall (r = 11.75 mm) for various wall thermal conductivities. The effects of thermal conductivity were similar to that of wall thickness discussed in the previous section. The temperature gradient near the combustor lid increased as the conductivity decreased. The axial conduction to the lid decreased from 30 W at k = 21.5 W/m.K to 3 W at k = 1.0 W/m.K. However, the combustor wall temperature increased as k

was reduced. The higher combustor wall temperature increased radiation heat flux across the preheating annulus from 29 to 42 W, as seen in Fig. 6.6.

Decreasing the wall thermal conductivity had similar effects as decreasing the combustor wall thickness. Both reduced heat loss by axial conduction, but increased radiation heat flux in the annulus, yielding a modest decrease in the overall heat loss to the surroundings. These results indicate that a combustor wall of smaller thermal conductivity material could be used to reduce heat loss when combined with a technique for reducing heat loss by radiation. In order to simultaneously reduce heat loss by radiation and axial conduction, multiple materials with varying thermal conductivities could be employed. One such example is presented in the next section.

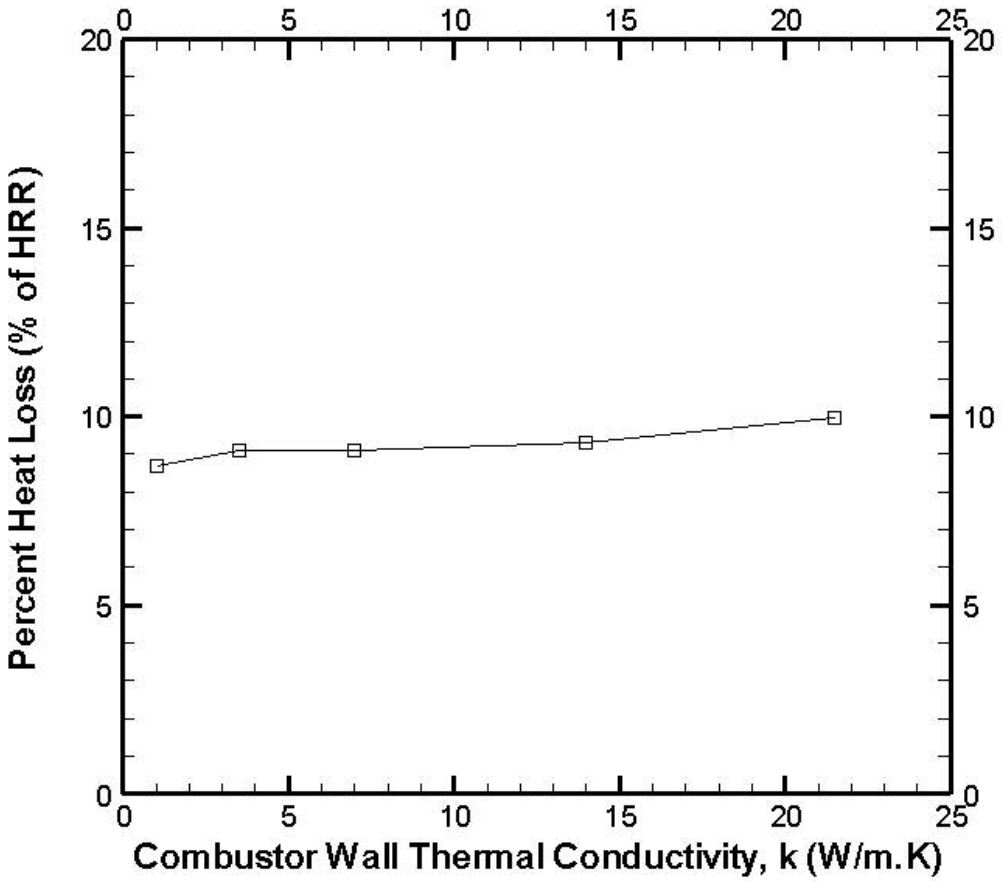

Figure 6.4. Effect of wall thermal conductivity (k) on heat loss to the surroundings.

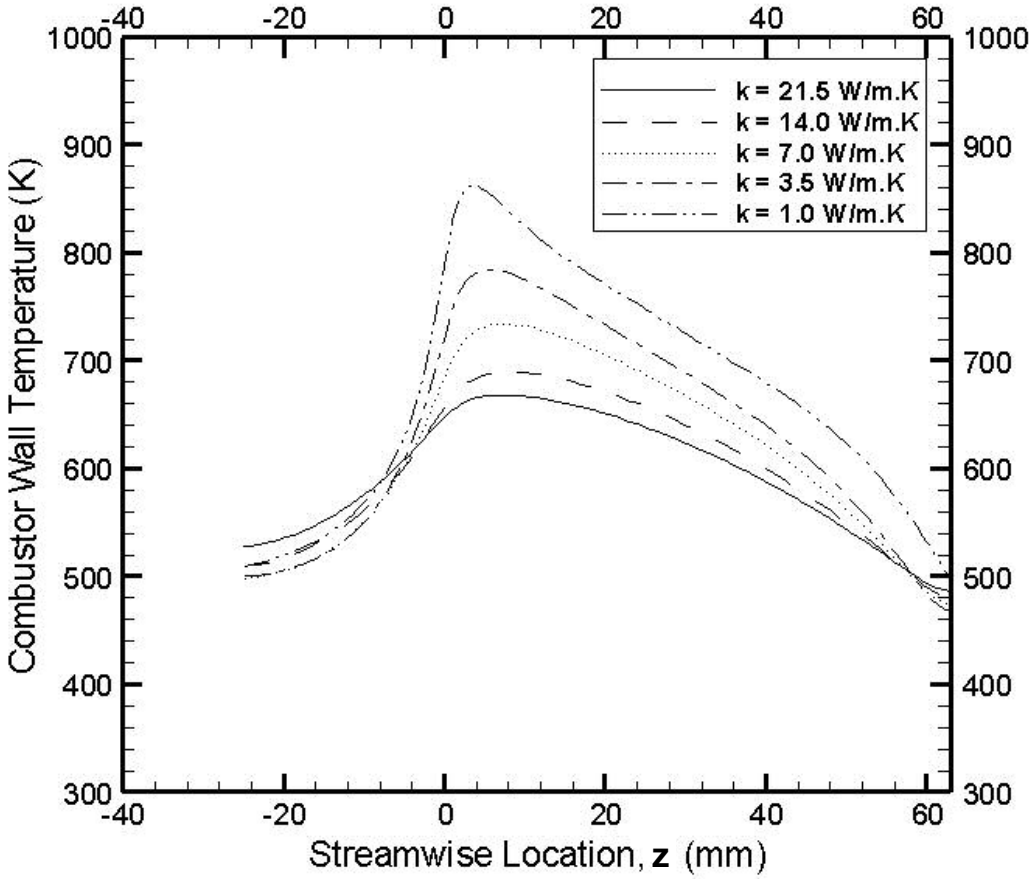

Figure 6.5. Effect of wall thermal conductivity on temperature at midplane of the combustor wall (r = 11.75 mm).

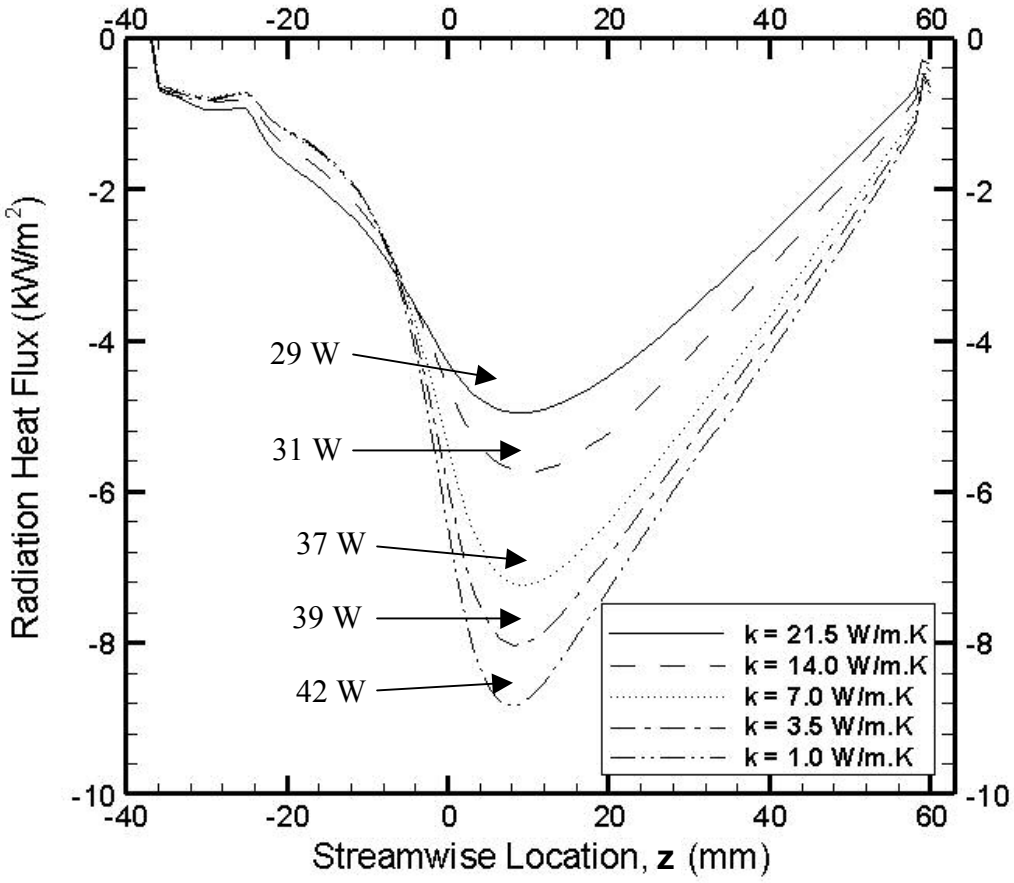

Figure 6.6. Effect of combustor wall thermal conductivity on radiation heat flux on the outer wall of the annulus (r = 17.0 mm).

6.1.3 Lid Thermal Conductivity (k_{lid})

In the previous section, the thermal conductivity of the combustor wall was varied uniformly. More than one material with a range of thermal conductivity could improve the design further by strategically promoting conduction in some regions and reducing it in others. One potentially effective strategy would be to use a high thermal conductivity material for the combustor wall and a low thermal conductivity material for the lid. The high conductivity wall near the heat source zone would help to distribute heat along the combustor wall, creating a more uniform temperature profile. Such heat transfer would minimize regions of localized high temperature and hence, radiation heat transfer across the annulus. Moreover, the low thermal conductivity lid would reduce axial conduction.

The combustor lid was defined as the region from z = 60 mm to z = 63 mm, as illustrated in Fig. 6.7. The reactant velocity was V_{in} = 1.0 m/s, the equivalence ratio was Φ = 0.50, and t = 3.5 mm. Figure 6.8 presents the percent heat loss for various lid thermal conductivities. For k_{Lid} = 0.5 W/m.K the heat loss was 8.1 % compared 10.0 % for k_{Lid} = 21.5 W/m.K. Interestingly, reducing the lid thermal conductivity from 21.5 W/m.K to 1.0 W/m.K reduced heat loss to the surroundings more than that for reducing the entire combustor wall thermal conductivity by the same amount. Hence, strategic use of materials of different thermal conductivity helps improve the design by reducing heat loss to the surroundings.

Figure 6.9 presents temperature contours for k_{Lid} = 0.5 W/m.K and 21.5 W/m.K. The temperature gradient across the combustor lid was much greater for the

lower thermal conductivity material, making the exterior surface temperature lower and reducing heat loss.

Figure 6.10 presents the temperature at the midplane of the combustor wall (r = 11.75 mm) for various lid thermal conductivities. Decreasing the lid thermal conductivity increased the combustor wall temperature. However, effect on peak temperature was less significant compared to that observed when decreasing the wall thickness or thermal conductivity, as discussed in the previous sections. Hence, high temperature peaks which promote radiation heat transfer were reduced. The temperature gradient near the lid decreased as the lid thermal conductivity was reduced. The total axial conduction at z = 60 mm decreased from 30 W at k_{Lid} = 21.5 W/m.K to 8 W at k_{Lid} = 0.5 W/m.K.

Figure 6.11 presents the radiation heat flux on the outer wall of the preheating annulus (r = 17.0 mm). As the lid conductivity was reduced from 21.5 W/m.K to 0.5 W/m.K, the radiation heat transfer increased from 29 W to 39 W. Figure 6.12 presents the exterior surface temperature profiles for various lid thermal conductivities. As k_{Lid} was reduced, the exterior surface temperature decreased, especially nearby the lid. In the center region of the combustor, radiation heat transfer increased because of the rise in the exterior surface temperature near z = 0 mm.

Results indicate that thermal conductivity should be selectively employed to optimize system performance. In particular, high thermal conductivity materials should be used to distribute heat and eliminate localized high temperature regions

with dominant radiation heat transfer. Low thermal conductivity materials should be used to reduce axial conduction to exterior surfaces. This analysis shows that a low thermal conductivity lid would be ideal for limiting heat loss. The materials must however be able to withstand the harsh environment of the combustor. For a practical system, low conductivity ceramics such as alumina could be used. Alumina ($k = 3.0$ W/m.K) has been used in harsh combustion environments over extended periods of time [Van Roode et al., 1994].

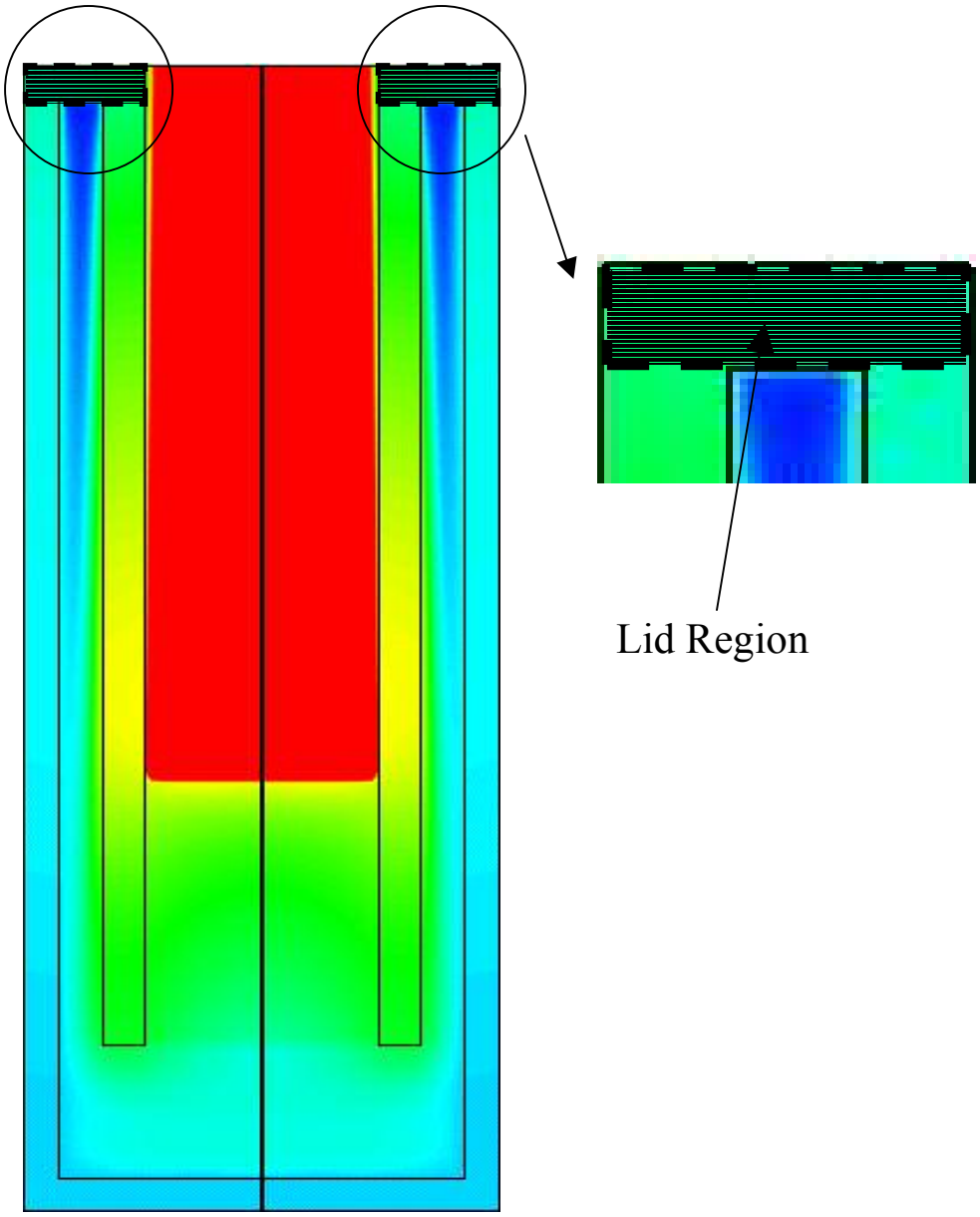

Figure 6.7. Illustration of combustor lid region.

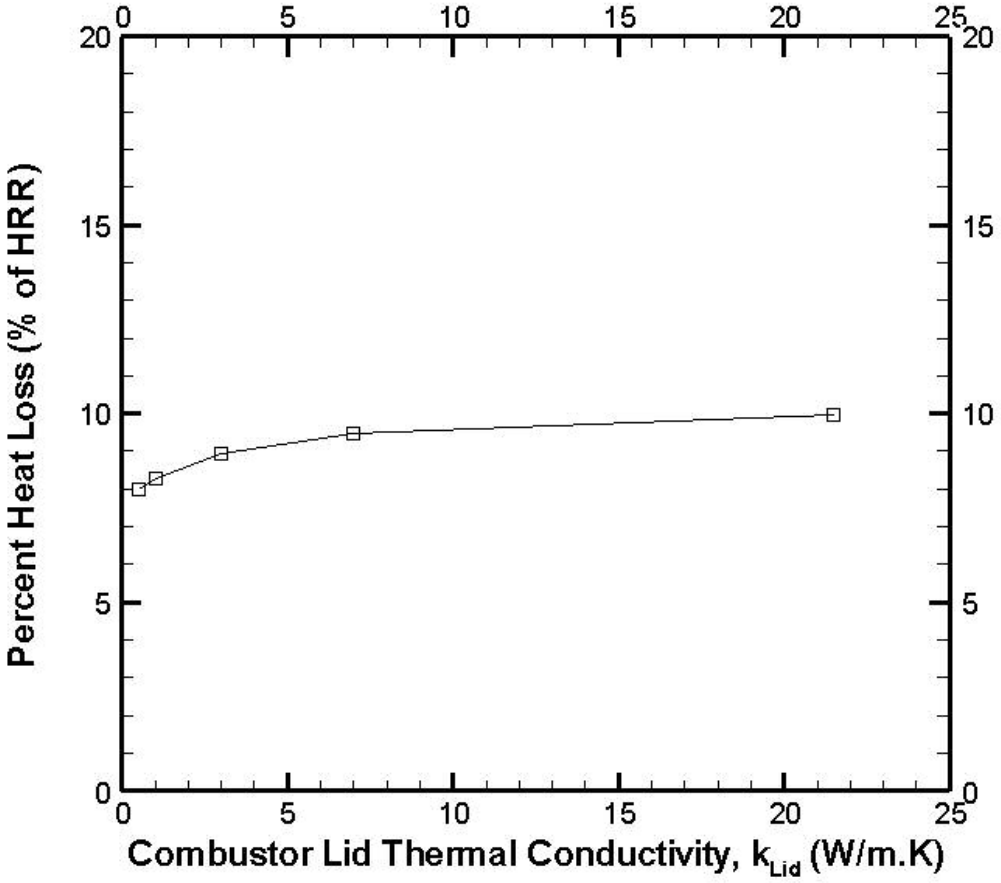

Figure 6.8. Effect of lid thermal conductivity on heat loss to the surroundings.

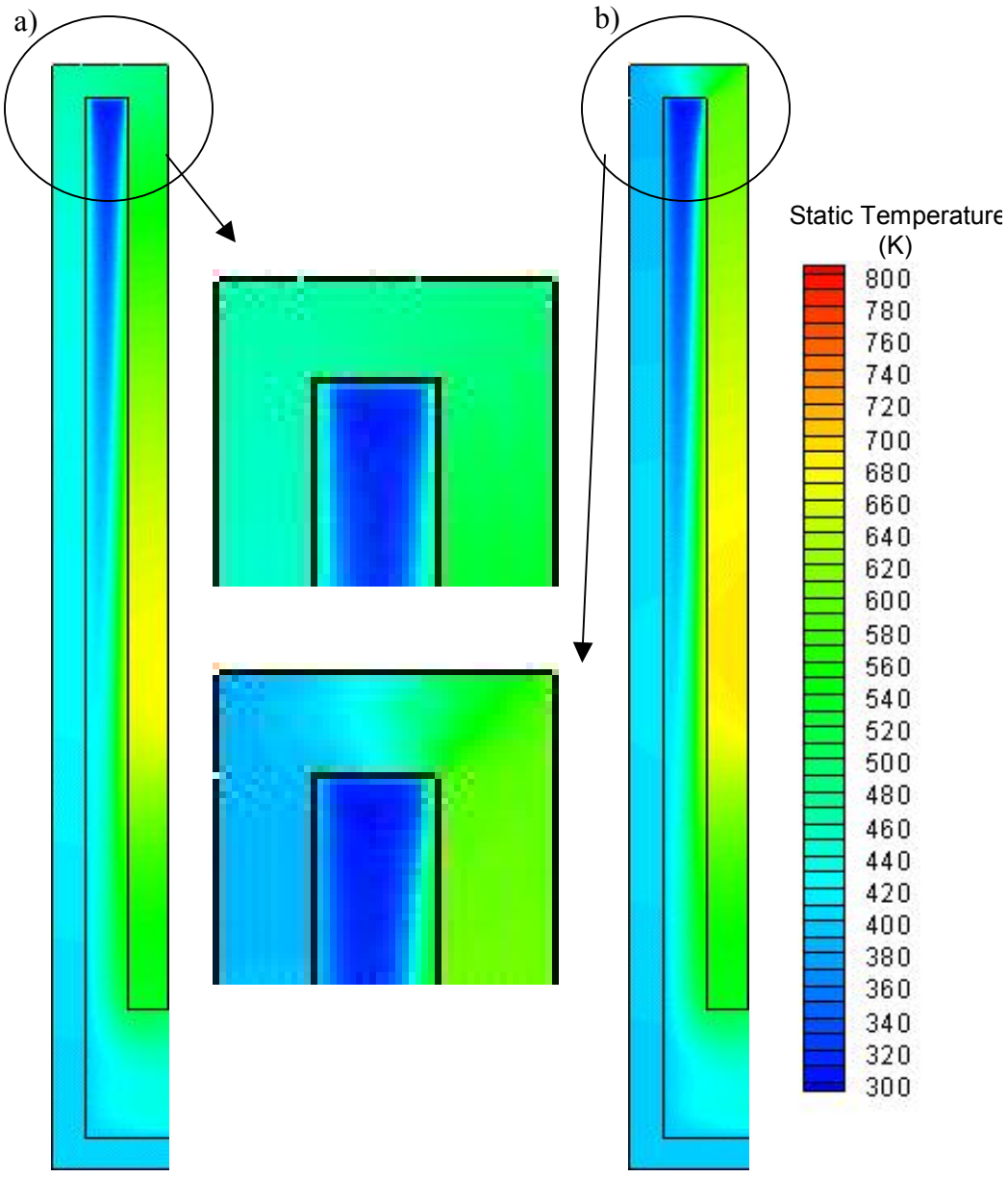

Figure 6.9. Temperature contours in the combustor wall, preheating annulus and outer wall for (a) k_{lid} = 21.5 W/m.K and (b) k_{lid} = 0.5 W/m.K.

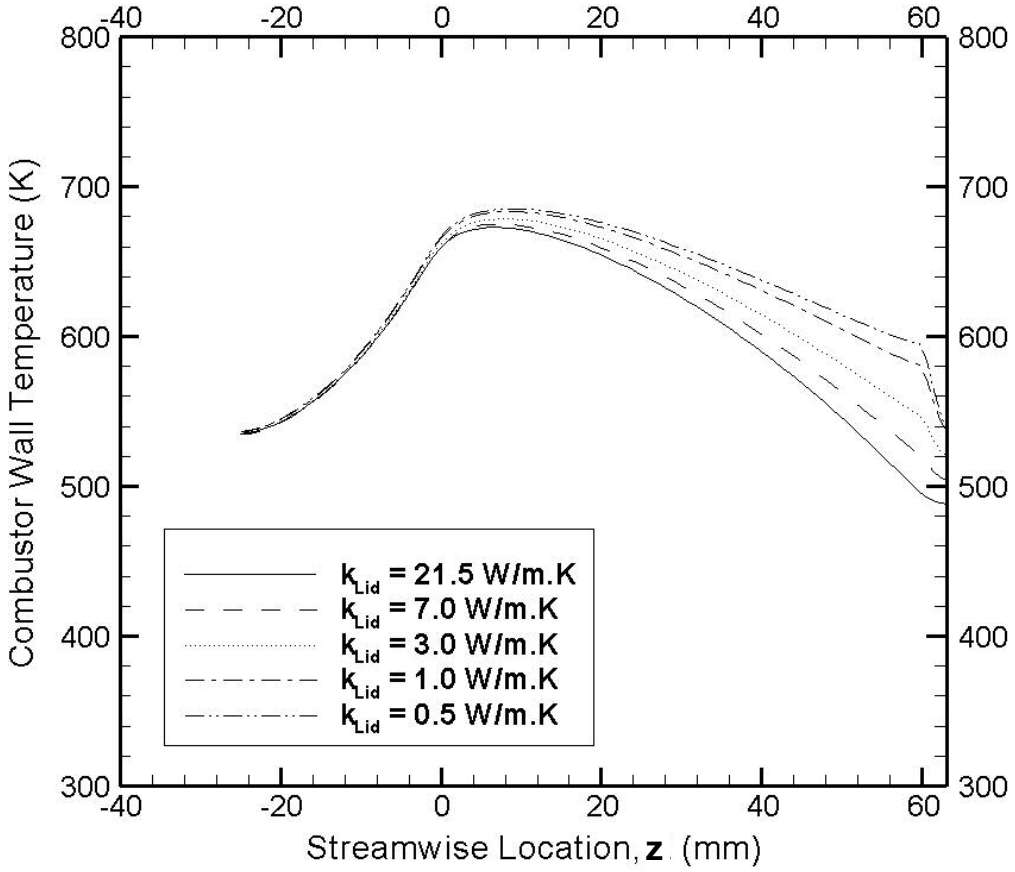

Figure 6.10. Effect of lid thermal conductivity on temperature at midplane of combustor wall (r = 11.75 mm).

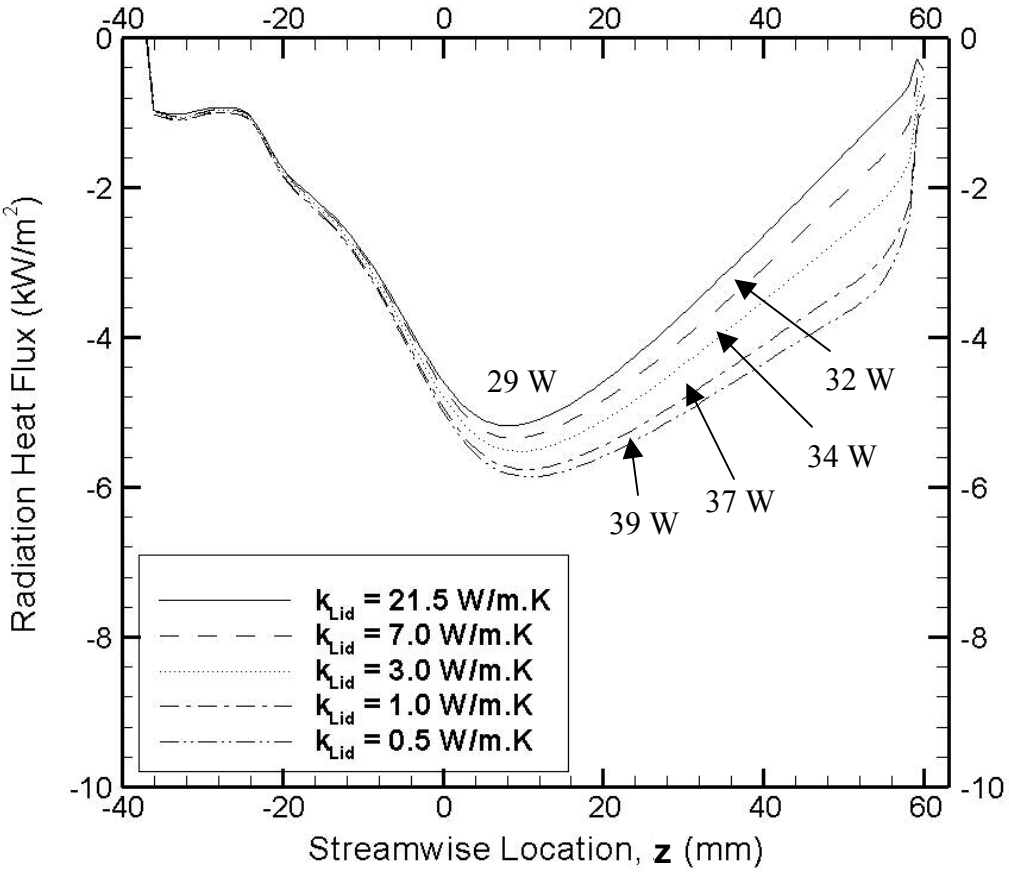

Figure 6.11. Effect of lid thermal conductivity on radiation heat flux on the outer wall of the annulus (r = 17.0 mm).

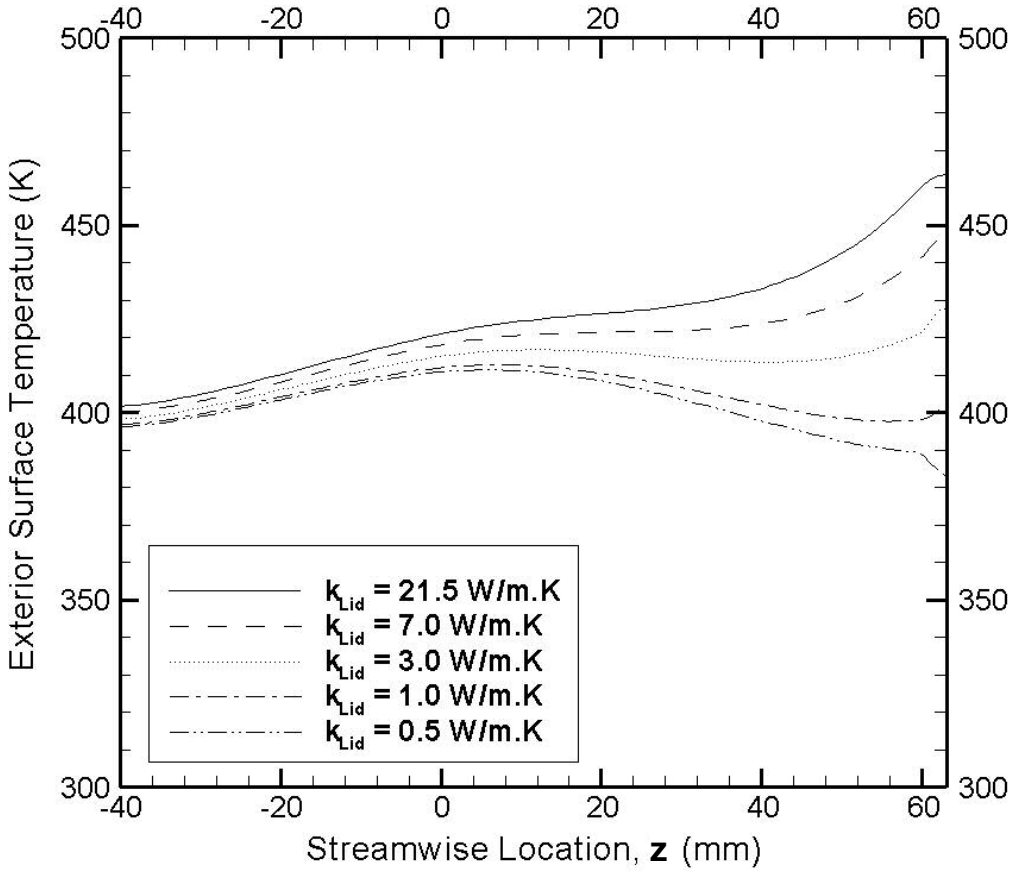

Figure 6.12. Effect of lid thermal conductivity on exterior surface temperature (r = 20.0 mm).

6.1.4 Conclusions

Three parameters to reduce axial conduction were investigated; combustor wall thickness, combustor wall thermal conductivity and lid thermal conductivity. All three methods significantly reduced heat loss by axial conduction. Reducing t and k created localized high temperature regions in the combustor wall, which promoted heat loss by radiation. Reducing k_{Lid} had a similar effect, but the peak temperature was less affected and hence, heat loss by radiation was less influenced. Based on these results, reduction in the lid thermal conductivity was the most effective method of reducing heat loss by axial conduction. All subsequent analyses will be performed with a high thermal conductivity (21.5 W/m.K) combustor wall and a low thermal conductivity (3.0 W/m.K) lid. Heat loss for the low conductivity lid was 9.0 % of the HRR. For practical considerations, the k_{comb} = 21.5 W/m.K material corresponded to stainless steel and the k_{Lid} = 3.0 W/m.K material corresponded to ceramic alumina. Other low thermal conductivity materials could be used for the lid to further reduce axial conduction. However, these materials must be proven to withstand extended use in the high temperature, oxidizing environment of the combustor.

6.2 Radiation Across the Preheating Annulus

Three methods to reduce radiation across the preheating annulus were investigated. Modifying the emissivity of the surfaces in the preheating annulus would directly reduce radiation heat exchange between the combustor wall and the outer wall. Filling the preheating annulus with a PIM would block radiation heat transfer across the annulus by absorbing incident radiation and transferring it to the reactants. Inserting a radiation shield into the preheating annulus would also block radiation and recirculate heat to the reactants. System performance was evaluated by examining the heat flux across the annulus and heat loss to the surroundings. Conclusions drawn from these analyses served as the basis for the phase II combustor design, presented at the end of this Chapter.

6.2.1 Surface Emissivity

The optical properties of the surfaces in the preheating annulus could be used to reduce radiation and heat loss to the surroundings. If we approximate the heat recirculating combustor as two long (infinite) concentric cylinders, radiation heat transfer from the inner cylinder ("Comb") to the outer cylinder ("Out") is given by equation 6.2:

$$\dot{Q}_{1-2} = \frac{A_{Comb} \cdot \sigma \cdot (T_{Comb}{}^4 - T_{Out}{}^4)}{\frac{1}{\varepsilon_{Comb}} + \left(\frac{1-\varepsilon_{Out}}{\varepsilon_{Out}}\right)\left(\frac{r_{Comb}}{r_{Out}}\right)} \qquad (6.2)$$

where A_{Comb} is the surface area of combustor wall, σ is the Stefan-Boltzmann constant, T is the absolute temperature, ε is the surface emissivity, and r is the radius [Muneer, et al., 2003]. In order to minimize radiation heat transfer, we must decrease the emissivity of the combustor wall, the outer wall, or both. Since the quantity r_{Comb}/r_{Out} is less than unity, the effect of varying the combustor wall emissivity would be greater than the effect of varying the outer wall emissivity.

The surface emissivity of the combustor wall was varied from 0.00 to 1.00 while keeping the emissivity of the outer wall at $\varepsilon = 0.80$. Then, the surface emissivity of the outer wall was varied from $\varepsilon = 0.00$ to 1.00 while keeping the combustor wall emissivity constant at 0.80.

Figure 6.13 shows the effect of varying the wall emissivities on heat loss to the surroundings. As expected, decreasing the emissivity reduced heat loss to the surroundings. The effect of varying the combustor wall emissivity was greater than that of varying the outer wall emissivity, but the difference was very small. Heat loss to the surroundings decreased from 9.0 % to less than 6.0 % when the emissivity of the combustor or outer wall was changed from 1.00 to 0.00. Practically, surface emissivity of approximately 0.10 is achievable by using polished metals. Since the effects of varying the combustor wall and outer wall emissivities were nearly identical, only results of varying the combustor wall emissivity are presented.

Figure 6.14 presents streamwise temperature profiles at the combustor wall midplane (r = 11.75 mm) for various combustor wall emissivities. The wall temperature increased as the emissivity decreased and the temperature gradient near

the lid increased as well. Axial conduction to the lid increased from 28 W to 41 W over the range of emissivities from 1.00 to 0.00. Thus, reducing the combustor wall emissivity increased heat loss by axial conduction.

Figure 6.15 presents streamwise profiles of radiation heat flux across the outer wall in the preheating annulus (r = 17.0 mm). Although the combustor wall temperature increased (as seen in Fig. 6.14), the radiation heat flux decreased because of the lower emissivity of the combustor wall. For a blackbody combustor wall, approximately 39 W of radiation occurred. As the combustor wall emissivity was reduced to 0.00, the radiation heat transfer decreased to only 1 W from the lid and base to the outer wall. Nearly identical trends were observed when keeping the combustor wall emissivity constant and varying the outer wall emissivity.

Figure 6.16 presents exterior surface temperature profiles for various combustor wall emissivities. The exterior surface temperature decreased as the emissivity decreased. The greatest reduction occurred in the post-flame zone (z = 10 mm), where radiation heat transfer was most significant.

These results indicate that the combustor wall and/or outer wall emissivities can be tailored to minimize heat loss from the heat recirculating combustor. In practice, we are limited by temperature and structural properties of the materials. In a combustion environment, surface emissivity often changes over time, affecting radiation. For example, a polished stainless steel combustor may have an initial emissivity of 0.10. Initial tests would yield little radiation and relatively low heat loss from the combustor. Over time, oxidation could build, increasing the emissivity to

0.80. This change would increase the radiation heat transfer and hence, heat loss to the surroundings. Therefore, radiation heat transfer over extended use should be considered when designing the heat recirculating combustor. Nevertheless, it would be possible to construct a combustor with low emissivity surfaces or coatings in the lower temperature regions, such as the outer wall of the preheating annulus, which can retain their properties over the lifetime of the combustor.

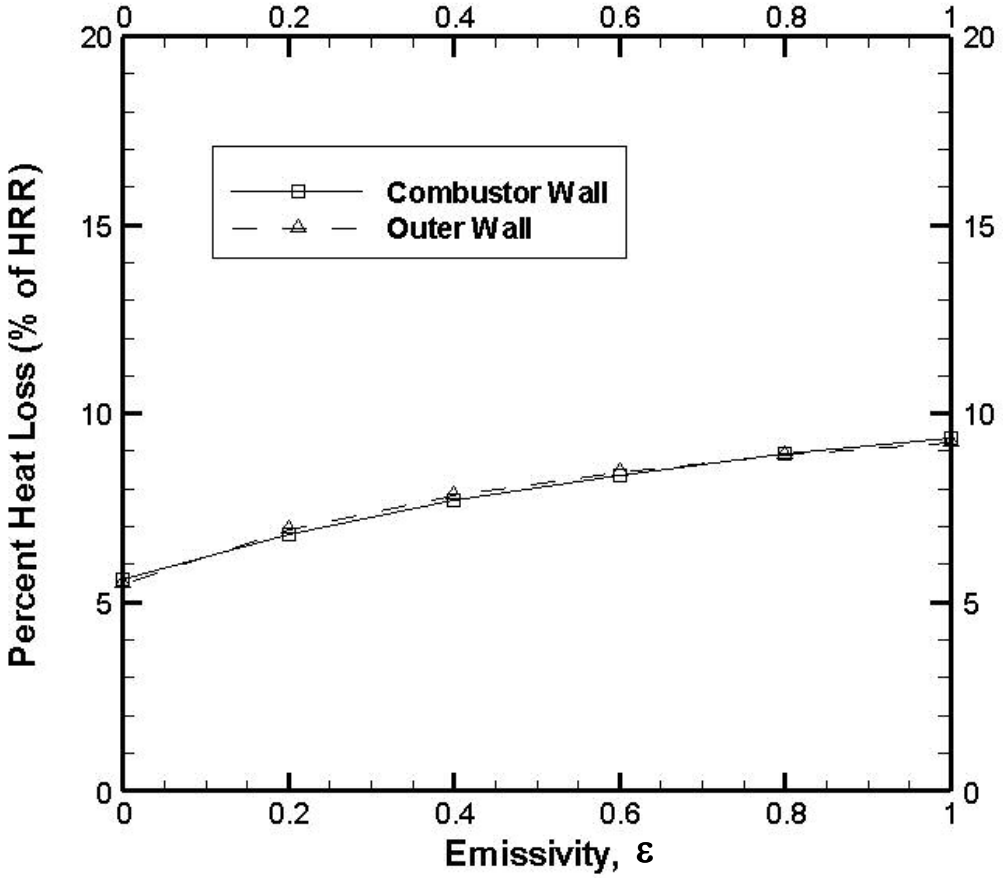

Figure 6.13. Effect of surface emissivity on percent heat loss to the surroundings.

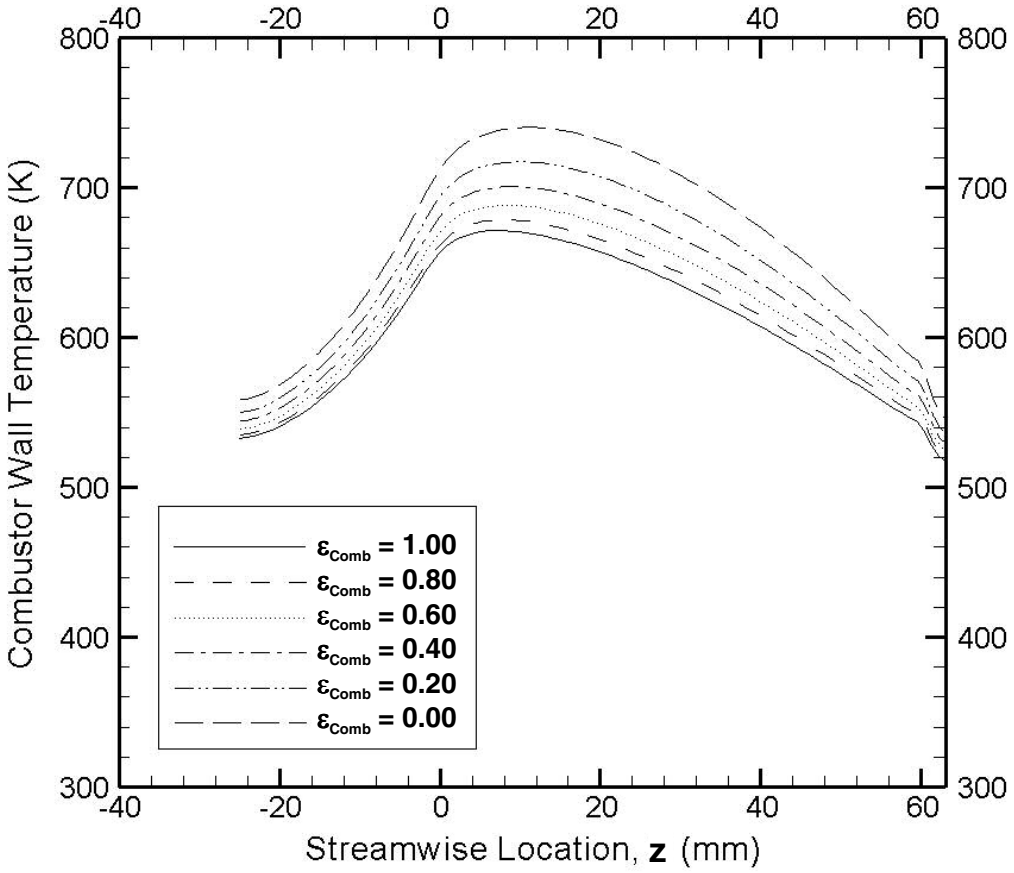

Figure 6.14. Effect of combustor wall emissivity on temperature at midplane of the combustor wall (r = 11.75 mm).

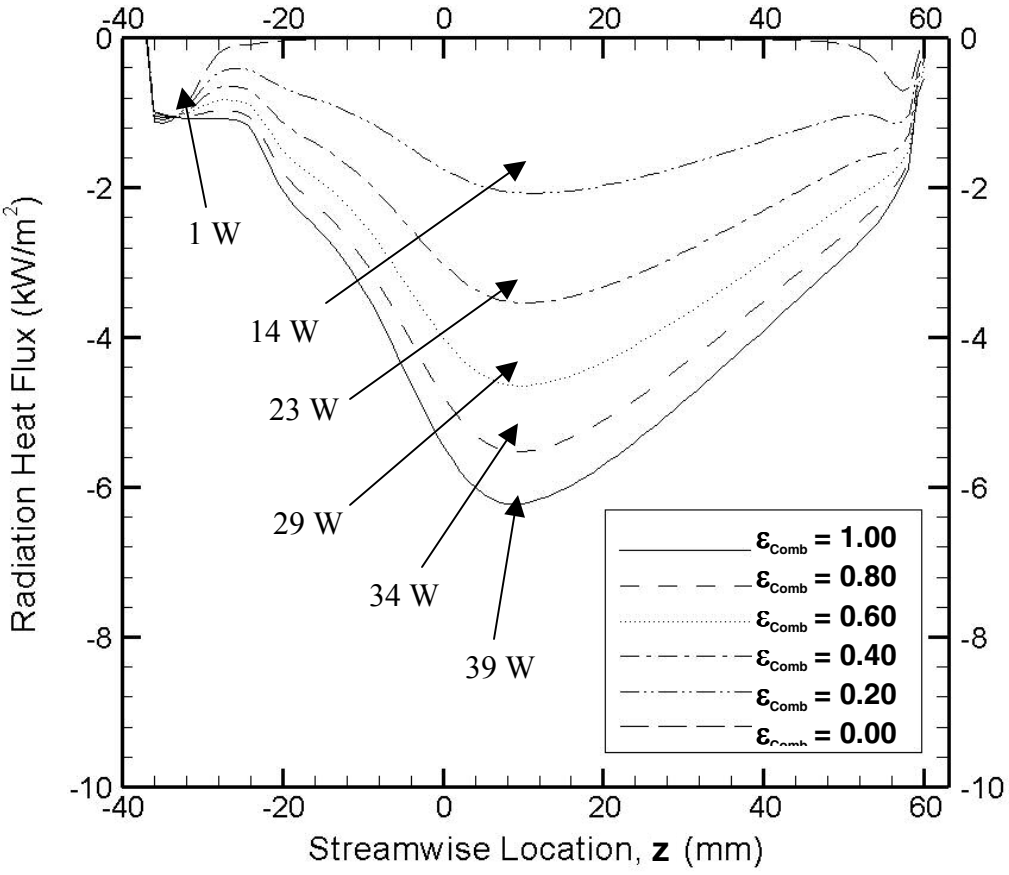

Figure 6.15. Effect of combustor wall emissivity on heat flux on outer wall of preheating annulus (r = 17.0 mm).

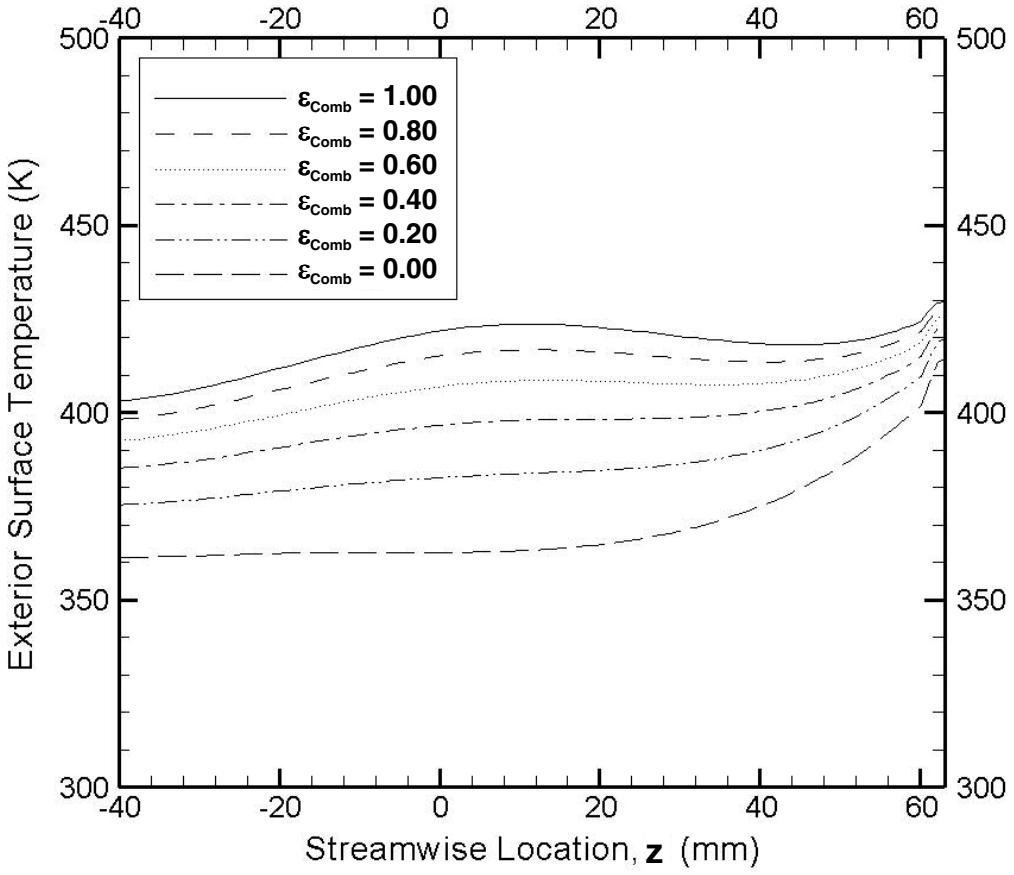

Figure 6.16. Effect of combustor wall emissivity on exterior surface temperature (r = 20.0 mm)

6.2.2 PIM in Preheating Annulus

PIM could be used to reduce radiation across the preheating annulus by adsorbing incident radiation and transferring it to the reactants through interfacial convection. Porous media would also, in effect, increase the surface area of the combustor wall and enhance convection heat transfer from the combustor wall to the reactants in the preheating annulus. This heat transfer would reduce axial conduction to the lid and hence, reduce heat loss to the surroundings. However, conduction through the solid PIM could create a new and significant mode of heat loss, radial conduction

The computational model described in Chapter 5 did not include physical blockage of the PIM. Thus, a PIM zone in the preheating annulus would affect conduction and convection heat transfer in the annulus, but not radiation. To approximate the effects of PIM on radiation, the adsorption coefficient of the fluid in the annulus was changed from 0.0 m^{-1} to 3200 m^{-1}, which was the average pore size of the flame stabilizing PIM used in the mesoscale combustion experiments, and a potential PIM for use in the annulus. The PIM porosity was taken as 0.80 and the viscous and inertial resistances were assumed to be the same as those for the flame stabilizing PIM. The thermal conductivity of the PIM was varied from 0.5 W/m.K to 21.5 W/m.K.

Figure 6.17 shows that heat loss to the surroundings increased with the addition of PIM to the annulus. Heat loss decreased as the thermal conductivity of

the PIM was reduced, but even at k_{PIM} = 0.5 W/m.K, heat loss was 10.6 %, compared to 9.0 % without PIM.

Figure 6.18 presents the combustor wall (r = 11.75 mm) temperature for various PIM thermal conductivities. Adding PIM to the annulus reduced the combustor wall temperature and increasing the conductivity of the PIM further decreased the combustor wall temperature. The temperature gradient near the lid was affected by the PIM thermal conductivity as well. Axial conduction decreased from 22.4 W with no PIM to 6.0 W with k_{PIM} = 21.5 W/m.K. The decreased axial conduction and lower combustor wall temperature were direct results of the increased heat transfer from the wall in the radial direction.

Figure 6.19 presents the radiation heat flux across the outer wall in the preheating annulus for various PIM thermal conductivities. The addition of PIM reduced radiation across the annulus from 34 W to less than 2.0 W for all cases with PIM. However, Fig. 6.20 shows that the total heat flux from the annulus to the outer wall increased significantly with the addition of PIM. Without PIM, the total heat transfer was 25 W from the combustor wall to the outer wall. The total heat transfer increased to 32 W with low thermal conductivity PIM and to 74 W with high thermal conductivity PIM. The effect of this new mode of heat transfer to the outer wall is seen in Fig. 6.21, where the exterior surface temperature profiles are presented. The reduction in axial conduction with the use of PIM is evident by the temperature difference between the cases with and without PIM at z = 60 mm. However, the increase in heat transfer across the annulus is also evident throughout the length of the

combustor as the exterior temperature increased for PIM of higher thermal conductivity. The limitations of the PIM model must be considered when analyzing these results. Contact resistance between the combustor wall, PIM and outer wall was not considered in the model. This resistance could be large and if so, radial conduction would be lower than the model predicts.

These results indicate that PIM is effective in simultaneously reducing axial conduction and radiation across the annulus. However, PIM introduced a new mode of heat loss, i.e. conduction across the annulus. The conduction heat transfer and hence, heat loss with PIM was higher than it was without PIM in the annulus. PIM may be beneficial when incorporated with a technique to reduce radial conduction, such as higher contact resistance with the outer wall.

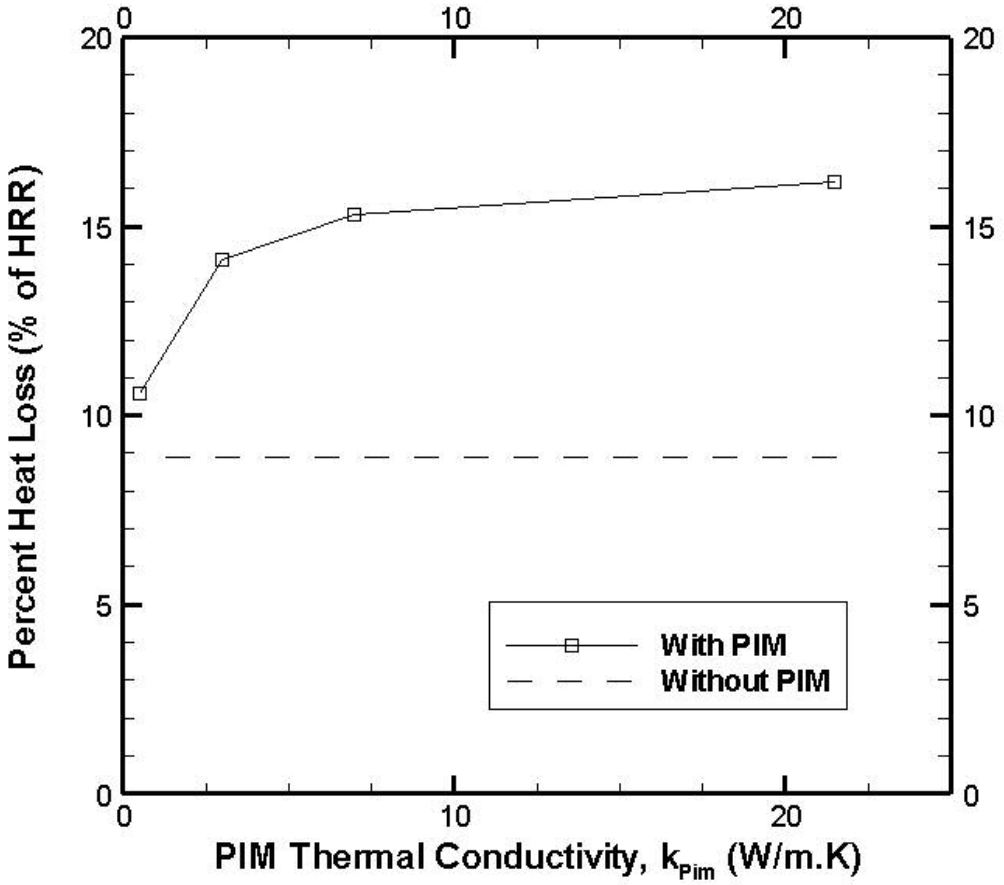

Figure 6.17. Effect of PIM thermal conductivity on heat loss to the surroundings.

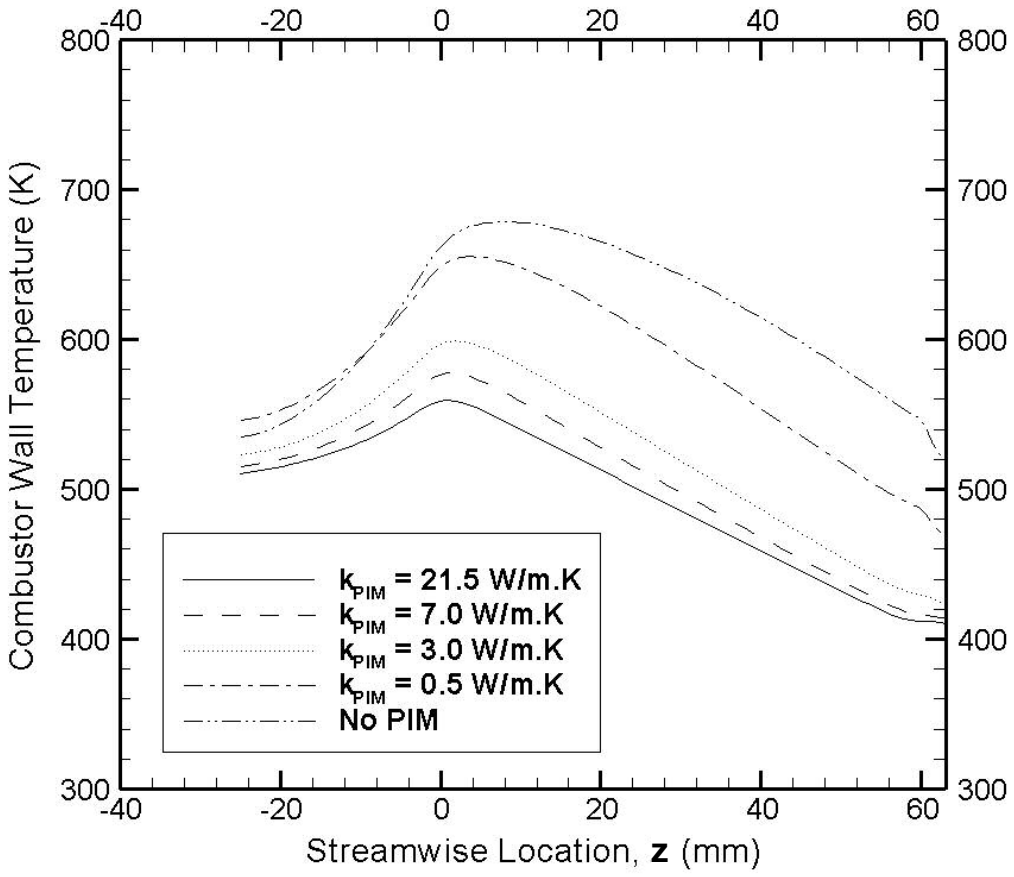

Figure 6.18. Effect of PIM thermal conductivity on temperature at midplane of the combustor wall (r = 11.75 mm).

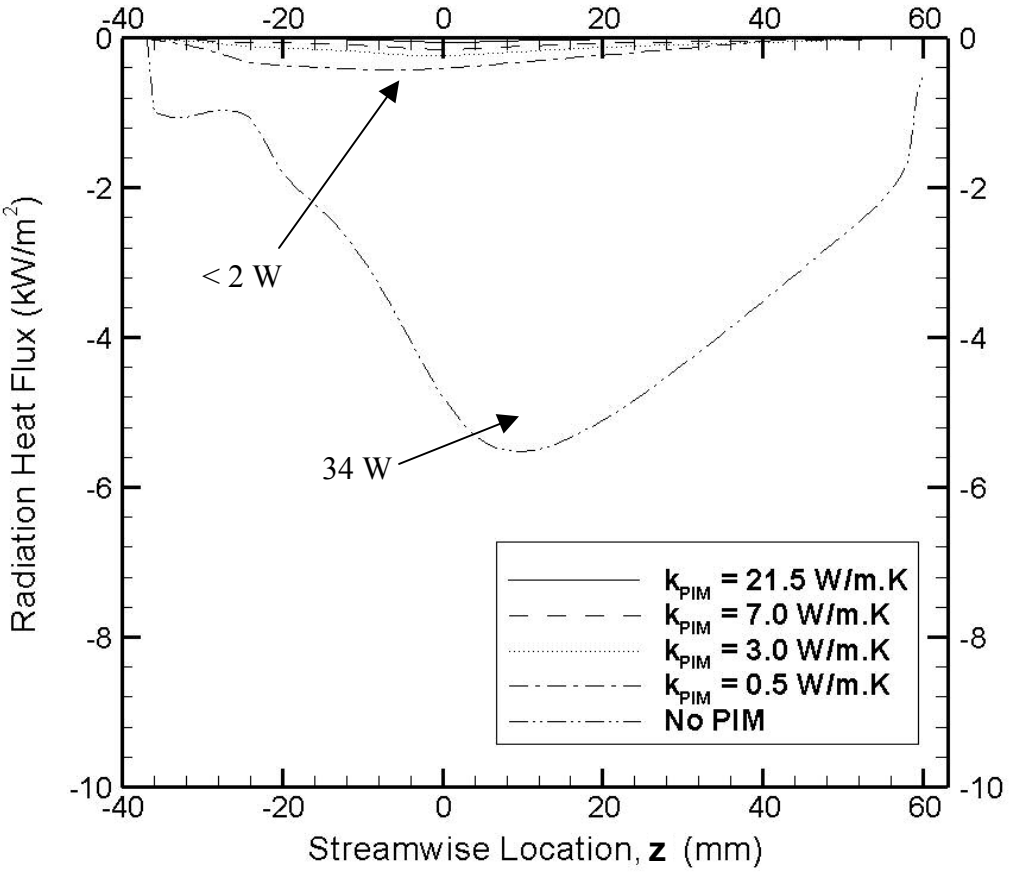

Figure 6.19. Effect of PIM thermal conductivity on radiation heat flux on outer wall of preheating annulus (r = 17.0 mm).

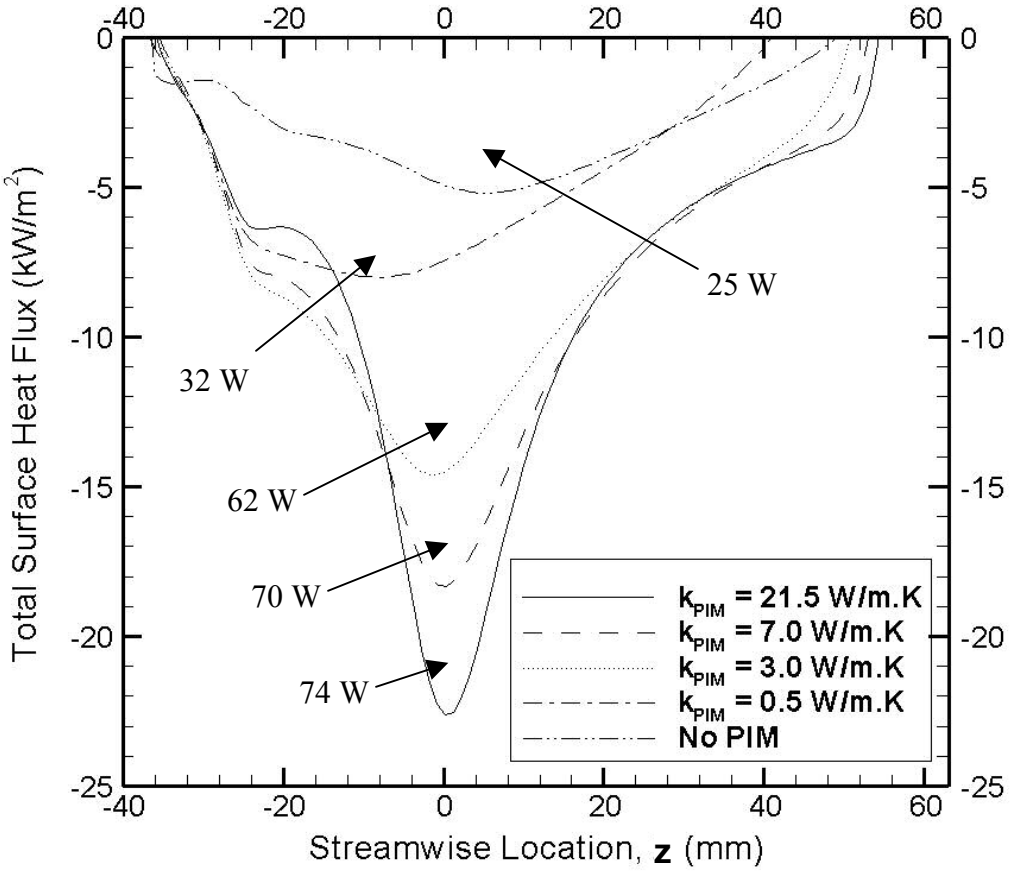

Figure 6.20. Effect of PIM thermal conductivity on total heat flux on outer wall of preheating annulus (r = 17.0 mm).

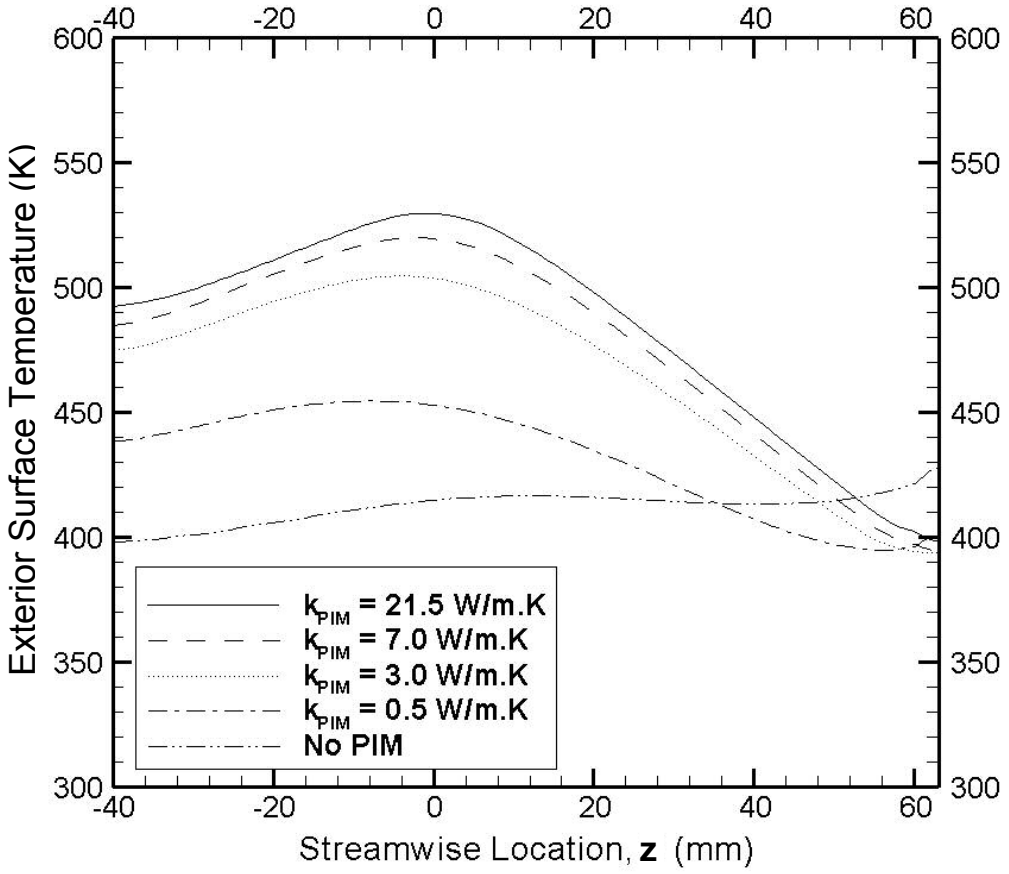

Figure 6.21. Effect of PIM thermal conductivity on exterior surface temperature (r = 20 mm).

6.2.3 Radiation Shield

A radiation shield in the annulus would block radiation from the combustor wall to the outer wall. However, unlike PIM the radiation shield would not affect heat conduction across the annulus. A radiation shield with the thermophysical properties of stainless steel was placed in the region from 15.5 mm < r < 16 mm and -25.0 mm < z < 55 mm, as seen in Fig. 6.22. The emissivity of the radiation shield was varied from 0.00 to 1.00 and the emissvity of oxidized steel, 0.80, was used for the combustor and outer walls. The reactant velocity was V_{in} = 1.0 m/s and the equivalence ratio was Φ = 0.50 for all cases.

Figure 6.23 presents heat loss with radiation shield of various emissivities. Without the radiation shield, system heat loss was 9.0 %. The addition of a blackbody radiation shield reduced heat loss to 8.0 % and a radiation shield with zero emissivity reduced heat loss to 6.0 % of the HRR.

Figure 6.24 presents streamwise temperature profiles at the midplane of the combustor wall (r = 11.75 mm). In general, the combustor wall temperature increased as the emissivity decreased. The effect of the radiation shield was greatest upstream of the heat source (z < 0 mm), where the wall temperature was significantly higher with the radiation shield. The temperature gradients near the combustor lid were relatively constant with and without the radiation shields. Without the shield, conduction to the lid was 23 W. Axial conduction increased from 21 W for a blackbody radiation shield to 28 W for a shield of zero emissivity. The coupled effect

of system heat transfer is apparent because reducing heat transfer across the annulus by radiation increased axial conduction.

Figure 6.25 presents the radiation heat flux at the outer wall in the preheating annulus (r = 17 mm). The radiation heat flux was significantly reduced from 34 W without a radiation shield to less than 9 W with a blackbody radiation shield. Radiation heat flux was further reduced to less than 5 W by decreasing the emissivity of the shield. The radiation heat flux for $-20 < z < 63$ mm was low, indicating that nearly all of the radiation was transferred from the shield to the reactants by convection. The temperature of the shield itself was not high enough to cause significant radiation. In the region $-40 \text{ mm} < z < -20$ mm, approximately 3 W of radiation from the combustor wall to the outer wall occurred. The radiation shield was not present in this region, allowing radiation from the combustor wall to the outer wall.

The effects of the radiation shield on heat loss can be seen in Fig. 6.26, where exterior surface temperature profiles are presented. The exterior surface temperature was reduced significantly with the use of a radiation shield. The exterior surface temperature was lower for radiation shields of lower emissivity.

These results indicate that an emissions shield in the preheating annulus can significantly reduce heat loss to the surroundings. Ideally, a low emissivity material would be used to minimize heat loss. A few practical challenges to implementing such a shield exist. The radiation shield was not attached to the combustor or outer wall for the axis-symmetric model used in this analysis. In practice, the radiation

shield should be attached to the combustor wall with a low conductivity, low cross-sectional area connector to minimize conduction to the radiation shield. Contact with the outer wall should be avoided to ensure that radial conduction does not occur. Such heat transfer would increase heat loss, as seen for analysis using PIM in the annulus.

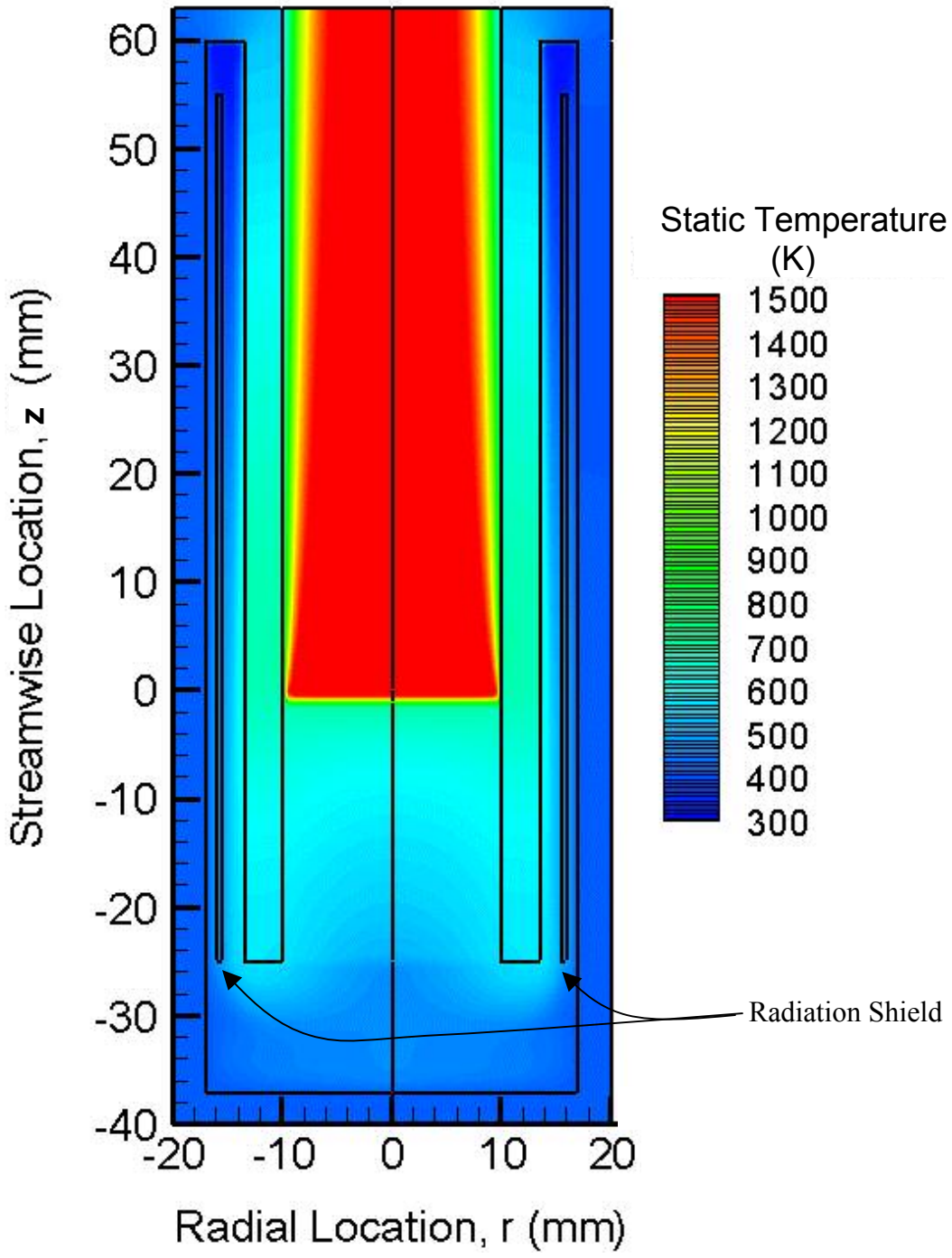

Figure 6.22. Temperature contours with radiation shield (ε_{Shield} = 1.00).

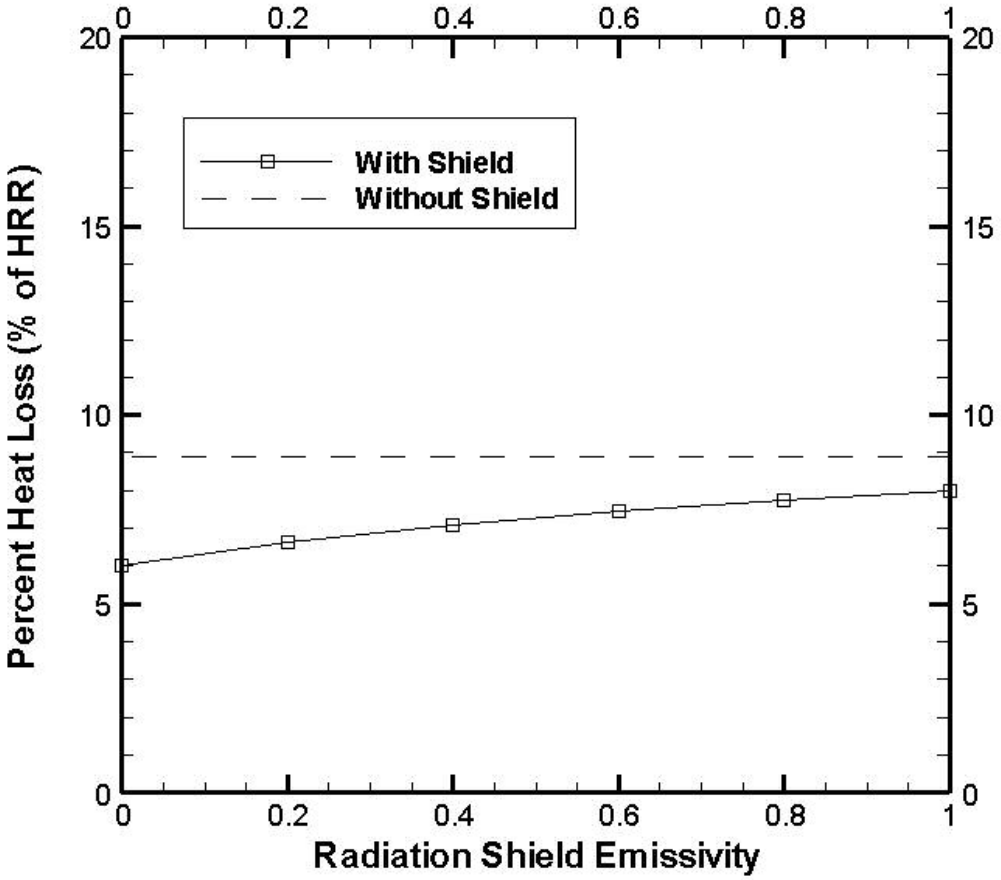

Figure 6.23. Effect of radiation shield emissivity on heat loss to the surroundings.

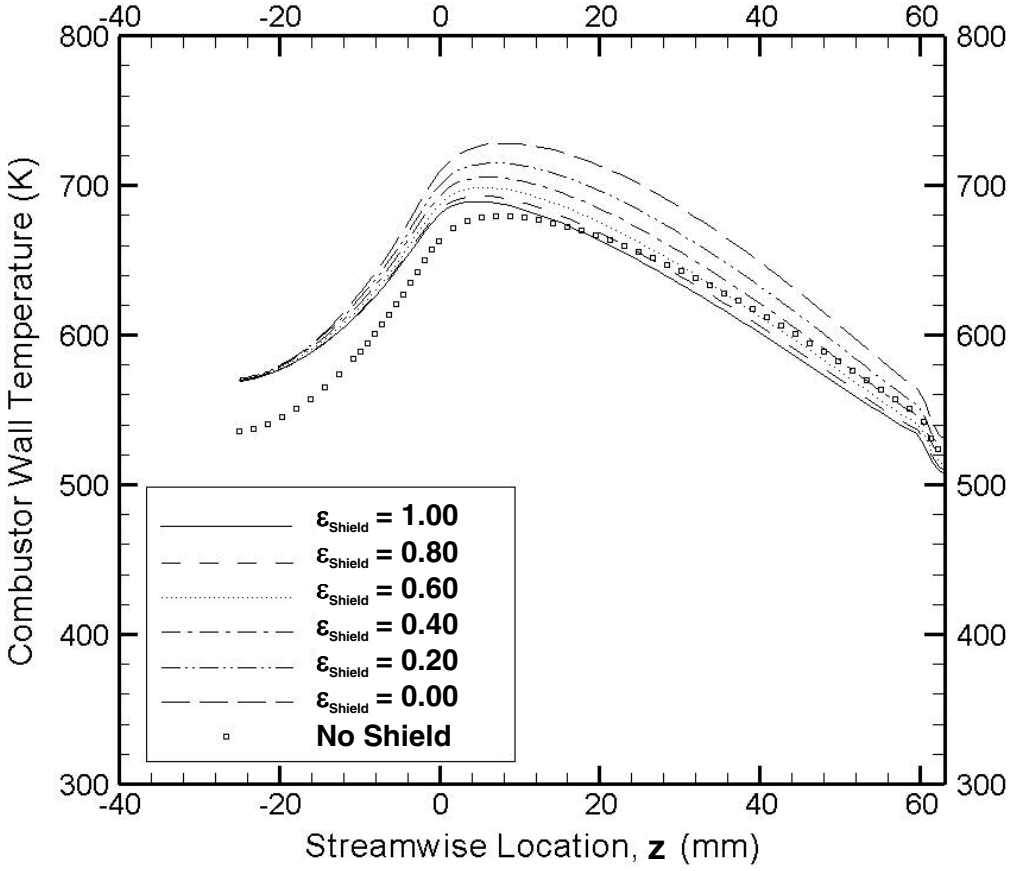

Figure 6.24. Effect of radiation shield emissivity on temperature at midplane of combustor wall (r = 11.75 mm).

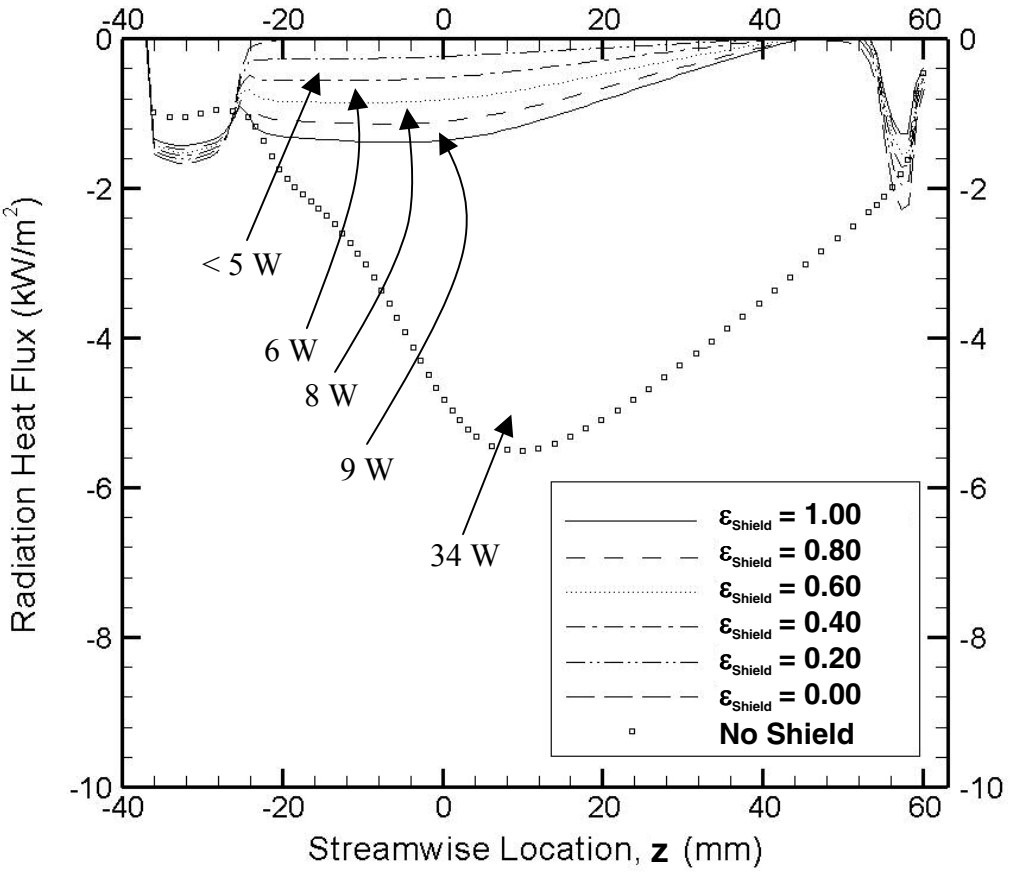

Figure 6.25 Effect of radiation shield emissivity on radiation heat flux on outer wall of preheating annulus (r = 17.0 mm).

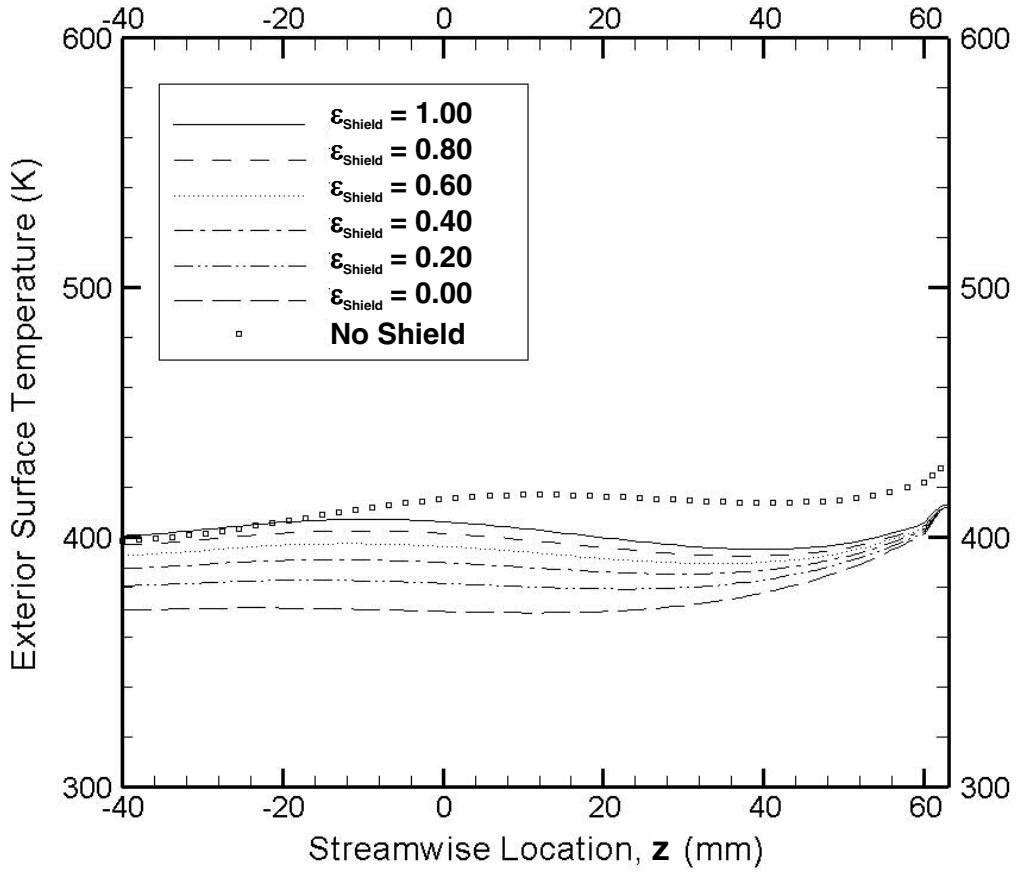

Figure 6.26 Effect of radiation shield emissivity on exterior surface temperature (r = 20.0 mm).

6.2.4 Conclusions

Three methods of reducing radiation heat transfer across the preheating annulus were investigated. Radiation was reduced by decreasing the surface emissivities of the combustor and/or outer wall. Although this technique was effective for reducing heat loss to the surroundings, practical implementation could be difficult. The high temperatures experienced within the annulus may cause oxidation of the combustor and outer walls, increasing emissivity over time. PIM in the preheating annulus nearly eliminated radiation from the combustor wall to the outer wall. However, PIM introduced a new mode of heat loss, i.e. radial conduction through the PIM. Heat loss to the surroundings significantly increased with PIM of any thermal conductivity. Radiation shield in the annulus was effective in reducing heat loss to the surroundings. The emissivity of the radiation shield was less critical than that of the combustor wall. Hence, a radiation shield is practically viable to reduce radiation, even after extended use. A low emissivity radiation shield was determined to be the most effective method of reducing radiation heat transfer. As a result, the phase II mesoscale design proposed in the next section will implement a radiation shield.

6.3 Proposed Phase II Combustor Design

Sections 6.1 and 6.2 show that the thermal performance of the heat recirculating combustor could be improved by varying the geometry and material properties to reduce axial conduction in the combustor wall and radiation across the annulus. When attempting to reduce heat loss, a tradeoff between axial conduction and radiation occurred due to the coupled nature of the system. Reducing heat loss by one mode increased heat loss by the other. Therefore, design changes aimed at simultaneously reducing axial conduction and radiation must be implemented together.

The most effective methods of reducing axial conduction were reducing the combustor wall thickness and reducing the combustor lid thermal conductivity. The most effective method of reducing radiation across the annulus was a low emissivity radiation shield in the preheating annulus. A phase II combustor design, which utilizes the findings from the parametric study, was developed. Details of the design and predictions of its performance are presented in this section.

6.3.1 Design Description

Two combustors designed for maximum HRRs of 100 W and 1000 W were developed. Combustor M100 (the 100 W system) was 11.0 mm in length with 11.0 mm diameter and combustor M1000 (the 1000 W system) was 26 mm long with 26 mm diameter. The combustion chamber featured PIM to preheat reactants and stabilize the flame. It was surrounded by a preheating annulus with radiation shield. Stainless steel was used for the combustor wall and ceramic alumina was used for the combustor lid to reduce axial conduction. The rationale for the combustor geometry sought to create the desired characteristics at the flame zone, combustor wall, preheating annulus and outer wall.

The macroscale PIM combustion experiments (Chapter 3) showed that LBO occurred at higher equivalence ratios as reactant flowrate was increased. At reactant cold flow velocities above 2.0 m/s, combustion could only be achieved at equivalence ratios greater than 0.70. Hence, V_{in} = 2.0 m/s was chosen to be the maximum reactant velocity based on ambient conditions. To balance the need for a high volumetric HRR, low pollutant emission and structural integrity, the maximum equivalence ratio was limited to 0.75. The corresponding maximum reactant flowrates were 0.0485 g/s and 0.485 g/s, respectively for combustors M100 and M1000. Based on these flowrates and V_{in} = 2.0 m/s, the combustion chamber diameters were 5.00 mm and 16.00 mm.

The parametric studies concluded that a thin, high thermal conductivity combustor wall should be used to reduce axial conduction and radiation across the

annulus. From a practical standpoint, stainless steel is simple to machine and it performed well for experiments discussed in Chapter 4. Hence, stainless steel was selected as the material of choice for the wall of the phase II mesoscale combustor. Wall thicknesses of 1.0 mm were chosen to ensure structural integrity.

The preheating annuli channel widths were 1.00 mm and 3.0 mm, for the M100 and M1000 combustors, respectively. These dimensions were chosen to keep the velocity in the preheating annulus relatively high for convection, but low enough to avoid large pressure loss. A stainless steel radiation shield was placed in the preheating annulus. The radiation shields were 0.05 and 0.10 mm thick, respectively for the M100 and M1000 combustors. The overall length of the system was selected to be the same as its outer diameter, 11.0 mm and 26.0 mm. The length of the PIM zones was two times the annulus channel width. The length of the heat source zone (flame length) was assumed to be independent of the combustor size and was 1.00 mm for both cases. The thermal conductivity of the alumina lid was taken as 3.0 W/m.K and stainless steel wall thermal conductivity was taken as 21.5 W/m.K. The emissivity of the combustor and outer wall was assumed to be 0.80, corresponding to oxidized steel. The radiation shield was assumed to have an emissivity of 0.20. Dimensions of the two designs are presented in Figs. 6.27 and 6.28.

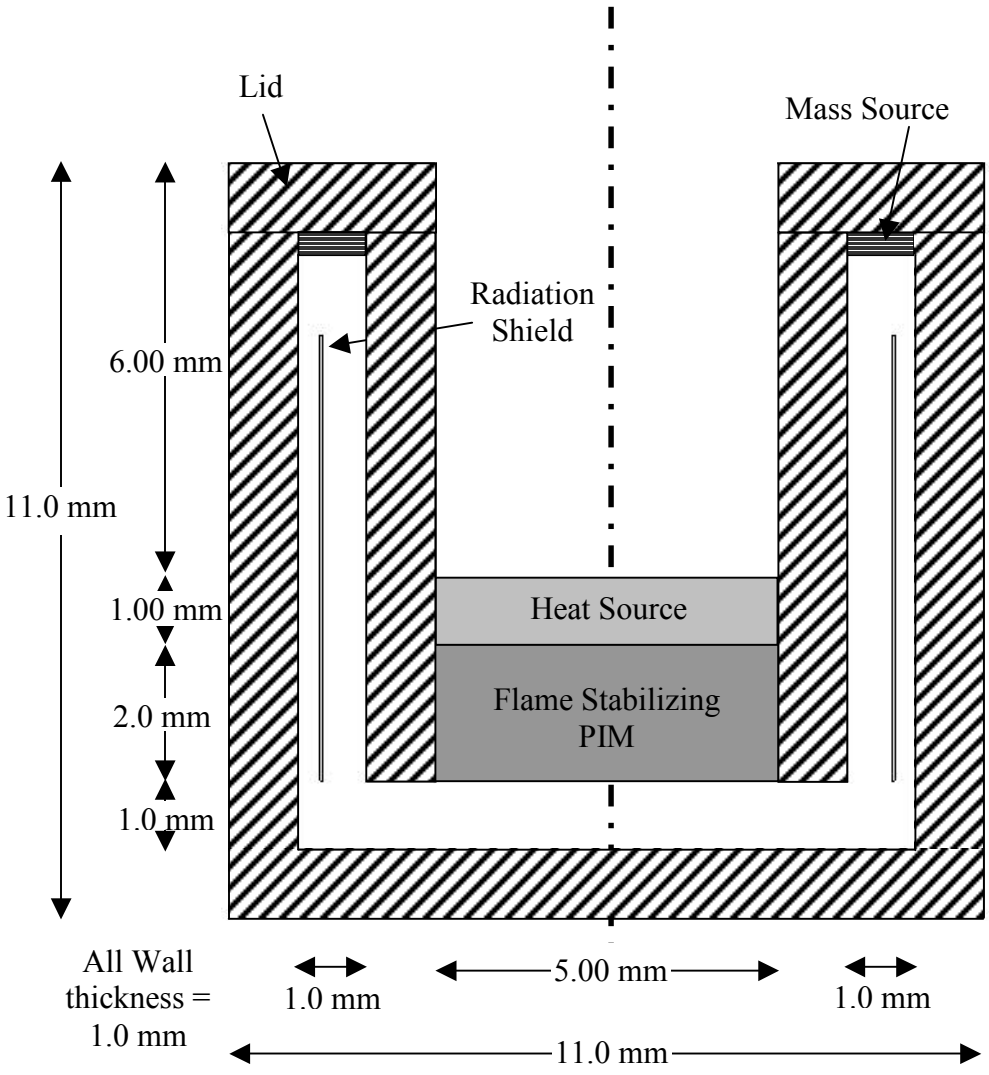

Figure 6.27. Proposed design for M100 mesoscale, heat recirculating combustor.

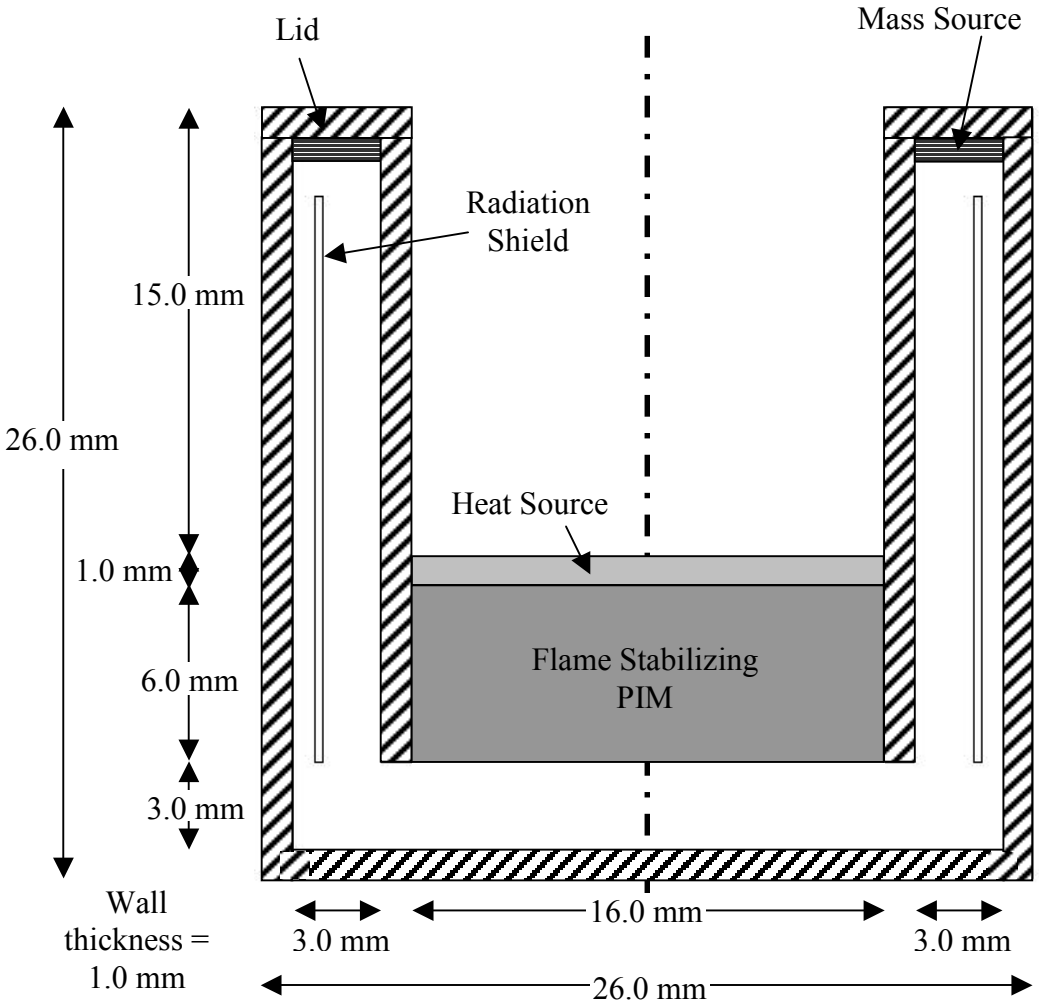

Figure 6.28. Proposed design for M1000 mesoscale, heat recirculating combustor.

6.3.2 Predicted Performance of Phase II Combustor Design

Analyses presented in sections 6.1 and 6.2 were performed at V_{in} = 1.0 m/s and Φ = 0.50. In practice, the combustor could be operated over a range of flow conditions. Hence, heat loss was computed at various flowrates and equivalence ratios. The findings were used to identify conditions that provided optimized thermal performance and those in which heat loss to the surroundings was high.

The predicted percent heat loss for the M100 and M1000 combustors are presented in Figs. 6.29 and 6.30. For the M100, heat loss of approximately 4.0 to 6.0 % of the HRR was predicted at V_{in} = 2.0 m/s. Heat loss increased to 30 % as the reactant flowrate decreased to V_{in} = 0.50 m/s. Heat loss increased with increasing equivalence ratio and it decreased significantly for the larger, M1000 combustor. The effects of flowrate, equivalence ratio and combustor size are presented in the following sections.

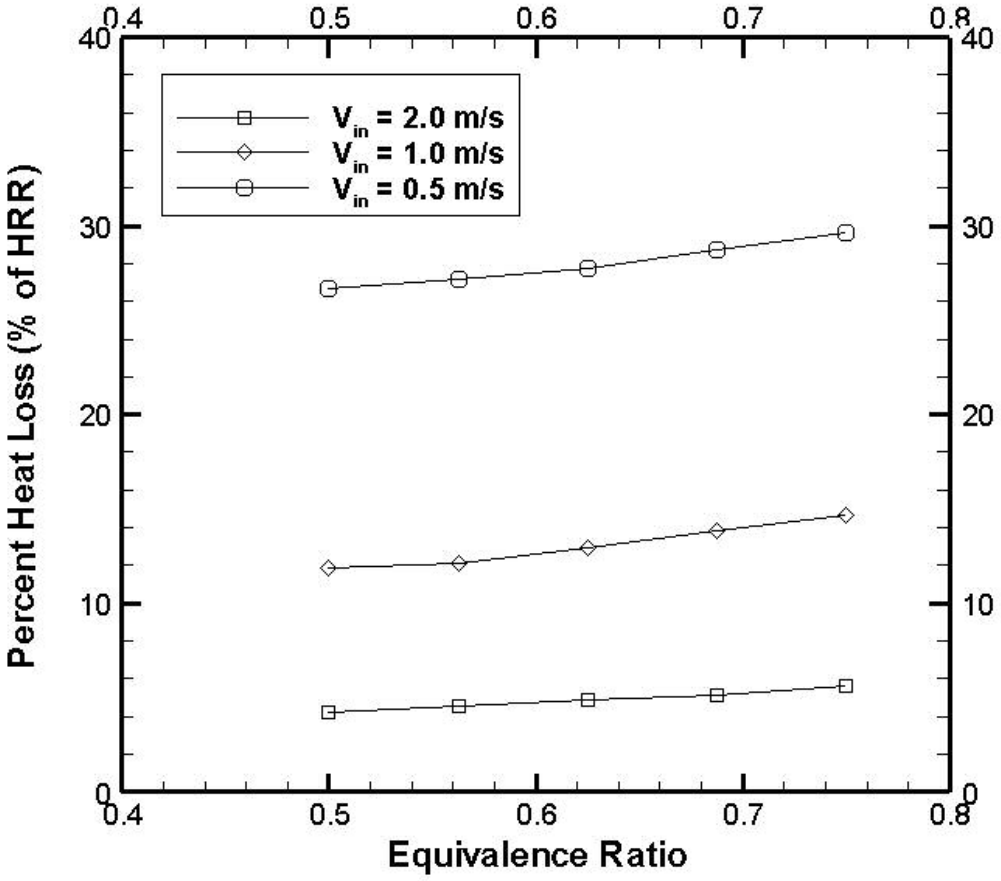

Figure 6.30. Predicted heat loss for M100 combustor.

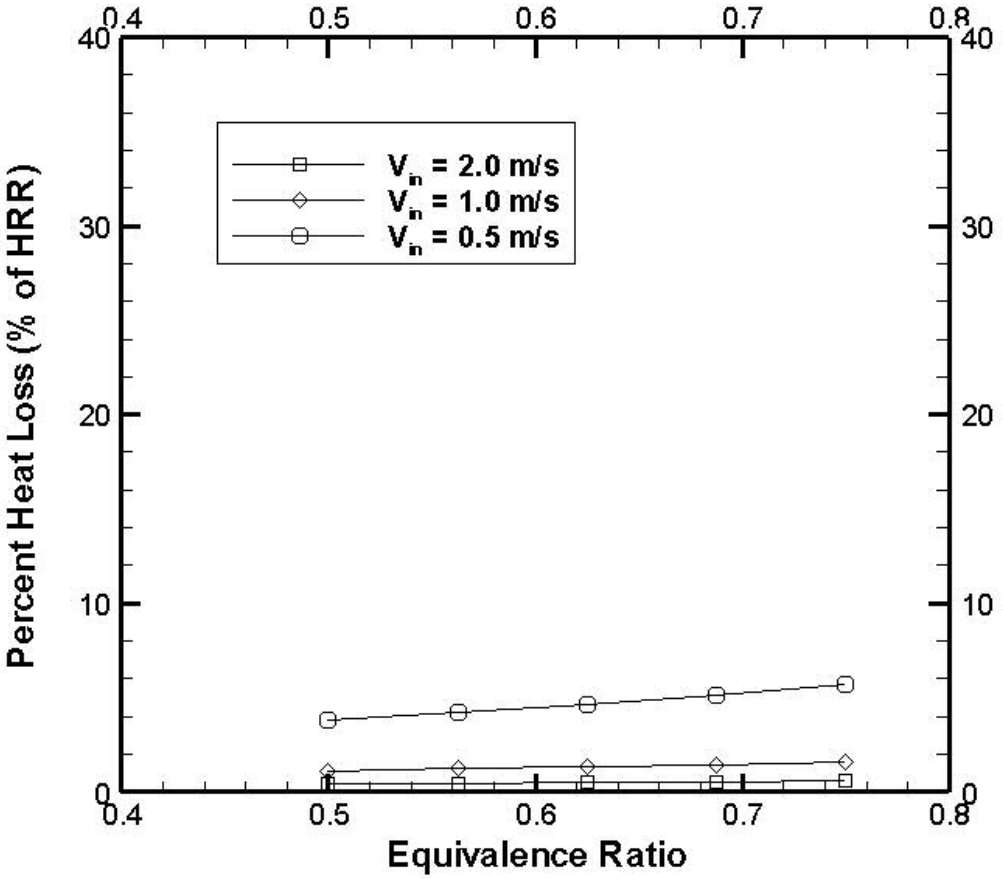

Figure 6.31. Predicted heat loss for M1000 combustor.

6.3.2.1 Effect of Equivalence Ratio

Increasing the equivalence ratio increases the volumetric HRR at a given reactant flowrate, increasing power density. However, it also increases the product gas temperature in the combustor chamber and hence, raises the combustor wall temperature. Higher wall temperature would increase heat loss by radiation and axial conduction.

The effect of equivalence ratio was analyzed for the M100 combustor. The reactant velocity was 2.0 m/s for all cases. The equivalence ratio was varied by adjusting the the heat source term. The equivalence ratios, flowrates, and HRRs are presented in Table 6.1.

Table 6.1. Effect of equivalence ratio operating conditions.

Equivalence Ratio	Fuel Flowrate	Air Flowrate	Total Flowrate	Heat Release Rate
0.500	1.35 mg/s	47.15 mg/s	48.5 mg/s	66.7 W
0.625	1.70 mg/s	46.80 mg/s	48.5 mg/s	83.3 W
0.750	2.03 mg/s	46.47 mg/s	48.5 mg/s	100.0 W

Figure 6.32 presents streamwise temperature profiles at the midplane of the combustor wall for various equivalence ratios. The combustor wall temperature increased significantly with increasing equivalence ratio. The temperature gradient near the combustor lid increased as well. Axial conduction to the lid increased from 2.7 W to 4.1 W as the equivalence ratio was increased from 0.50 to 0.75. Although the increase in axial conduction of 1.4 W with change of Φ seems relatively small, it represents about 2 % of the HRR and therefore, is important.

Figure 6.33 presents the radiation heat flux across the outer wall in the preheating annulus. As the equivalence ratio was increased from 0.50 to 0.75, radiation increased from 0.1 W to 0.4 W. The radiation shield was extremely effective for reducing heat transfer across the annulus, since the combustor wall temperature was nearly 1000 K at $\Phi = 0.75$ and radiation heat transfer to the outer wall was still less than 0.5 W.

Although the thin combustor wall and low lid thermal conductivity reduced axial conduction, it was still the most significant mode of heat loss. Figure 6.34 shows the effect of equivalence ratio on the exterior surface temperature of the combustor. At higher equivalence ratios, the surface temperature was higher, indicating greater heat loss.

These results indicate that the combustor should be operated at lean equivalence ratios to minimize heat loss to the surroundings. However, other factors must be considered when determining the optimal equivalence ratio. Operating at richer conditions would increase the power density of the system. Combustion considerations must be taken into account as well, since increasing the equivalence ratio tends to increase NOx emissions. The maximum operating temperature of the combustor wall must also be considered to ensure the structural integrity of the system. Operating at lean equivalence ratio would simultaneously minimize heat loss to the surroundings and NOx pollutant emissions, and ensure structural integrity.

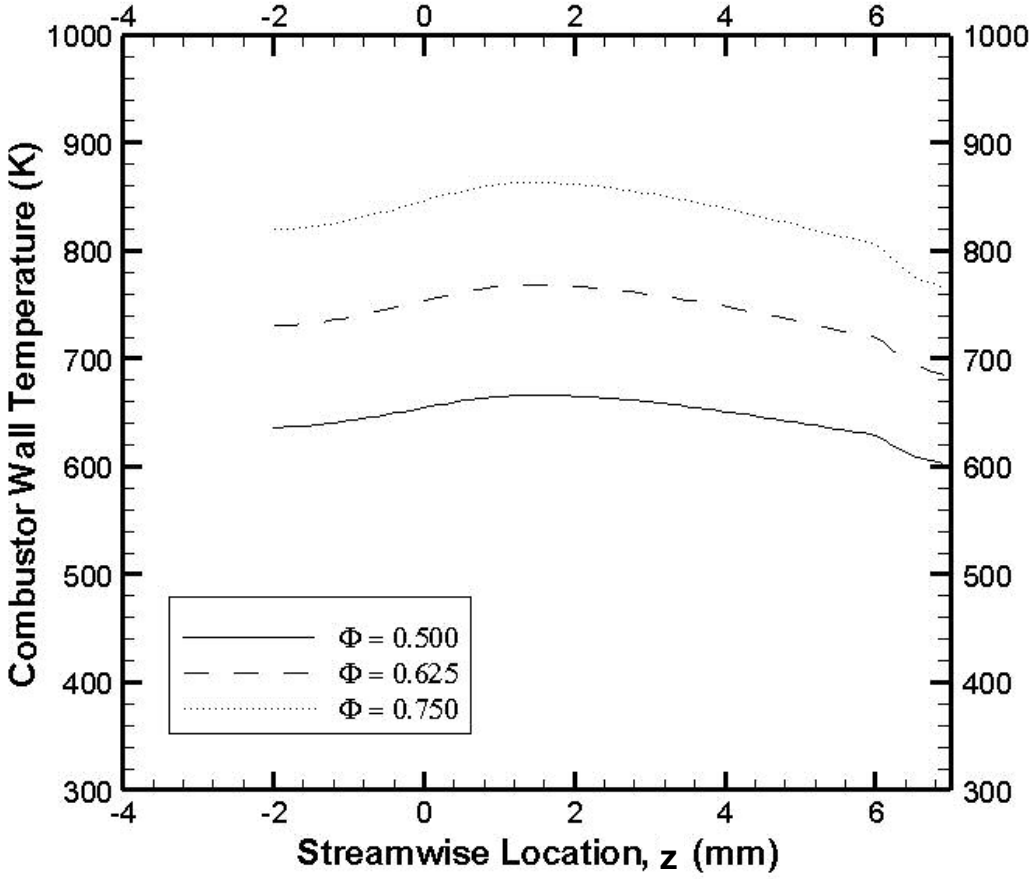

Figure 6.32. Effect of equivalence ratio on temperature at midplane of combustor wall (r = 3.0 mm).

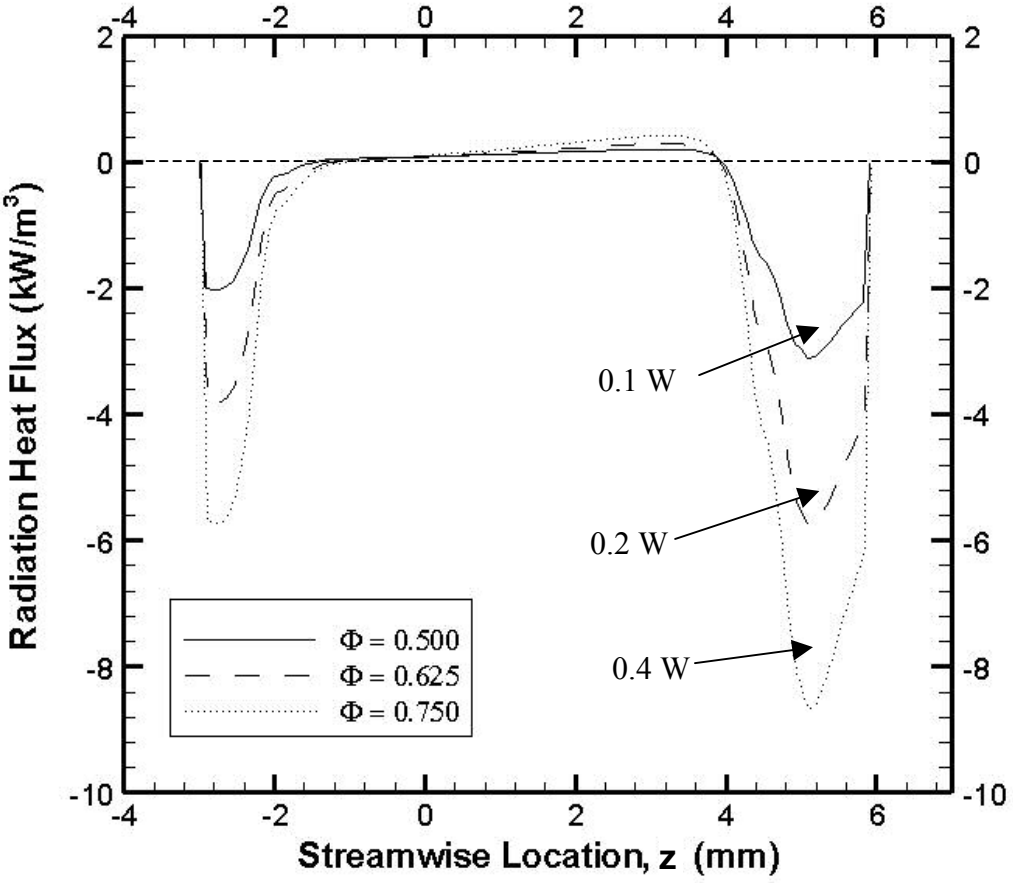

Figure 6.33. Effect of equivalence ratio on radiation heat flux on outer wall of preheating annulus (r = 4.5 mm)

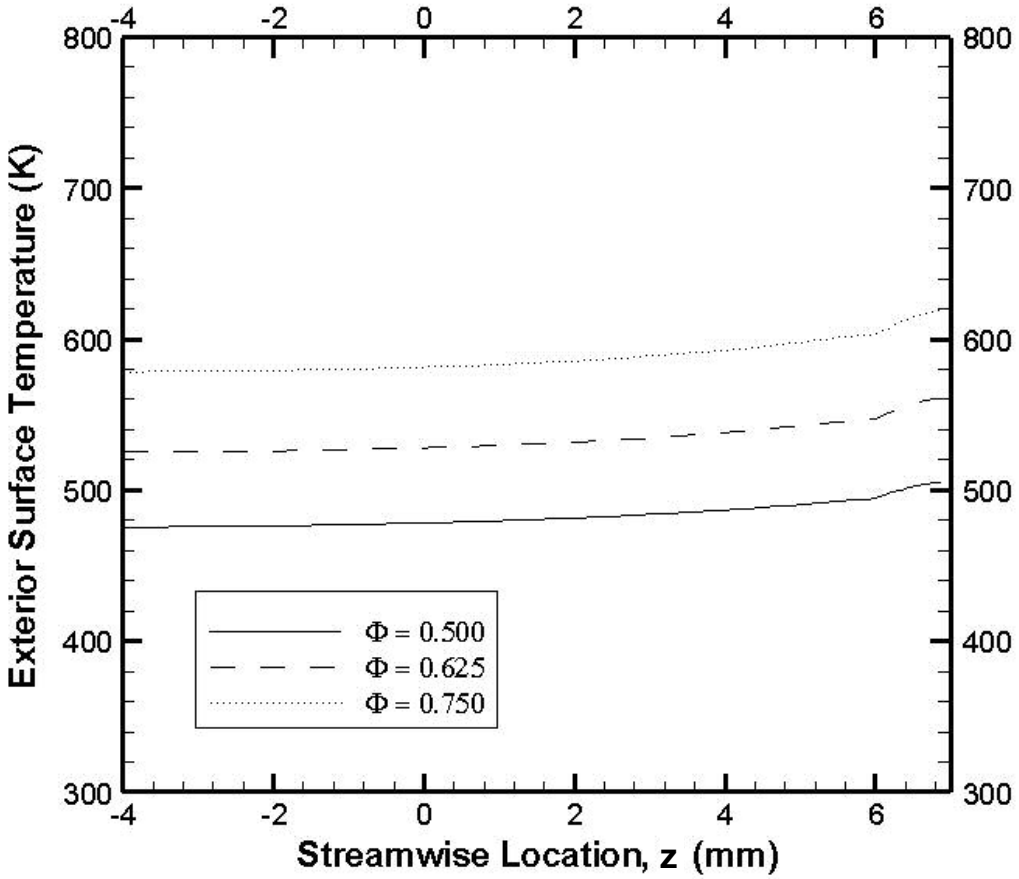

Figure 6.34. Effect of equivalence ratio on exterior surface temperature (r = 5.5 mm)

6.3.2.2 Effect of Reactant Flowrate

The mesoscale combustion experiments (Chapter 4) and Figure 6.30 indicated that heat loss to the surroundings decreased as V_{in} increased. The computational analysis in this section was performed to understand the effects of varying the reactant flowrate and to determine the optimum flowrate with minimum heat loss. The M100 combustor was used for the analysis at $\Phi = 0.50$. The reactant velocities, fuel, air and total mass flowrates, and HRRs are presented in Table 6.2.

Table 6.2. Effect of reactant flowrate operating conditions.

Reactant Velocity	Fuel Flowrate	Air Flowrate	Total Flowrate	Heat Release Rate
0.50 m/s	0.33 mg/s	11.77 mg/s	12.1 mg/s	16.7 W
1.00 m/s	0.67 mg/s	23.63 mg/s	24.3 mg/s	33.3 W
2.00 m/s	1.35 mg/s	47.15 mg/s	48.5 mg/s	66.7 W

Figure 6.35 presents the combustor wall temperature for various reactant flowrates. Increase in reactant velocity decreases the combustor wall temperature because of the higher convective heat transfer from the combustor wall to the reactants in the preheating annulus. The effect was greater in the region -2.0 mm $< z < 0.0$ mm because heat transfer from the wall to the reactants occurred on both sides of the wall in that region. Although the combustor wall temperature was higher for lower flowrates, the temperature gradient near the lid was approximately the same for all three flowrates. The axial heat conduction to the lid was approximately the same (4.2 W) and hence, the percentage heat transfer to the lid for $V_{in} = 0.5$ m/s was four

times greater than it was for V_{in} = 2.0 m/s. Increasing the reactant velocity improved heat recirculation by convection to the reactants and reduced axial heat conduction.

Figure 6.36 presents the radiation heat flux across the outer wall in the preheating annulus. Radiation was higher for lower flowrates, but it was less than 0.25 W for all cases. Figure 6.37 presents the exterior surface temperature for various reactant flowrates. The temperature was relatively uniform in the streamwise direction and it decreased with increasing reactant velocity.

These results indicate that increasing the reactant flowrate decreases heat loss by reducing combustor wall temperature (because of increased convection to the reactants) and reducing axial conduction to the combustor lid. Practically, V_{in} is limited by blowoff, where the velocity of the reactant mixture becomes greater than the laminar burning velocity, causing the flame to propagate downstream through the combustor chamber and extinguish.

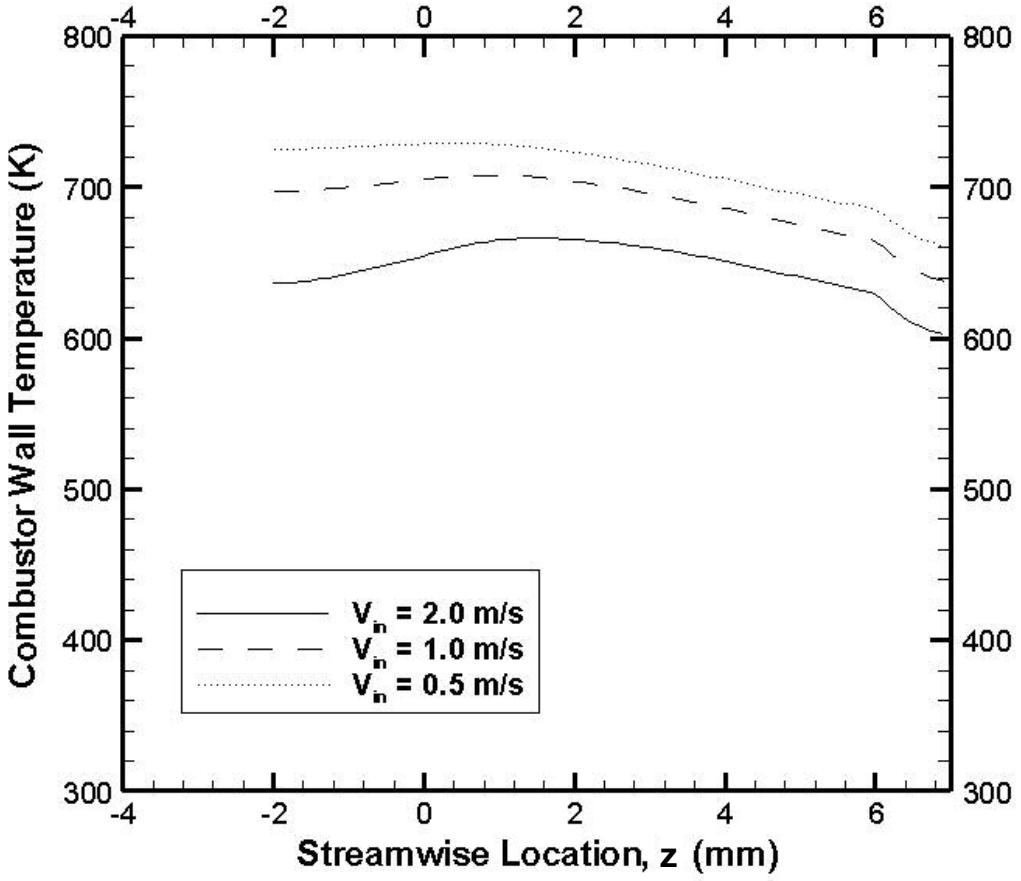

Figure 6.35. Effect of reactant flowrate on temperature at midplane of combustor wall (r = 3.0 mm).

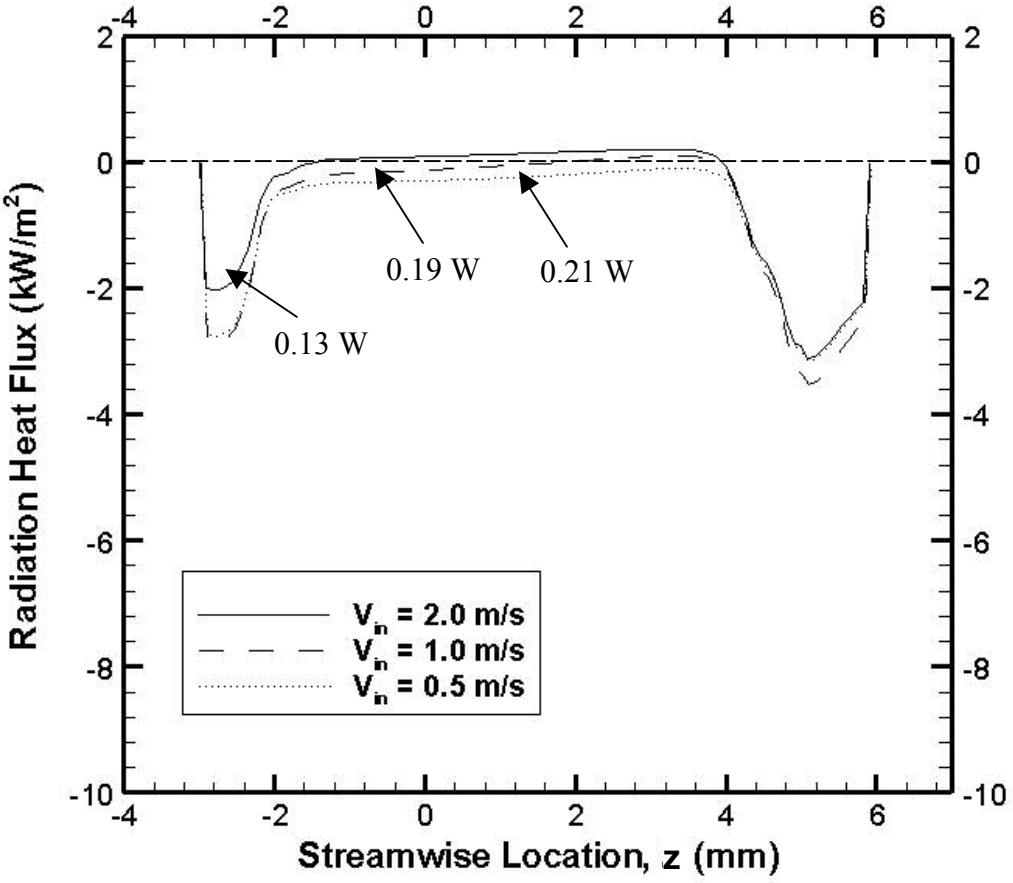

Figure 6.36. Effect of reactant flowrate on radiation heat flux on outer wall of preheating annulus (r = 4.5 mm).

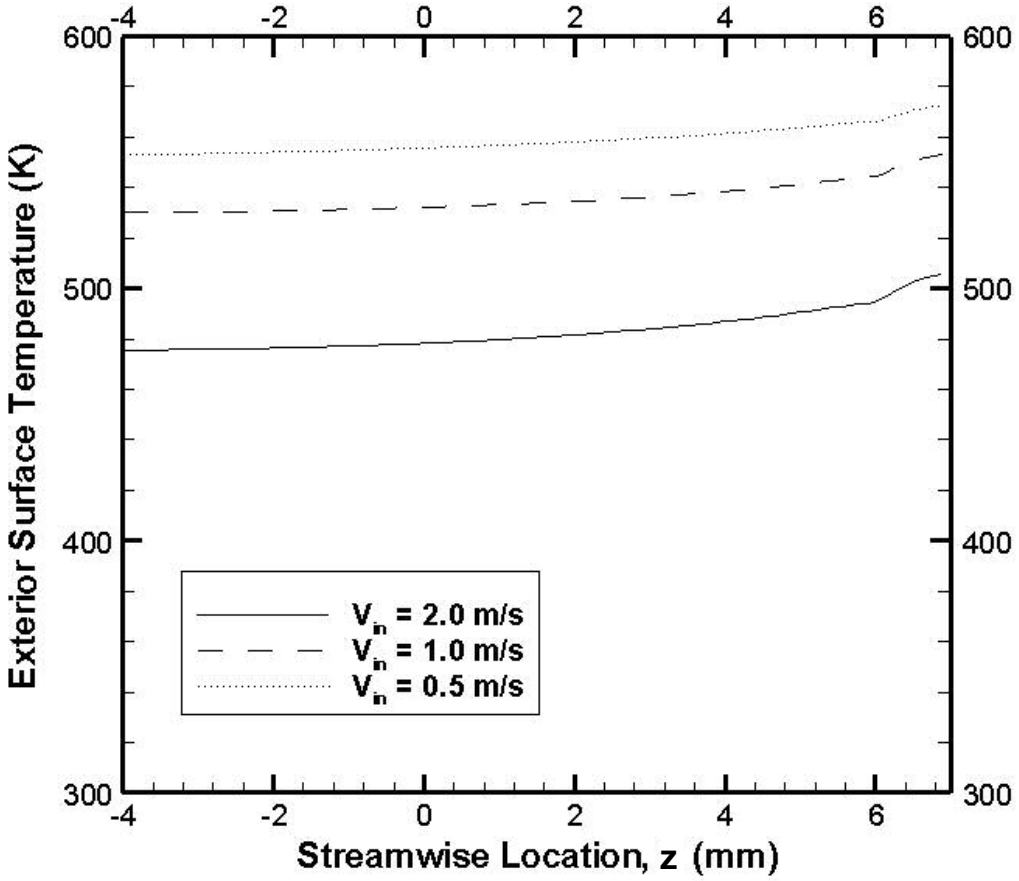

Figure 6.37. Effect of reactant flowrate on exterior surface temperature (r = 5.5 mm).

6.3.2.3 Effect of Combustor Size

Figures 6.30 and 6.31 indicate that combustor size significantly affects heat loss to the surroundings. The purpose of this section is to understand the effects of combustor size on heat transfer in the heat recirculating combustor design. The M100 and M1000 geometries were used at V_{in} = 2.0 m/s and Φ = 0.50. The streamwise distance z* represents the non-dimensional streamwise distance, normalized with z_{max}. Table 6.3 presents the operating conditions for the two cases.

Table 6.3. Combustor Sizes, Flowrates and HRRs.

Combustor	Fuel Flowrate	Air Flowrate	Total Flowrate	Heat Release Rate
M100	1.35 mg/s	47.15 mg/s	48.50 mg/s	66.7 W
M1000	13.5 mg/s	471.5 mg/s	485.0 mg/s	666.7 W

Figure 6.38 presents the effect of combustor size on combustor wall temperature. The peak temperature for both combustors was around 660 K, and it occurred downstream of the flame zone in the region $0.0 < z^* < 0.5$. The wall temperature for the M1000 combustor was much lower than the M100's in the region $-0.5 < z^* < 0.0$. Both combustor walls were 1.0 mm thick, but the M1000 combustor wall much longer. The longer length and greater surface area decreased heat conduction and increased heat convection to the reactants, decreasing the combustor wall temperature away from the flame zone. The temperature near the combustor lid was lower for the M1000 combustor. Axial conduction to the lid was 4.2 W for the

M100 and 11.4 W for the M1000. Thus, it was 3-4 times greater for the M100 combustor based on percentage of HRR.

Figure 6.39 presents the radiation heat flux on the outer wall of the preheating annulus. Radiation was low for both cases; 0.1 W for the M100 and 0.4 W for the M1000 combustor. Figure 6.40 shows that the exterior surface temperature was significantly lower throughout the length of the M1000 combustor. The lower exterior surface temperature corresponds to significantly lower heat loss. At V_{in} = 2.0 m/s and Φ = 0.50, heat loss was 4.2 % for the M100 and 0.43 % for the M1000. Thus, larger combustor exhibits less heat loss to the surroundings.

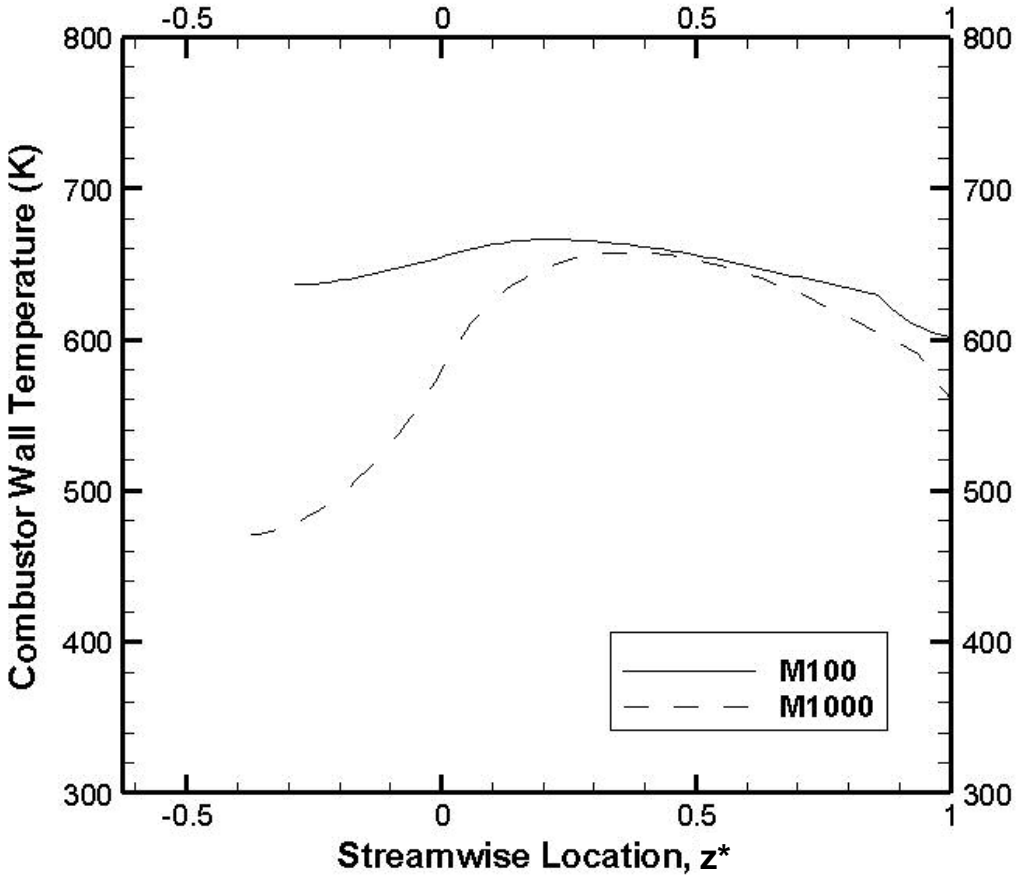

Figure 6.38. Effect of combustor size on temperature at midplane of the combustor wall.

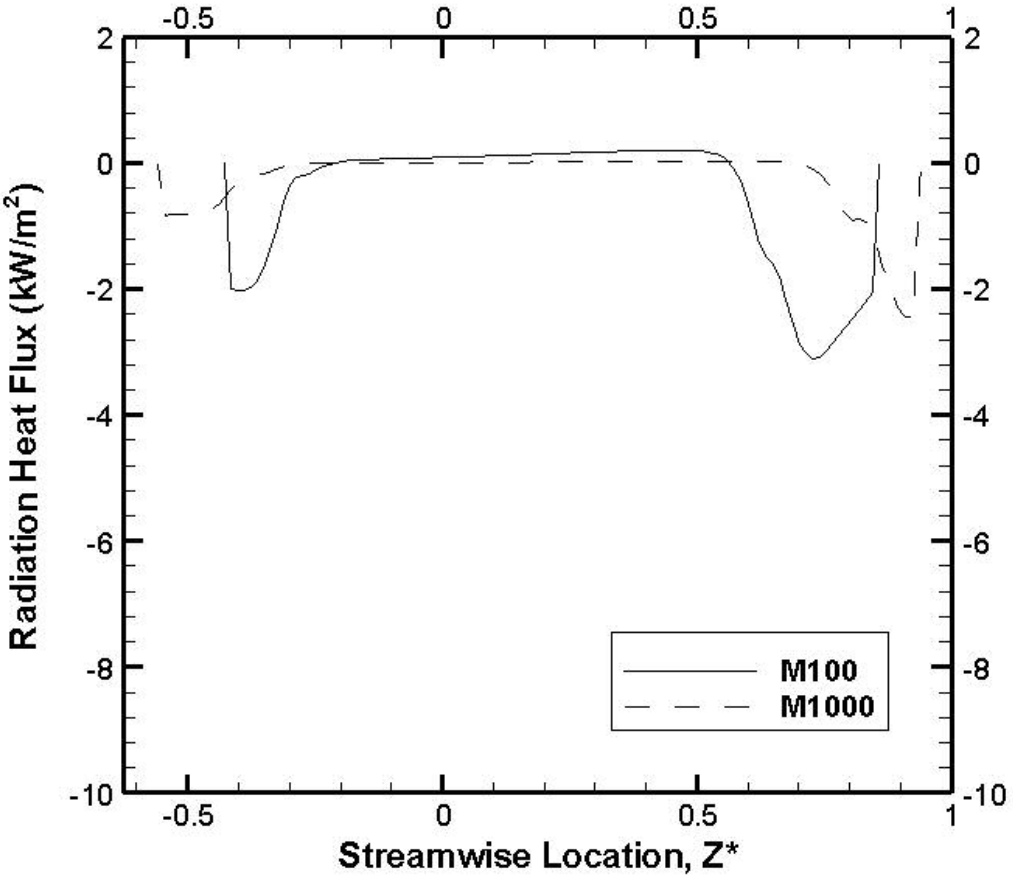

Figure 6.39. Effect of combustor size on radiation heat flux on outer wall of preheating annulus

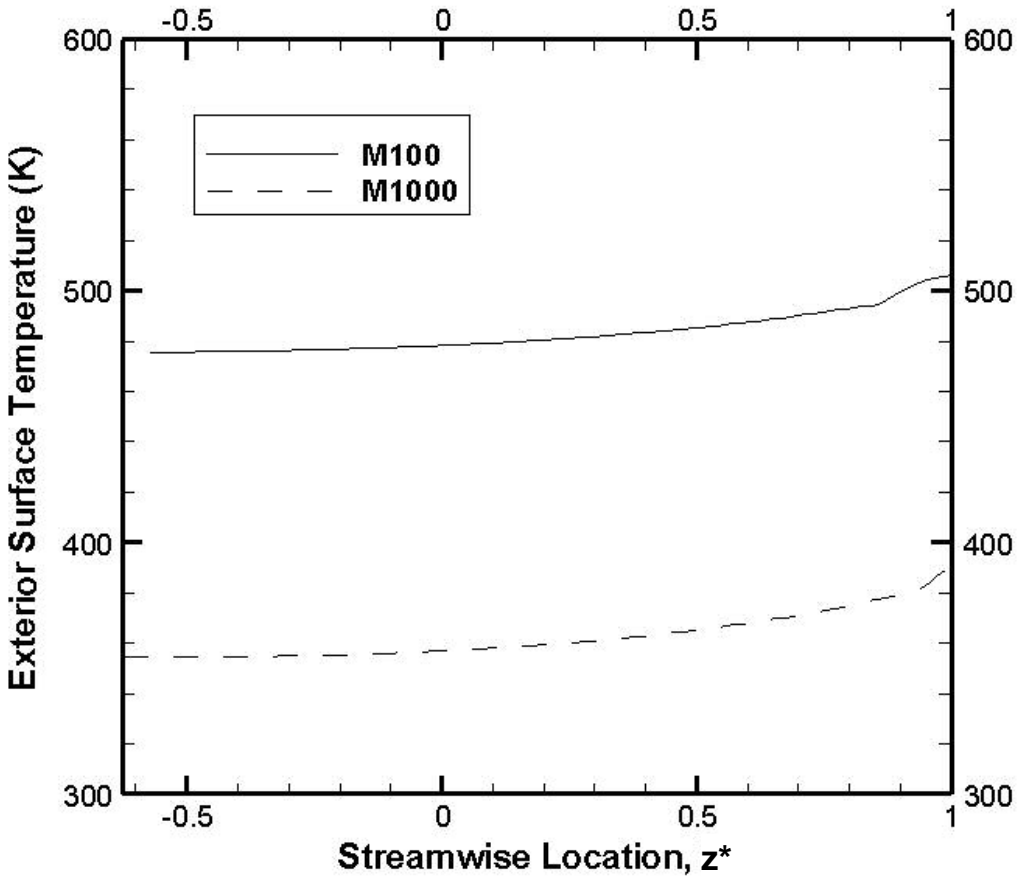

6.40. Effect of combustor size on exterior surface temperature.

6.4 Conclusions

Parametric studies were used to improve the heat recirculating combustor design. Effective methods of reducing axial conduction and radiation across the preheating annulus were developed and implemented into a proposed combustor design. Thermal performance of the proposed design was predicted and the effects of varying combustion control parameters were studied.

Important conclusions from the parametric study are listed below:

- Heat loss by axial conduction and radiation across the annulus are coupled. Increasing thermal resistance to one mode of heat transfer increases heat loss by the other mode. Therefore, both axial conduction and radiation across the annulus should be reduced simultaneously.
- The combination of a high thermal conductivity combustor wall and a low thermal conductivity lid can be used to simultaneously reduce axial conduction and radiation across the annulus.
- Insertion of a PIM into the preheating annulus reduces axial conduction and radiation across the annulus, but it introduces a new mode of heat loss, radial conduction, which may increase heat loss.
- The radiation shield is effective in reducing radiation heat transfer across the annulus, regardless of its emissivity.
- Mesoscale combustors should be operated at high flowrates and low equivalence ratios to minimize heat loss to the surroundings.

7. Phase II Mesoscale Combustion Experiments

Mesoscale combustion experiments presented in Chapter 4 showed that the heat recirculating combustor effectively minimizes heat loss to the surroundings. However, the combustor was relatively large (125 cm^3) compared to other mesoscale systems in the literature. Analysis presented in Chapter 6 indicated that smaller combustors with low heat loss are possible. The phase II mesoscale combustor was developed to demonstrate the heat recirculating design for a system of approximately 1 cm^3. The analysis presented in Chapter 6 guided the design of the phase II system, but machining prevented incorporation of the features of the M100 or M1000 combustor designs. Thus, the phase II system represents a first step towards an optimized, practical system. The operating range, product gas temperature, exterior surface temperature, and CO and NOx emissions were measured for various flowrates and equivalence ratios.

7.1 Experimental Setup and Procedure

Figures 7.1 and 7.2 show schematic drawings of the phase II heat-recirculating combustor. As described above, the system was intended to demonstrate the feasibility of the heat recirculating combustor design at small scales and it does not represent a fully optimized system. It was manufactured from 304 stainless steel using standard machine shop equipment. The outer cylinder and base were created as one solid piece with the inner cylinder and lid made separately. A photograph of the three pieces is presented in Fig. 7.3(a). SiC coated PIM of 39

ppcm, 9.5 mm diameter, and 2 mm thickness was placed at the bottom of the outer cylinder. A groove was cut into the PIM so that the inner cylinder would protrude 1.0 mm into the PIM, as shown in Figs. 7.1 and 7.2. After the inner cylinder and lid were placed, they were welded to seal the system. Figure 7.3(b) shows a photograph of the assembled system. The fuel/air mixture was injected through the outer wall by four equally spaced, threaded injection ports of 1.2 mm diameter as seen in Fig. 7.4. Welds and threads were selected to eliminate adhesives, which could fail at high temperatures. The overall system was 14.5 mm long and 11.5 mm in diameter, occupying a volume of 1.5 cm^3. The annulus channel width was 0.575 mm and the cross-sectional area of the annulus was half of the combustor chamber cross-sectional area.

Air was supplied by a compressor, dried and measured with a mass flowmeter calibrated in the range 0 to 5.0 slm with an uncertainty of ± 0.075 slm. Methane fuel was supplied by a compressed cylinder. The combustion equivalence ratio was determined from O_2 concentration measurements in the product gases because a flowmeter of desired accuracy at low flowrates, less than 0.05 slm, was not readily available. The product gas O_2 gas concentrations were measured with an electrochemical gas analyzer calibrated in the range 0 to 25 % with an uncertainty of 1 %. The equivalence ratio calculation procedure is presented in Appendix D. Concentrations of NOx and CO were measured with electrochemical gas analyzers calibrated in the range 0 to 200 ppm with an uncertainty of ± 4 ppm. Emissions samples were obtained through a quartz probe of 3 mm outer diameter with a tapered

tip of 4:1 expansion ratio to quench the reactions. Concentrations are reported on an uncorrected, dry basis. The exterior surface temperature was measured with a K-type thermocouple at four equally spaced locations around the circumference of the combustor. Product gas temperatures were measured with an R-type thermocouple with 0.075 mm bead diameter and uncertainty of ± 20 K. Temperatures are reported uncorrected for radiation and the maximum correction was estimated to be 40 K (Appendix F).

Combustion was initiated by igniting the fuel/air mixture at the exit plane. Initially, the reaction stabilized near the exit plane and a blue flame was observed downstream of the combustor chamber. The fuel and air flowrates were reduced until the flame propagated into the system and was stabilized on the PIM surface. The system was allowed to warm-up for approximately 30 minutes to reach steady state conditions. Experiments were conducted at four reactant flow velocities, V_{in} = 0.25 m/s, 0.50 m/s, 0.75 m/s, and 1.0 m/s. The cold flow Reynolds number based on the diameter of the combustion chamber ranged from 110 to 430. The HRRs ranged from 15 W to 90 W with space heating rates of 0.5 MW/m^2 to 2.8 MW/m^2 based on the cross-sectional area of the combustion chamber.

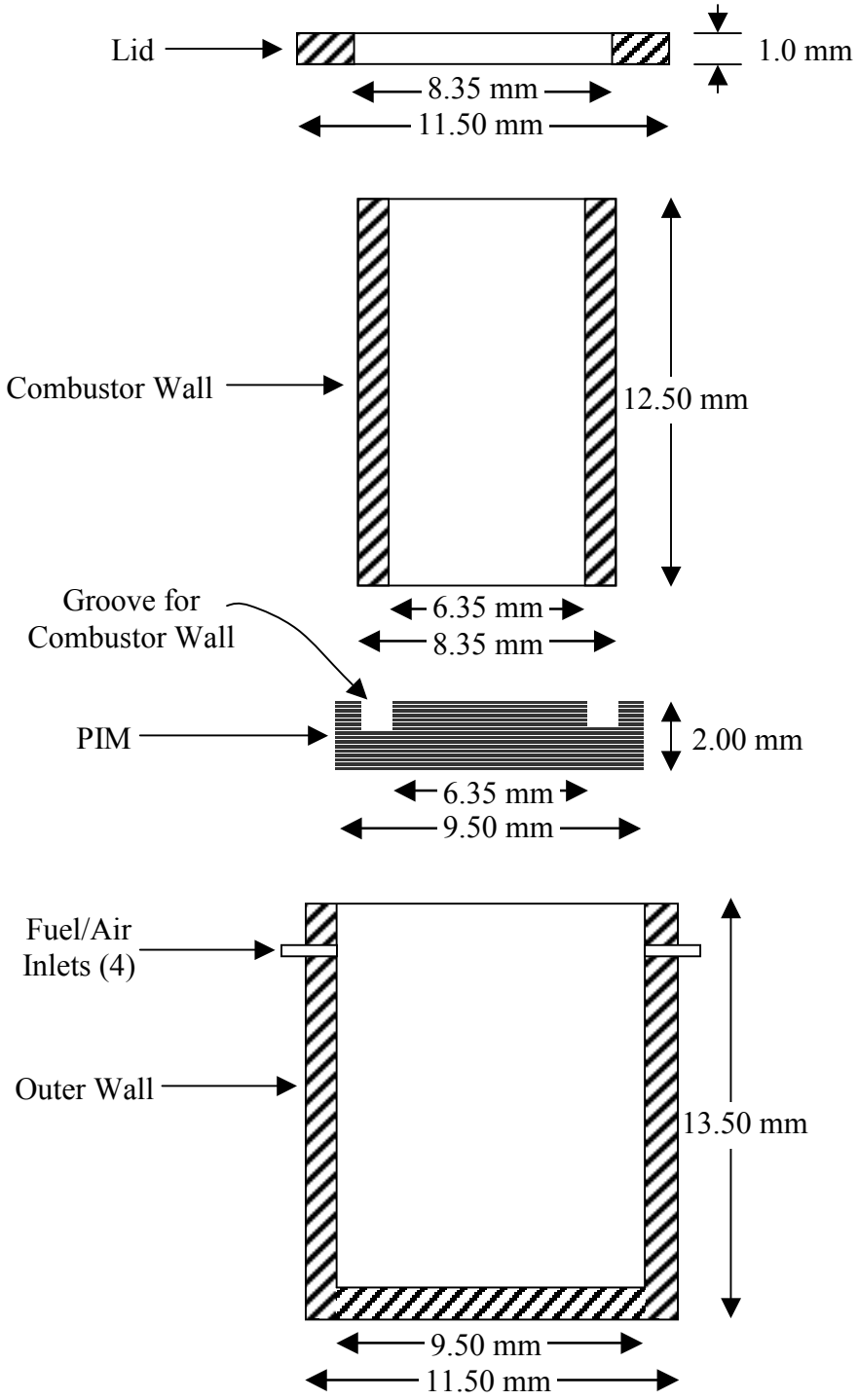

Figure 7.1. Schematic of phase II combustor components.

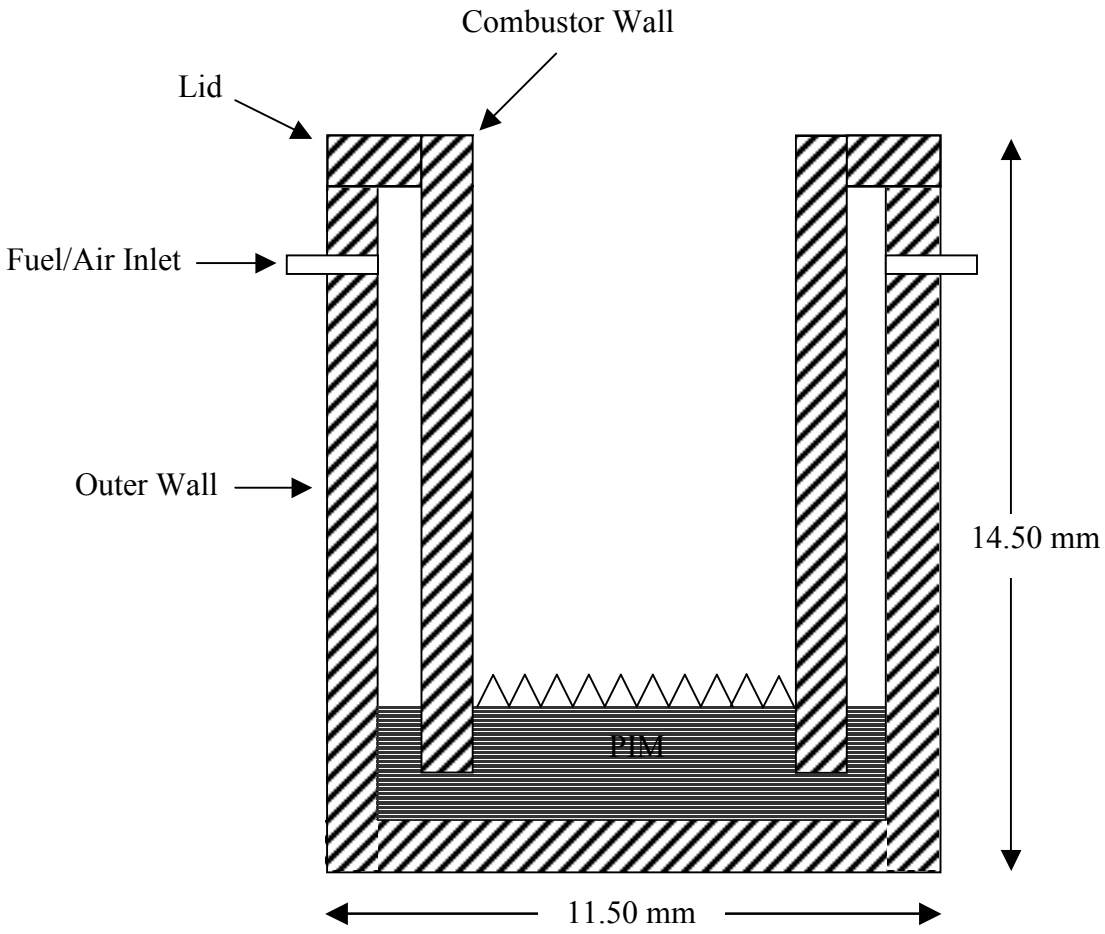

Figure 7.2. Schematic of assembled phase II combustor.

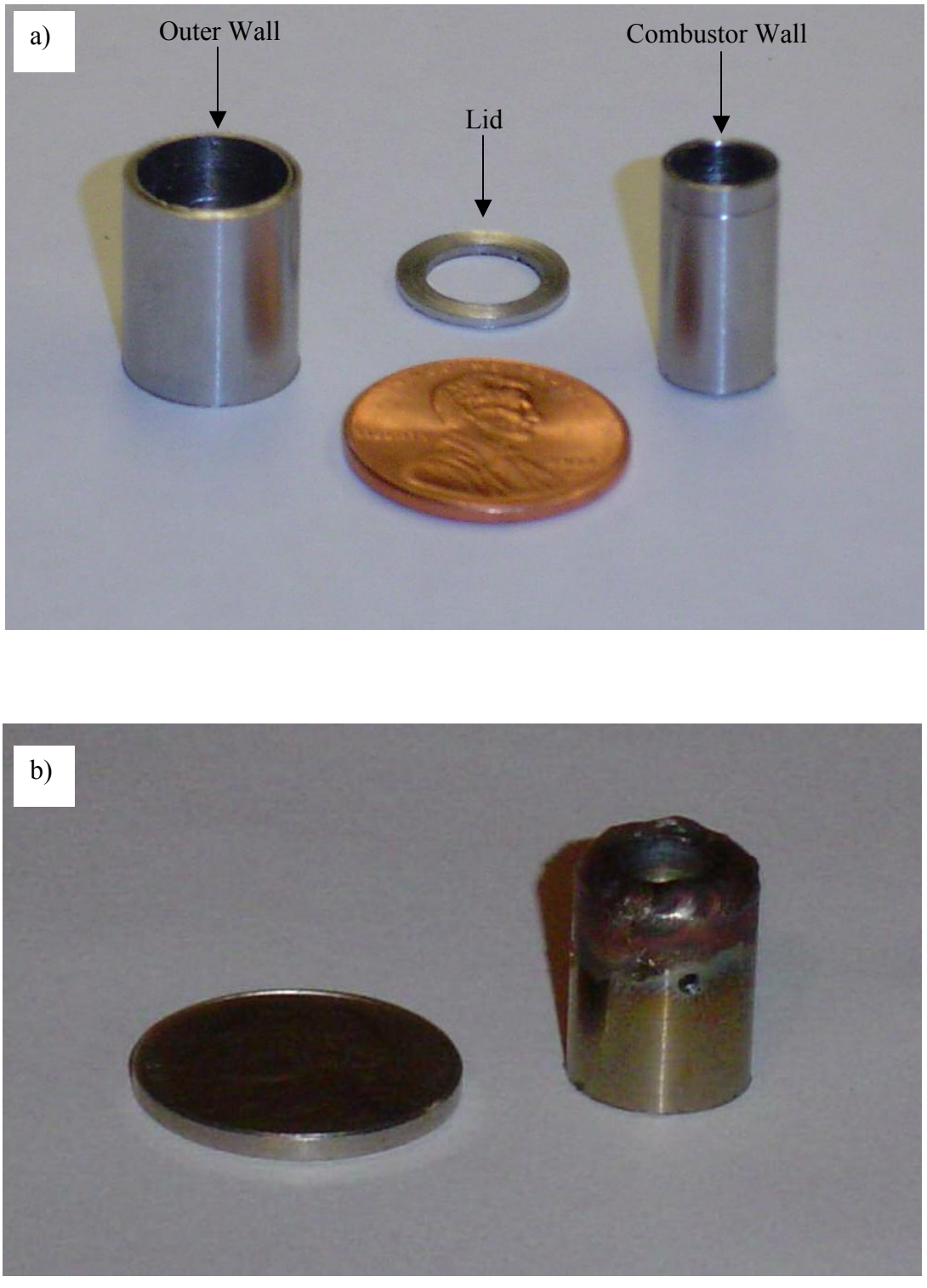

Figure 7.3. Photographs of phase II combustor (a) before and (b) after assembly.

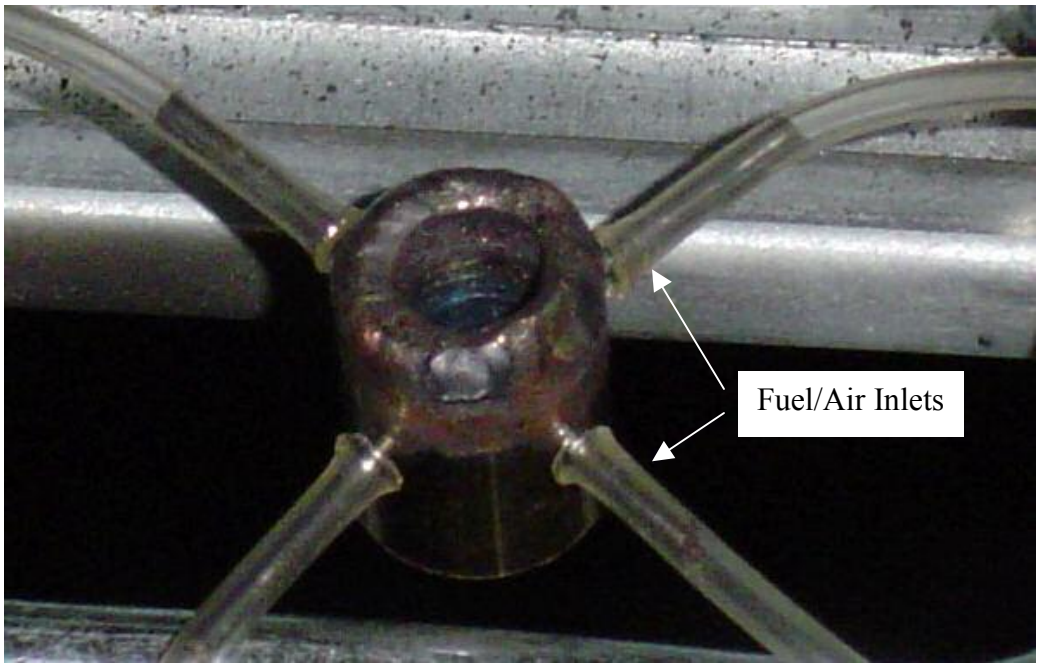

Figure 7.4. Photograph of phase II combustor experimental setup.

7.2 Results and Discussion

Combustion was achieved within the phase II combustor over a range of flowrates and equivalence ratios. In this section, the operating range, product gas and exterior surface temperatures, and CO and NOx emissions are presented and discussed.

The maximum HRR was 90 W (60 MW/m^3) at V_{in} = 1.0 m/s and Φ = 0.80. The volumetric HRR was significantly higher than the 20 MW/m^3 achieved with a 0.78 cm^3 Swiss-roll design [Vican, et al., 2002] and the 2.3 MW/m^3 HRR achieved with a 43 cm^3 electrospray liquid fuel combustor [Kyritsis et al., 2002]. The volumetric HRR of our system exceeds that of other mesoscale designs, such as the Swiss-roll design, because the combustor chamber occupies a larger fraction of the system volume.

Figure 7.4 presents the effect of reactant flowrate on product gas temperature at the exhaust plane of the combustor chamber (z = 11.5 mm). The equivalence ratio for all cases was 0.70. The product gas temperature increased as the reactant flowrate increased, meaning larger flowrates resulted in less heat loss to the surroundings. A similar trend was observed with the previous mesoscale combustor (Fig. 4.20) and it was predicted by the CFD model in section 6.3.2.2. The peak temperature at V_{in} = 1.00 m/s was 1680 K, which was less than the adiabatic flame temperature of 1810 K, predicted using CHEMKIN. These results indicate that heat loss is significant at all flowrates and it increases dramatically as the reactant flowrate is reduced.

Table 7.1 presents the average exterior surface temperature, $T_{exterior}$, for various flowrates. The equivalence ratio was 0.70 and temperatures were measured at five locations; four on the exterior surface at z = -2 mm, 2, mm, 6 mm and 10 mm and one at the center of bottom surface. $T_{exterior}$ decreased from 650 K to 590 K as the flowrate was increased from V_{in} = 0.25 m/s to 1.00 m/s. The exterior surface temperature measurements indicate that heat loss was significant for all flowrates and that it decreased as the flowrate increased.

Table 7.1. Effect of flowrate on average exterior surface temperature and percent heat loss to the surroundings (Φ = 0.70).

V_{in}	HRR	$T_{exterior}$
0.25 m/s	20 W	654 K
0.5 m/s	40 W	638 K
0.75 m/s	60 W	621 K
1.00 m/s	80 W	595 K

Heat loss from the phase II combustor was estimated using the product gas temperature profiles presented in Fig. 7.5 and the calculation procedure described in section 4.2.6.3. Table 7.2 shows that percent heat loss to the surroundings increased from 13 % to over 50 % as the flowrate was reduced from V_{in} = 1.0 m/s to 0.25 m/s. In agreement with the analysis presented in Chapter 6, experimental results indicate

that the system should be operated at the maximum flowrate for optimal performance. Additionally, the 12.6 % heat loss calculated for V_{in} = 1.0 m/s agrees with the predicted heat loss of 11.9 % for the M100 combustor at identical conditions.

Table 7.2. Effect of reactant flowrate on heat loss to the surroundings (Φ = 0.70).

Mean Reactant Velocity, V_{in}	Total Heat Release Rate	Total Heat Loss	Percent Heat Loss
0.25 m/s	20 W	11.6 W	55.3 %
0.5 m/s	40 W	12.6 W	31.5 %
0.75 m/s	60 W	12.2 W	20.3 %
1.00 m/s	80 W	10.1 W	12.6 %

Figure 7.5 presents CO emissions taken at the centerpoint of the exhaust plane. As seen in the macroscale (Fig. 3.10) and mesoscale (Fig. 4.21) experiments, the equivalence ratio at LBO was higher at higher flowrates. The equivalence ratio at LBO increased from Φ = 0.49 to 0.70 as the reactant flowrate was increased from V_{in} = 0.25 m/s to 1.0 m/s. The CO concentrations increased with increasing equivalence ratio, also seen from results in Chapters 3 and 4. Relatively high CO concentrations of over 100 ppm occurred for all conditions. High CO concentrations produced near the wall, as seen in the larger setups, are likely dominating CO production in the phase II system. However, the emissions analyzer used for these experiments

detected UHCs with CO emissions and the maximum concentration was less than 400 ppm or 0.4 %, indicating combustion efficiency greater than 99 %.

In Fig. 7.6, NOx emissions show a trend similar to the one presented in Chapter 4, where NOx increased with increasing flowrate and equivalence ratio (Fig. 4.21). NOx emissions were less than 10 ppm for $V_{in} \leq 0.75$ m/s, but they increased to over 20 ppm at $V_{in} = 1.00$ m/s. The high heat loss at low flowrates reduced product gas temperatures and hence, resulted in low NOx emissions. At $V_{in} = 1.0$ m/s, heat loss was lower, product gas temperatures were higher and hence, NOx production by the thermal mechanism increased.

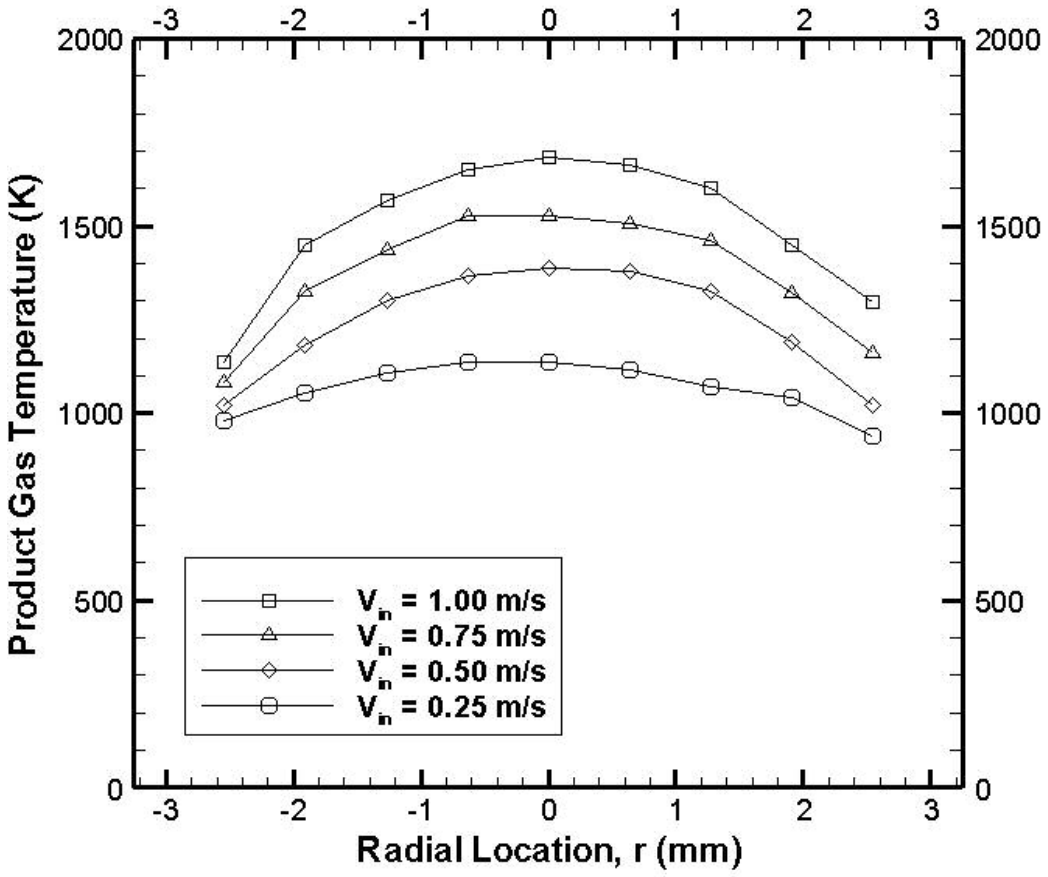

Figure 7.4. Effect of reactant flowrate on product gas temperature (z = 11.5 mm) for the Phase II combustor.

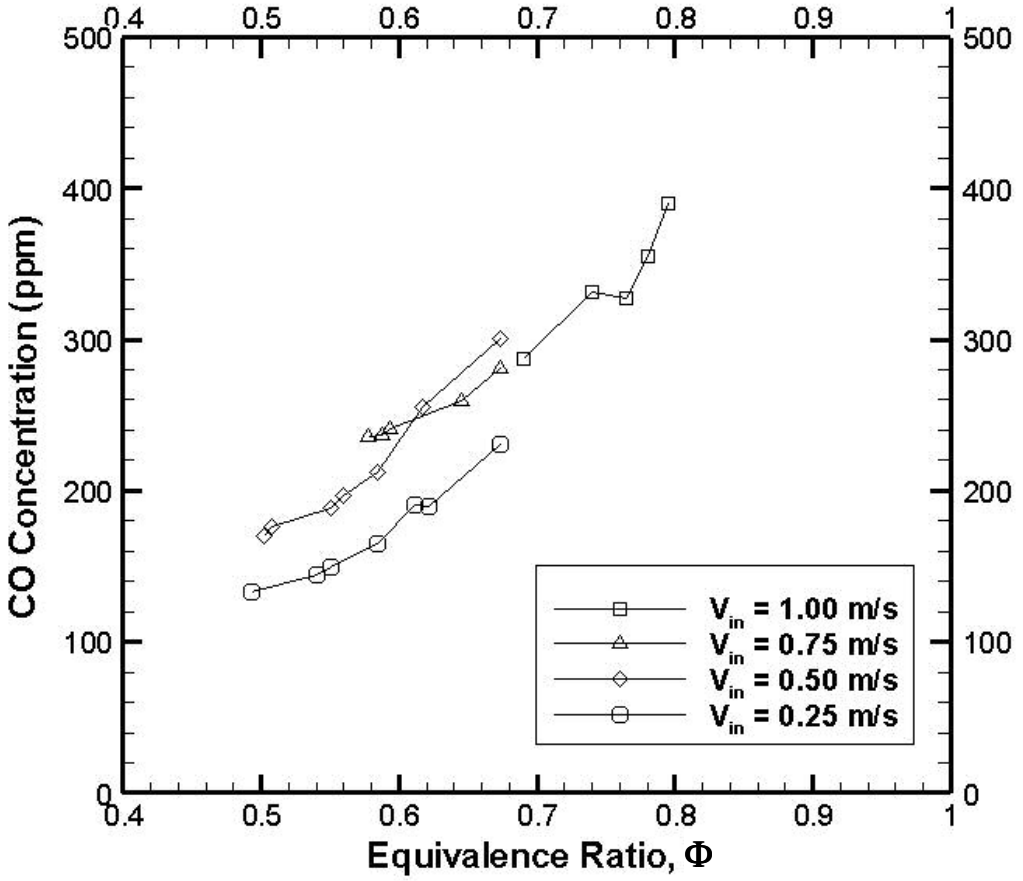

Figure 7.5. Effect of flowrate on phase II mesoscale combustor CO emissions.

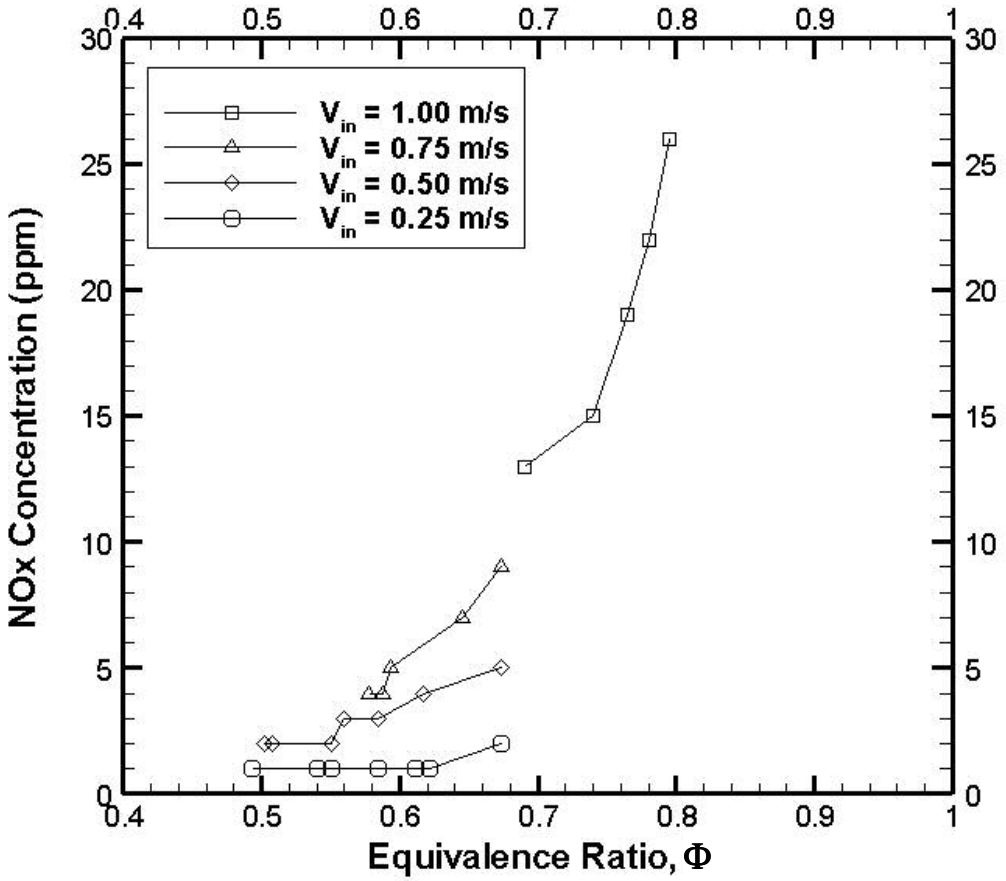

Figure 7.6. Effect of flowrate on phase II mesoscale combustor NOx emissions.

7.3. Conclusions from Phase II Experiments

Combustion was achieved at HRRs exceeding 90 W within a mesoscale, heat recirculating system of 1.5 cm^3. Product gas temperatures increased with increasing flowrate, indicating reduction in heat loss. At V_{in} = 1.0 m/s, product gas temperatures were 100-200 K lower than the adiabatic flame temperature, indicating heat loss of 13 % of HRR. Exterior surface temperatures ranged from 590 K to 650 K and they decreased as the reactant flowrate increased. High combustion efficiency was observed with CO and UHC emissions of less than 0.4 % and NOx emissions of less than 30 ppm. These results demonstrate that the present design is effective for achieving combustion in small-scale systems. In the future, the system should be improved by incorporating the findings from Chapter 6, such as a low thermal conductivity lid and a radiation shield in the annulus.

8. Conclusions and Recommendations

Heat recirculation with the use of PIM is an effective method of achieving efficient combustion in small volumes with low heat loss. A few of the important findings from this work are summarized below.

- The surface and interior combustion modes were directly compared. Interior combustion extended the LBO limit, allowing for ultra-low NOx emissions and making it attractive for large scale applications.
- Feasibility of the heat recirculating combustor design was demonstrated using a 125 cm^3 combustor. Pressure loss was less than 0.5 % of the operating pressure, reactants were preheated to temperatures exceeding 500 K, CO and NOx emissions ranged from 30-40 ppm, and heat loss was approximately 10 % of the HRR.
- A computational model was developed and validated with experimental data. Flow and temperature fields were visualized and heat transfer throughout the combustor was determined by analyzing gas enthalpy, solid conduction and surface heat fluxes. The most important sources of heat loss were axial conduction through the combustor wall and radiation across the annulus.
- Parametric studies were performed to improve the design by minimizing the two sources of heat loss listed above. A combination of low thermal conductivity lid and a radiation shield in the annulus

was most effective for reducing heat loss to the surroundings. These features were incorporated into the proposed phase II combustor designs.

- The heat recirculating combustor design was demonstrated with a 1.5 cm^3 combustor that was modeled after the phase II designs. Heat release rates exceeding 90 W, heat loss of less than 15 %, and combustion efficiency greater of 99 % were achieved experimentally.

The findings of this work should guide small-scale combustor design. Future combustors should utilize advanced manufacturing techniques to incorporate design features such as a low thermal conductivity lid and a radiation shield in the annulus. Future research should focus on understanding and optimizing liquid fuel vaporization, mixing, and combustion. Perhaps radiation, axial conduction, and/or PIM may be used to achieve lean premixed, pre-vaporized combustion in small-scale systems. The effects of miniaturizing heat recirculating combustor into the microscale should also be explored. Beyond the combustion phenomena, small scale pumping and metering devices and efficient power converters, such as micro-gas turbine engines or thermoelectric generators, are required to advance this technology into widespread practical use.

Bibliography

Ahn, J., Eastwood, C., Sitzki, L., and Ronney, P., "Gas Phase and Catalytic Combustion in Heat Recirculating Burners," Proceedings of the Combustion Institute, Vol. 30, pp. 2463-2472, 2005.

Assael, M.J. and Gialou, K, "Measurement of the Thermal Conductivity of Stainless Steel AISI 304L Up to 550 K," International Journal of Thermophysics, Vol. 24, No. 4, pp. 1145-1153, 2003.

Bauer, T.H., "A General Analytical Approach Toward the Thermal Conductivity of Porous Media," International Journal of Heat and Mass Transfer, Vol. 36, No. 17, pp. 4181-4191, 1993.

Boyarko, G A., Sung, C.-J., Schneider, S. J., "Catalyzed Combustion of Hydrogen-Oxygen in Platinum Tubes for Micro Propulsion Applications," Proceedings of the Combustion Institute, Vol. 30, pp. 2481-2488, 2005.

Collins, R.E., Flow of Fluids Through Porous Materials, Engelwood, Colorado, Research and Engineering Consultants, Inc., 1990.

Epstein, A. H., "Millimeter-Scale, MEMS Gas Turbine Engines," Proceedings of the ASME Turbo Expo 2003, ASME Paper GT-2003-38866, 2003.

Fernandez-Pello, A. C., "Micropower Generation using Combustion: Issues and Approaches," Proceedings of the Combustion Institute, Vol. 29, pp. 883-889, 2002.

Hardesy, D.R. and Weinberg, F.J., "Converter Efficiency in Burner Systems Producing Large Excess Enthalpies," Combustion Science and Technology, Vol. 12, pp. 153-157, 1976.

Howell, J.R., Hall, M.J., and Ellzey, J.L., "Radiation Enhanced/Controlled Phenomena of Heat and Mass Transfer in Porous Media," Progress in Energy and Combustion Science, Vol. 22, pp. 121-145, 1996.

Hsu, P.F., Evans, W.D., and Howell, J.R., "Experimental and Numerical Study of Premixed Combustion within Nonhomogeneous Porous Ceramics," Combustion Science and Technology, Vol. 90, pp. 149-172, 1993.

Insulfrax Thermal Insulation Product Data Sheet, Unifrax Corporation, available at www.insulfrax.com, 2002.

Ju, Y. and Xu, B., "Theoretical and Experimental Studies on Mesoscale Flame Propagation and Extinction," Proceedings of the Combustion Institute, Vol. 30, pp. 2445-2454, 2005.

Kee, R.J., Rupley, F.M., and Miller, J.A., "Chemkin-II: A FORTRAN Chemical Kinetics Package for the Analysis of Gas Phase Chemical Kinetics," Sandia National Laboratories Report No. SAND89-809B-UC-706.

Khanna, V, Goel, R, Ellzey, J.L., "Measurements of Emissions and Radiation for Methane Combustion within a Porous Medium Burner," Combustion Science and Technology, Vol. 99, pp. 133-142, 1994.

Kotani, Y., and Takeno, T., "An Experimental Study on Stability and Combustion Characteristics of an Excess Enthalpy Flame, Proceedings of the Combustion Institute, Vol. 19, pp.1503-1509, 1982.

Kyritsis, D. C., Roychoudhury, S., McEnally, C. S., Pfefferle, L. D., and Gomez, A., "Mesoscale Combustion: A First Step Towards Liquid Fueled Batteries," Experimental Thermal and Fluid Science, Vol. 28, pp 97-104, 2004.

Leach, T. T. and Cadou, C. P., "The Role of Structural Heat Exchange and Heat Loss in the Design of Efficient Silicon Micro-Combustors," Proceedings of the Combustion Institute, Vol. 30, pp. 2437-2444, 2005.

Lee, D. H. and Kwon, S., "Scale Effects on Combustion Phenomena in a Microcombustor," Microscale Thermophysical Engineering, Vol. 7, pp. 235-251, 2003.

Marbach, T. L and Agrawal, A. K., "Experimental Study of Surface and Interior Combustion Using Composite Porous Inert Media," Journal of Engineering for Gas Turbines and Power, Vol. 127, pp. 307-313, 2005.

Mital, R., Gore, J.P., Viskanta, R., "A Study of the Structure of Submerged Reaction Zone in Porous Ceramic Radiant Burners," Combustion and Flame, Vol. 111, pp. 175-184, 1997.

Muneer,.Kubie, and Grassie, Heat Transfer, London, Francis and Taylor, 2003.

Norton, D. G. and Vlachos, D. G., "Hydrogen Assisted Self-Ignition of Propane/Air Mixtures in Catalytic Microburners," Proceedings of the Combustion Institute, Vol. 30, pp. 2473-2480, 2005.

Patankar, S.V., Numerical Heat and Fluid Flow, New York, McGraw Hill, 1980.

Pickenaker, O., Pickenacker, K., Wawrzinek, K., Trimis, D., Pritzkow, W.E.C., Muller, C., Goedtke, P., Papenburg, U., Adler, J., Standke, G., Heymer, H., Tauscher, W., and Jansen, F., "Innovative Ceramic Materials for Porous-Medium Burners," Interceram, Vol. 48, No. 5 and 6, pp. 1-12, 1999.

Raithby, G.D. and Chui, E.H., "A Finite-Volume Method for Predicting a Radiant Heat Transfer in Enclosures with Participating Media," Journal of Heat Transfer, Vol. 112, pp. 415-423, 1990.

Ronney, P.D., "Analysis of Non-Adiabatic Heat Recirculating Combustors," Combustion and Flame, Vol. 135, pp. 421-439, 2003.

Rumminger, M.D., and Dibble, R.W., "Gas Temperature above a Porous Radiant Burner: Comparison of Measurements and Model Predictions," Proceedings of the Combustion Institute, Vol. 26, pp. 1755-1762, 1996.

Saravanamuttoo, H., Rogers, G., and Cohen, H., Gas Turbine Theory, New York, Prentice Hall, 2001.

Sherman, A.J., Williams, B.E., DelaRosa, M.J. and LaFerla, R., "Characterization of Porous Cellular Materials Fabricated by CVD", Proceedings of the 1990 MRS Fall Meeting, Boston, 1990.

Sirignano, W.A., Pham, T.K., and Dunn-Rankin, D., "Miniature Scale Liquid-Fuel Film Combustor, " Proceedings of the Combustion Institute, 2002.

Sullivan, J.D., Kendall, R.M., and McDougald, N.K., "Development of a Low Emission Gas Turbine Combustor," Proceedings of the AFRC International Symposium, Newport Beach, CA, 2000.

Trimis, D., and Durst, F., "Combustion in a Porous Medium- Advances and Applications," Combustion Science and Technology, Vol. 121, p. 153, 1996.

Turns, S.R., Introduction to Combustion: Concepts and Applications, New York, McGraw Hill, 2000.

Van Roode, M., Brentnall, W.D., Norton, P.F., and Edwards, B.D., "Ceramic Stationary Gas Turbine Development," Proceedings of the International Gas Turbine and Aeroengine Congress and Exposition, ASME Paper 95-GT-459, 1995.

Vican, J., Gajdeczko, B.F., Dryer, F.L., Yetter, R.A., Milius, D.L. and Aksay, I.A., "Development of a Microreactor as a Thermal Source for MEMS Power Generation," Proceedings of the Combustion Institute, Vol. 29, 2002.

Viskanta, R., 1995, "Interaction of Combustion and Heat Transfer in Porous Inert Media," in Transport Phenomena in Combustion, Ed. S.H. Chan, pp. 64-87, Taylor and Francis.

Waitz, I.A., Gauba, G., and Tzeng, Y.S., "Combustors for Micro-Gas Turbine Engines," Journal of Fluids Engineering, Vol. 120, pp. 109-117, 1998.

Wharton, J.A., Ellzey, J.L., Bogard, D.G, "An Experimental Study of Turbulence and Nonuniformities in the Exit Flow From a Porous Burner, Proceedings of the Joint Meeting of the Combustion Institute, Vol. 3, Paper PJ07, 2003.

Yetter, R.A., Yang, V., Wang, Z., Wang, Y., Milius, D. L., Peluse, M. J., Aksay, I. A., Angioletti, M. and Dryer, F. L., "Development of Meso and Micro Scale Liquid Propellant Thrusters," Proceedings 41st Aerospace Science Meeting, Paper AIAA 2003-0676, 2003.

Yuasa, S., Oshimi, K., Nose, H., Tennichi, Y., "Concept and Combustion Characteristics of Ultra-Micro Combustors with Premixed Flame," Proceedings of the Combustion Institute, Vol. 30, pp. 2455-2462, 2005.

Appendix A: Uncertainty Analysis Sample Calculations

This is the sample uncertainty calculations for the product gas temperature in Phase I combustor at z = 63 mm and the centerline. Twelve samples were collected.

Average Temperature: $T_{avg} = 1593.8$ K

Standard Deviation of Population: $s_x = 10.2$ K

Standard Deviation of the Mean: $s_{\bar{x}} = \frac{s_x}{\sqrt{n}} = \frac{10.2}{\sqrt{12}} = 2.95\,\text{K}$

Precision Error (95% Confidence): $P = t_{\alpha/2} \cdot s_{\bar{x}} = 2.201 \cdot 2.95 = 6.48\,\text{K}$

Bias Error: B = 1 K (reported by manufacturer)

Total Uncertainty: $w = \left(P^2 + B^2\right)^{0.5} = \left(6.48^2 + 1^2\right)^{0.5} = 6.56$ K

Appendix B: User Defined Function for Heat Source Calculation

```
/*********************************************/
/* UDF for specifying an energy source term    */
/*********************************************/

#include "udf.h"

DEFINE_SOURCE(energy_source, c, t, dS, eqn)
{
  real source, Qdot, r, length, Vavg, rho;

    Qdot = 460;
    r = 0.010;
    length = 0.001;
    Vavg = 1.0;
    rho = 1.25

    source = (Qdot/(3.1415*r*r*length))*C_U(c,t)*C_R(c,t)
               /(rho*Vin);
    dS[eqn] = 0;

  return source;
}
```

Appendix C: Comparison of Specific Heat Capacity of Air, Reactants and Products

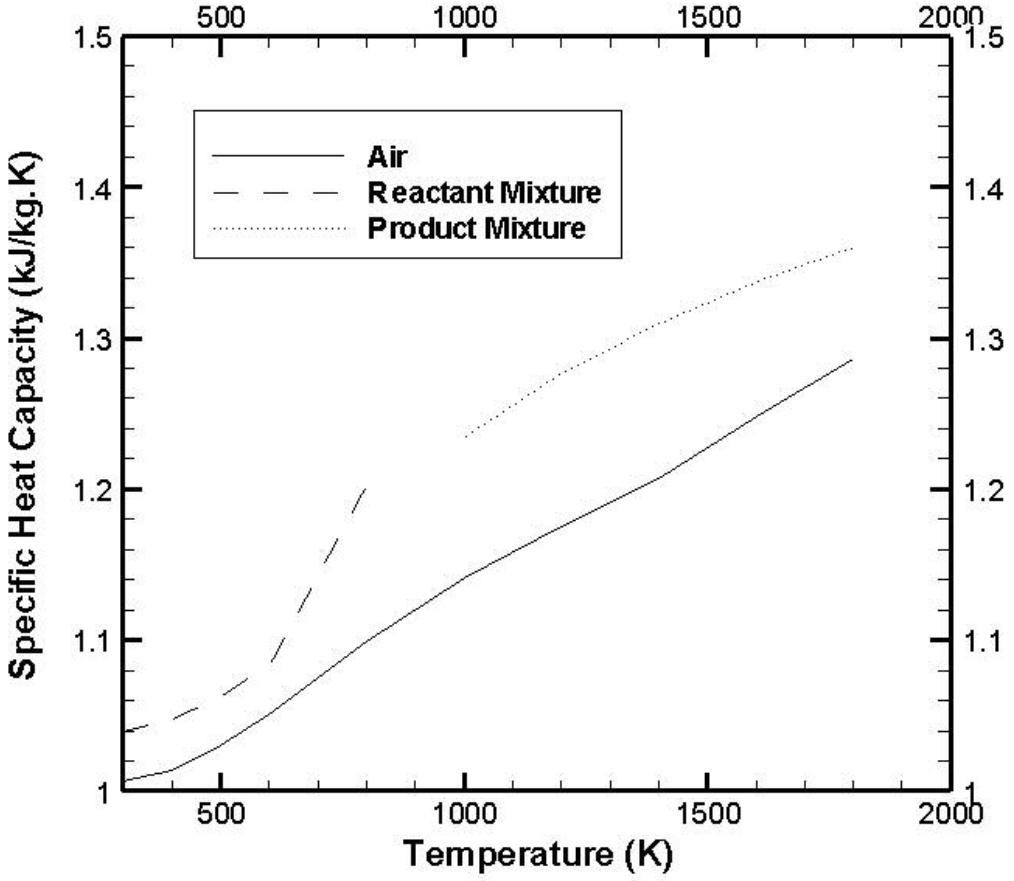

Figure AC.1. Specific heat capacity of air, reactant and product mixtures.

Appendix D: Physical Properties for Computational Model

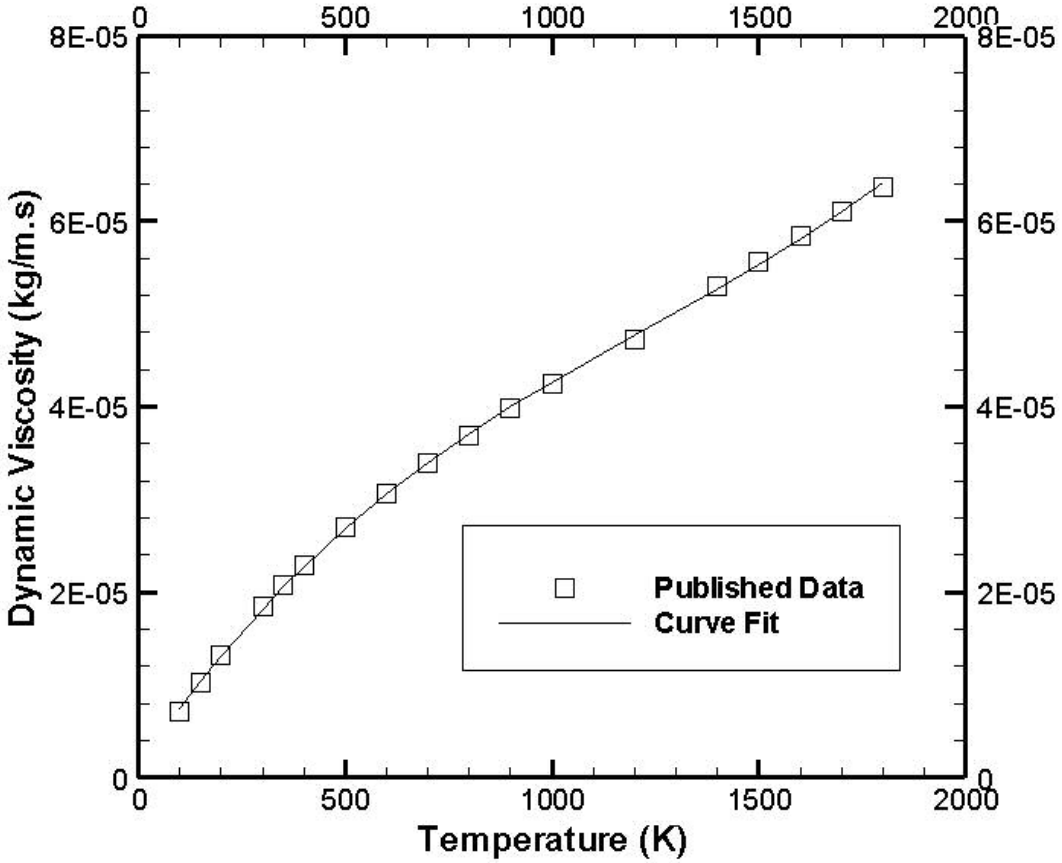

Figure A1-1. Curve Fit for Dynamic Viscosity

Equation: $\mu(T) = 1.3095 \cdot 10^{-6} + 6.5402 \cdot 10^{-8} T - 3.2924 \cdot 10^{-11} T^2 + 8.8854 \cdot 10^{-15} T^3$

$R^2 = 0.9920$

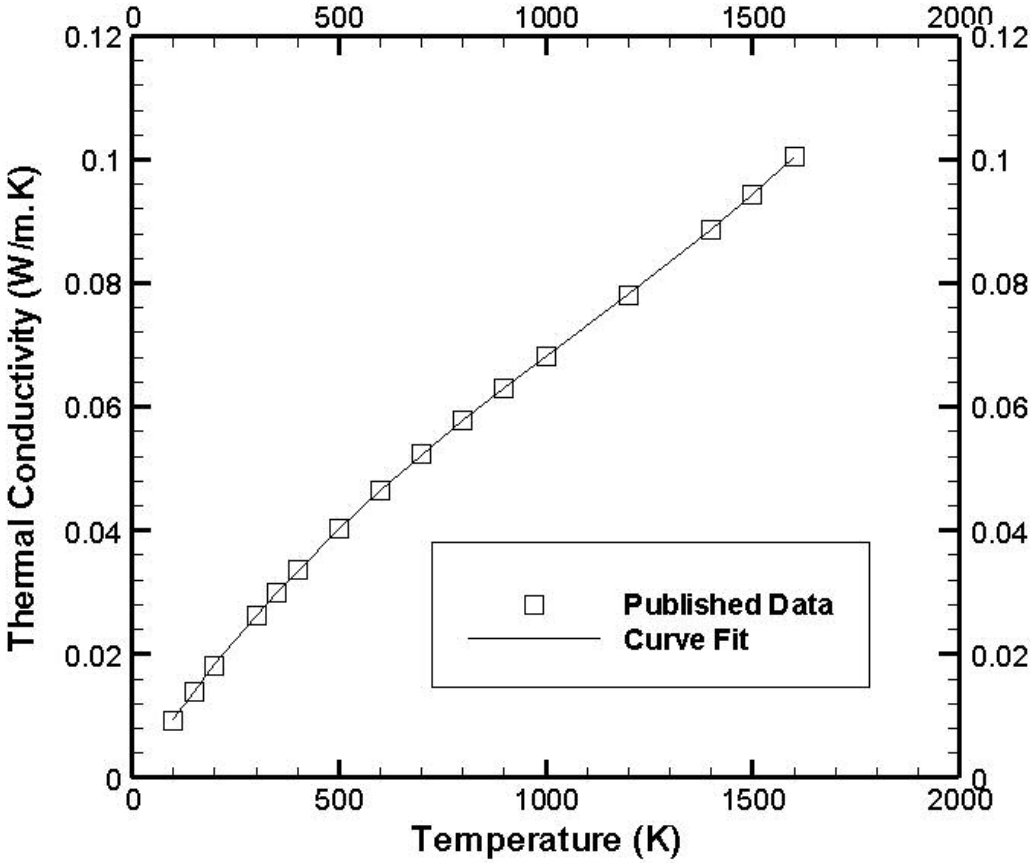

Figure A1-2. Curve Fit for Thermal Conductivity

Equation: $k(T) = 9.9902 \cdot 10^{-5} T - 4.6093 \cdot 10^{-8} T^2 + 1.4301 \cdot 10^{-11} T^3$

$R^2 = 0.9997$

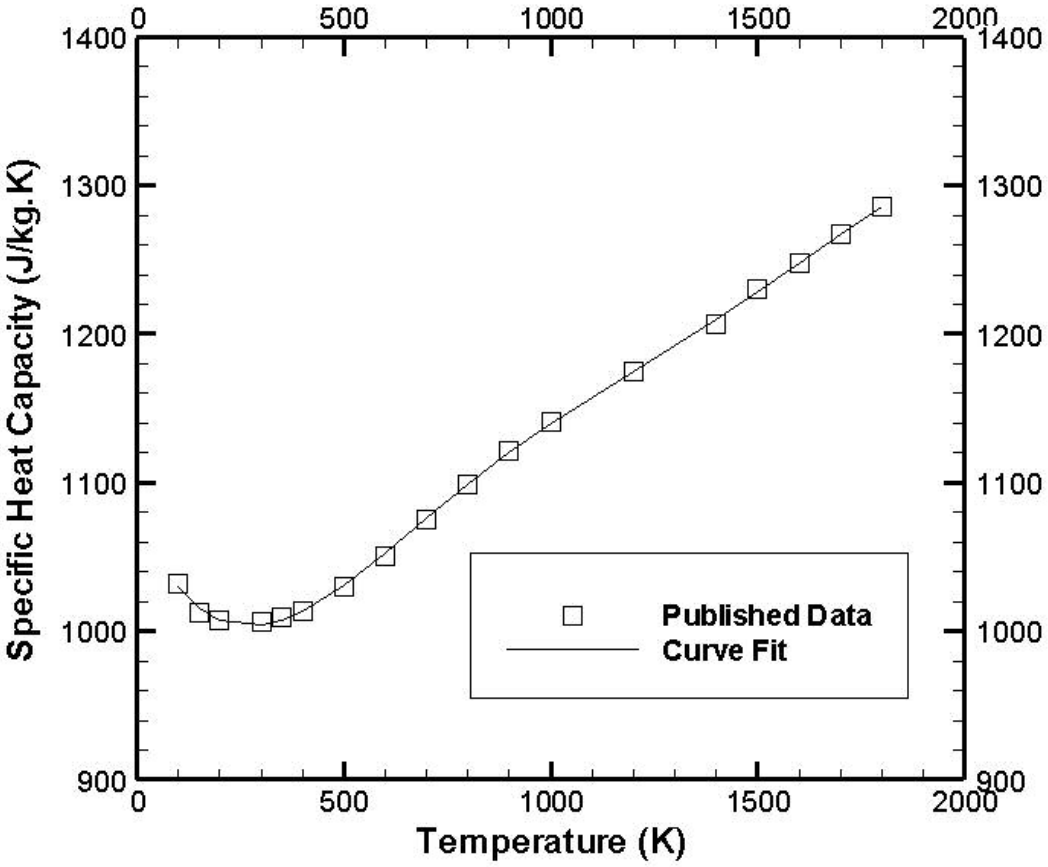

Figure A1-3. Curve Fit for Specific Heat Capacity

Equation: $$c_P(T) = 1075.8\text{-}0.60922 \cdot T + 0.0015797 \cdot T^2\text{-}1.2345 \cdot 10^{-6} \cdot T^3 + 2.5518 \cdot 10^{-10} \cdot T^4 + 1.1751 \cdot 10^{-13} \cdot T^5\text{-}4.4427 \cdot 10^{-17} \cdot T^6$$

$R^2 = 0.9997$

Appendix E: Equivalence Ratio Calculation for Phase II Mesoscale Combustor

The chemical equation for methane/air combustion is:

$$CH_4 + \frac{2}{\Phi}(O_2 + 3.76N_2) \rightarrow CO_2 + 2H_2O + \left(\frac{2}{\Phi}\right)(3.76)N_2 + \left(\left(\frac{2}{\Phi}\right) - 2\right)O_2 \qquad \text{(AD.1)}$$

Water vapor was removed from the product mixture prior to emissions concentration measurements. Therefore, the oxygen percentage (molar) is:

$$\%O_2 = \frac{\frac{2}{\Phi} - 2}{\frac{9.52}{\Phi} - 1} \qquad \text{(AD.2)}$$

The oxygen concentration was measured with an electrochemical gas analyzer and equation AD.2 was solved to determine the equivalence ratio.

Appendix F: Radiation Correction for Product Gas Temperature Measurements

The worst-case radiation error occurred when the highest temperature was measured with the thermocouple and the temperature of the surroundings was lowest. To approximate the maximum radiation error, the thermocouple temperature was taken to be 1700 K and the temperature of the surroundings was taken to be 300 K. In the experiments, 1700 K was the highest measured temperature. The thermocouple was inserted into the combustor and hence, the temperature of the surroundings was actually greater than 300 K. Taking the thermocouple bead to be our system and assuming steady state conditions, the energy balance is presented in equation F.1 and the energy balance was rearranged to give the radiation correction in equation F.2

$$0 = hA(T_t - T_f) - \sigma \varepsilon A (T_t^4 - T_\infty^4)$$

$$T_{corr} = (T_f - T_t) = \frac{\sigma\varepsilon}{h}\left(T_t^4 - T_\infty^4\right) \approx \frac{\sigma\varepsilon d}{2k_f}\left(T_t^4 - T_\infty^4\right)$$

Hence, the maximum radiation for correction is

$$T_{corr} = (5.67*10^{-8}\ W/m^2K^4)(0.20)(0.000075\ m)/(2*0.1\ W/m.K)*[(1700\ K)^4 - (300\ K)^4]$$

$$= \underline{35.5\ K}$$